TECHNISCHE UNIVERSITÄT MÜNCHEN

Fakultät für Chemie

Lehrstuhl für Biotechnologie

Molecular Insights into Antibody Light Chain Pathogenicity

Pamina Kazman

Vollständiger Abdruck der von der Fakultät für Chemie der Technischen Universität München zur Erlangung des akademischen Grades eines

Doktors der Naturwissenschaften (Dr. rer. nat.)

genehmigten Dissertation

Vorsitzende: Prof. Dr. Cathleen Zeymer

Prüfer der Dissertation:

1. Prof. Dr. Johannes Buchner
2. Prof. Dr. Bernd Reif
3. Prof. Linda Hendershot, Ph.D.

Die Dissertation wurde am 01.07.2020 bei der Technischen Universität München eingereicht und durch die Fakultät für Chemie am 17.08.2020 angenommen.

CONTENTS

ABSTRACT

Light chain (AL) amyloidosis is a rare disease caused by an underlying plasma cell dyscrasia. It is characterized by the extracellular deposition of insoluble amyloid fibrils derived from antibody light chain (LC) truncations. Usually, multiple organs are involved and the amyloid deposits gradually impair organ function. Symptoms vary widely, depending on the affected organs. The experience of symptoms mostly indicates an advanced stage of disease and a poor prognosis, stressing the importance of increasing the scientific knowledge about AL amyloidosis

In most cases, fibril formation of LCs occurs upon a proteolytic cleavage event whereupon destabilizing point mutations in the variable domain (V_L) of the LC develop their pathogenic effect. In the scope of this thesis, the aim was to determine the LC truncation causing AL amyloidosis in one specific patient, to trace back the destabilization and amyloidogenicity to a specific point mutation and to elucidate the molecular mechanism of pathogenicity. It was found that in the V_L fragment a valine at position 81 causes domain destabilization and amyloidogenicity. The mutant exhibited surface hydrophobicity and enhanced the conformational dynamics mainly affecting the C-terminal region. A back mutation to leucine leads to retrieval of domain stability and prevents the domain from entering the pathogenic pathway.

Different immunohistochemical studies revealed the co-aggregation of other proteins or plasma factors in deposits of amyloid-related diseases. Therefore, the effect of some of these proteins that potentially come into contact with the LCs during disease development upon fibril formation was tested *in vitro*. The ER resident chaperone BiP and its co-chaperone ERdj3 are involved in antibody folding and were found to inhibit fibril formation in a concentration-dependent manner. Furthermore, ERdj3 was present in fibril deposits extracted from the patient's abdominal fat tissue, indicating an involvement in disease as an extracellular chaperone. Additionally, the extracellular chaperone Apolipoprotein E4 (ApoE4) that was detected in amyloid deposits of different diseases, was found to in- or decrease fibril formation of a pathogenic LC truncation in a concentration dependent way.

A lag phase precedes the formation of fibrils. The comparably long time of this phase and the significantly different structural features of monomeric and fibrillar LCs indicate the occurrence of important structural rearrangements. Here, the events taking place during the lag phase were decrypted in detail. They include the formation of specific short-lived oligomers and the further stabilization of these intermediates by the formation of fibrils. The ER co-chaperone ERdj3 was identified as a stabilizing factor for intermediate species.

Further, it is unclear how exactly LCs are able to escape ER quality control and reach the circulation without pairing with corresponding heavy chains (HC). In cell culture studies, the expression, secretion, dimerization and aggregation of different patient-derived LCs was tested. Different patterns of LC secretion could be identified that fit the LC concentration in patient serum. Pathogenic LCs that are not severely compromised in their structural features pass through the ER without being recognized by the ER quality control. Those that are strongly destabilized are recognized, retained and degraded.

Together, the studies performed in the context of this thesis reveal novel insights into the molecular events and mechanisms occuring during LC amyloidogenesis.

ZUSAMMENFASSUNG

Leichtketten (AL) Amyloidose ist eine seltene Erkrankung, die durch eine zugrunde liegende Plasmazelldyskrasie verursacht wird. Sie ist durch die extrazelluläre Ablagerung unlöslicher Amyloidfibrillen gekennzeichnet, die aus Verkürzungen der leichten Kette (LC) bestehen. Normalerweise sind mehrere Organe betroffen, deren Funktion durch die Amyloidablagerungen allmählich beeinträchtigt wird. Die Symptome variieren stark, abhängig von den betroffenen Organen. Deren Auftreten weist meist auf ein fortgeschrittenes Krankheitsstadium und eine schlechte Prognose hin, was eine allgemeine Verbesserung der wissenschaftlichen Kenntnisse über Leichtketten Amyloidose hervorhebt.

Die Fibrillenbildung der LCs tritt meist nach einer proteolytischen Spaltung auf, woraufhin destabilisierende Punktmutationen in der variablen Domäne (V_L) der LC ihre pathogene Wirkung entwickeln. Im Rahmen dieser Doktorarbeit war es das Ziel, die LC Verkürzung, die bei einem bestimmten Patienten krankheitsauslösend ist, zu bestimmen. Des Weiteren sollten die Mutation(en) identifiziert werden, die für die Destabilisierung und Amyloidogenität verantwortlich sind und der damit verbundene molekulare Mechanismus der Pathogenität aufgeklärt werden. Es konnte gezeigt werden, dass ein Valin an Position 81 ausschlaggebend für die Destabilisierung und die Amyloidbildung der Domäne, nach proteolytischer Spaltung, ist. Bedingt ist der amyloidogene Effekt durch eine Erhöhung der Oberflächen-Hydrophobizität und die Verstärkung der Konformationsdynamik, die hauptsächlich den C-terminalen Bereich der Domäne betrifft. Eine Rückmutation zu Leucin führt zu einer Wiederherstellung der Domänenstabilität und verhindert die Entwicklung der pathogenen Eigenschaften.

Verschiedene immunohistochemische Studien zeigten die Co-Aggregation mehrerer anderer Proteine oder Plasmafaktoren in vielen Amyloid Krankheiten. Im Rahmen der Arbeit wurde die Wirkung verschiedener Proteine, die möglicherweise während der Krankheitsentwicklung mit den LCs in Kontakt kommen getestet. Die ER Chaperone BiP und ERdj3 sind an der Antikörperfaltung beteiligt. Hier wurde festgestellt, dass beide die Fibrillenbildung in konzentrationsabhängiger Weise inhibieren. Des Weiteren wurde ERdj3 in Amyloidablagerungen des abdominalen Fettgewebes des Patienten gefunden, was auf eine Beteiligung des Co-Chaperons an der Krankheit hinweist. Zusätzlich wurde festgestellt, dass das extrazelluläre Chaperon Apolipoprotein E4 (ApoE4), das in Ablagerungen verschiedener Krankheiten nachgewiesen wurde, die Fibrillenbildung einer pathogenen LC-Verkürzung konzentrationsabhängig verstärkt oder verringert.

Der Fibrillenbildung geht eine Lag-Phase voraus. Die vergleichsweise lange Dauer dieser Phase und die signifikant unterschiedlichen Strukturmerkmale von monomeren und fibrillären LCs weisen auf wichtige strukturelle Umlagerungen hin. Im Rahmen dieser Arbeit wurden die Ereignisse während der Verzögerungsphase im Detail entschlüsselt. Sie umfassen die Ausbildung eines spezifischen kurzlebigen Oligomermusters und die darauffolgende

Stabilisierung dieser Zwischenform durch Fibrillenbildung. Das ER Co-Chaperon ERdj3 stabilisiert die intermediären Spezies.

Es ist weiterhin unklar, wie LCs der Qualitätskontrolle im ER entkommen und in den Blutkreislauf gelangen können ohne mit entsprechenden schweren Ketten (HC) zu assemblieren. In Zellkulturstudien wurde die Expression, Sekretion, Dimerbildung und Aggregation verschiedener Patienten LCs getestet. Es konnten verschiedene Muster identifiziert werden, die möglicherweise mit der LC Konzentration im Patientenserum und mit dem Schweregrad der Krankheit korrelieren. Pathogene LCs, die nicht maßgeblich in ihren strukturellen Eigenschaften beeinträchtigt sind, passieren das ER ohne von der Qualitätskontrolle erkannt zu werden. Solche LCs, die stark destabilisiert oder fehlgefaltet sind werden erkennt, im ER zurückgehalten und abgebaut.

Zusammenfassend zeigen die Experimente, die in dieser Arbeit durchgeführt wurden, neuartige Einblicke in molekulare Ereignisse und Mechanismen, die während der Amyloidbildung von LCs stattfinden.

1. Introduction

1.1. Biosynthesis of Secretory Pathway Proteins – The Endoplasmic Reticulum

Proteins are among the most abundant organic molecules in cells. They are highly diverse and carry out a wide variety of functions. Each of these macromolecules is composed of a unique amino acid sequence. In order to obtain functionality, the formation of a specific three-dimensional fold is indispensable (Dobson, 2003).

For folding of secretory pathway proteins, the endoplasmic reticulum (ER) plays an important role. The ER is the largest membrane-bound organelle in the eukaryotic cell. It is a large, dynamic structure and displays the major site of protein synthesis, protein folding, lipid and steroid synthesis, carbohydrate metabolism and calcium storage (Schwarz and Blower, 2016). Almost a third of all human proteins enter the ER and traverse the secretory pathway for integration into the membrane or secretion into organelles or the extracellular space (Buck et al., 2007). Newly synthesized polypeptide chains carrying an N-terminal ER signal sequence are recognized by the signal recognition particle (SRP) which targets the complex of ribosome:polypeptide:SRP to the SRP-receptor on the ER membrane. The growing peptide chain is co-translationally transported across the ER membrane via the Sec61 translocon (Jomaa et al., 2017). Proteins that do not carry N-terminal signal sequences and are thus not detected by SRP can be posttranslationally translocated into the ER. Chaperones and co-chaperones like Hsp70 and Hsp40 recognize the hydrophobic stretches on the unfolded protein, keep it in an unfolded, translocation-competent state and direct it to the translocation complex composed of Sec61 and the transmembrane proteins Sec62/Sec63 (Jung et al., 2014; Shao and Hegde, 2011). Exact details about the translocation mechanism are still unclear, but most likely they involve binding of the ER luminal chaperones and co-chaperons (Nicchitta and Blobel, 1993). A nascent protein in the ER destined for secretion undergoes a number of processing steps which may include cleavage of the signal sequence, disulfide bond formation or N-linked glycosylation. Concomitantly, protein folding takes place (Bulleid, 2012; Schwarz and Blower, 2016).

1.2. Principles of Protein Folding

During the process of protein folding, polypeptide chains convert into a specific three-dimensional fold. The correct fold is prerequisite to the biological function of any protein and is therefore indispensable for organism integrity (Orengo et al., 1999). The concept of Anfinsen states that the characteristic fold is already determined by the individual amino acid sequence (Anfinsen et al., 1961). According to Ramachandran, this already restricts the field of possible

conformations for a protein by the limited options of peptide bond arrangements due to unfavorable steric conflicts between the β carbon of side chains and/or carbonyl oxygens (Ramakrishnan and Ramachandran, 1964). However, this still leaves a large number of possible conformations and a random sampling would take an astronomous amount of time (Levinthal, 1969). Another force that reduces the complexity of folding pathways are the side chain characteristics. They dictate protein folding by intramolecular non-covalent interactions like hydrogen bonds, salt bridges and hydrophobic interactions (Stevens and Argon, 1999). The latter display the major driving force in folding and assembly, overall known as the hydrophobic effect (Camilloni et al., 2016). Due to the aqueous surrounding of proteins, hydrophobic side chains pack to a tightly arranged core that is shielded from polar water molecules. Hydrophobic interactions are driven by the entropy increase of water molecules and lead to an energetically favored state of the protein (Levy and Onuchic, 2006; Privalov and Makhatadze, 1993). Thus, folding guides the protein to adopt the most thermodynamically stable conformation while at the same time ensuring the flexibility for fulfilling their biological function. The folding funnel describes the energy landscape of the transition of a protein from its unfolded state to the native state (Figure 1) (Bartlett and Radford, 2009; Bryngelson et al., 1995; Neira and Fersht, 1999). According to this model, polypeptide chains in their unfolded states are driven to select lower energy structures as interactions occur with the ultimate goal to fold into the native state accomplishing minimal Gibbs free energy (Dobson, 2003). Folding pathways include multiple routes with transient intermediates that are present as non-native local minima in the funnel. These folds can act as kinetic traps along the route to the native fold. The loss of entropy, depicted by the transition from a broad into a narrower funnel, is large in early folding stages and becomes limited by the formation of native stabilizing side chain interactions. Depending on the conditions modulating entropy and free energy, the folding pathway is either stopped or paused at an intermediate state. Intermediates can be on- or off-pathway and thus either lead to the native state or to partially unfolded intermediates, aggregates or amyloid fibrils, respectively (see chapter 1.7) (Onuchic and Wolynes, 2004).

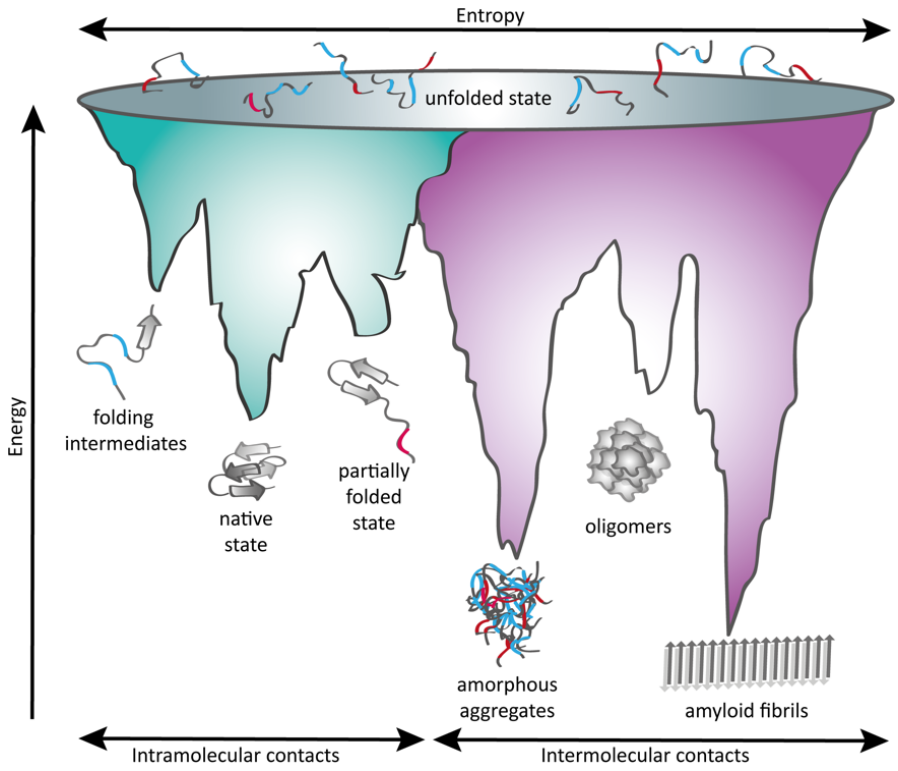

Figure 1. Schematic representation of the folding funnel energy landscape (adapted with permission from Hartl and Hayer-Hartl, 2009). The green surface shows unfolded high energy state conformations "funneling" via intramolecular contacts towards the native state. The green surface shows the conformations formed by intramolecular contacts directed towards the native state. The purple surface shows the higher order conformations moving towards conformations formed by intermolecular contacts.

Besides the amino acid sequence, known as the primary structure, proteins also adopt a secondary, tertiary and potentially quaternary structure upon folding. Secondary structure elements are made up from α-helices, β-strands, loops and random coil elements. These folds were already predicted in 1951 by Pauling and colleagues (Pauling et al., 1951). They result from repetitive hydrogen bonds between protein backbone segments. The tertiary structure evolves from the three-dimensional orientation of secondary structure elements. It is stabilized by interactions between amino acid side chains. Quaternary structure involves two or more individually folded polypeptide chains (Richardson, 1981).

1.3. Protein Folding In The Cell – Molecular Chaperones

While all the above aspects of protein folding are also valid in a cellular environment, the environment *in vivo* is significantly different. With protein concentrations of 300-400 g/l^{-1} in the cytosol and 100-400 g/l^{-1} in the ER, the intracellular space is extremely crowded and the temperatures are high which both challenges folding (Araki and Nagata, 2012; Hartl et al., 2011). Thus, the correct processing of a protein requires a myriad of other proteins to fold efficiently and on a biologically relevant timescale. Most prominent components assisting *de*

novo protein folding include molecular chaperones, defined as factors that help other proteins to adopt their functional active fold by inhibiting unproductive interactions in the client. They are widely known as heat-shock proteins (HSPs), as they were first discovered in correlation with heat shock and are upregulated upon cell stress when aggregation-prone folding intermediates accumulate (Richter et al., 2010). Nevertheless, many HSPs are constitutively expressed, and are involved in a large number of proteome-maintenance functions like *de novo* folding, proteins assembly, protein trafficking and protein degradation. Based on their molecular weight, molecular chaperones are divided into several subclasses, i.e. HSP40, HSP70, HSP90, small HSPs (sHSPs) (Buchner, 1996; Hartl et al., 2011). They often bind to hydrophobic regions that are surface-exposed in unfolded or partially folded polypeptides during early folding stages or upon protein misfolding (Walter and Buchner, 2002). The mechanism of folding assistance varies between the subclasses. Often, ATP binding and hydrolysis are involved as an energy source. In general, chaperone function is a complex cellular interplay including many other factors like co-chaperones or nucleotide exchange factors (NEFs) (Young et al., 2004).

1.4. Protein Folding in the ER

1.4.1. ER Quality Control

The ER milieu differs from that of the cytosol regarding ions, redox conditions and molecular chaperones. As a result, it displays an optimized environment for folding and maturation of proteins destined for membrane integration, transfer into other organelles or secretion. Such proteins are important for i.e. gene regulation, extracellular carrier functions, transport or receptor functions. Thus, unassembled or only partially folded proteins can be damaging and toxic to the cell. As downstream organelles usually don't support further protein folding, a strict ER quality control (ERQC) system is essential (Ellgaard and Helenius, 2003). The term ERQC covers all processes to monitor and control the maturation of nascent secretory proteins. In this context, the ER possesses a number of molecular chaperones and folding factors including the heavy chain binding protein BiP, the calnexin/calreticulin system coming along with a number of co-chaperones, GRP94, oxidoreductases, and ERp57 (Braakman and Hebert, 2013). The ER chaperones and folding factors recognize basic structural and biophysical characteristics in a protein to distinguish native from non-native proteins. These features are hydrophobic regions, free SH groups of cysteines and the tendency to aggregate. A protein possessing one or more of these features is bound and retained in the ER (Araki and Nagata, 2012).

1.4.2. Misfolding in the ER

1.4.2.1. ER-Associated Degradation (ERAD)

Despite numerous cellular factors for protein folding, some newly synthesized proteins fail to attain their correct structure. Proteins that are unable to mature correctly and can't be brought into their native, functional state are recognized and either retained in the ER or retro-translocated to the cytosol to enter the ER-associated degradation pathway (ERAD) and be degraded (Nakatsukasa et al., 2014). ERAD involves the ubiquitine - 26S proteasome system. Misfolded proteins subjected to ERAD are transported across the ER membrane via a channel formed by the E3 ubiquitin ligase. On the cytosolic side of the ER, the substrate becomes polyubiquitinated by the ligase. Thereupon, it is extracted from the membrane and ATP-dependently released into the cytosol for degradation by the proteasome (Ruggiano et al., 2014; Wu and Rapoport, 2018).

1.4.2.2. Unfolded Protein Response (UPR)

The degree of misfolding varies and can have several reasons, i.e. mutations. In general, the protein folding capacity in the ER is dictated by the capacity of ER chaperones and folding factors. An imbalance of chaperones and the load of misfolded proteins leads to ER stress. The cellular response is called the Unfolded Protein Response (UPR) (Figure 2). It initiates an ER-to-nucleus signal transduction pathway aiming to globally halt further protein synthesis while at the same time enhancing the folding and degradation capacities in the ER. UPR comprises three steps, sensed by different transmembrane proteins: i) dsRNA-activated protein kinase-like protein kinase (PERK), ii) inositol-requiring enzyme 1α (IRE1α) and iii) activating transcription factor 6 (ATF6). BiP keeps the UPR sensors in a stable inactive complex until the accumulation of un- and misfolded proteins in the ER sequester BiP, leading the UPR activation (Bertolotti et al., 2000; Kopp et al., 2019; Walter and Ron, 2011) (Figure 3).

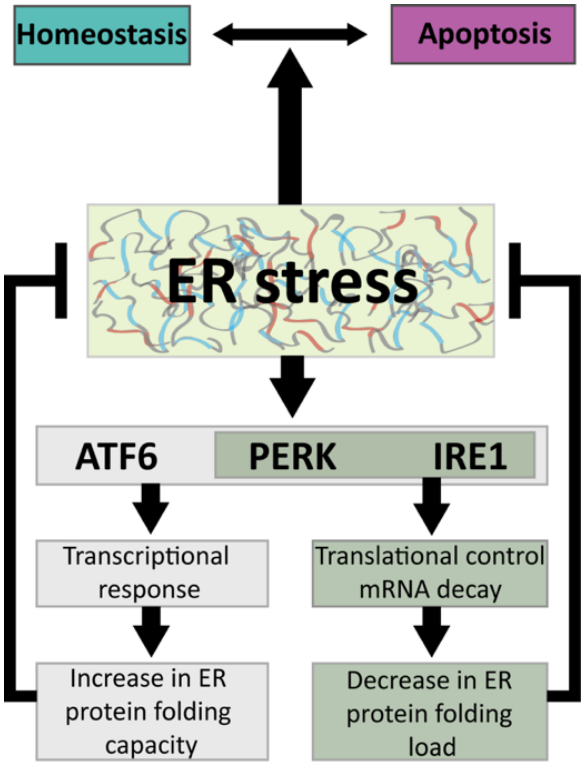

Figure 2. Diagram of the core elements of the UPR signaling network (adapted with permission from Walter and Ron, 2011). High misfolded protein load in the ER causes ER stress. This activates the three UPR stress sensors ATF6, PERK and IRE1. All activated factors lead to the production of transcription factors increasing protein folding capacity in the ER. PERK and IRE1 additionally decrease the protein load in the ER via eIF2α phosphorylation. Both pathways lead to a negative feedback loop to cope with ER stress. If protein homeostasis can't be restored, cell apoptosis is activated.

BiP dissociation leads to PERK activation by homodimerization and autophosphorylation. Active PERK phosphorylates the eukaryotic translation initiation factor 2α (eIF2α), which leads to a global translation arrest and a reduction of the protein load in the ER (Liu and Kaufman, 2003).

IRE1 oligomerizes upon BiP dissociation and is thereupon activated by autophosphorylation of its cytosolic domain. Active IRE1 cleaves XBP1 mRNA leading to an active XBP1 protein, which regulates genes that encode for proteins enhancing ER folding capacity like chaperones, co-chaperones or ERAD factors (Cox et al., 1993; Shamu and Walter, 1996; Walter and Ron, 2011).

ATF6 traffics to the Golgi upon UPR activation. There, it is activated by proteolytic cleavage and mediates adaptive response of UPR by inducing genes coding for proteins that increase the ER folding capacity. ATF6 also upregulates XBP1 mRNA leading to a feed-forward loop of the UPR (Shoulders et al., 2013). UPR also stimulates autophagy as its activation factors also aid in the regulation of autophagy related genes, which further lowers the load of misfolded proteins in the ER (Kouroku et al., 2007; Wang et al., 2014).

By transcriptionally remodeling the ER proteostasis pathways and by this the secretion of misfolded, aggregation-prone proteins during ER stress, the UPR also indirectly regulates extracellular proteostasis. Deficiencies in proteostasis facilitate numerous protein aggregation diseases (see chapter 1.6) (Genereux et al., 2015).

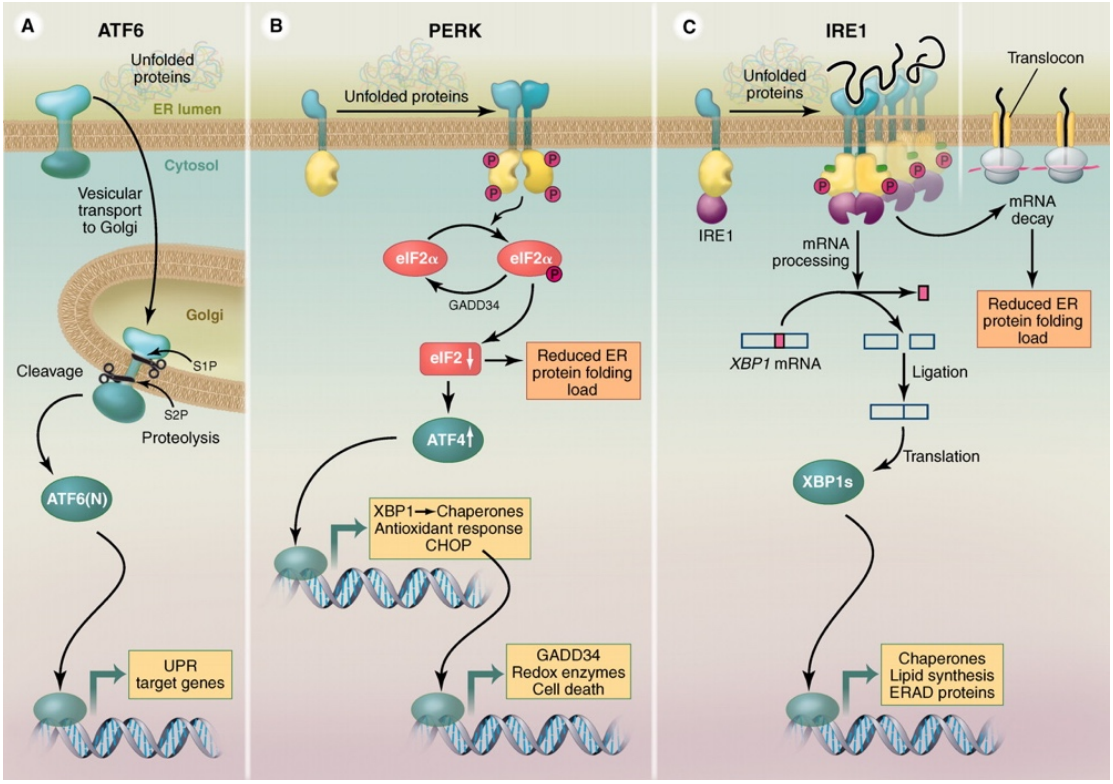

Figure 3. Three branches of UPR mediated stress response by the stress sensors A) ATF6, B) PERK and C) IRE1 (reprinted with permission from AAAS (Walter and Ron, 2011)). Sensor proteins sense protein folding conditions in the ER. ATF6 transmits stress response by regulating proteolysis, PERK by translational control and IRE1 by mRNA splicing. Additionally, PERK and IRE1 decrease the protein load in the ER by suppressing translation and degrading mRNA.

1.4.2.3. Heavy Chain Binding Protein BiP and the DnaJ-like Co-Factor ERdj3

During ER stress, most ER molecular chaperones are transcriptionally upregulated through UPR pathways to alleviate the aggregation of misfolded proteins and to promote protein refolding. One major ER resident chaperone is the Hsp70 family member BiP. It plays a role in interacting with newly synthesized proteins and is responsible for maintaining the permeability barrier of the ER during co-translational protein translocation and retro-translocation of misfolded proteins. Besides, it senses ER stress conditions and activates the unfolded protein response (UPR), as described in chapter 1.4.2.2 (Pobre et al., 2019). BiP comprises an N-terminal binding domain (NBD) containing the ATPase site, a C-terminal substrate binding domain (SBD) containing a β-sandwich domain that binds the substrate and an α-helical lid (Figure 4). The chaperone can form dimers and higher oligomers. However, only the monomeric form binds substrates. In the ATP state, BiP has a low protein binding

affinity and high on and off rates for substrates, whereas in the ADP state it is vice-versa (Kassenbrock and Kelly, 1989; Marcinowski et al., 2013).

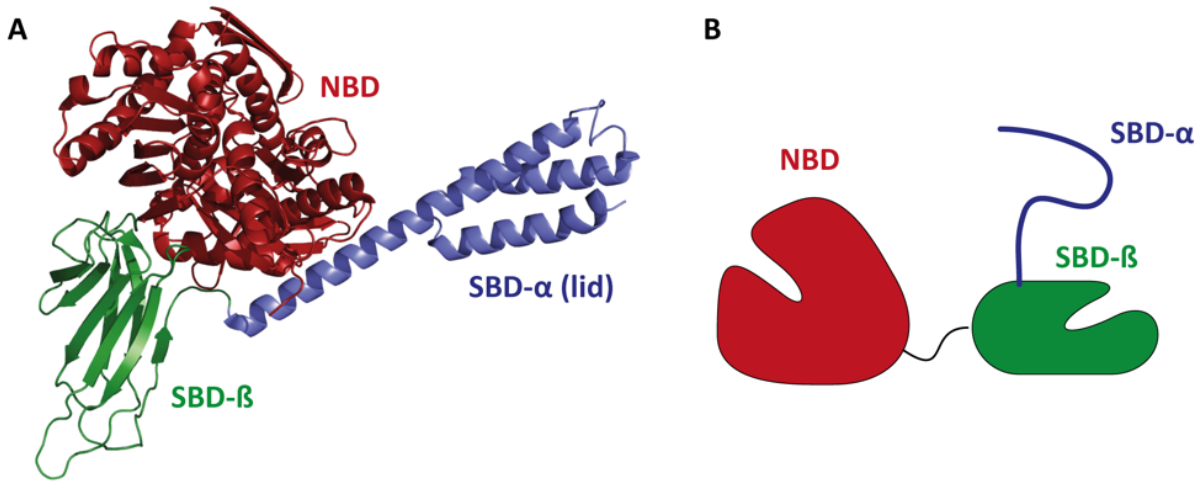

Figure 4. Domain organization of the ER Hsp70 BiP. A) Crystal structure of human BiP (PDB: 5E84). BiP comprises an N-terminal nucleotide binding domain (NBD), shown in red, and a C-terminal substrate binding domain (SBD) separated in an α a β sub-domain, depicted in blue and green, respectively. B) Schematic presentation of the BiP domains in the same colors as in A.

Under non-stress conditions, the functions of BiP are assisted by ER-localized DnaJ (also called Hsp40) co-factors called ERdjs. To date, seven ER DnaJ family members are known. Based on their domain structure, they can be divided into three sub-types: Type I-III or DNAJA, DNAJB and DNAJC (Figure 5A) (Cheetham and Caplan, 1998). All types share the common feature of harboring a J domain. This domain comprises four α-helices with a highly conserved His-Pro-Asp (HPD)- motif which is essential for the stimulation of ATPase activity in BiP (Figure 5B) (Kampinga and Craig, 2010; Tsai and Douglas, 1996). Type I J proteins further incorporate a Gly/Phe rich region, that is thought to provide a flexible linker for the substrate binding domain, a cysteine-rich zinc-binding domain and a C-terminal dimerization domain. Type II proteins possess the same domains as type I J proteins, except the cysteine-rich domain. Type III proteins only contain the J domain. Type I and type II J proteins can directly bind to clients, whereas only some proteins belonging to type III share this feature. In the ER J proteins of all sub-classes are present. They were numbered and named ERdj1-7, according to their discovery (Pobre et al., 2019).

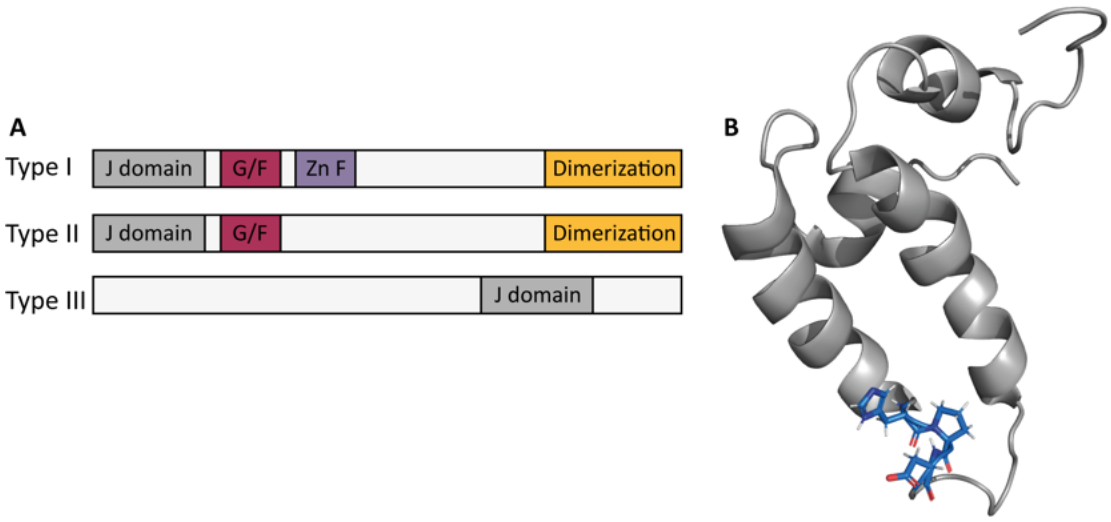

Figure 5. Domain organization of Type I-III J proteins (*adapted from Tamadaddi and Sahi, 2016).* A) Schematic overview of J proteins. Type I J proteins comprise a J domain (grey), a Gly/Phe rich domain (magenta), a Cys-rich zinc finger domain (purple) and a dimerization domain (yellow). Type II J proteins possess the same domains except the zinc finger domain. Type III J proteins comprise only the typical J domain at a random position in the protein. B) J domain structure of the *E. coli* DnaJ with with HPD motif depicted in blue (PDB: 1BQ0).

1.4.2.4. ERdj3 – The Link Between ER Stress and Extracellular Proteostasis

ERdj3 is an ER resident type II J protein that is present as a tetramer (Chen et al., 2017). Its mRNA and protein levels were found to be significantly upregulated upon UPR activation. In the ER it binds to misfolded or unfolded proteins and delivers them to BiP for ATP-dependent chaperoning (Shen and Hendershot, 2005). Lacking the C-terminal KDEL ER-retention sequence, as well as a transmembrane domain, ERdj3 is a secretion-potent ER co-chaperone and is known to be involved in extracellular proteostasis. In response to ER stress, the J protein can be secreted, alone or in a complex with its substrate, into the extracellular space to prevent misfolding or aggregation of secreted proteins. The process is regulated by BiP availability. Therefore, ERdj3 can either function as an ATP-independent extracellular chaperone, or as an "ATP-dependent" co-chaperone of BiP (Figure 6) (Genereux et al., 2015; Shen and Hendershot, 2005).

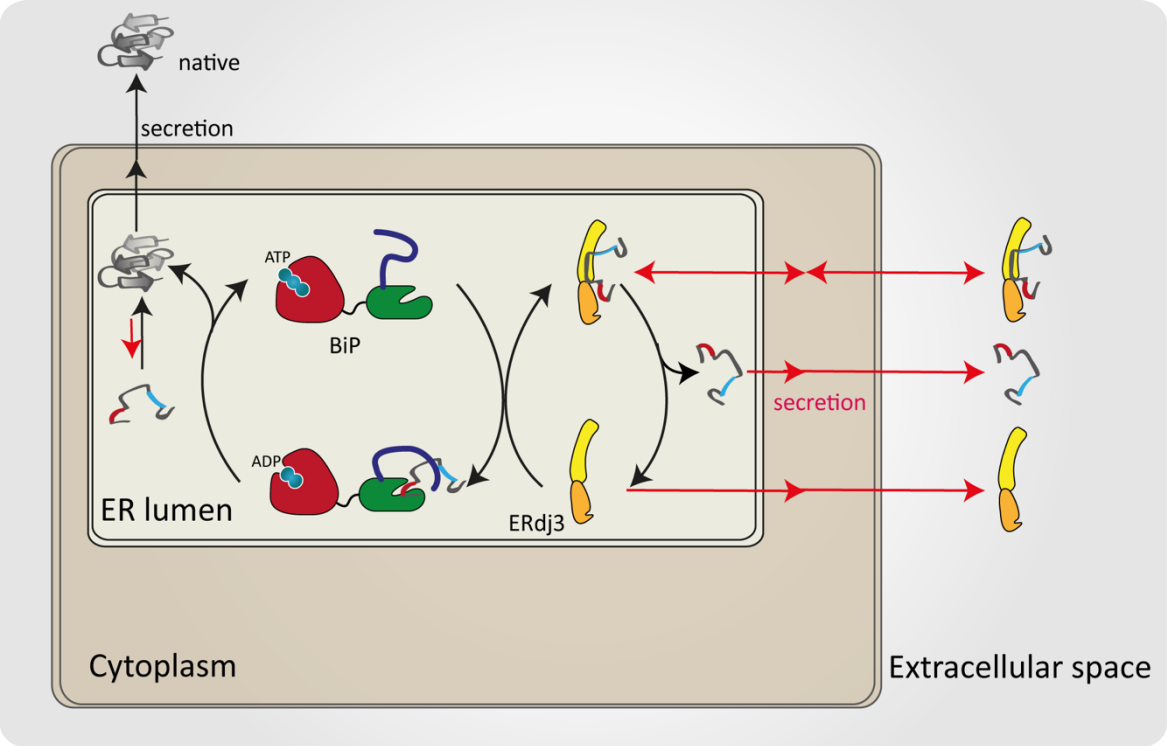

Figure 6. Cellular chaperone cycle of the ER chaperones BiP and ERdj3 under normal and stress conditions. Under normal conditions (black arrows) ERdj3 transports mis- or unfolded protein substrates to BiP and increases ATP hydrolysis which increases substrate affinity. The substrate is folded and released by BiP. Under stress conditions (red arrows), when misfolded protein accumulates in the ER lumen, ERdj3 and the misfolded protein can escape the ER either alone or in a complex and reach the extracellular space. Also, native secreted protein can enter fibrillation pathway if unstable.

1.5. Extracellular Proteostasis

Once, proteins are secreted into the extracellular space, the environment changes significantly (Araki and Nagata, 2012). Proteins are surrounded by extracellular fluids like blood or interstitial fluid that contain many other proteins, plasma factors and more. Additionally, pH changes or, in the case of blood plasma, shear forces deriving from enforced circulation display stress factors for the overall protein fold. As a consequence, protein stability is of major importance in the extracellular space to prevent proteins from misfolding (Mărgineanu and Ghetie, 1981). Aggrevating physical differences between the intra- and extracellular environment hamper the possible existence of similar chaperone systems. One significant variance is the low concentration of ATP outside of the cell (Farias et al., 2005). Also, intracellular chaperones have only been found in trace amounts in extracellular fluids, indicating the unlikeliness of them to play a substantial role in proteostasis upon secretion (Genereux et al., 2015; Molvarec et al., 2006; Walsh et al., 2001). A number of specific extracellular chaperones have been identified during recent years (Table 1). Most of them possess similarities to the sHsp family and lack ATPase activity. Despite their inability to actively refold proteins, they are able to stabilize misfolded proteins and thus inhibit their

irreversible aggregation and prevent them from developing cytotoxic effects (Wyatt et al., 2012). Numerous human diseases arise from the misfolding and aggregation of extracellular proteins, stressing the need of a better understanding of the extracellular interplay. Additionally, increasing evidence hints towards the high cytotoxicity of intermediate oligomeric forms of disease-causing proteins. Thus, the interest towards the discovery of extracellular chaperones as possible targets for intervention or as biomarkers rises (Thambisetty, 2010; Wyatt et al., 2012). A list of abundant extracellular chaperones is given in table 1. Most of them have been found and studied in the context of Alzheimer's disease.

Table 1. Overview over some abundant extracellular chaperones. Data are summarized from (Wyatt et al., 2012).

Extracellular chaperone	Function	Plasma concentration	Role in disease
Clusterin (apoJ)	Regulation of complement Apoptosis Protease inhibition Lipid transport	0.035-0.105 mg/ml (Wyatt et al., 2012)	Alzheimer's Disease
Haptoglobin (Hp1-1, Hp1-2, Hp1-3)	Sequestration of hemoglobin Regulation of cathepsin B activity Angiogenesis Immune system	0.3-2.0 mg/ml (Wyatt et al., 2012)	Atherosclerosis
α_2-Marcroglobulin	Protease inhibition Carrier protein	1.5-2.0 mg/ml (decline with age) (Wyatt et al., 2012)	Alzheimer's disease
Apolipoprotein E4 (ApoE4)	Lipid and cholesterol transportation	0.027 – 0.065 µg/ml for ε4/ε4 genotype (Rezeli et al., 2015)	Alzheimer's disease, Down syndrome, spongiform encephalopathies, Diabetes

1.6. Protein Misfolding Disorders

Cellular processes like regulation of the cell cycle, translocation, secretion, trafficking or the immune response directly depend on correct folding and unfolding events. Consequently, aberrant folding often gives rise to disease (Radford and Dobson, 1999). Some misfolding diseases, i.e. cystic fibrosis, result from the loss-of-function which is the inability of a misfolded protein to fulfill its proper function. Others result from the toxic gain-of-function. In this case, the misfolded and aggregation-prone protein escapes protective mechanisms and reaches into the extracellular space. Such proteins are likely to aggregate in tissues and organs which is accompanied by cell toxicity. A large number of diseases can directly be linked to deposited protein aggregates, including Alzheimer's or Parkinson's disease, type II diabetes, forms of amyloidoses or some types of cancer (Dobson, 2003; Hartl, 2017). The majority of them occur in an age-dependent manner and are facilitated by the decline of proteostasis capacity during aging. Thus, the healthcare burden linked to these diseases is steadily increasing.

Protein misfolding often results in the formation of a rigid fibrillar structure, commonly known as amyloid. Depending on the localization of amyloid deposits, protein aggregation diseases can be divided into three subclasses: i) neurodegenerative diseases, ii) non-neuropathic systemic amyloidoses, iii) non-neuropathic localized amyloidoses (Knowles et al., 2014). An overview of the most common protein aggregation diseases including the underlying protein is given in table 2.

Table 2. Human diseases associated with protein misfolding and amyloid formation (Chiti and Dobson, 2017; Knowles et al., 2014)**.**

Disease	**Affected organ**	**Protein/Peptide**	**Structure of precursor protein**	**Number of residues**
Neurodegenerative disease				
Alzheimer's disease	Brain	Amyloid-β peptide (Aβ)	Intrinsically disordered	40 or 42
Parkinson's disease	Brain	α-synuclein	Intrinsically disordered	140
Creutzfeldt-Jakob disease / Spongiform encephalopathy	Brain	Prion protein (PrP)	Intrinsically disordered (1-102), α-helical (103-208)	208
Amyotrophic lateral sclerosis (ALS)	Brain	Superoxide dismutase 1	β-sheet and Ig-like	154

Disease	Affected organ	Protein/Peptide	Structure of precursor protein	Number of residues
Huntington's disease	Brain	Huntingtin fragments (exon 1)	Intrinsically disordered	103-187
Non-neuropathic disease				
Systemic amyloidosis				
AL amyloidosis	Heart, kidney, liver, soft tissue etc.	Fragments of Ig light chains	β-sheet and Ig-like	~100
AA amyloidosis	Spleen, kidney, adrenal glands, liver	Serum amyloid A1 protein fragments	α-helical, SAA-like four-helix bundle	45-104
Senile systemic amyloidosis	Mainly heart	Transthyretin	β-sheet, prealbumin-like	127
Dialysis-related amyloidosis	Bones, periarticular structures, viscera	β_2-microglobulin	β-sheet and Ig-like	99
Lysozyme amyloidosis	Salivary glands, gastrointestinal tract, vasculature	Lyzozyme	α-helical and β-sheet, lysozyme fold	130
Localized amyloidosis				
Type II diabetes	Pankreas	Islet amyloid polypeptide (IAPP)	Intrinsically disordered	37
Injection-localized amyloidosis	Injection site	Insulin	α-helical, insulin-like	21 and 30
Cataract	Eye	γ -Crystallins	β-sheet, γ -crystallins-like	174

1.7. Destabilization Of The Native Fold: Protein Aggregation And Fibril Formation

1.7.1. Formation of Amyloid Fibrils

The native state of a protein is thermodynamically favored. As described in the preceding chapters, cells have evolved highly complex mechanisms to ensure the conservation of a protein's native fold and prevent aggregation. Nevertheless, the stability under physiological conditions is not always sufficient. As a consequence, misfolded states, off-pathway intermediates and aggregates can occur. When these structures escape all protective mechanisms, they can act as precursors to insoluble amyloid fibrils (Figure 7A). It was thought that the ability to form fibrillar structures was a property of only a few proteins or polypeptide chains. However, in 1998 it was shown that a protein, that was not associated to any disease, was able to form fibrils at acidic pH (Guijarro et al., 1998). This finding resulted in the conclusion that amyloid formation is a generic property of polypeptide chains and not a characteristic of only a few disease associated sequences (Dobson, 2003; Fändrich and Dobson, 2002; Stefani and Dobson, 2003; Uversky and Fink, 2004).

Several models for amyloid formation were suggested, depending on the precursor protein. In general, amyloid structures have been reported to form by a nucleated polymerization mechanism. The rate-limiting step, called lag phase, is the formation of an oligomeric nucleus by partially folded or misfolded monomers. This phase is followed by a rapid growth phase during which monomers add to the ends of the growing fibrils and a final plateau (Figure 7B) (Harper and Lansbury, 1997). The formation of oligomers is much slower than of fibrils suggesting a significant structural difference between these two forms. The oligomeric nucleus possesses the highest Gibbs free energy along the aggregation pathway (Figure 7C) (Arosio et al., 2015a). Thus, its concentration is low, while the monomeric form is the predominant soluble species at all times. More and more evidence allocates major cellular toxicity to smaller oligomeric intermediates but their transient behavior makes them hard to study. Monomers and fibrils are comparably stable and thus easy detectable during amyloid formation kinetics (Arosio et al., 2015a; Monsellier and Chiti, 2007). Another important factor regarding protein solubility is supersaturation, happening when amyloidogenic proteins remain soluble above their thermodynamic solubility because the energy barrier towards nucleation is too high. This can result in spontaneous aggregation or seeding and was reported in the context of several amyloid-related diseases (Muta et al., 2014).

Besides the intrinsic ability of a protein to form fibrillar structures, many factors can contribute to a protein's amyloid formation propensity. Destabilization of the native fold is often mediated through mutations in the amyloid precursor protein (Baden et al., 2008b; Hurle et al., 1994; Ramirez-Alvarado, 2012). In addition, proteolytic cleavage or other events like membrane binding, the presence of seeds, molecular crowding or interaction with other proteins can affect

the intrinsic stability. Also, as aggregation is a multimolecular process, its rate is highly dependent on protein concentration. Age plays an important role, since quality control mechanisms underlie progressive deterioration (Nuvolone and Merlini, 2016).

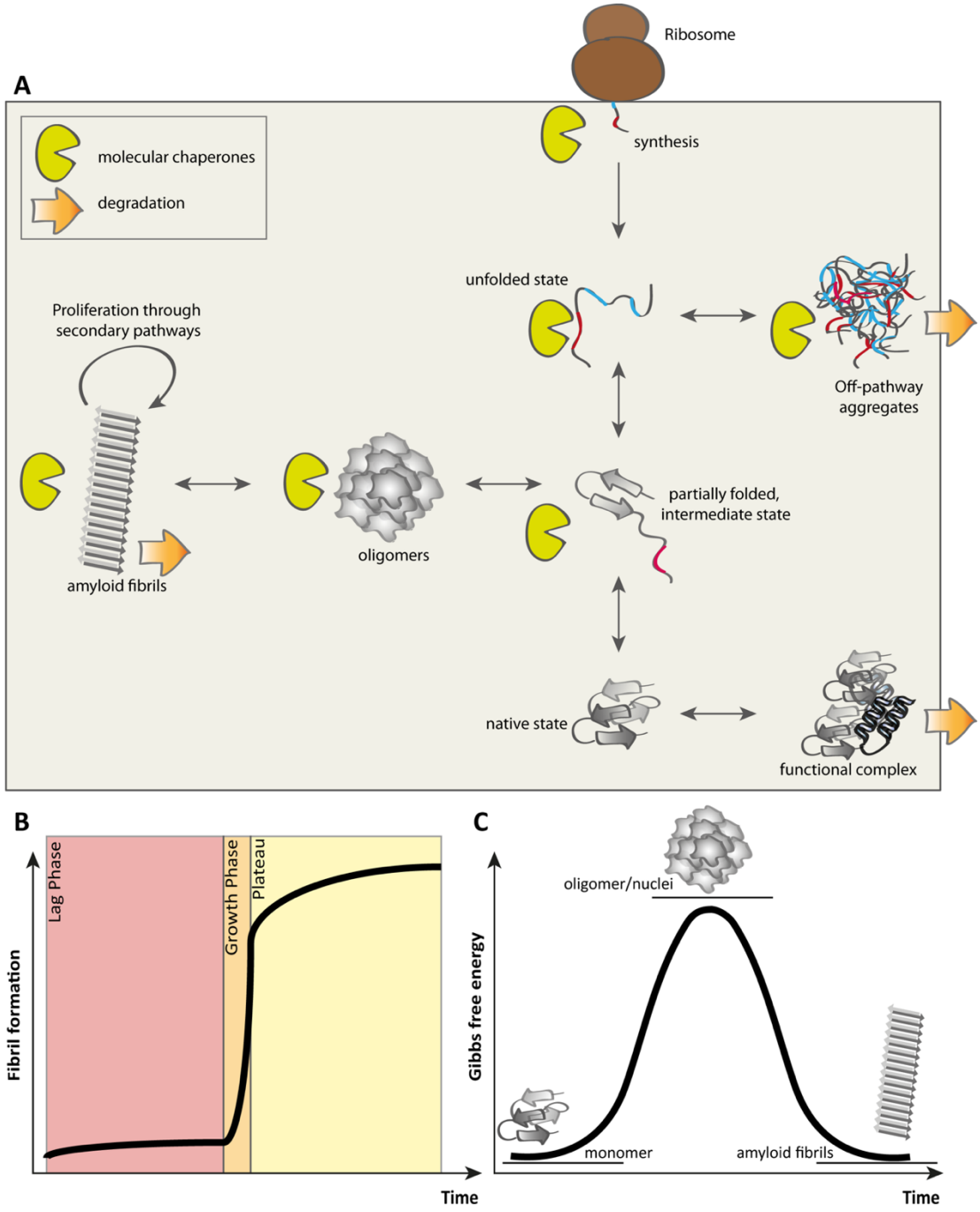

Figure 7. Overview of different conformational states of a protein. A) Protein populations depend on many factors like thermodynamic stability, synthesis rate, degradation, interactions with molecular chaperones or other factors. Stable fibrils and aggregates usually form from unfolded monomers in an off-pathway and are stable. The on-pathway leads to the native, functional state of a protein (*adapted with permission from Knowles et al., 2014).* B) Fibril formation curve showing the lag phase, fast fibril growth phase and final plateau phase. C) Free energy diagram of monomer, oligomers/nuclei and fibrils. The transient oligomeric nucleus is the state with the highest free energy. Monomers and fibrils have low free energy and are stable *(adapted with permission from Arosio et. al, 2015).*

1.7.2. AMYLOID STRUCTURE

The changes occuring during the lag phase of amyloid formation lead to a weakening of tertiary structure elements while at the same time favoring highly conserved secondary structure interactions in amyloid fibrils. X-ray analysis and EM studies showed that the amyloid fold is a cross-β structure. It is composed of an iteration of tightly packed intermolecular β-strands that are stabilized by interactions via hydrogen bonds. Due to the high number of these interactions along the cross-β core, this fold warrants a high rigidity and stability (Chiti and Dobson, 2017). Overall, amyloid structures are characterized by the appearance of straight, long and unbranched fibrils of approximately 7-13 nm in width and an undefined length. They are insoluble in aqueous solutions (Marshall and Serpell, 2009). X-ray fiber diffraction analysis shows diffuse reflection at 4.7 Å along the meridian which indicates that the β-sheets are perpendicular to the fibril axis (Eanes and Glenner, 1968; Geddes et al., 1968). Diffuse reflections at 10 Å equatorial suggest β-sheets spaced 10 Å apart (Figure 8) (Fändrich and Dobson, 2002). This architecture underlies *in vitro* and *in vivo* formed fibrils and is common to all amyloid proteins, regardless of the primary sequence (Jahn et al., 2008; Makin and Serpell, 2005; Rambaran and Serpell, 2008). However, the specific shape and morphology of the fibril results from side chain interactions and is thus dependent on the primary sequence of the precursor protein (Baldwin et al., 2011).

To detect amyloid, Congo Red and Thioflavin T are commonly used dyes. Congo Red was first used in 1922 by Bennhold when clinicians were searching for ways to diagnose amyloidoses (Bennhold, 1922). When stained with Congo Red and viewed between crossed polarizers, fibrils exhibit birefringence which causes transmission of a characteristic bright green color (Howie, 2019). The binding of Congo Red to fibrillar structures induces an increase and red shift in absorption. As Congo Red gives many false positives, Thioflavin T (ThT) became the dye of choice for amyloid detection in 1959 (Vassar and Culling, 1959). ThT selectively binds to cross-β structures and shows an increase of fluorescence intensity at 480 nm upon binding, when excited at 440 nm. Fluorescence intensity increases proportional to amyloid fibril mass and can thus be transferred to fibril concentration (Yakupova et al., 2019).

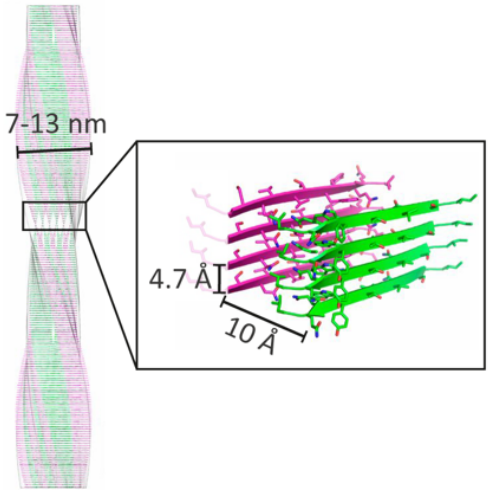

Figure 8. Cryo EM image of an amyloid light chain fibril (adapted and modified with permission from Schmidt et al., 2016). The hierarchically structured fibril is 7-13 nm in width. β-sheets pack perpendicular to the fibril axis. Each strand is 4.7 Å apart. The β-sheets are 10 Å apart.

1.8. AL AMYLOIDOSIS

Systemic amyloidoses are a group of amyloid deposition diseases characterized by the misfolding of a precursor protein and its deposition as insoluble amyloid fibrils in extracellular compartments of different tissues and organs. Over time this leads to cell death, subversion of tissue architecture, organ dysfunction and death. The forms of amyloidoses differ in their amyloid precursor protein (Merlini et al., 2011; Merlini and Bellotti, 2003). The most common type of systemic amyloidosis is immunoglobulin light chain (AL) amyloidosis with an incidence range from 9.7 to 14 cases per million persons per year (Quock et al., 2018). The average age of patients at diagnosis is 65 years. It is caused by an underlying clonal plasma cell dyscrasia. Upon proliferation of the plasma cell clone in the bone marrow, the specific misfolding-prone amyloidogenic light chains (LC) of either κ or λ subtype is overproduced (Desport et al., 2012). LCs of λ subtype are, with a ratio of approximately 3:1, more frequently disease-causing than κ LCs (Sanchorawala, 2006). Free HCs are aggregation prone and their free forms are toxic to the cell. To ensure high rates of HC incorporation, plasma cells naturally express an excess of LCs to ensure HC incorporation. In contrast to healthy plasma cells, these LCs deriving from diseased plasma cells are not paired with heavy chains (HC) to form a functional antibody but are secreted and circulate as free light chains (FLC) in the bloodstream of the patient. The systemic presence of the FLCs enables a theoretical deposition of amyloid fibrils in almost any organ except the brain and central nervous system. Consequently, patients often suffer from multiple disrupted organs with a varying affection pattern. Most involved organs are kidney and heart with an occurrence in patients of over 60 % and 50 %, respectively (Pepys, 2006; Witteles and Liedtke, 2019). A renal manifestation is characterized by a proteinuria, with nephrotic syndrome and impaired renal function in 50 % of the patients (Desport et al., 2012).

Heart involvement leads to restrictive cardiopathy. Survival of AL patients depends on the spectrum of organ involvement. Typically, affected patients die within two to three years after diagnosis and within only a year if the affected organs involve the heart (Abraham et al., 2003; Piehl et al., 2017). There are two other diseases arising from clonal plasma cell proliferation that appear more frequently and often display comorbidity: monoclonal gammopathy of undetermined significance (MGUS) and multiple myeloma (Merlini et al., 2011; Witteles and Liedtke, 2019). It is perspicuous that deposition of amyloid fibrils causes stress to vital organs and affects their function. However, soluble oligomeric intermediates are considered to largely contribute to pathophysiology (Liao et al., 2001). Soluble LC oligomeric intermediates can be taken up in cardiac fibroblasts and their presence can impair cardiomyocyte function (Brenner et al., 2004; Trinkaus-Randall et al., 2005). Also, soluble amyloidogenic LCs were reported to trigger programmed cell death via the p38a MAPK pathway (Shi et al., 2010).

Current therapeutic approaches aim to halt synthesis of amyloidogenic LCs to improve organ dysfunction and increase survival. While in 1997 chemotherapy with melphalan-prednisone was the only treatment method, the repertoire of effective treatments and the prognosis of AL amyloidosis improved significantly during the past decades (Kyle et al., 1997). Therapy may include chemotherapy using high-dose dexamethasone (immunosuppressive glucocorticoids) medication combined with melphalan (cytostatic, alkylating guanines, causing plasma cell death), thalidomide (immunomodulatory drug inhibiting cancer cell proliferation and angiogenesis), cyclophosphamide-thalidomide (similar to thalidomide) and high-dose melphalan treatment with a subsequent autologous stem cell transplantation. The most recent medications include lenalidomide (similar to thalidomide) and bortezomib (proteasome inhibitor blocking metabolic pathways in cancer cells) (Dispenzieri et al., 2004; Kastritis et al., 2007; Palladini et al., 2005, 2004; Reece et al., 2011; Wechalekar et al., 2007). Daratumumab, a monoclonal antibody to CD38 is successfully applied for multiple myeloma and is currently in phase III trials for treatment of AL amyloidosis (Sidiqi and Gertz, 2019). The choice of treatment is based on consideration of the balance between anticipated treatment efficacy and tolerability. The primary reason of a plasma cell clone to cause AL amyloidosis is thought to be the specific conformation induced by disease-specific mutations that differs with every clone and thus with every patient. Patient biopsies revealed the predominant deposition of N-terminal LC fragments mainly comprising the variable LC domain (Blancas-Mejía et al., 2015; Buxbaum, 1986; Glenner et al., 1970; Hurle et al., 1994; Olsen et al., 1998). This domain carries naturally occuring somatic mutations (see chapter 1.9) that are often destabilizing. Thermodynamically destabilized LCs require less energy to transit from their native fold into an intermediate state. (Baden et al., 2008a; Ramirez-Alvarado, 2012; Wall et al., 1999). To decipher the molecular mechanism of AL amyloidosis, it is important to understand the structural basis of immunoglobulin LCs.

1.9. IMMUNOGLOBULINS

1.9.1. BIOLOGICAL DEVELOPMENT AND ASSEMBLY OF IMMUNOGLOBULINS

Immunoglobulins (Ig), also known as antibodies, play a major role in the adaptive immune response. They serve as cell surface antigen receptors on B cells and are secreted as soluble effector molecules upon antigen stimulation and plasma cell differentiation. In the bloodstream and the lymphatic system they neutralize foreign pathogens, bacteria, viruses and microbial toxins by recruiting molecular and cellular immune factors (Schroeder and Cavacini, 2010). They are heterodimeric glycoprotein complexes composed of two identical heavy chains (HC) and two identical light chains (LC) that are linked by disulfide bonds. These Y-shaped molecules consist of three roughly equally sized structural elements connected by a flexible hinge region (Figure 9). Fully assembled antibodies can be divided into two main parts: an antigen binding fragment (F_{ab}), responsible for antigen binding and a crystallizable fragment (F_c), which can bind to cell-bound receptors and components of the complement system.

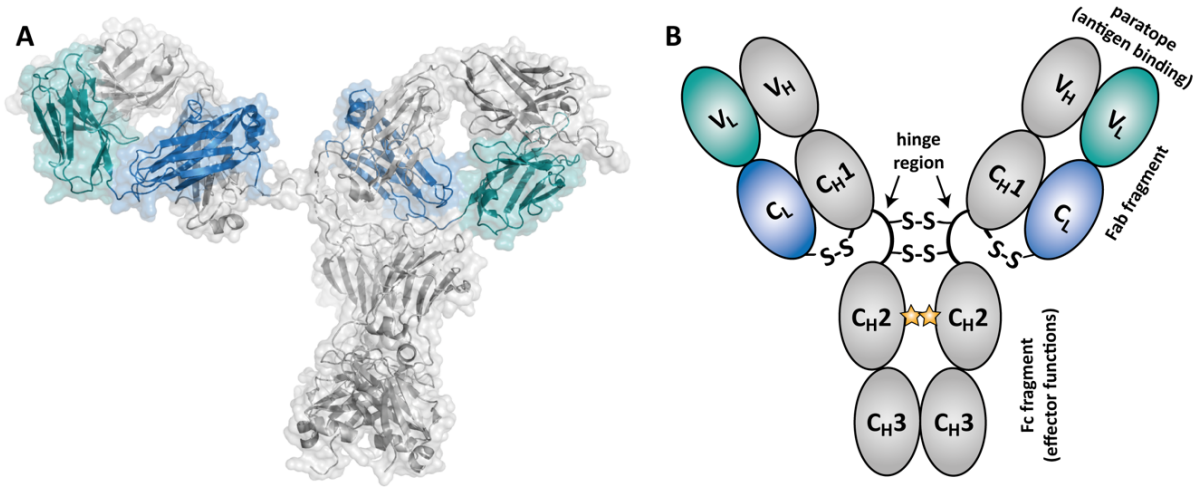

Figure 9. Structure of an IgG antibody. A) Crystal structure of an IgG antibody (PDB:1HZH). The HCs are shown in grey, the LC V_L domain is depicted in turquoise, the C_L in blue. B) Schematic domain arrangement in an IgG antibody. The chains have the same color as in A. The HCs are connected by two disulfide bonds in the flexible hinge region. HC and LC are linked by a disulfide bond between C_H1 and C_L, each. The C_H2 domains interact via oligosaccharides, pictured as orange stars. *(Adapted and modified with permission from Feige et al., 2010).*

LCs are either of λ or κ subtype and can pair with all HC classes. Both chains comprise multiple domains of approximately 100 amino acids each. Most higher vertebrates produce five different classes of antibodies: IgM, IgG, IgA, IgE and IgD. They differ in the HC constant regions. In one cell only one HC and one LC allele are expressed. Consequently, the given cell can only secrete a single specific antibody. HCs consist of four domains and the LCs comprise two domains. IgM represents an exception as it includes two five-domain HCs (Feige

et al., 2010). The antigen binding ability is mediated by the N-terminal domain of each chain: the variable light chains (V_L) and the variable heavy chains (V_H). Each of the V domains comprise three hypervariable complementarity determining regions (CDR) which enable the specific antigen binding. The diversity of antibodies, the antigen specificity and thus the variability of these regions is a result of the combination of a variable (V), a diversity (D) and a joining (J) gene segment on the DNA level, called VDJ rearrangement (Bernard et al., 1978; Hozumi and Tonegawa, 1976; Maki et al., 1980; Tonegawa, 1983). At later stages of B cell maturation, directed somatic hypermutation of the V region exon further increases the natural diversity of the variable domains (Feige et al., 2010; Jung and Alt, 2004; Wilson et al., 1998). Thus, each variable region possesses a different set of somatic mutations. All other domains are so-called constant domains (C_L and C_H1-4) and specify effector functions. After co-translational ER import, most IgGs assemble as HC dimers. Dimerization is mediated by the C_H3 domains and stabilized by disulfide bonds in the hinge region. C_H2 domains interact via co-translationally attached N-linked glycans (Bergman and Kuehl, 1978). The LCs are subsequently linked to HCs via disulfide bonds between the C_L and C_H domain (Baumal et al., 1971). A detailed overview on the LC is given in chapter 1.9.3.

1.9.2. Antibody Structure – The IG Fold

The Ig superfamily displays the largest superfamily in the human genome. Despite highly variable primary sequences, all Ig domains share a conserved tertiary structure, called the Ig fold (Bork et al., 1994). This structural module is also present in other proteins like cell surface receptors, epidermal growth factor domains or muscle proteins (Clothia and Joney, 1997; Holden et al., 1992). The basic feature of the Ig fold is the formation of a similar β-sandwich structure in which two β-sheets pack face to face forming a greek-key β-barrel topology. The variable domains of Igs comprise nine β-strands: A, B, C, C', C'', D, E, F and G. Constant domains comprise seven β-strands and lack the C' and C'' strands (Figure 10). Strand B and F are connected by a conserved disulfide bond that significantly contributes to domain stabilization (Bork et al., 1994; Goto and Hamaguchi, 1979; Huber et al., 1976). In close proximity to the disulfide bond is a conserved Trp residue. The side chain indole ring packs against the disulfide bond, forming part of the hydrophobic core of the Ig domain. In the native fold, Trp fluorescence is quenched due to the adjacent disulfide bond. The fluorescence intensity increase upon domain unfolding is commonly used for unfolding analysis of antibodies (Goto and Hamaguchi, 1979).

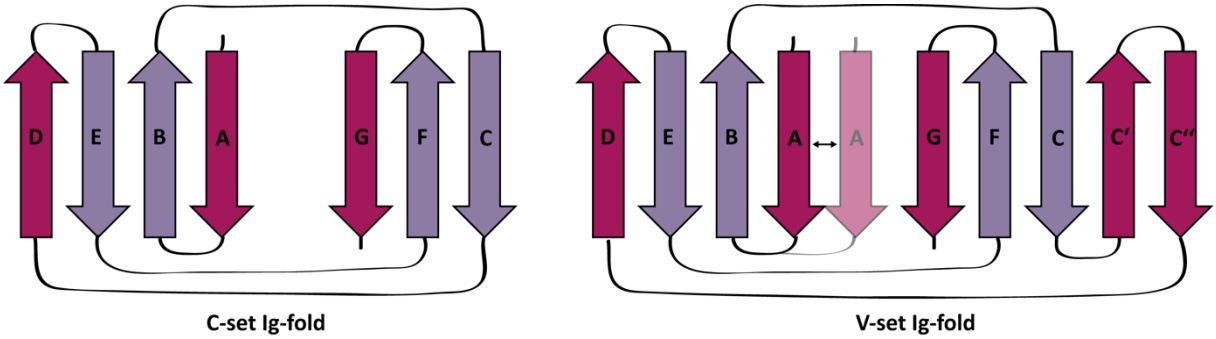

Figure 10. Ig fold topologies. The schematic topology diagram of a C-set Ig fold for constant Ig domains is shown on the left, the V-set Ig fold for variable Ig domains is depicted on the right. Strands are labelled from A-G with two extra strands in the V-set: C' and C''. Strand A in the V-set can take two alternative positions as depicted by a face strand. Strands in the same color are part of one β-sheet in the β-sandwich structure.

1.9.3. The Antibody Light Chain (LC)

1.9.3.1. Structure of LCs

The antibody LC consists of two domains: an N-terminal variable (V_L) and a C-terminal constant (C_L) domain. They are connected by a short unstructured linker (Figure 11) (Weber et al., 2018). Each domain has an average mass of 11,000 – 13,000 Da which gives a typical LC a mass of approximately 24,000 Da. The LC is either of κ or λ isotype, depending on the encoding gene locus. The κ locus is located on chromosome 2p11.2, whereas the λ locus is on chromosome 22q11.2. The isotypes exhibit distinct sequential and conformational preferences (Schroeder and Cavacini, 2010). The V_L domain comprises three CDRs that exhibit a high sequence variability and mediate antigen binding. They form variable loops at the top of each variable domain, creating the antigen binding site. The loops are supported by a conserved scaffold of four framework regions (FR). As described before, the CDRs within the V_L obtain their variability by VDJ gene rearrangement followed by subsequent somatic hypermutations. The high sequence variability requires a compensating tolerance to misfolding and a potent quality control system in the ER (see chapter 1.4).

Kabat et. al introduced a standardized nomenclature system for variable regions in Igs. It is widely adopted for numbering antibody residues and analyzing amino acid frequencies and variabilities. For this purpose, antibody sequences were aligned and the most variable positions (CDRs) were identified by taking into account the number of different amino acids at a specific position. This numbering scheme also considers insertions (Johnson and Wu, 2000a; Wu and Kabat, 1970).

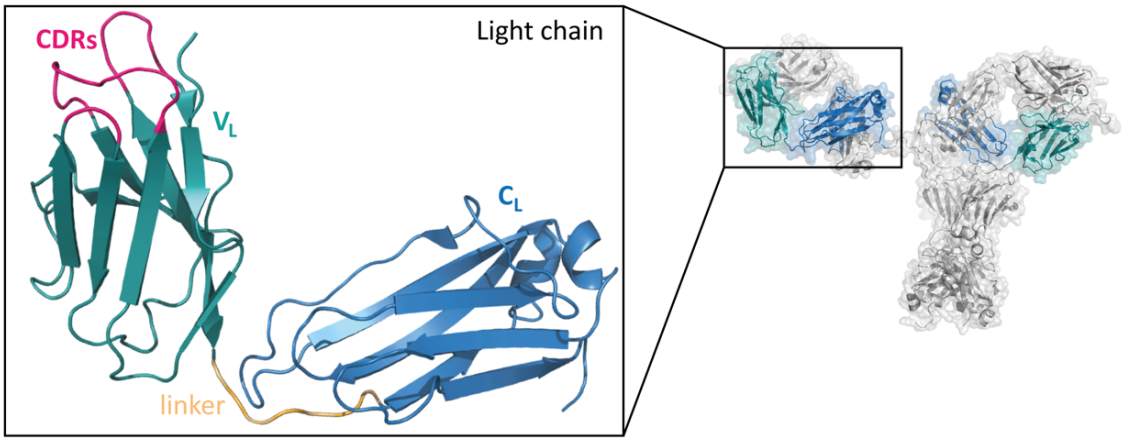

Figure 11. Structure of the Ig light chain (LC) (PDB:1HZH). The C_L domain (blue) and the V_L domain (turquoise) are connected by a short flexible linker (yellow). The highly variable CDR loops in the V_L mediating antigen specificity are colored in pink.

1.9.3.2. LCs IN THE CONTEXT OF AL AMYLOIDOSIS

In AL amyloidosis, disease-causing LCs can be either of κ or λ subtype (see chapter 1.9.3.1.). While the λ:κ ratio in non-diseased adults and multiple myeloma patients is 2:1, AL patients, due to unknown reasons, often show a threefold higher concentration of λ LCs (ratio 3:1), suggesting a predisposition of λ LCs to form amyloid structures (Gertz et al., 2002). Therefore, calculation of the secreted subtype ratio can be a helpful tool to diagnose AL amyloidosis (Perfetti et al., 1995). The LC subtypes can be further classified into several subgroups based on mostly FR1 sequence homologies. The 33 V_λ germline genes are classified into $V_{\lambda I}$ - $V_{\lambda VI}$, the 40 V_κ variants are grouped into $V_{\kappa I}$ - $V_{\kappa IV}$ (Ramirez-Alvarado, 2012; Solomon and Weiss, 1995). Especially genes of the $V_{\lambda VI}$ subgroup are disease-associated, but also $V_{\lambda I}$, $V_{\lambda II}$ and $V_{\lambda III}$ and $V_{\kappa I}$ are often found (Abraham et al., 2004; Poshusta et al., 2009; Ramirez-Alvarado, 2012; Solomon et al., 1982). Mutations in the variable domain often lead to the reduction of thermodynamic stability, enable misfolding and disease development (Baden et al., 2008b; Blancas-Mejía et al., 2015; Hurle et al., 1994; Nokwe et al., 2016). The enormous diversity of especially the V-region of LCs due to a high number of V_κ and V_λ genes and the naturally occuring somatic mutations (see chapter 1.9.1) impede the determination of underlying disease-causing characteristics. Nevertheless, some manifestations regarding germline gene and amino acid substitutions were found to be preferentially associated with the destabilization of the V_L domain and the development of AL amyloidosis. Statistical analysis by Abraham et al. (2004) of 27 AL patients revealed a DNA-based mutation rate of 16 % for λ and 7 % for κ patients, whereby the CDR regions are especially prone to mutations. Effectively this mostly leads to 1-9 amino acids substitutions in λ and 3-7 substitutions in κ patients. However, this

number can be higher and the nature of the mutations varies individually (Abraham et al., 2004; Connors et al., 2007). The destabilizing effect of mutations on the LC truncation can have multiple molecular reasons i.e. change of β-sheet propensity, steric effect of side chain size, modified charge of amino acid, loss of interaction to the heavy chain etc. (Abraham et al., 2004; Ramirez-Alvarado, 2012; Street and Mayo, 1999; Weber et al., 2018). The mutational diversity in patient-derived LCs awards a high complexity to the understanding of underlying molecular mechanisms and the identification of amyloidogenic variants. Stevens et al. analyzed 121 of $V_{\kappa I}$ LCs and identified mutations of Arg61, Ile27 and general Pro substitutions in β-turn regions as risk factors (Stevens, 2000). Also, the introduction of an additional N-glycosylation site by asparagine residues (i.e. N70 or N20) or the change of basic to acidic residues (i.e. K45E or K42E) were found in patient LCs (Connors et al., 2007). Analysis of amyloidogenic λ and κ LCs further lead to the assumption that not the total number or the specific nature of a mutation but the location is causative for destabilization (Poshusta et al., 2009). So far, no clear conclusion can be drawn from the identified and few characterized somatic mutations in pathogenic LCs.

As mostly the N-terminal LC fragments were found in amyloid deposits, even though it's the full-length LC that circulates in the blood, it is important to understand the interplay of the V_L and C_L domain. Most LCs do not form fibrils under physiological conditions, even if they contain mutations in the V_L domain, that render the individual domain amyloidogenic. This suggests that the conformational stability does not necessarily correlate with fibril formation propensity (Nokwe et al., 2016). The C_L domain often showed a stabilizing effect *in vitro* and seems to protect the LC from fibril formation. However, *in vitro* experiments showed a direct correlation of fibril formation propensity of LC mutants and susceptibility to proteolysis (Morgan and Kelly, 2016a). Independent of thermodynamic factors, the V_L-C_L domain orientations and interactions influence proteolytic cleavage and thus fibril formation propensity (Weber et al., 2018). Referring to FLCs in the bloodstream, disrupted domain orientation can make LCs more susceptible to endoproteolysis, which results in free circulating, aggregation-prone light chain fragments. The same effect could be obtained by thermodynamically destabilized V_L domains that need less energy to misfold, which can lead to a structural opening and a linker more susceptible to proteolysis (Baden et al., 2008b; Ramirez-Alvarado, 2012).

1.10. Objectives Of The Thesis

In the scope of this thesis, four different scientific questions in the context of the disease AL amyloidosis were addressed. The work is based on patient data from the Amyloidosis Center at the University Hospital in Heidelberg. The first three parts comprise investigations on one patient-derived LC that was named Pat-1. Results predominantly originate from *in vitro* experiments using recombinantly purified proteins. The fourth part was performed at St. Jude Children's Research Hospital in Memphis, TN, USA in the laboratory of Linda Hendershot, PhD. Here novel attempts to analyze the fate of amyloidogenic LCs in the ER of mammalian cells were made.

The first part addresses the specific point mutations that were found in the patient-derived and disease-causing light chain truncation Pat-1. Amyloidogenicity is thought to be accompanied by thermodynamic destabilization. Thus, the effect of single point mutations regarding both features was investigated with the goal to disclose the sequence-based reason for pathogenicity and further, the underlying molecular mechanism. Additionally, a proteolytic cleavage step prior to fibril formation is thought to be necessary for most LCs (Buxbaum, 1986; Hurle et al., 1994). Thus, the susceptibility towards proteolysis as a result of somatic mutations was investigated.

The second goal was to investigate the effect of molecular chaperones and plasma factors that potentially come into contact with the LC during disease development. The first critical step in the biosynthesis of LCs is their folding in the ER. The two ER resident chaperones BiP and ERdj3 play a major role in folding. They are also part of the ERQC that is responsible for the detection of misfolded protein. Especially ERdj3 is an important factor, since it can be secreted from the ER and was found to impact the fibril formation of Aβ in the context of Alzheimer's disease (Genereux et al., 2015). Thus, the impact of these ER-resident chaperones was tested. Further, LCs are exposed to a variety of proteins and plasma factors upon secretion. The impact of such factors is only barely explored. As the extracellular chaperone Apolipoprotein E4 is known to be a risk factor for Alzheimer's disease (Huynh et al., 2017; Liu CC, Kanekiyo T, Xu H, 2013), the effect of this plasma factor on fibril formation was investigated here.

The third objective targeted the elucidation of events occuring prior to fibril formation. Amyloid formation followed by ThT fluorescence usually displays a sigmoidal curve. The lag phase is relatively long compared to the very rapid growth phase which indicates the occurrence of major structural rearrangements during this time. Oligomers have been found in many of amyloid-related disease and hypotheses attribute the major cytotoxic effects to these

intermediate forms (Fändrich, 2012). Thus, the pathway from monomeric to fibrillar Pat-1 was deciphered in this study.

The fourth aim of the thesis was the analysis of early *in vivo* events during the synthesis of pathogenic LCs. Each patient possesses a unique LC sequence, yet the disease development follows common features. Different LCs were investigated regarding their overall expression, secretion, dimerization and aggregation behavior. This part of the thesis targeted the analysis of pathogenic LC behavior and should serve as a scaffold for the classification of the cellular processing of different LCs.

2. MATERIAL AND METHODS

2.1. MATERIALS

2.1.1. DEVICES

Device	Supplier
Analytical Ultracentrifuge	
XL-A equipped with absorbance and fluorescence detection systems	Beckman Coulter (Krefeld, Germany) and AVIV biomedical (Lakewood, USA)
XL-I equipped with absorbance and interference optics	Beckman Coulter (Krefeld, Germany)
Optima AUC equipped with absorbance and interference optics	Beckman Coulter (Krefeld, Germany)
Centrifuges	
Avanti J25 and J26 XP equipped with JA-10, JLA 16.250 and JA-25.50 rotors	Beckman, Krefeld, Germany
Optima MAX-E ultracentrifuge	Beckman, Krefeld, Germany
Rotina 420 R	Hettich (Tuttlingen, Germany)
Rotina 46R	Hettich (Tuttlingen, Germany)
Tabletop centrifuge 5418	Eppendorf (Hamburg, Germany)
Tabletop centrifuge Mikro R200	Hettich (Tuttlingen, Germany)
Chromatography systems	
ÄKTA Pure	GE Healthcare (Freiburg, Germany)
ÄKTA Purifier	GE Healthcare (Freiburg, Germany)
ÄKTA Explorer	GE Healthcare (Freiburg, Germany)
Shimadzu Prominence HPLC systems	Shimadzu (Munich, Germany)
Frac-900/950 fraction collectors	GE Healthcare (Freiburg, Germany)
Superloops (150 mL, 10 mL)	GE Healthcare (Freiburg, Germany)
Circular dichroism spectropolarimeters	
J710 (with PFD-350S Peltier device)	Jasco (Großumstadt, Germany)
J715 (with PTC 348 WI Peltier device)	Jasco (Großumstadt, Germany)
Chirascan™ (with CS/PCS Peltier device)	Applied Photophysics (Leatherhead, UK)

Device	Supplier
Fluorescence spectrophotometers	
Jasco FP-6500	Jasco (Großumstadt, Germany)
Jasco FP-8500 FDP spectrofluorimeter with polarizers	Jasco (Großumstadt, Germany)
Fluoromax-4	Horiba Jobin Yvon (Edison, USA)
Gel electrophoresis	
Hoefer Mighty Small II dual gel caster	GE Healthcare (Freiburg, Germany)
Pharmacia EPS 3500, 301, 1001 power supply	GE Healthcare (Freiburg, Germany)
Hydrogen/deuterium exchange instruments	
ACQUITY M-Class UPLC	Waters (Milford, USA)
PAL RTC	Leap technologies (Carrboro, USA)
Synapt G2-S ESI-TOF mass spectrometer	Waters (Milford, USA)
Microplate readers	
GENios	Tecan (Männedorf, Schweiz)
Infinite M Nano Microplate Reader	Tecan (Männedorf, Schweiz)
Microscopes	
Transmission electron microscope JEM-1400 Plus	JOEL (Freising, Germany)
Scales	
BP 121 S	Sartorius (Göttingen, Germany)
BL 310	Sartorius (Göttingen, Germany)
Thermal cycler	
MJ Mini 48 well	Biorad (Munich, Germany)
Primus 25	MWG (Ebersberg, Germany)
Temperature controlled incubator	
Digital heat block	VWR (Darmstadt, Germany)
Eppendorf-Thermomixer	Eppendorf (Hamburg, Germany)

Device	Supplier
TB1 Thermoblock	Biometra (Göttingen, Germany)
UV-Vis spectrophotometers	
UltroSpec 1100 pro	Amersham Biosciences (Buckinghamshire, UK)
Nanodrop ND-1000	Peqlab (Erlangen, Germany)
Additional Equipment	
Autoclave Varioclav EP-Z	H+P (Oberschleißheim, Germany)
Cell Disruption Apparatus Basic Z	Constant Systems (Warrick, USA)
Homgenizer Heidolph DIAX 900	Heidolph (Staufen, Germany)
Image Scanner III	GE Healthcare (Freiburg, Germany)
Incubator	New Brunswick Scientific (Nürtingen, Germany)
pH meter 538 MultiCal	WTW (Weilheim, Germany)
Vortex MS2	IKA (Staufen, Germany)
Water bath F6-K	Haake (Karlsruhe, Germany)
LI-COR Odyssey CLx Imaging System	LI-COR Biotechnology (Lincoln, NE, USA)
MALDI-TOF/TOF mass spectrometer Bruker Ultraflex-2	Bruker Daltonics (Hamburg, Germany)

2.1.2. CHEMICALS

Chemical	Supplier
2-Mercaptoethanol	Merck (Darmstadt, Germany)
8-Anilino-1-naphtalenesulfonic acid (ANS)	Sigma (St. Louis, USA)
Acetic acid	Roth (Karlsruhe, Germany)
Acetonitrile	Merck (Darmstadt, Germany)
Acrylamide/Bisacrylamide solution 38:2 (40% w:v)	Serva (Heidelberg, Germany)
Agar Agar	Serva (Heidelberg, Germany)
Agarose	Serva (Heidelberg, Germany)
Ammonium chloride (NH_4Cl)	Merck (Darmstadt, Germany)
Ammonium persulfate (APS)	Roth (Karlsruhe, Germany)

Chemical	Supplier
Ampicillin sodium salt	Roth (Karlsruhe, Germany)
Bromphenol blue	Serva (Heidelberg, Germany)
cOmplete™, EDTA-free Protease Inhibitor Cocktail	Sigma (St. Louis, USA)
Coomassie Blue R	Serva (Heidelberg, Germany)
Coomassie Brilliant Blue R-250	Serva (Heidelberg, Germany)
Desoxynucleoside triphosphates (dNTPs)	NEB (Frankfurt, Germany)
Dimethyl sulfoxide (DMSO)	NEB (Frankfurt, Germany)
Dithiothreitol (DTT)	Roth (Karlsruhe, Germany)
EDTA	Merck (Darmstadt, Germany)
Ethanol	Merck (Darmstadt, Germany)
Formic acid	Merck (Darmstadt, Germany)
GeneCellin	Bulldog Bio, Inc., Portsmouth, NH
Glucose	Merck (Darmstadt, Germany)
Glutaraldehyde solution (25 %)	Merck (Darmstadt, Germany)
Glutathione, oxidized (GSSG)	Merck (Darmstadt, Germany)
Glutathione, reduced (GSH)	Merck (Darmstadt, Germany)
Glycerol	Roth (Karlsruhe, Germany)
Glycine	Roth (Karlsruhe, Germany)
Guanidinium chloride (GdmCl)	Merck (Darmstadt, Germany)
HEPES	Merck (Darmstadt, Germany)
Hydrochloric acid (HCl) 32%	Merck (Darmstadt, Germany)
Imidazole	Sigma (St. Louis, USA)
Isopropanol	Merck (Darmstadt, Germany)
Isopropyl β-d-1-thiogalactopyranoside (IPTG)	Serva (Heidelberg, Germany)
Kanamycin sulfate	Roth (Karlsruhe, Germany)
L-Arginine	Merck (Darmstadt, Germany)
LB medium	Serva (Heidelberg, Germany)
Lipofectamine® LTX	Thermo Fisher Scientific (Waltham, USA)
Magnesium sulfate ($MgSO_4$)	Merck (Darmstadt, Germany)

Chemical	Supplier
Manganese (II) chloride	Merck (Darmstadt, Germany)
Para-formaldehyde (EM Grade)	Electron Microscopy Sciences (Munich, Germany)
Potassium chloride (KCl)	Roth (Karlsruhe, Germany)
Potassium phosphate, monobasic (KH_2PO_4)	Merck (Darmstadt, Germany)
Protease inhibitor Mix G, HP	Serva (Heidelberg, Germany)
Sodium acetate anhydrous (NaOAc)	Merck (Darmstadt, Germany)
Sodium azide (NaN_3)	Merck (Darmstadt, Germany)
Sodium chloride (NaCl)	Merck (Darmstadt, Germany)
Sodium dodecylsulfate (SDS)	Serva (Heidelberg, Germany)
Sodium hydroxide (NaOH)	Merck (Darmstadt, Germany)
Sodium phosphate, dibasic (Na_2HPO_4 * 2 H_2O)	Merck (Darmstadt, Germany)
Sodium phosphate, monobasic (NaH_2PO_4 * 2 H_2O)	Merck (Darmstadt, Germany)
Stain G	Serva (Heidelberg, Germany)
Tetraethylendiamin (TEMED)	Roth (Karlsruhe, Germany)
Thioflavin T (ThT)	Merck (Darmstadt, Germany)
Tris	Roth (Karlsruhe, Germany)
Tris(2-carboxyethyl)phosphine hydrochloride (TCEP)	Merck (Darmstadt, Germany)
Triton X-100	Merck (Darmstadt, Germany)
Tween-20	Merck (Darmstadt, Germany)
Uranyl acetate	Science Services (Munich, Germany)
Urea	Merck (Darmstadt, Germany)

2.1.3. CONSUMABLES

Consumable	Supplier
200-mesh copper grids	Merck (Darmstadt, Germany)
Amicon-0.5 Centrifugal Filter Units	Millipore (Darmstadt, Germany)
Amicon-15 Centrifugal Filter Units	Millipore (Darmstadt, Germany)
Amicon-0.5 Centrifugal Filter Units	Millipore (Darmstadt, Germany)

Consumable	Supplier
Crystal Clear PP sealing foil	HJ-Bioanalytik GmbH (Erkelenz, Germany)
Cuvettes, plastic, 1ml	Brand (Darmstadt, Germany)
Dialysis membranes Spectra/Por (MWCO: 6-8 kDa)	Spectrum Laboratories (Houston, USA)
Immuno-Blot PVDF Membrane	Bio-Rad (Hercules, USA)
MatTek dish, 35 mm	MatTek (Ashland, USA)
Membrane discs	Sartorius (Göttingen, Germany)
Membrane filter 0.22 µm	Millipore (Darmstadt, Germany)
Microplates 96 well, black (#437112)	Nunc (Schwerte, Germany)
Millex – GS 0.22 µm syringe filter units	Millipore (Darmstadt, Germany)
Millex – GV 0.22 µm syringe filter units	Millipore (Darmstadt, Germany)
Mini-PROTEAN® TGX™ Precast Protein Gels (4 - 20 %)	Bio-Rad (Munich, Germany)
Nitrocellulose membrane, pore size 0.2 µl	Amersham Biosciences (Uppsala, Sweden)
PCR tubes	BioRad Laboratories (Munich, Germany)
Pellet pestles	Sigma (St. Louis, USA)
PE tubes, 15 and 50 ml	Greiner & Söhne (Frickenhausen, Germany)
Petri dishes, PS, 94 mm	Greiner & Söhne (Frickenhausen, Germany)
Reaction tubes, various volumes	Sarstedt (Nümbrecht, Germany)

2.1.4. BUFFERS

2.1.4.1. PROTEIN PURIFICATION AND ASSAY BUFFERS

Buffer name	Composition	Concentration
5x Inclusion body preparation buffer	Tris/HCl, pH 7.5 EDTA NaCl addition of protease inhibitor mix prior to use	250 mM 50 mM 50 mM
Q-Sepharose buffer A, low salt	Tris/HCl, pH 8.0 EDTA Urea	50 mM 10 mM 5 M
Q-Sepharose buffer B, high salt	Tris/HCl, pH 8.0 EDTA Urea NaCl	50 mM 10 mM 5 M 1 M
Inclusion body dissolving buffer	Tris/HCl, pH 8.0 EDTA Urea 2-Mercapothanol, before use	50 mM 10 mM 8 M 0.1% (v/v)
Refolding buffer	Tris/HCl, pH 8.0 EDTA L-arginine GSH, before use GSSG, before use	250 mM 10 mM 100 mM 0.5 mM 1.0 mM
10x Phosphate buffered saline (PBS)	Na_2HPO_4 x 2 H_2O KH_2PO_4 KCl NaCl pH 7.4	100 mM 18 mM 27 mM 1.37 M
HKM	HEPES, pH 7.5 KCl	50 mM 150 mM 10 mM

Buffer name	Composition	Concentration
	$MgCl_2$	
HAKM	HEPES, pH 7.5 NH_4Cl KCl $MgCl_2$	50 mM 1 M 150 mM 10 mM
J3-Buffer A, binding buffer	HEPES, pH 7.5 NaCl Imidazole	50 mM 400 mM 20 mM
J3-Buffer B, elution buffer	HEPES, pH 7.5 NaCl Imidazole	50 mM 400 mM 1 M

2.1.4.2. BUFFERS FOR MOLECULAR BIOLOGY AND SDS-PAGE

Buffer name	Composition	Concentration
Fairbanks A (staining)	Isopropanol Acetic acid Coomassie Blue R	25 % (v/v) 10 % (v/v) 0.05 % (w/v)
Fairbanks D (destaining)	Acetic acid	10 % (v/v)
5x Laemmli buffer, reducing	Tris/HCl, pH 6.8 SDS Glycerol Bromphenol blue 2-Mercaptoethanol	0.3 M 10 % (w/v) 50 % (v/v) 0.05 % (w/v) 5 %
5x Laemmli buffer, non-reducing	Tris/HCl, pH 6.8 SDS Glycerol Bromphenol blue	0.3 M 10 % (w/v) 50 % (v/v) 0.05 % (w/v)
10x SDS running buffer	Tris/HCl, pH 8.0 Glycine SDS	0.25 M 2 M 1 % (w/v)

Buffer name	Composition	Concentration
4x Separation gel buffer	Tris/HCl, pH 8.8 SDS	1.5 M 0.8 % (w/v)
2x Stacking gel buffer	Tris/HCl, pH 6.8 SDS	0.25 M 0.4 % (w/v)
TAE	Tris/acetate, pH 8.0 EDTA	2 M 50 mM

2.1.4.3. Buffers for Fibril Formation Assay

Buffer name	Composition	Concentration
Assay buffer	1x PBS, pH 7.4 SDS ThT NaN_3	 0.5 mM 10 µM, final concentration 0.05 % (w/v)
ThT stock solution	1x PBS, pH 7.4 ThT	 500 µM

2.1.4.4. Buffers for Chemical Competent Cells

Buffer name	Composition	Concentration	Volume
Solution A	NaOAc, pH 5.5 $CaCl_2$ $MnCl_2$ H_2O	3 M 1 M 2.8 M	13 ml 100 ml 25 ml 862 ml
Solution B	Glycerol Solution A	87 %	69 ml 331 ml

2.1.4.5. Buffers for Hydrogen/Deuterium Exchange Mass Spectrometry Experiments

Buffer name	Composition	Concentration
Quenching buffer	Na_2HPO_4, pH 2.2 Na_2HPO_4 Tris(2-carboxyethyl)phosphine GdmCl	200 mM 200 mM 250 mM 3 M

2.1.4.6. Buffers for Tissue Culture

Buffer name	Composition	Concentration
NP40 buffer	Tris/HCl (pH 7.5) NaCl Nonidet P40 substitute Sodium deoxycholate PMSF Roche complete protease inhibitor tablets w/o EDTA	50 mM 150 mM 0.5 % 0.5 % 0.1 mM 1x
NP40 lysis buffer	NP40 buffer 2 M $MgCl_2$ Glucose 5000 U/ml Hexokinase	1x 5 µl/ml 6 mg/ml 10 µl/ml
NP40 washing buffer	Tris/HCl (pH 7.5) NaCl Nonidet P40 substitute Sodium deoxycholate	50 mM 400 mM 0.5 % (v/v) 0.5 % (w/v)
Gelatin buffer	Gelatin Tris/HCl (pH 7.5) NaCl EDTA Triton X-100 NaN_3	0.1 % (v/v) 15 mM 130 mM 1 mM 0.1 % (v/v) 0.002 % (w/v)

2.1.4.7. Buffers for Fibril Extraction from Patient Tissue

Buffer name	Composition	Concentration
Tris calcium buffer	Tris/HCl (pH 8.0) NaCl $CaCl_2$ NaN_3	20 mM 138 mM 2 mM 0.1 % (w/v)
Tris/EDTA buffer	Tris/HCl (pH 8.0) NaCl EDTA NaN_3	20 mM 140 mM 10 mM 0.1 % (w/v)

2.1.4.8. Buffers for Limited Proteolysis

Buffer name	Enzyme	Composition	Concentration
Ca^{2+} containing assay buffer	Proteinase K	Tris/HCl (pH 7.5) $CaCl_2$	50 mM 5 mM
1xPBS	Trypsin Chymotrypsin Plasma		1:200 (Enzyme:LC) 1:200 (Enzyme:LC) 1:50 (Enzyme:LC)

2.1.4.9. Buffers for Immunofluorescence Microscopy

Buffer name	Composition	Concentration
Blocking buffer	BSA TX-100 PBS	5 % (w/v) 0.1 % (v/v) 1 x
Antibody Dilution Buffer	BSA TX-100 PBS	1 % (w/v) 0.1 % (v/v) 1 x

2.1.5. CELL STRAINS

	Strain	Genotype	Origin
Bacterial strain	*E. coli* BL21-Codon+ (DE3)-RIL	F- *ompT hsdS*(rB- mB-) *dcm*+ Tetr *gal endA* The (*argU proL* Cam^R)	Stratagene (LaJolla, USA)
	E. coli XL1 blue	*recA1 endA1 gyrA96 thi-1 hsdR17 supE44 relA1 lac*	Stratagene (LaJolla, USA)
	E. coli Shuffle	F' *lac, pro,* $lacI^q$ / *Δ(ara-leu)7697 araD139 fhuA2 lacZ::T7 gene1 Δ(phoA)PvuII phoR ahpC* gale (or U) galK λatt::pNEB3-r1-cDsbC* ($Spec^R$, $lacI^q$) *ΔtrxB* ($rpsL150(Str^R)$) *Δgor Δ(malF)3*	New England Biolabs (Ipswich, USA)
Cell culture strain	*COS-1 monkey fibroblasts*		Kindly provided by Dr. Linda Hendershot, Memphis, TN, USA
	CHO (Chinese Hamster Ovary) WT		
	CHO (Chinese Hamster Ovary) ERdj3-knock-out		
	HEK293T human embryonic kidney cells		

2.1.6. MEDIA FOR BACTERIA

Medium	Composition	Concentration
Luria Bertani (LB_0)	LB medium Agar agar plates	20 g/l 15 g/l
Super Optimal Broth (SOC)	Yeast extract Tryptone KCl $MgCl_2$ $MgSO_4$ D-(+)-glucose	0.5 % (w/v) 1% (w/v) 2.5 mM 10 mM 10 mM 20 mM
Antibiotics (1000x stock)	Kanamycin	35 ug/l (in ddH_2O)

All media were sterilized usind an autoclave at 121 °C for 20 min. Antibiotic and IPTG stocks were passed through a sterile 0.22 µm filter and stored at -20 °C.

2.1.7. MEDIA FOR TISSUE CULTURE

Medium	Composition	Concentration
DMEM (Cellgro, USA)	DMEM FBS L-Glutamine Penicillin-streptomycin	 10 % (v/v) 2 mM 100 U/ml
F12 (Thermo Fisher, USA)	F-12 Nutrient mix + L-Glutamine	

2.1.8. ENZYMES, STANDARDS AND KITS

Reagent/Kit	Manufacturer
Chameleon® Vue Pre-stained Protein Ladder	LI-COR Biotechnology (Lincoln, NE, USA)
Clostridium histolyticum collagenase	Sigma (Taufkirchen, Germany)
DNAseI	Roche (Mannheim, Germany)
DpnI	New England Biolabs (Ipswich, USA)
Hexokinase	Sigma (St. Louis, USA)

Low Range molecular weight marker	Serva (Heidelberg, Germany)
Labeling Kit RED NHS 2nd Generation	NanoTemper Technologies (Munich, Germany)
NEBuffer 2.1	New England Biolabs (Ipswich, USA)
PeqGold 1kb ladder	PeqLab (Erlangen, Germany)
Phusion HF DNA polymerase	New England Biolabs (Ipswich, USA)
Polynucleotide kinase (PKA)	New England Biolabs (Ipswich, USA)
Prolong® Gold Antifade Reagent	Thermo Fisher Scientific (Waltham, USA)
Q5 HF DNA Polymerase	New England Biolabs (Ipswich, USA)
Q5 Site-Directed Mutagenesis Kit	New England Biolabs (Ipswich, USA)
Restriction enzymes	New England Biolabs (Ipswich, USA)
Serva Dual Color Proteinstandard III	Serva (Heidelberg, Germany)
T4 DNA Ligase	New England Biolabs (Ipswich, USA)
T4 DNA Ligase Buffer (10x)	New England Biolabs (Ipswich, USA)
T4 DNA Polymerase	New England Biolabs (Ipswich, USA)
Ulp1 protease	Kindly provided by Christina Nickels
Wizard Plus SV Minipreps DNA Purification System	Promega (Madison, USA)
Wizard SV Gel and PCR Clean-up System	Promega (Madison, USA)

2.1.9. ANTIBODIES

Antibody	**Manufacturer**
IRDye® 680 Donkey anti-Goat IgG (H + L)	LI-COR Biotechnology (Lincoln, NE, USA)
IRDye® 680 Goat anti-Mouse IgG (H + L)	LI-COR Biotechnology (Lincoln, NE, USA)
IRDye® 800 Goat anti-Rabbit IgG (H + L)	LI-COR Biotechnology (Lincoln, NE, USA)
IRDye® 800 Goat anti-Mouse IgG (H + L)	LI-COR Biotechnology (Lincoln, NE, USA)

Antibody	Manufacturer
Goat Anti-Human Lambda-Alexa Fluor® 647	SouthernBiotech (Birmingham, AL, USA)
Mouse Anti-ERdj3 (C-7) – Alexa Fluor® 647	Santa Cruz Biotechnology (Heidelberg, Germany)
Rabbit Anti-BiP	Kindly provided by Dr. Linda Hendershot

2.1.10. COLUMNS

Column	Manufacturer
HisTrap Fast Flow (5 ml)	GE Healthcare (Freiburg, Germany)
PD10 Desalting Columns	GE Healthcare (Freiburg, Germany)
Q Sepharose Fast Flow	GE Healthcare (Freiburg, Germany)
HiLoad Superdex 200 Prep Grade 16/60 or 26/60	GE Healthcare (Freiburg, Germany)
Superdex 75 10/300 GL	GE Healthcare (Freiburg, Germany)
HiLoad Superdex 75 Prep Grade 16/60 or 26/60	GE Healthcare (Freiburg, Germany)

2.1.11. PLASMIDS

Construct	Vector	Reference	Origin
V_L Pat-1	pET28b	Kazman et al., 2020	GeneArt (Regensburg, Germany)
V_L Pat-1 L15P	pET28b		This work
V_L Pat-1 S26T	pET28b		This work
V_L Pat-1 N28S	pET28b		This work
V_L Pat-1 F30V	pET28b		This work
V_L Pat-1 D32G	pET28b		This work
V_L Pat-1 D53E	pET28b		This work
V_L Pat-1 D55S	pET28b		This work

Construct	Vector	Reference	Origin
V_L Pat-1 V81L	pET28b		This work
V_L Pat-1 V81I	pET28b		This work
V_L Pat-1 L82Q	pET28b		This work
V_L Pat-1 F90Y	pET28b		This work
V_L Pat-1 S105T	pET28b		This work
V_L Pat-1 L15P V81L	pET28b		This work
V_L Pat-1 L15P L82Q	pET28b		This work
V_L Pat-1 V81L L82Q	pET28b		This work
V_L Pat-1 L15P V81L L82Q	pET28b		This work
V_L WT-1	pET28b		This work
V_L WT-1 P15L	pET28b		This work
V_L WT-1 T26S	pET28b		This work
V_L WT-1 S28N	pET28b		This work
V_L WT-1 V30F	pET28b		This work
V_L WT-1 G32D	pET28b		This work
V_L WT-1 E53D	pET28b		This work
V_L WT-1 S55D	pET28b		This work
V_L WT-1 L81V	pET28b		This work
V_L WT-1 Q82L	pET28b		This work
V_L WT-1 Y90F	pET28b		This work
V_L WT-1 T105S	pET28b		This work
C_L Pat-1	pET28b		GeneArt (Regensburg, Germany)
C_L Pat-1 C105S	pET28b		This work

Construct	Vector	Reference	Origin
LC Pat-1	pET28b		GeneArt (Regensburg, Germany)
LC Pat-1 C216S	pET28b	Kazman et al., 2020	Lioba Hunziger
LC Pat-1 V81L C216S	pET28b		Lioba Hunziger
LC WT-1	pET28b		GeneArt (Regensburg, Germany)
LC WT-1 C216S	pET28b	Kazman et al., 2020	Lioba Hunziger
LC Pat-1	pcDNA3.1(+)		GeneArt (Regensburg, Germany)
LC WT-1	pcDNA3.1(+)		GeneArt (Regensburg, Germany)
LC Pat-2	pcDNA3.1(+)		GeneArt (Regensburg, Germany)
LC WT-2	pcDNA3.1(+)		GeneArt (Regensburg, Germany)
LC Pat-3	pcDNA3.1(+)		GeneArt (Regensburg, Germany)
LC WT-3	pcDNA3.1(+)		GeneArt (Regensburg, Germany)
LC Pat-4	pcDNA3.1(+)		GeneArt (Regensburg, Germany)
LC WT-4	pcDNA3.1(+)		GeneArt (Regensburg, Germany)
LC Pat-5	pcDNA3.1(+)		GeneArt (Regensburg, Germany)
LC WT-5	pcDNA3.1(+)		GeneArt (Regensburg, Germany)
LC Pat-6	pcDNA3.1(+)		GeneArt (Regensburg, Germany)
LC WT-6	pcDNA3.1(+)		GeneArt (Regensburg, Germany)
hERdj3	pSUMO		Christina Nickels

Construct	Vector	Reference	Origin
mBiP	pProEx	Rosam et al., 2018	Christina Nickels
mBiP-167C	pProEx	Rosam et al., 2018	Christina Nickels

2.1.12. OLIGONUCLEOTIDES

Template	Method	Name	Strand	Sequence (5' to 3')
V_L Pat-1	Q5 SDM	Pat-1 L15P	+	TAGCGGTAGCCCGGGTCAGAGCATTA
			-	ACGCTTGCAGGCTGGGTC
		Pat-1 S26T	+	CTGTACCGGTACATCAAATGATTTTGGC
			-	CTAATGGTAATGCTCTGAC
		Pat-1 N28S	+	CTGTACCGGTAACTCAAATGATTTTG
			-	CTAATGGTAATGCTCTGACC
		Pat-1 F30V	+	CTCAAATGATGTTGGCGATTATAAC
			-	CTACCGGTACAGCTAATG
		Pat-1 D32G	+	TGATTTTGGCGGTTATAACTACG
			-	TTTGAGCTACCGGTACAG
		Pat-1 D53E	+	GATGATTTATGAGGTTGATAATCGTC
			-	AGTTTCGGTGCTTTACCC
		Pat-1 D55S	+	TTATGATGTTTCTAATCGTCCGAGCG
			-	ATCATCAGTTTCGGTGCTTTAC
		Pat-1 V81L	+	CATTAGCGGTTTGCTGGCAGAAG
			-	GTCAGGCTTGCGGTATTA
		Pat-1 L82Q		TAGCGGTGTTCAGGCAGAAGATG
				ATGGTCAGGCTTGCGGTA

Template	Method	Name	Strand	Sequence (5’ to 3’)
		Pat-1 F90Y	+	AGCAGATTATTACTGTAGCAGCTATAC
			-	TCATCTTCTGCCAGAACAC
		Pat-1 S105 T	+	TGTTTTTGGTACCGGCACCAAAGTTAC
			-	TACAGGGTGCTGCTGCTG
		Pat-1 L15P V81L	+	CATTAGCGGTTTGCTGGCAGAAG
			-	GTCAGGCTTGCGGTATTA
		Pat-1 L15P L82Q	+	TAGCGGTAGCCCGGGTCAGAGCATTA
			-	ACGCTTGCAGGCTGGGTC
		Pat-1 V81L L82Q	+	CATTAGCGGTCTTCAGGCAGAAG
			-	GTCAGGCTTGCGGTATTA
		Pat-1 L15P V81L L82Q	+	CATTAGCGGTCTTCAGGCAGAAGATGAAG
			-	GTCAGGCTTGCGGTATTA
V_L WT-1	QuikChange	WT-1 P15L	+	CGTTAGCGGTAGTCTGGGTCAGAGCATTAC
			-	GTAATGCTCTGACCCAGACTACCGCTAACG
		WT-1 T26S	+	CATTAGCTGTACCGGCTCCAGCAGTGATGTTG
			-	CAACATCACTGCTGGAGCCGGTACAGCTAATG
		WT-1 S28N	+	CGGCACCAGCAACGATGTTGGTG
			-	GTACAGCTAATGGTAATGC
		WT-1 V30F	+	CCGGCACCAGCAGTGATTTCGGTGGTTATAACTATG
			-	CATAGTTATAACCACCGAAATCACTGCTGGTGCCGG
		WT-1 G32D	+	CAGCAGTGATGTTGGTGACTATAACTATGTTAGCTGG

Template	Method	Name	Strand	Sequence (5’ to 3’)
			-	CCAGCTAACATAGTTATAGTCACCAACATCACTGCTG
		WT-1 E53D	+	GAAACTGATGATTTATGATGTTAGCAATCGTCCGAGC
			-	GCTCGGACGATTGCTAACATCATAAATCATCAGTTTC
		WT-1 S55D	+	GATGATTTATGAGGTTGACAATCGTCCGAGCGGTG
			-	CACCGCTCGGACGATTGTCAACCTCATAAATCATC
		WT-1 L81V	+	CTGACCATTAGCGGTGTGCAGGCAGAAGATG
			-	CATCTTCTGCCTGCACACCGCTAATGGTCAG
		WT-1 Q82L	+	CCATTAGCGGTCTGCTGGCAGAAGATGAAG
			-	CTTCATCTTCTGCCAGCAGACCGCTAATGG
		WT-1 Y90F	+	GAAGATGAAGCAGATTATTTCTGTAGCAGCTATACCAGC
			-	GCTGGTATAGCTGCTACAGAAATAATCTGCTTCATCTTC
		WT-1 T105S	+	CACCTTATATGTTTTTGGTTCAGGCACCAAAGTTACCG
			-	CGGTAACTTTGGTGCCTGAACCAAAAACATATAAGGTG

2.2. SOFTWARE, DATABASE AND WEB-BASED TOOLS

Software

Name	Supplier
Adobe Illustrator CS5	Adobe Inc., San Jose, USA
Adobe Photoshop CS5	Adobe Inc., San Jose, USA
ASTRA 5.3.4	Wyatt Technology, Dernbach, Germany

Name	Supplier
CDNN	Gerald Böhm, www.gerald-boehm.de
DynamX 3.0	Waters (Eschborn, Germany)
Epson TT8 Launch Silver Fast	Epson (Kiel, Germany)
Image J	NIH, www.imagej.nih.gox
Image Studio™	LI-COR Biosciences (Lincoln, USA)
Image Quant TL	GE Healthcare (Pittsburgh, USA).)
Mendeley Desktop	Mendeley Ltd., www.mendeley.com
Microsoft Office 2016	Microsoft (Redmond, USA)
NTAnalysis software	NanoTemper Technologies (Munich, Germany)
Origin 8.6	OriginLab Corp. (Northhampton, USA)
Origin 2018b	OriginLab Corp. (Northhampton, USA)
Prism8	GraphPad (San Diego, USA)
Protein Lyns Global Server PLGS 3.0.3	Waters (Eschborn, Germany)
PyMOL v1.3	Schrödinger (New York, USA)
Sedfit	Peter Schuck
Serial Cloner 2.5	Franck Perez

Databases

Name	Website
abYsis	https://www.abysis.org
ALBase	https://www.albase.bumc.bu.edu/aldb
Clustal Omega alignment	https://www.ebi.ac.uk/Tools/msa/clustalo/
NCBI IgBLAST	https://www.ncbi.nlm.nih.gov/igblast/
PubMed	https://www.ncbi.nlm.nih.gov/pubmed/

Name	Website
Phyre2	http://www.sbg.bio.ic.ac.uk/phyre2
RCSB Protein Data Bank (PDB-ID)	https://www.rcsb.org
UniProt	https://www.uniprot.org

Web-based tools

Name	Website
abYsis	https://www.abysis.org
Clustal Omega alignment	https://www.ebi.ac.uk/Tools/msa/clustalo/
ExPASy ProtParam	https://web.expasy.org/protparam/
NCBI IgBLAST	https://www.ncbi.nlm.nih.gov/igblast/
NEBaseChanger	https://nebasechanger.neb.com
NEBuilder	https://nebuilder.neb.com
Phyre2	http://www.sbg.bio.ic.ac.uk/phyre2
PrimerX	https://www.bioinformatics.org/primerx/

2.3. Molecular Biology Methods

2.3.1. DNA Isolation and Storage

Cloned plasmids were amplified in 5 ml liquid *E. coli* culture supplemented with the appropriate antibiotic. Isolation were performed using the Wizard® SV Mini-Prep Kit according to the manufacturer's manual. DNA concentration was determined using a Nanodrop spectrophotometer. The sequence was verified by sequencing at GATC Biotech AG or Eurofins Genomics GmbH using the T7 forward or T7 reverse primer. Isolated DNA was stored in nuclease free ddH_2O at -20 °C.

2.3.2. Agarose Gel Electrophoresis

DNA was separated using 1 % agarose gels (w/v) with 1:50000 DNA stain G in TAE buffer for size determination of DNA fragments and PCR products. FastLoad 1kb DNA ladder was used as a standard. Agarose gels were run at 120 V for 30 min.

2.3.3. DNA AMPLIFICATION

Polymerase Chain Reaction (PCR) was used to amplify DNA and for site-directed mutagenesis. Depending on the cloning strategy, different polymerases and protocols were used for the PCR as described below. For the QuikChange® site-directed mutagenesis method (Stratagene) the Phusion DNA Polymerase was used. Q5 site-directed mutagenesis was performed using the Q5 DNA Polymerase.

QuikChange® site-directed mutagenesis

QuikChange® site-directed mutagenesis pipetting scheme	
Template DNA	1.5 µl (~5 ng)
5x Phusion buffer	10 µl
dNTP mix (10 mM)	2 µl
Primer forward (100 pmol/µl)	2 µl
Primer reverse (100 pmol/µl)	2 µl
DMSO	1.5 µl
Phusion DNA Polymerase	0.5 µl
Nuclease free H_2O	ad 50 µl

QuikChange® PCR reaction			
Initial denaturation	95 °C	2 min	
Denaturation	95 °C	30 sec	25 x
Annealing	54 – 70 °C	1 min	
Elongation	72 °C	10 min	
Final Elongation	72°C	2 min	
Storage	4 °C	hold	

Q5 site-directed mutagenesis

Q5 site-directed mutagenesis pipetting scheme	
Template DNA	1.5 µl (~5 ng)
5x Q5 reaction buffer	10 µl
dNTP mix (10 mM)	2 µl
Primer forward (100 pmol/µl)	2 µl
Primer reverse (100 pmol/µl)	2 µl
DMSO	1.5 µl
Q5 DNA Polymerase	0.5 µl
Nuclease free H_2O	ad 50 µl

Q5 site-directed mutagenesis PCR reaction			
Initial denaturation	95 °C	1 min	
Denaturation	95 °C	15 sec	25 x
Annealing	54 – 70 °C	30 min	
Elongation	72 °C	4 min	
Final Elongation	72°C	2 min	
Storage	4 °C	hold	

2.3.4. CLONING STRATEGIES

2.3.4.1. QUIKCHANGE® SITE-DIRECTED-MUTAGENESIS (SDM)

One method to generate single point mutations was to use an optimization of the QuikChange® protocol by Stratagene (LaJolla, USA). Primers carrying the point mutation were designed using the web-based QuikChange® Primer Design tool. The annealing temperature was adjusted to the properties of the primer. The Template DNA was amplified as stated above (see chapter 2.3.3). After amplification, the PCR product was digested using DpnI for 1 h at 37 °C. DpnI specifically cuts hemimethylated, parental DNA and thus separates the mutated PCR product from the template. 10 µl of the digested PCR product was transformed into 100 µl XL1 cells according to the transformation protocol (see chapter 2.3.7), plated on LB_{Kan} plates and incubated at 37 °C overnight. DNA isolation and sequence verification were performed as described in chapter 2.3.1.

2.3.4.2. Q5 Site-Directed-Mutagenesis (SDM)

An equivalent method to incorporate single point mutations was Q5 site-directed-mutagenesis by NEB (Ipswich, USA). Primers were designed using the web-based NEBaseChanger tool. In this approach, only the forward primer carried the desired mutation. Annealing temperatures were given by the tool. The PCR reaction was carried out as stated above (see chapter 2.3.3). After the reaction, 1 µl of the PCR product was subjected to a kinase, ligase, DpnI (KLD), 0.5 uM each, treatment according to the manufacturer's protocol. The reaction was allowed to take place for 1 h. 10 ul of the digested prodict were transformed into 100 ul XL1 cells (see chapter 2.3.7), plated on LB_{Kan} cells and incubated at 37 °C overnight. DNA isolation and sequence verification were performed as described in chapter 2.3.1.

2.3.5. Growth and storage of *E. coli* cells

E. coli cells were grown in liquid LB medium or on LB plates at 37 °C. For selection of the cells harboring plasmids, the respective antibiotics (Kanamycin, Chloramphenicol) were added to the medium. Inoculation of liquid cultures was done using a single colony from a plate or in 1:100 dilution from an overnight culture. Cell growth was photometrically monitored at 600 nm, whereby an OD of 1 equals approximately $5x10^8$ to $1x10^9$ cells per ml of medium (Sambrook et al., 1989). For long-term storage of *E. coli* cells, glycerol stocks were prepared by mixing 600 µl of 87 % sterile glycerol with 300 ul of *E. coli* culture, snap-frozen and stored at -80 °C.

2.3.6. Preparation of Competent Cells

Chemically competent *E. coli* cells were prepared following the protocol of Sambrook et al., 1989. In brief, cells were grown over night in LB_0 medium without antibiotics at 37 °C under continuous shaking. Reaching an OD_{600} of 0.5 to 1.0, they were supplemented with 2 ml of 1 M $MgCl_2$, incubated for 10 min at 37 °C under agitation and cooled down on ice for 1 h. Cells were harvested by centrifugation at 4500 rpm for 5 min. Pellets were resuspended in 20 ml solution A and incubated on ice for 1 h. The cells were pelleted again and resuspended in 2 ml of Solution B. Aliquots were snap-frozen and stored at -80 °C.

2.3.7. Transformation of *E. coli* Cells

100 µl of competent *E. coli* cells (XL1 blue for vector preparation, BL21-DE3 for overexpression) were thawed on ice for 10 min. 1µl of plasmid DNA (50-100 ng) or 10 µl of QuickChange®/Site Directed Mutagenesis reaction product was added, mixed and incubated for 10 min on ice. Heat shock was performed for 45 s at 42 °C and put on ice for another 5 min. 900 ul of LB_0 medium was added and the cells were incubated at 37 °C at 500 rpm for 45 min. Cells were spun down at 7000 rpm, resuspended in 200 µl LB_0 and plated on LB plates with the appropriate antibiotic. Plates were incubated at 37 °C overnight.

2.4. Protein Biochemistry

2.4.1. Protein Expression and Cell Disruption

For expression of all IgG V_L, C_L and LC domain variants, the plasmid carrying the gene of interest was transformed into *E. coli* BL21 (DE3) cells. A starter culture was used to inoculate LB media with Kanamycin to an OD_{600} of 0.1. Cells were grown at 37 °C under agitation and protein expression was induced with 1 mM IPTG at an OD_{600} of 0.6-0.8. The cells were grown over night at 37 °C under continuous shaking. For ERdj3 expression, the plasmid was transformed in *E. coli* SHuffle cells. LB media with Kanamycin was inoculated with a starter culture to an OD_{600} of 0.1 and grown at 30 °C under agitation. Reaching an OD_{600} of 0.6-0.8, protein expression was induced with 0.5 mM IPTG and grown overnight at 30 °C. Cells were harvested by centrifugation (10 min, 7,000 rpm, JA 10 rotor, 4 °C). For Ig domains, inclusion bodies were prepared as previously described (Thies and Pirkl, 2000). Briefly, cell pellets were resuspended in ~100 ml IB preparation buffer containing Protease Inhibitor Mix G. After addition of DNAseI, cells were disrupted using a pressure-operated cell disruption apparatus at 1.8 kbar and centrifuged (40 min, 10,000 rpm, JLA 16.250 rotor, 4 °C) for inclusion body harvest. Inclusion bodies were washed with IB preparation buffer and stored until purification at -20 °C. For ERdj3, cells were harvested and homogenized in J3-Buffer A supplemented with Protease Inhibitor Mix HP and DNAseI. Cells were disrupted at 1.8 kbar and the cell debris was removed by centrifugation (30 min, 20,000 rpm, JA 25.50 rotor, 4 °C). Cell lysate was snap-frozen in liquid nitrogen and stored at -80 °C until purification.

2.4.2. Protein Purification

Ig domains

All Ig domains were purified as previously described (Nokwe et al., 2014). In short, inclusion bodies were solubilized in the denaturing IB dissolving buffer containing β-Mercaptoethanol and loaded on a Q-Sepharose anion exchange column. The flow-through containing the Ig domains was subjected to overnight dialysis refolding in refolding buffer at 4 °C (protein solution to refolding buffer 1:20 (v/v)). Aggregates were removed by centrifugation (30 min, 20,000 rpm, JA 25.50 rotor, 4 °C) and the refolded soluble protein was further purified by a Superdex 75 16/60 gel filtration column. Protein fractions and purity was determined by SDS-PAGE.

ERdj3

For ERdj3 purification, protein lysate was applied on a 5 ml His-Trap column equilibrated in J3-Buffer A and eluted with a 0-100 % J3-Buffer B gradient. Ulp1 protease was added to the protein containing fractions and the mixture was dialyzed overnight against J3-Buffer A at 4 °C for SUMO tag cleavage. The cleaved product was again applied on a 5 ml His-Trap column,

the flow-through collected, concentrated and applied on a Superdex 200 26/60 column equilibrated in HAKM buffer. Protein fractions and purity was determined by SDS-PAGE.

2.5. Cell Biology

2.5.1. Cell Culture and Transfection

DNA constructs

All LC sequences were obtained by cDNA sequencing of CD138-enriched bone marrow plasma cells of AL amyloidosis patients from the University Hospital in Heidelberg. The sequencing was performed as described elsewhere(Annamalai et al., 2016). Corresponding germline sequences were identified by database search. All Patient and germline LC sequences were cloned in pcDNA3.1(+) vectors and an N-terminal ER-targeting signal sequence was added. The pMT vector expressing BiP has been described previously (Gaut and Hendershot, 1993).

Cos-1 / HEK293T

Cos-1/HEK293T cells were transfected using GeneCellin. The day prior to transfection, p60 dishes containing ~0.5 million cells/dish were prepared and incubated at 37 °C and 3 % CO_2. For Immunofluorescence, p35 dished containing ~0.25 million cells/dish were used. 2 µg DNA, 200 µl serum free media and 12 µl GeneCellin were mixed and incubated at room temperature for 15 min. Media on the p60/p35 dishes was changed to 5/2 ml fresh DMEM media. 200 µl of the DNA mixture was added dropwise to the dish and the dished were returned to incubation at 37 °C, 3 % CO_2.

CHO WT/CHO j3 KO

CHO cells were transfected using Lipofectamine® LTX according to the manufacturer's protocol. In brief, p60 dishes containing ~1.1 million cells/dish were prepared the day prior to tranfection and incubated at 37 °C and 5 % CO_2. For transfection, 2.5 µl DNA was used per dish.

2.5.2. Metabolic Labeling and Pulse-Chase Experiments

24 h after transfection, medium was aspirated and cells were washed twice with PBS. Cells were starved by changing media to 1.5 ml cysteine/methionine-free DMEM labeling media (Cellgro, USA) for 30 min and pulse-labeled with 100 µCi/p60 dish of EasyTag™ EXPRESS35S Protein Labeling Mix (Perkin Elmer, USA) for 3 h. For anaylsis of secreted and non-secreted proteins after labeling, the media and the lysate were subjected to immunoprecipitation as described in chapter 2.5.4. To quantify metabolically labeled proteins,

a Storm 860 phosphorimager scanner was used. Signals were analyzed using the ImageQuant TL software.

2.5.3 Cell Lysis

24 h after transfection or 3 h after metabolic labeling, cells were washed twice with PBS and lysed for 20 min in 1 ml of NP40 lysis buffer supplemented with 2 M $MgCl_2$ (5 µl/ml), Glucose (6 mg/ml) and 5000 U/ml Hexokinase (10 µl/ml). Cells were scraped, transferred in a 1.5 ml tube and the lysate was clearified by centrifugation (20,000 g, 15 min, 4 °C). The supernatant, designated as NP40-soluble fraction, was used for SDS-PAGE and Western blot analysis. The NP40-insoluble pellets were washed in NP40 lysis buffer and solubilized by adding 1x Laemmli buffer with β-Mercaptoethanol, incubating at 95 °C for 10 min, sonicating for 10 min and incubating again at 95 °C for 10 min.

2.5.4. Immunoprecipitation

900-950 µl lysate or media samples were mixed with 2 µl anti-λ antibody and rotated at 4 °C overnight. Immune complexes were pulled down with CaptivA™ PriMAB Protein A agarose slurry (RepliGen, USA) for 1 h, washed three times with 1 ml NP40 washing buffer and eluted with 22 µl 2x Laemmli buffer for SDS-PAGE analysis, as described in chapter 2.6.1. Gels were amplified by incubating in Amplify (GE Healthcare, Pittsburgh, USA) supplemented with 3 % glycerol for 30 min and dried on filter paper covered with cellophane in a gel dryer at 80 °C for 2 h.

2.6. Protein Analysis

2.6.1. SDS-Polyacrylamide Gel Electrophoresis (SDS-PAGE)

SDS-PAGE was carried out to separate protein samples according to their molecular weight (Berg et al., 2011) and thus examine the size and purity of the samples. The anionic detergent forms complexes with proteins via hydrophobic interactions. Thus, proteins display a negative charge correlating with their sizes. Upon disruption of the tertiary protein structure by boiling the sample with SDS and β-Mercaptoethanol. Thus, the migration of the proteins in an electric field is only dependent on their molecular weight. For *in vitro* protein purifications and *in vivo* experiments with proteins from tissue culture, gels were selfmade and depending on the expected size, the separating gels contained either 15 or 18 % (w/v) acrylamide/bisacrylamide for bacterial and 13 % for cell culture experiments. The stacking gel contained 5 % (w/v) acrylamide/bisacrylamide. SDS-PAGE gels were freshly prepared according to the following protocols:

	Stacking gel	**Separating gel**		
	5 %	13 %	15 %	18 %
Acrylamide/bisacrylamide (40 % w/v)	0.625 ml	3.25 ml	3.75 ml	4.5 ml
2x stacking gel buffer	2.5 ml		-	-
4x separation gel buffer	-	2.5 ml	2.5 ml	2.5 ml
10 % (w/v) APS	65 µl	65 µl	65 µl	65 µl
TEMED	3.3 ul	3.3 ul	3.3 ul	3.3 ul
H_2O	1.875 ml	4.0 ml	3.75 ml	3.0 ml

Protein samples were mixed with Laemmli buffer (1-5x, ± β-Mercaptoethanol, depending on the performed experiment), heated for 5 min at 95 °C and loaded on the gel. SDS running buffer was poured into the gel chamber. For purification gels, electrophoresis was performed at a constant current of 35 mA per gel for ~40 min. For estimation of protein size, a low molecular weight marker was used. For *in vivo* experiments, electrophoresis was performed at a constant voltage of 100 mV for ~60 min and a Chameleon® Vue Pre-stained Protein Ladder. Gels were stained with Fairbanks A solution for staining (Fairbanks et al., 1971) and incubated for ~15 min on a shaker. Destaining occurred in Fairbanks D solution until the protein bands were clearly visible and background was removed.

2.6.2. IMMUNOBLOTTING (WESTERN BLOT)

Tissue culture lysates, pellets or media were separated with SDS-PAGE, subsequently electrophoretically transferred to an Immuno-Blot® PVDF membrane (Bio-Rad) by blotting with wet-transfer overnight at 35 V or for 2-4 h at 100 V at 4 °C. Proteins were detected by blotting with the specific antibodies following the standard protocol using Gelatin Buffer for blocking. The primary anti-λ antibody was used in a 1:1000 dilution and the anti-BiP antibody in a 1:2500 dilution. Secondary antibodies were diluted 1:10,000. All used antibodies were fluorescently tagged, detected with an LI-COR Odyssey CLx scanner and analyzed with Image Studio™.

2.6.3. MALDI-TOF

Purity and molecular weight analysis of purified proteins was performed on a MALDI-TOF/TOF mass spectrometer. To remove potassium ions from PBS buffer, a Zip Tip preparation was

performed according to the manufacturer's instructions (Millipore). The HCCA matrix was dissolved in 0.1 % TCA, 80 % acetonitrile and 20 % ddH_2O. The full-length proteins were spotted in the matrix solution and were analyzed after evaporation of the solvent.

2.6.4. Glutaraldehyde Crosslinking

For analysis of oligomeric species, a fresh solution of 2.3 % Glutaraldehyde was prepared. 5 µl of the solution were added to 100 µl of a 15 µM protein sample and incubated for 3 min at 37 °C. The reaction was quenched by the addition of 10 µl of 1 M Tris/HCl (pH 8.0).

2.6.5. Analytical Ultracentrifugation

Analytical ultracentrifugation (AUC) allows the investigation of interactions, complex formation or oligomerization of proteins by analyzing their sedimentation (Laue and Stafford, 1999). AUC measurements were carried out using an Optima AUC or a ProteomLab XL-I (Beckman, Krefeld, Germany) equipped with absorbance optics. Protein concentration for measurements were 15-20 µM in a total volume of 350 µl PBS (± SDS). Samples were loaded into assembled cells with quartz windows and 12-mm-path-length charcoal filled epon double sector centerpieces. Measurements were performed at 42,000 rpm in an eight-hole Beckman-Coulter AN50-ti rotor at 20 °C. Absorbance was measured at 280 nm and sedimentation was continuously scanned with a radial resolution of 10 µm. Data analysis was carried out with SedFit using the continuous c(S) distribution mode (Brown and Schuck, 2006; Schuck, 2000).

2.6.6. Microscale Thermophoresis (MST)

MST measurements were applied to detect interactions between Ig domains and ERdj3 and determine a K_D. The method is based on thermophoresis, which is the directed movement of molecules upon a temperature gradient. It strongly depends on size, charge, hydration shell and conformation and is thus very sensitive for changes of molecular properties (Jerabek-Willemsen et al., 2014). During the experiment an infrared laser induces a temperature gradient. The following movement of molecules is detected and quantified. Prior to the measurement, the antibody domains were fluorescently labeled using the Monolith Protein Labeling Kit RED NHS 2nd Generation (Amine Reactive) according to the manufacturer's protocol. MST measurements were carried out at 25 °C on a NanoTemper Monolith NT.115 (NanoTemper Technologies) using MST Premium coated capillaries and the laser powers suggested by the instrument. The resulting thermophoresis data were analyzed using the NTAnalysis software (NanoTemper Technologies).

2.7. SPECTROSCOPY

2.7.1. UV-VIS SPECTROSCOPY

UV-Vis spectroscopy was applied to determine protein concentration. The principal is based on the UV-light absorbance of proteins and peptides at around 200-280 nm according to their amino acid content (Layne, 1957; Stoscheck, 1990). Aromatic amino acid side chains (tryptophan, tyrosine, phenylalanine) show a strong absorption of UV-light between 240-300 nm. Peptide bonds absorb UV-light at 180-230 nm due to their carbonyl groups. The strong UV-light absorption of the indole group of tryptophan at 280 nm allows the determination of protein concentration according to the Lambert-Beer-law (Equation 1):

$$A_{280} = \varepsilon \cdot c \cdot d \qquad \text{(Equation 1)}$$

Equation 1. Lambert-Beer equation. A_{280}: absorbance at 280 nm; ε: molar extinction coefficient (M^{-1} $cm^{-1)}$; c: protein concentration (M); d: path length (cm).

UV absorption measurements were performed using a NanoDrop ND 1000 spectrophotometer with baseline correction. Molar extinction coefficients were calculated based on the amino acid sequence by the web-based tool ExPASy ProtParam.

2.7.2. CIRCULAR DICHROISM SPECTROSCOPY

Circular dichroism (CD) measurements in the far UV region were performed to analyze the secondary structure fold of proteins (Kelly et al., 2005). This method was applied to confirm the correct fold after the refolding step for antibody domains or to follow fold changes during oligomerization and amyloid formation of V_L domains. Furthermore, it was used to monitor protein unfolding upon increasing temperature (thermal unfolding) as an indicator for protein stability. CD spectroscopy monitors differential absorption of right and left linear polarized light. Due to the chirality of the α-carbon atom and asymmetric polypeptide chain, proteins are optically active. Peptide bonds with their characteristic binding angles in secondary structure elements absorb polarized far-UV light (180-260 nm) in different quantities, leading to characteristic far UV (FUV) CD spectra. The monochromator of the CD spectrometer polarizes light at the wavelength λ which is then further polarized right-handed or left-handed through a modulator in a high frequency alternating field. A synchronous detector measures the light intensities I_L/I_R. The chiral protein solution absorbs I_L/I_R differently at different wavelengths. The measured ellipticity θ quantitatively describes the circular dichroism. The molar ellipticity is calculated as follows:

$$\theta_{MRW} = \frac{\theta \cdot 100 \cdot \mathrm{M}}{d \cdot c \cdot N_{aa}} \qquad \text{(Equation 2)}$$

Equation 2. Mean residue molar ellipticity. θ_{MRW}: mean residue molar ellipticity (deg cm^2 dmol^{-1}); θ: ellipticity (deg); M: Molecular mass (g/mol); d: path length (cm); c: concentration (M); N_{aa}: number of amino acids.

α-helical proteins show two characteristic minima at 222 and 208 nm and a maximum at around 190 nm. β-sheets comprise one minimum at 218 nm and a maximum at 198 nm. Random coiled structures have a maximum at 212 nm and a minimum at 195 nm. CD measurements were performed using a J-720 spectropolarimeter (Jasco, Großumstadt, Germany) or a Chirascan-plus D spectrometer (Applied Photophysics, Leatherhead, UK) equipped with a Peltier element for temperature control. FUV measurements were performed in a 1 mm path length quartz cuvette using 10 or 15 µM protein solution. Spectra were recorded between 200-260 nm with a 1 nm bandwidth at 20 °C. Spectra were buffer corrected and accumulated 16 times for the Jasco CD spectrometer and 10 times for the Chirascan. Thermal transitions were recorded at 205 nm with a heating rate of 30 °C/h for the Jasco instrument and 60 °C/h for the Chirascan, respectively. Transitions were fitted using a Boltzmann function.

2.7.3. Fluorescence Spectroscopy

Fluorescence emission is generated by excitation of an aromatic system. A photon is absorbed and transfers its energy to an electron whereby the electron excites from its ground state (S_0) to a higher energy state (S_1 and S_2), depending on the amount of energy transferred. The return from the S_1 to the S_0 state can either be driven by internal conversion, conversion to the triplet state (intersystem crossing) or emission of a photon (Jablonski, 1933). The latter is called fluorescence. Fluorescence is a widely used method in biochemistry, as the amino acids tryptophan (Trp), tyrosine (Tyr) and phenylalanine (Phe) contain natural fluorophores with the following properties at neutral pH ordered from highest to lowest quantum yields at emission wavelength:

Trp: λ_{max} (ex) = 280 nm, λ_{max}(em) = 353 nm
Tyr: λ_{max} (ex) = 275 nm, λ_{max}(em) = 304 nm
Phe: λ_{max} (ex) = 258 nm, λ_{max}(em) = 282 nm

2.7.3.1 Intrinsic Tryptophan Fluorescence

Since the fluorescence emission and signal intensity depends strongly on the environment of the amino acid and many proteins contain one or more Trp residues, intrinsic Trp fluorescence is a suitable method to monitor conformational changes of a protein. This is well established

for antibody domains due to their highly conserved Trp residue in close proximity to the quenching disulfide bond in the hydrophobic core of the domain (Feige et al., 2010). Therefore, intrinsic Trp fluorescence was used to investigate local structural changes of Ig domains during chemical unfolding or during oligomer and fibril formation. Increasing concentrations of GdmCl as a denaturant induced protein unfolding leading to solvent exposure of the Trp residue. This displacement induces to a change in Trp fluorescence visible by increase in signal intensity. For these measurements a protein concentration of 1 µM and GdmCl concentrations from 0-4 M were used. For oligomer formation, antibody domains were incubated over time and the occuring structural changes were followed by Trp fluorescence. For oligomer formation analysis, a protein concentration of 15 µM was used. Measurements were performed in a 1 cm quartz cuvette at 20 °C for unfolding and at 37 °C for oligomer analysis using a FP-6500 spectrofluorometer and a FP-8500 spectrofluorometer, respectively. Spectra were recorded between 300 and 400 nm with an excitation wavelength of 280 nm. Slit width were set to 5 nm for both excitation and emission. All spectra were recorded three times and averaged.

2.7.3.2. EXTRINSIC FLUORESCENCE

8-Anilino-1-naphtalenesulfonic acid (ANS) fluorescence

ANS is hardly fluorescent in aqueous solutions. Interaction with hydrophobic binding sites within proteins is accompanied by a blue shift and intensity increase of the emission peak (Stryer, 1965). Thus, extrinsic fluorescence upon ANS binding was used for investigations of protein surface hydrophobicity. For measurement of ANS binding, samples were incubated with 150 µM ANS for 2 h. Spectra were recorded with an excitation at 380 nm and emission from 400 to 650 nm on a FP-8500 spectrofluorometer (Jasco, Großumstadt, Germany) at 20 °C for regular measurements and at 37 °C for oligomerization analysis with a protein concentration of 1 µM in a 1-cm quartz cuvette. Excitation and emission slit widths were set to 5 nm each. All spectra were averaged from three individual measurements.

Thioflavin T (ThT) and fibril formation assay

ThT is an extrinsic fluorescent dye specific for amyloid fibril detection (Malmos et al., 2017). It binds protein independently to the amyloid specific cross-β structure. ThT assays were performed in triplicates in black 96 well microplates (#437112, Nunc, ThermoFisher Scientific, Schwerte, Germany) and measured with a Genios microplate reader (Tecan, Männerdorf, Switzerland) or an Infinite M Nano$^+$ microplate reader (Tecan) at 440 and 480 excitation and emission wavelength, respectively. To remove aggregates and oligomers from the protein solution and prevent seed formation during the assay, monomer isolation was performed prior to the experiment by ultracentrifugation in an Optima MAX-E ultracentrifuge (Beckman, Krefeld, Germany). Assays were performed in a final volume of 250 µl per well with 15-20 µM Protein, 10µM ThT and 0.05 % NaN_3 in PBS buffer (pH 7.4) containing 0.5 mM SDS to support

fibril formation (Kihara et al., 2005; Nokwe et al., 2015; Yamamoto et al., 2004). Microplates were covered with a Crystal Clear PP sealing foil (HJ-Bioanalytik GmbH, Erkelenz, Germany) and kept in the plate reader at 37 °C under continuous orbital shaking at 180 rpm. For data analysis the triplicates were averaged.

For oligomerization analysis the ThT assay was performed in 1.5 ml tubes in a thermoblock at 37 °C, 700 rpm to accelerate fibril formation. Kinetics were followed by measuring in a 1-cm quartz cuvette using a FluoroMax-4 spectrofluorometer (Horiba Jobin Yvon, Edison, USA) with excitation at 440 nm and emission at 480 nm and slit widths of 3 nm and 4 nm, respectively.

2.8. Transmission Electron Microscopy (TEM)

TEM measurements were performed to confirm the presence or absence of fibrils after a ThT assay and to analyze the size of oligomers formed prior to fibril formation. For TEM samples preparation 10 µl of the microplate well or the oligomer solution were applied onto a 200-mesh activated copper grid and incubated for 1 min. The grids were washed twice with 10 µl H_2O and negatively stained with 8 µl of a 1.5 % (w/v) uranyl acetate solution for 1 min. Excess solutions were removed with filter paper. TEM micrographs were recorded on a JEOL JEM-1400 Plus transmission electron microscope (JEOL Germany GmbH, Freising, Germany) at 120 kV.

2.9. Immunofluorescence Microscopy

For Immunofluorescence specimen preparation, Cos-1 cells were grown on MatTek dishes to 50-70 % confluency. The media was aspirated, rinsed twice with 1 ml PBS each. After that, the cells were incubated in 0.5 ml 4 % formaldehyde (EM Grade) for 20 min. The fixative was aspirated, the cells rinsed with 1 ml PBS and permeabilized with 0.3 % TX-100 in PBS for 10 min at RT. The cells were rinsed with 1 ml PBS and blocked in blocking buffer for 60 min. The solution was aspirated and the plate rinsed with 1x antibody dilution buffer (1 ml). The primary antibody was applied (1:1000 for anti human λ; 1:100 for anti-calnexin) and incubated for 1 h. The solution was aspirated and the cells rinsed with 1x antibody dilution body for 5 min. The secondary antibody was applied (1:2000) for 45 min at 37 °C. The solution was aspirated and the plate rinsed three times with PBS. 10 ul of Prolong® Gold Antifade Reagent was applied on cover slides and put on the cells. The plates were allowed to cure for 72 h in the dark at RT prior to microscopy.

2.10. Fibril Extraction from Abdominal Fat Tissue

To isolate fibril deposits from abdominal fat tissue of a patient, 25 mg tissue was diced with a scalpel and washed 5 x with 0.5 ml Tris calcium buffer each. Prior to each washing step, the sample was vortexed, centrifuges at 3.100 g for 1 min at 4 °C and the supernatant was discarded. The pellet was dissolved in a solution of 5 mg/ml *Clostridium histolyticum* collagenase in Tris calcium buffer. The mixture was incubated overnight at 37 °C under orbital shaking in a thermoblock at 750 rpm and then centrifuged at 3.100 g for 30 min at 4 °C. The pellet was resuspended in 0.25 ml Tris/EDTA buffer and homogenized using a Kontes pellet pestle. The homogenate was centrifuged at 3.100 g for 5 min at 4 °C and the supernatant was kept as wash fraction 1. The homogenization step was repeated twice resulting in wash fraction 2 and 3. The remaining pellet was again homogenized with the pestle in 0.1 ml ice-cold water and centrifuged at 3.100 g for 5 min at 4 °C. The step was repeated 4 more times and the supernatants were kept as water extracts 1-5.

2.11. Limited Proteolysis

Limited proteolysis experiments were used to investigate the susceptibility of full-length light chains to different proteases. For proteolytic cleavage with proteinase K, 0.5 mg/ml LC Pat-1 C216S and LC WT-1 C216S were mixed in an enzyme:substrate ratio of 1:10 with the protease in Ca^{2+} containing assay buffer (50 mM Tris, 5 mM $CaCl_2$, pH 7.5) and incubated at 37 °C and 300 rpm. For digestion with trypsin and chymotrypsin 1 mg/ml of the respective LC was incubated in PBS (pH 7.4) with an enzyme:substrate ratio of 1:200 and for human plasma the ratio of plasma:substrate was 1:50. Samples were taken at different timepoints and the reaction was stopped by adding PMSF to 2 mM. All limited proteolysis samples were immediately boiled in 5x reducing Laemmli buffer and stored at room temperature. For analysis of the proteolytic cleavage progress, SDS-PAGE was applied. 4-20 % Mini-PROTEAN® TGX™ Precast Protein Gels were used. After the run, colloidal Coomassie staining was utilized for visualization of the protein bands. Quantification of the respective digestion progress was performed using the software ImageJ.

2.12. Crystallography (Performed By Marie-Theres Vielberg and Prof. Michael Groll, Department Chemie, TUM)

For initial crystallization hits for the V_L domains of WT-1 and Pat-1 the vapor diffusion method at 20 °C was applied. 30 mg/ml protein in 20 mM Tris-HCl (pH 7.5) and 40 mM NaCl was mixed with reservoir solution to set up 0.4 µl sitting drops. For WT-1, crystallization was successful in 0.2 M $CaCl_2$, 0.1 M HEPES (pH 7.5), 28 % PEG400. Crystals were vitrified in liquid nitrogen at 100 K. High-resolution data were measured at beam line ID30 at the European Synchrotron

Radiation Facility (ESRF, Grenoble, France) with radiation of λ = 0.98 Å. Pat-1 crystallized in 2 µl hanging drops with 0.5 M $(NH_4)_2SO_4$, 0.1 M tri-sodium-citrate (pH 5.6), 1.0 M Li_2SO_4 as reservoir solution. Mother liquor with 40 % glycerin was used for cryo-protection. For experimental phasing information, crystals were soaked in drops containing potassium tetrachloroaureate-(III)-hydrate dissolved in mother liquor for 4 h. An anomalous data set was measured at beam line X06SA at the peak wavelength of the Au (L-III) edge (λ = 1.039 Å, f'=−17.0, f''=10) at the Paul Scherrer Institute, Swiss Light Source (Villingen, Switzerland). Additionally, a native data set was recorded at beam line ID30 at the ESFR. Initial Analysis, data processing, scaling and reduction was performed using the XDS software package (Kabsch, 1993). For structure determination, the ccp4i program suite was used (Winn et al., 2011). The structure of WT-1 was solved to a resolution of 1.55 Å using the Patterson search calculation with PHASER (McCoy et al., 2007) and the atomic coordinates of PDB: 5NKI (Hao et al., 2015). Using the experimental phase information from the Au-SAD data set of the Pat-1 crystal, Crank2 (Skubák and Pannu, 2013) generated an initial 3.5 Å model. With this, the native Pat-1 data set could be solved to 2.5 Å. Iterative round of model building and refinement using Coot (Emsley et al., 2010) and Refmac5 (Vagin et al., 2004) followed by addition of water molecules with the ARP/wARP software package (Perrakis et al., 1997) improved the structure models for both V_Ls. This lead to final R_{values} of R_{work} = 14.2% and R_{free} = 16.5% or R_{work} = 19.8% and R_{free} = 24.5%, respectively. Analysis with Molprobity (Chen et al., 2010) revealed good stereochemistry for both models. Atomic coordinates and structure factors were deposited in the RCSP Protein Data Bank under the PDB IDs 6SM1 and 6SM2.

2.13. Hydrogen/Deuterium Exchange Mass Spectrometry (H/DX-MS)

H/DX-MS was used to analyze protein dynamics. In this method, accessible hydrogen atoms are exchanged with deuterium upon incubation with a deuterium-containing buffer and subsequent mass spectrometry to analyze the mass in the digested peptides. H/DX-MS experiments were performed using a fully automated system equipped with a Leap robot (HTS PAL; Leap Technologies, NC), a Waters ACQUITY M-Class UPLC, a H/DX manager (Waters Corp., Milford, MA) and a Synapt G2-S mass spectrometer (Waters Corp., Milford, MA), as described elsewhere (Zhang et al., 2014). Protein samples were diluted in a ratio of 1:20 with deuterium oxide containing PBS buffer (pH 7.4) and incubated for 0 s, 10 s, 1 min, 10 min, 30 min and 2 h. The exchange was stopped by dilution of the labeled protein 1:1 with quenching buffer (200 mM Na_2HPO_4 x 2 H_2O, 200 mM NaH_2PO_4 x 2H_2O, 250 mM Tris (2-carboxyethyl)phosphine, 3 M GdmCl, pH 2.2) at 1 °C. Digestion was performed on-line with an immobilized Waters Enzymate BEH Pepsin Column (2.1 x 30 mm) at 20 °C. Peptides were

trapped and separated on a Waters AQUITY UPLC BEH C18 column (1.7 µm, 1.0 x 100 mm) by a H_2O to acetonitrile gradient with both eluents containing 0.1% formic acid (v/v) at 0 °C. Eluting peptides were subjected to the Synapt TOF mass spectrometer using electrospray ionization. Samples were pipetted by a LEAP autosampler (HTS PAL; Leap Technologies, NC). Data analysis was conducted with the Waters Protein Lynx Global Server PLGs (version 3.0.3) and DynamX (Version 3.0) software package.

2.14. Molecular Dynamics Simulations (performed by María Daniela Pulido Cendales and Prof. Martin Zacharias, Department Physik, TUM)

Molecular dynamics (MD) simulations were performed employing the Amber16 simulation package (D.A. Case et al., 2016). To analyze the stability of the V_L domain with specific mutations, Umbrella sampling (US) simulations were carried out with the pmemd.cuda module of the Amber16 package. The simulated variants were the wild type WT-1, the patient mutant Pat-1, the single back mutation of the patient mutant Pat-1 V81L and the double back mutation of the patient mutant Pat-1 V81L L15P. For this purpose, the Amber ff14SB force field and the TIP3P solvent model (Jorgensen et al., 1983) were utilized. Each construct was solvated in water in a periodic solvent octahedron box with a minimum distance of 10.0 Å between each atom in the protein and the edge of the periodic box. Except for that, a neutralization of the solution was achieved by adding Na^+ and Cl^- ions. Relaxation of the structure was performed with an energy minimization of maximum 1500 minimization cycles. Each system was then heated up in steps of 100K, for 10ps each, until reaching a temperature of 300 K, whereby the system was harmonically restraint to the start structure with a restraint force constant of 25.0 kcal/molÅ². Then, the system was equilibrated by gradual reduction of the restraint force, in 5 steps of 10ps each, to a restraint force constant of 0.5 kcal/molÅ². For the heating and equilibration, MD-steps of 2 ps were applied. Subsequently, hydrogen mass repartitioning (HMR) was performed to enable an increment in the simulation time step from 2 ps to 4 ps for the production simulations (Hopkins et al., 2015).

The US method allows the system to overcome an energy barrier by implementing an additional quadratic restraining potential guiding the system along a selected reaction coordinate. Extraction of the free energy along the reaction coordinate of interest is possible in which the configurations vary energetically and the system overcomes possible energy barrier. To obtain information about the folding stability of the protein, the system was simulated along a path in which the C-terminus dissociates from the protein. Therefore, the dissociation path was divided in 19 umbrella windows, which vary in the used harmonic restraining potentials, i.e. the restraining force constant (K) and the reference value around

which the system is forced to stay close to (dref). These penalty potentials were then selected so that the distribution of states was shifted along the reaction coordinate, the distribution of states converged around the desired reference value for every umbrella window and allowing for sufficient overlap between neighboring distributions. In this case, the reaction coordinate was the distance between the center of mass of the C-terminal (residues 103 to 109) and the remaining residues of the protein (1 to 102). The sets of umbrella windows generated were the following: i) 11 consecutive simulations with dref varying between 12.0 Å - 22.0 Å with a step of 1.0 Å and a force constant of K = 2.5 kcal / $Å^2$ mol, ii) 8 consecutive simulations with dref varying between 14.0 Å - 17.5 Å with a step of 0.5 Å and a force constant of K = 4.0 kcal / $Å^2$ mol. Here, positional restraints with a force constant of Kpos = 0.05 kcal / $Å^2$ were applied to the a α-carbons (Cα) of residues 1 to 102. Simulation time of each umbrella window was 100ns, but only for the last 50 ns of each window a trajectory was written and used to calculate the free energy profile (or potential-of-mean-force: PMF) by means of the WHAM algorithm (Kumar et al., 1992) along the reaction coordinate.

3. Fatal Amyloid Formation of a Patient-derived Antibody Light Chain is caused by a Single Mutation

While it is well established, that the disease AL amyloidosis can be caused by mutations in the V_L domain of a LC, only few mutations have been identified and investigated so far (Hurle et al., 1994). Mechanisms rendering LCs amyloidogenic are ill-defined. In this part of the thesis, an in-depth analysis of a patient-derived amyloidogenic LC of λ subtype was performed with respect to the factors and mutations that are responsible for the pathogenic transformation. Major parts of this chapter were published in *eLife* (Kazman et al., 2020).

3.1. Results

3.1.1. Origin, Sequence and Truncation of the Patient-Derived Amyloidogenic LC

The analyzed λ LC derived from a 50 years old, female patient diagnosed with a smoldering myeloma and AL amyloidosis at the Amyloidosis Center of the University of Heidelberg. The free LC level of λ isotype in the serum was highly elevated with 7564 mg/ml. Free κ LC levels were normal with 8 mg/ml. Clonal plasma cell infiltration in the bone marrow was high and reached 80 %. The patient suffered from multiple affected organs. Heart, kidney, lung and soft tissue were positive for amyloid deposits and were clinically involved. The cardiac score was IV (Kumar et al., 2012) or III b (Wechalekar et al., 2013) indicating highly advanced cardiac involvement. The kidney was also largely affected with a renal score of III (Palladini et al., 2015). Both scores indicate an advanced course of disease with poor prognosis. 4 weeks after initiation of chemotherapy treatment, the patient passed away form cardiac arrest. The amino acid sequence of the disease-causing LC was obtained from cDNA sequencing of the affected plasma cell clone. The corresponding germline sequence was determined by IgBLAST and abYsis as the germline LC with the lowest amount of mutations compared to the patient-derived LC. The underlying V_L germline gene is IGLV2-14*01. The LCs were named Pat-1 and WT-1 for the patient and germline sequences, respectively (Figure 12A). The two sequences differ in eleven point mutations, all located in the V_L domain. Five of these are in conserved FRs, six in the hypervariable CDRs. Using the Kabat classification system, the relative amino acid frequencies for the residues in the patient and germline V_L at the mutated position were determined (Figure 12B). For nine of the eleven mutated positions, the amino acids present in the germline were more abundant than the ones in the patient variant, indicating a potential negative effect on antibody stability or structure. The other two positions are part of the CDR loops.

To identify the exact LC truncation site and thus the disease-causing LC fragment, fibril extraction from abdominal fat tissue derived from the patient followed by SDS-PAGE (Figure

12C) and mass spectrometry were performed (Figure 12D). The analyses revealed the predominant deposition of the complete V_L domain and not the entire LC in the fibrils.

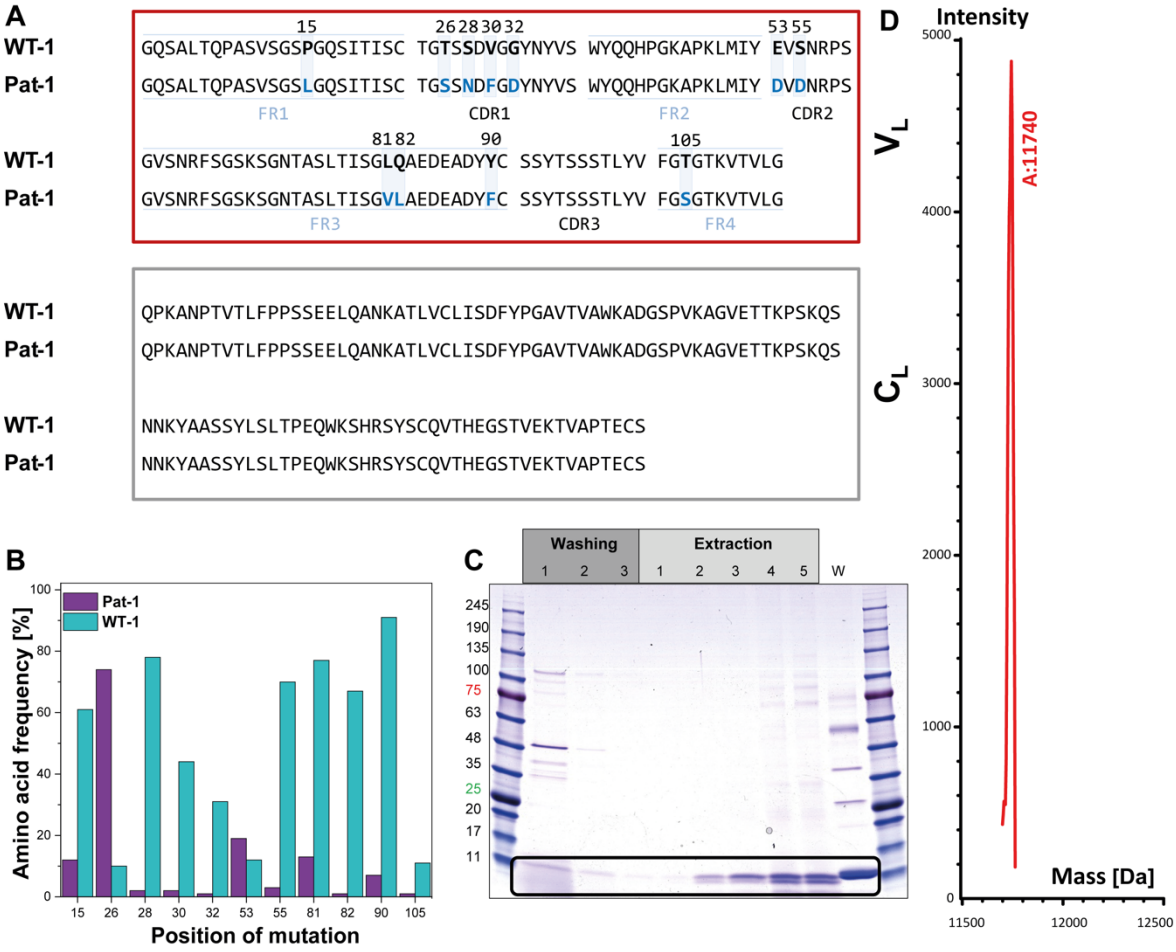

Figure 12. LC sequence analysis and identification of the V_L domain as the predominant depositing LC truncation. A) Sequence of the patient-derived and corresponding germline LC. Patient sequence derives from cDNA of the underlying plasma cell clone, the germline sequence was determined by database search. V_L domains, that are found in deposits are in the red square, C_L in the grey square. Mutations in the V_L are colored in blue. B) Frequency of the amino acids present in WT-1 and in Pat-1 at the mutated positions. The frequencies of the residues in WT-1 are shown in cyan, the ones of Pat-1 in purple. C) SDS-Page analysis of the fibril extraction from the patient's abdominal fat tissue. The predominantly deposited LC truncation runs at ~11 kDa. D) Mass spectrometry revealed that the mainly deposited truncation has a mass of 11,740 Da which corresponds to the V_L domain with an N-terminal pyro-glutamate.

To analyze whether the proteolytic processing of the LC is necessary for its conversion into amyloid, fibril formation assays monitored by thioflavin T (ThT) fluorescence were performed with the full-length LC and the determined LC truncations of both, WT-1 and Pat-1 (Figure 13A). Under physiological conditions, fibril formation at 37 °C takes a long time. In this study, low concentrations (0.5 mM) of SDS, that do not affect the native secondary structure, were

used to accelerate the process (Kihara et al., 2005; Nokwe et al., 2015; Yamamoto et al., 2004). Full length LCs and the WT-1 truncation stayed soluble during the time of the assay, whereas the Pat-1 V_L domain readily formed fibrils. The absence and presence of fibrillar structures was confirmed with transmission electron microscopy (TEM) (Figure 13B-E). Thus, proteolytic cleavage of the LC in the patient is required for fibril formation. As a consequence of the exclusive amyloidogenic behavior of Pat-1 V_L, the further investigations were mostly carried out with the V_L domains. Whenever Pat-1 or WT-1 is named without further specification about the construct length, the statement refers to the respective V_L domain.

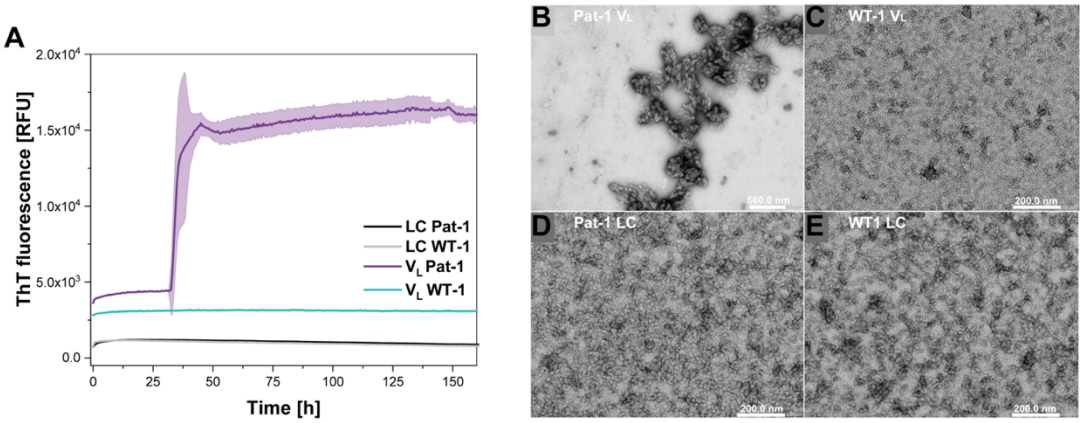

Figure 13. Fibril formation of full-length LCs WT-1 and Pat-1 and the truncated V_L variants. A) ThT fluorescence intensity of the different variants monitored over time. Increase of fluorescence intensity indicates fibril formation. The continuous lines show the mean of triplicates with SD as transparent colored background. B) Transmission electron microscopy (TEM) confirmed the presence of fibrils for Pat-1 V_L and the absence of fibrils for C) WT-1 V_L, D) Pat-1 LC and E) WT-1 LC.

3.1.2. Structure of the Pat-1 and WT-1 V_L Domains

To determine potential structural differences between the V_L domains of Pat-1 and WT-1, they were subjected to crystallization. For Pat-1, diffracting crystals belonging to the space group $P6_122$ were obtained and the structure was solved to 2.5 Å. WT-1 V_L crystals belonged to the space group $P6_322$ and were solved to 1.55 Å resolution in the group of Prof. Michael Groll (see Table 3 for data collection and refinement statistics). Atomic coordinates and structure factors have been deposited in the RCSB Protein Data Bank under the PDB IDs **6SM1** (WT-1) and **6SM2** (Pat-1).

Both domains exhibit the typical Ig fold consisting of nine ß-strands forming a greek-key ß-barrel topology (Figure 14A, B). The three CDR loops are in spatial proximity to form the antigen binding site. The location of all eleven mutations did not reveal explanations about the differences in fibril formation propensity. Six mutations are found in CDR loops (T26S, S28N, V30F, G32D, E53D and S55D) and five in FRs (P15L, L81V, Q82L, Y90F and T105S). The FR mutations Y90F and T105S flank the third CDR loop. P15L, V81L and L82Q are located

opposite to the antigen binding site and in close proximity to the C-terminal truncation site between V_L and C_L domain. The superposition of the two domains shows an additional small α-helical region in the CDR2 loop of Pat-1 that is not present in the WT-1. It forms part of the antigen binding site. However, judging from the superposition of both crystal structures, no reasonable conclusion regarding the differences in fibril formation could be drawn (Figure 14C).

Table 3. Crystallographic data collection and refinement statistics.

	WT-1	**Pat-1**
Crystal parameters		
Space group	$P6_322$	$P6_122$
Cell constants	a = b = 104.5 Å c = 55.2 Å	a = b = 127.3 Å c= 81.8 Å
Subunits / AU[a]	1	2
Data collection		
Beam line	ID-30, ESRF	ID-30, ESRF
Wavelength (Å)	0.976	0.976
Resolution range (Å)[b]	50 – 1.55 (1.65 – 1.55)	50 – 2.5 (2.6 – 2.5)
No. observed reflections	162247	115993
No. unique reflections[c]	26220	13924
Completeness (%)[b]	99.7 (99.8)	99.4 (100)
R_{merge} (%)[b, d]	4.3 (58.7)	5.5 (49.6)
I/σ (I)[b]	20.9 (3.2)	20.6 (4.2)
Refinement (REFMAC5)		
Resolution range (Å)	15 – 1.55	15 – 2.5
No. refl. working set	24867	13148
No. refl. test set	1309	692
No. non hydrogen	1025	1653
Solvent (H_2O, ions, PEG)	178	39
R_{work} / R_{free} (%)[e]	14.2 / 16.5	16.2 / 22.7
r.m.s.d. bond (Å) / (°)[f]	0.007 / 1.3	0.003 / 1.2
Average B-factor (Å^2)	25.4	83.6
Ramachandran Plot (%)[g]	95.4 / 4.6 / 0	95.3 / 4.7 / 0
PDB accession code	6SM1	6SM2

[a] Asymmetric unit
[b] The values in parentheses for resolution range, completeness, R_{merge} and I/σ (I) correspond to the highest resolution shell
[c] Data reduction was carried out with XDS and from a single crystal.
[d] $R_{merge}(I) = \Sigma_{hkl}\Sigma_j \mid I(hkl)_j - \langle I(hkl)\rangle \mid / \Sigma_{hkl}\, \Sigma_j I(hkl)_j$, where $I(hkl)_j$ is the j^{th} measurement of the intensity of reflection hkl and $\langle I(hkl)\rangle$ is the average intensity
[e] $R = \Sigma_{hkl} \mid |F_{obs}| - |F_{calc}| \mid / \Sigma_{hkl} |F_{obs}|$, where R_{free} is calculated without a sigma cut off for a randomly chosen 5% of reflections, which were not used for structure refinement, and R_{work} is calculated for the remaining reflections
[f] Deviations from ideal bond lengths/angles
[g] Percentage of residues in favored / allowed / outlier region

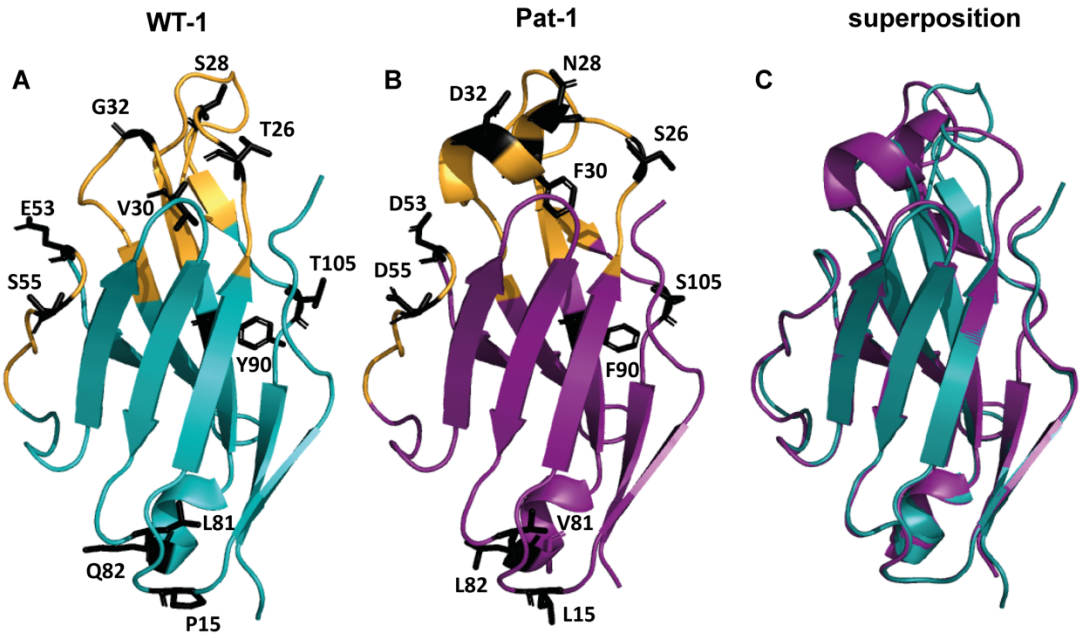

Figure 14. Comparison of the crystal structures of WT-1 and Pat-1 V_L domains. A) WT-1 is highlighted in cyan, B) Pat-1 in purple. The CDR regions are colored in yellow and the amino acids at the mutated positions are depicted as black sticks. C) The superposition of the two domains reveals only minor differences.

3.1.3. Biophysical Characterization of Pat-1 and WT-1

For further insights into the consequences of the mutations, the two domains were biophysically characterized regarding quaternary structure and stability. One important issue is whether the LC is in a monomeric or dimeric state, as LC dimerization was reported for some LCs and LC fragments (Brumshtein et al., 2014; Rennella et al., 2019). Analytical ultracentrifugation (AUC) analysis revealed that the Pat-1 and WT-1 V_L domains both exclusively formed monomers in solution with sedimentation coefficients of approximately 1.6 S (Figure 15A).

To investigate differences caused by the mutations, the thermal stabilities of both domains were measured by monitoring the loss of secondary structure upon heating using far-UV CD-spectroscopy (Figure 15B). The melting temperature (T_m), defined as the point at which 50 % of the protein is unfolded, were 48.9 °C for Pat-1 and 57.0 °C for WT-1. Chemical unfolding was used as an orthogonal method for stability determination. Here, the tryptophan fluorescence intensity in the presence of increasing concentrations of GdmCl was measured. Both V_L domains showed sigmoidal unfolding curves and the c_m - value, defined as the GdmCl concentration at which 50 % of the protein is unfolded, was increased by 0.46 M GdmCl for WT-1 compared to Pat-1 (Figure 15C). In summary, the stability results revealed that Pat-1 is significantly less stable than the germline V_L.

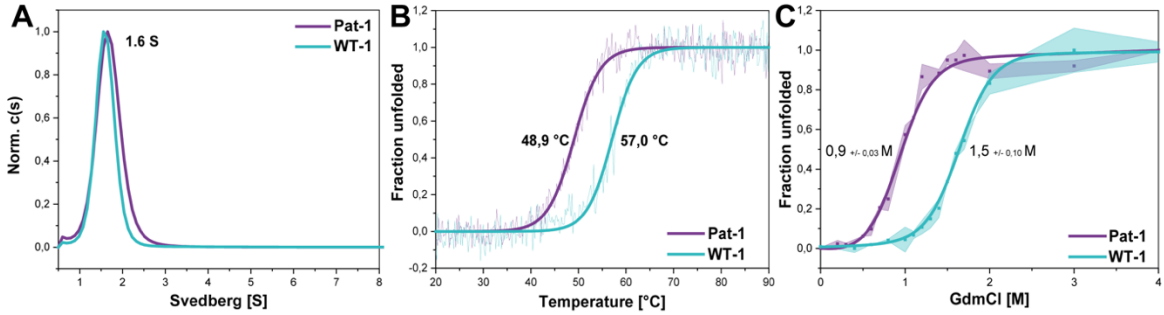

Figure 15. Biophysical characterization of Pat-1 and WT-1. A) Analytical ultracentrifugation sedimentation velocity runs show monomeric organization with a Svedberg value 1.6 S for both domains. The data were analyzed using the continuous c(S) distribution mode in SedFit. B) Stability information were obtained by thermal unfolding transitions of Pat-1 and WT-1. The dots show the raw data, the continuous lines show the Boltzmann fit. C) GdmCl-induced chemical unfolding monitored by tryptophan fluorescence at 349 nm was used for chemical stability analysis. The measurements were performed in triplicates. The continuous lines show the mean data fit to a two-state unfolding mechanism with SD.

3.1.4. Analysis of the Effect of Single Mutations on Stability and Fibril Formation

To determine the impact of the sequence variations and identify the mutation(s) decisive for stability and amyloidogenicity of Pat-1, all point mutations in Pat-1 were substituted individually with the respective residue present in WT-1. Thermal and chemical stabilities revealed that ten out of the eleven mutations either had (i) minor effects on stability (S26T, N28S, S105T), (ii) were even further destabilizing the domain (L15P, F30V, D53E), (iii) showed a negative effect on thermal stability (D32G, D55S), or, (iv) showed a slight increase in chemical stability (L82Q, F90Y) (Figure 16A, B). In contrast, the mutation V81L resulted in a significant shift of Pat-1 towards the stability values of WT-1 with a T_M of 54.6 °C and a c_M of 1.36 M (WT-1: T_M = 57.0 °C, c_M = 1.43 M). This trend could also be seen in the fibril formation assay, where all Pat-1 point mutants except V81L formed amyloid structures (Figure 16C). The absence of fibrils was confirmed by TEM micrographs (Figure 16D). Performing the experiments vice versa showed that the replacement of leucine by valine (L81V) in WT-1 had the exact opposite effect as V81L in Pat-1. Thermal stability of WT-1 L81V was decreased by 5.5 °C compared to WT-1 (Figure 16E) and the c_M value was reduced by 0.42 M GdmCl (Figure 16F). Thus, the introduction of valine at position 81 shifts the germline V_L domain towards the stability of Pat-1. Following ThT fluorescence upon incubation of the WT-1 L81V variant, an increase of intensity indicating fibril formation could be observed (Figure 16G). The presence of fibrils was confirmed by TEM micrographs (Figure 16H). Together, these results suggest that the pathogenicity of the AL patient LC truncation can be traced back to only one amino acid change in the wild-type V_L.

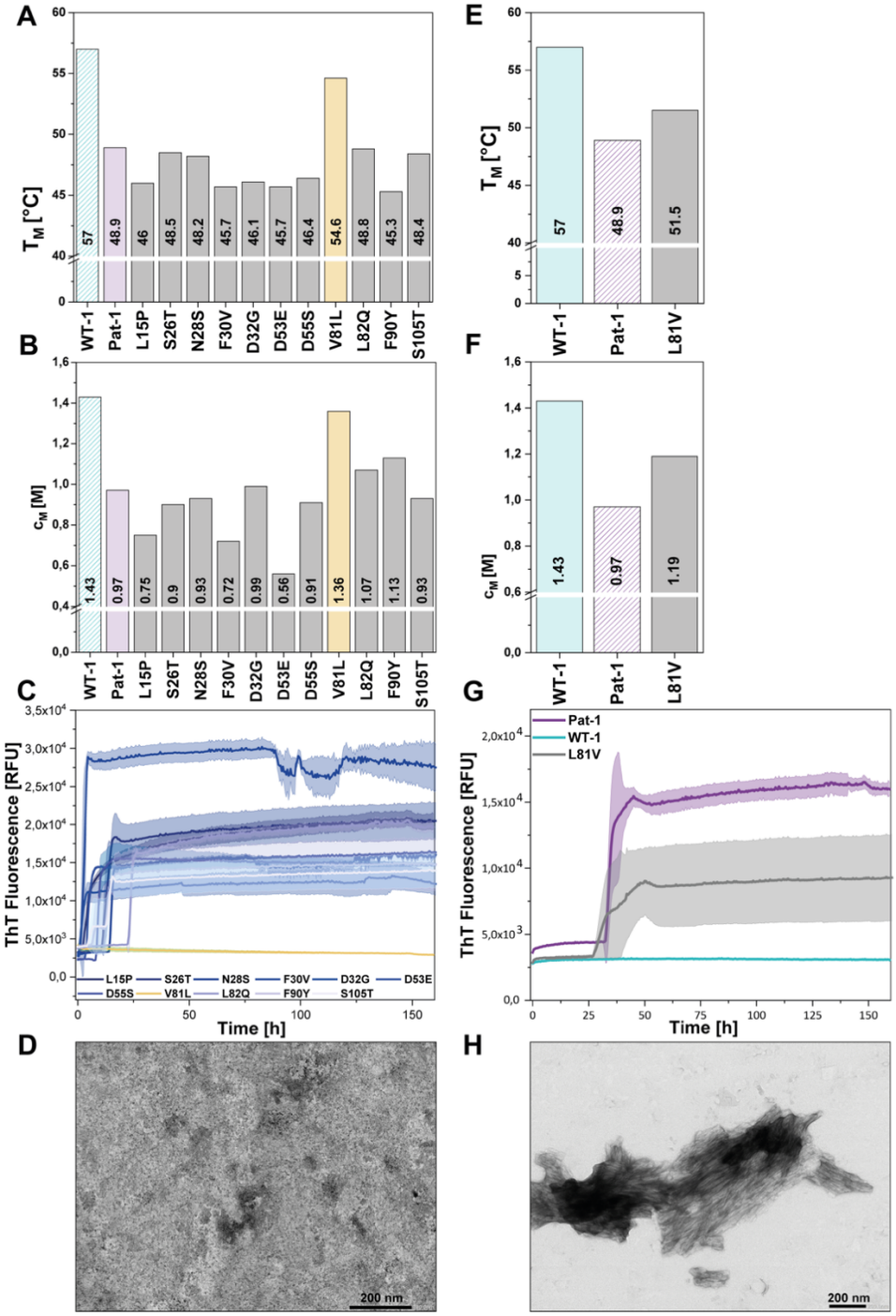

Figure 16. Effect of point mutations on stability and fibril formation propensity of Pat-1 and WT-1. A) Comparison of T_M and B) c_M values of Pat-1, WT-1 and single point mutant of Pat-1. T_M values were derived from fitting the thermal-induced unfolding transition data to a Boltzmann function. c_M values were obtained by fitting the chemical unfolding data according to a two-state unfolding model. C) Fibril formation assay of single point variants followed by ThT fluorescence. D) TEM micrograph proving the absence of fibrils for Pat-1 V81L. E) Comparison of T_M and F) c_M values of Pat-1, WT-1 and the WT-1 single point mutant L81V. G) Fibril formation assay followed by ThT fluorescence. The ThT Assays were performed in PBS buffer containing 0.5 mM SDS at 37 °C and shaking. The continuous lines show the mean value of triplicates with SD as transparent colored areas. H) Detection of fibrils for WT-1 L81V was confirmed by TEM.

The identified sequence change concerns two closely related amino acids: leucine and valine. Both residues exhibit hydrophobic characteristics and differ in only one methylene moiety. To test if the effect of the V81L mutation in Pat-1 is specific to a substitution with leucine, V81 was mutated to an isoleucine residue. Isoleucine is similar to leucine regarding the constituent atoms and hydrophobic characteristics. The V81I variant did not significantly increase in thermal stability compared to Pat-1 (Figure 17A). Furthermore, V81I, in contrast to V81L, did not protect the antibody domain from forming amyloid fibrils (Figure 17B). Consequently, the protective effect observed for V81L is highly specific to leucine.

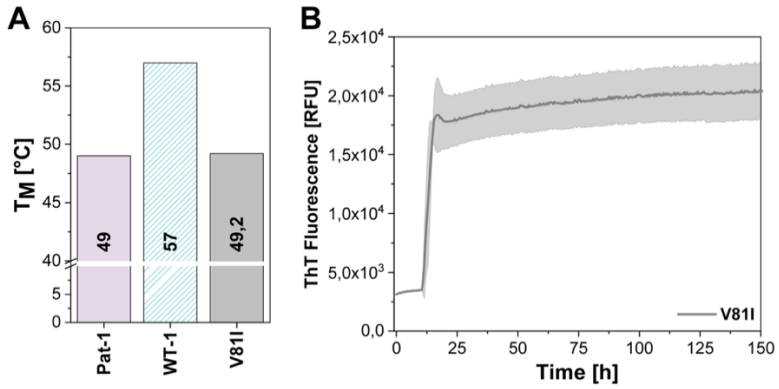

Figure 17. Impact of the V81I substitution in Pat-1 on the thermal stability and fibril formation propensity of the V_L. A) Substitution of V81 to Isoleucine did not result in an increase of thermal stability compared to Pat-1. T_M values were derived from fitting the thermal unfolding data to a Boltzmann function. B) Fibril formation kinetics of V81I showed an increase of ThT fluorescence indicating fibril formation. The continuous lines show the mean value of triplicates with SD as transparent colored areas.

3.1.5. A Surface-Exposed Hydrophobic Spot Harboring V81 is Crucial for Stability and Fibril Formation Propensity

The location of V81 alone could not explain the accompanied effect. However, the close proximity to the other mutations L15 and L82 was striking (see chapter 3.1.2). Investigating the surface properties in this region with respect to hydrophobicity revealed the location of these three amino acids in a surface-exposed hydrophobic patch that is not present in WT-1 (Figure 18A, B). Thus, the combined effect of these three residues was analyzed regarding stability and fibril formation. For this, all possible combinations of the mutations were designed as double and triple mutants. Thermal and chemical unfolding showed that the combination of mutations at positions 81 and 82 (V81L L82Q) enhanced the increase in stability slightly compared to V81L alone, whereas integrating the L15P substitution in combination with the two others, alone or combined, led to a decrease in stability (Figure 18C,D). Fibril formation kinetics showed a correlation of the stability data and amyloidogenicity. The protective effect of V81L was preserved in combination with L82Q. The presence of L15P increased fibril formation (Figure 18E). This gives rise to the conclusion that the hydrophobic surface area in

Pat-1 plays a key role in pathogenesis. Minimizing the hydrophobic spot by the back-mutation of L82 to glutamine supports the anti-amyloidogenic effect of V81L and L15P alone and in all combinations had negative effects on stability and fibril formation.

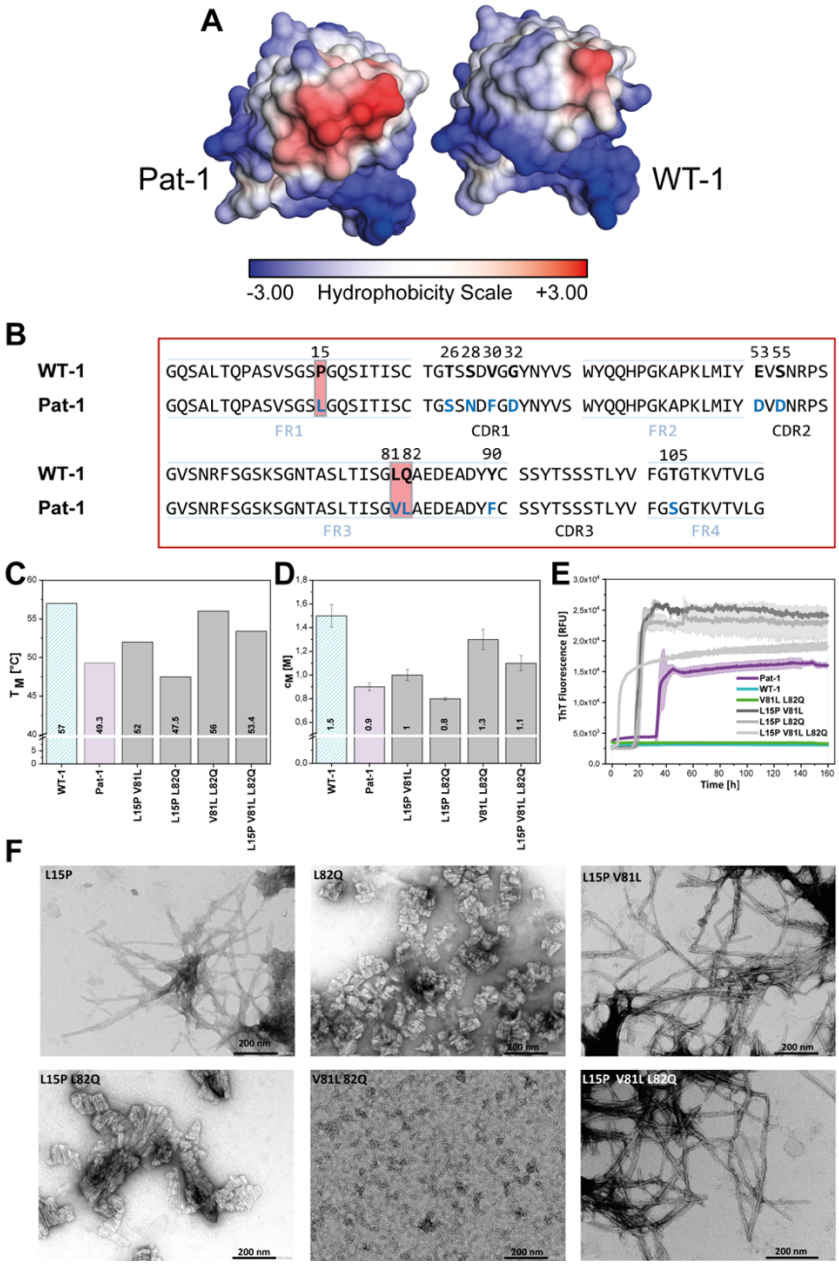

Figure 18. Impact of amino acid substitutions altering the hydrophobic surface area of Pat-1. A) Surface view of the crystal structures of Pat-1 and WT-1 show the larger hydrophobic area of Pat-1 in red. Hydrophilic residues are colored in blue. B) Sequence of Pat-1 and WT-1 with the residues located in the hydrophobic spot highlighted in red. Stability comparison by C) T_M values derived from thermal unfolding data and D) c_M values obtained by GdmCl unfolding of double and triple mutants. E) Fibril formation followed by ThT fluorescence intensity. The continuous lines show the mean of triplicates with SD. F) TEM micrographs of the V_L variants confirm the presence or absence of fibrils.

3.1.6. The Mutations And Truncation of The LC Lead to Enhanced Conformational Dynamics of Pat-1

To gain insight into conformational dynamics of Pat-1 and WT-1, the kinetics of hydrogen/deuterium exchange (H/DX) rate was followed by mass spectrometry (Bail and Englander, 1996; Rand et al., 2014). Measurements were performed after 10 s, 1 min, 10 min, 30 min and 2 h of exchange. Complete sequence coverage for both LC truncations was obtained. For visualization of the exchange rates at different timepoints, the values for each residue were mapped on the corresponding X-ray structure (Figure 19). Pat-1 V_L shows a higher exchange rate from the very beginning and a faster and higher exchange over time. This indicates higher conformational dynamics.

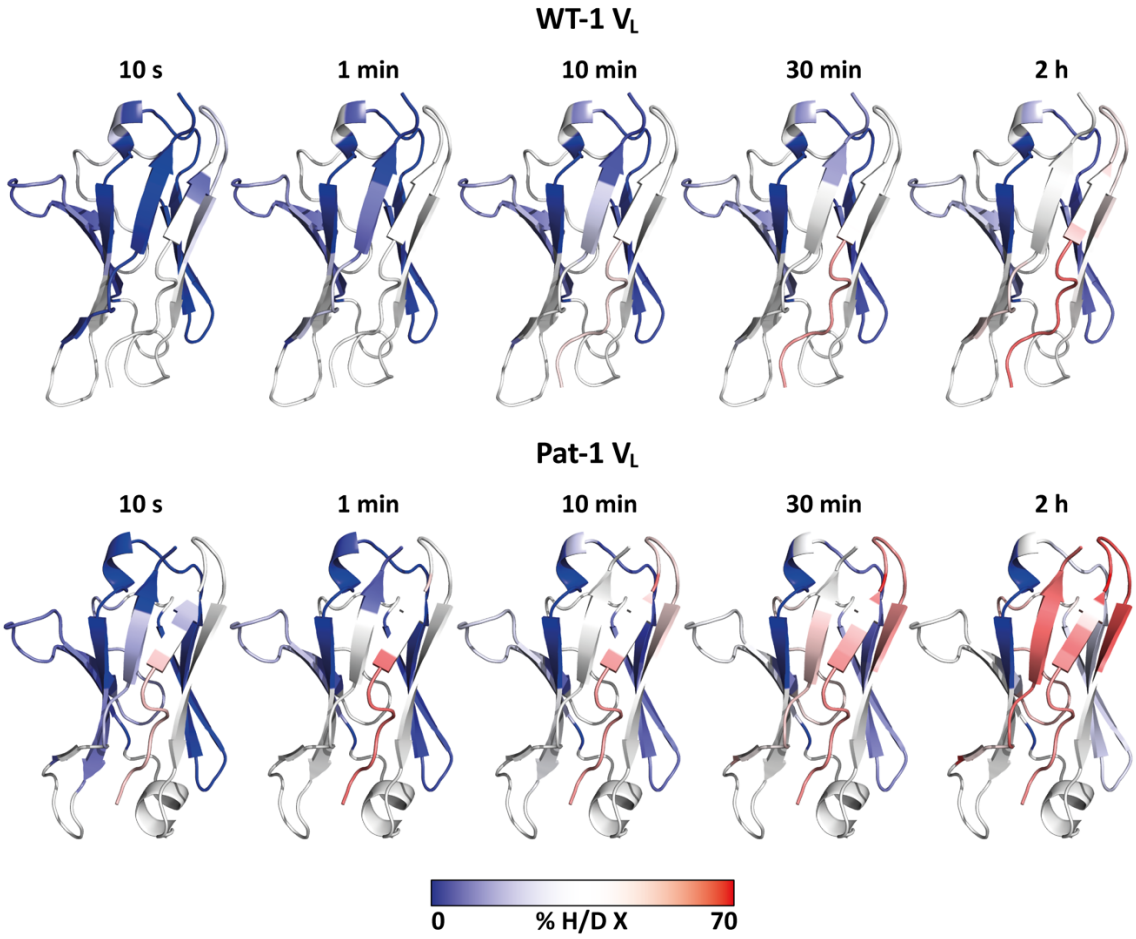

Figure 19. H/DX rates mapped on the crystal structures of WT-1 (top) and Pat-1 (bottom). Residues highlighted in blue show no exchange, residues in red show 70 % exchange of H to D at the specific timepoint.

As mentioned above, the analyses indicate that Pat-1 exhibits higher conformational dynamics as indicated by an overall higher HD/X rate (Figure 20A). The most affected sequence segment was the C-terminal end of Pat-1, where the cleavage between V_L and C_L took place (FR4, residues 101-113). This region is in close proximity to the three identified residues located in the hydrophobic surface spot in Pat-1. Also, a region in FR1 (residues 10-20) showed enhanced HD/X rates. This stretch harbors residue 15, which is part of the surface-exposed hydrophobic spot. To directly compare the conformational dynamics of WT-1 and Pat-1, the differences in the exchange rate of Pat-1 and WT-1 were calculated for every residue and mapped on the X-ray structure of Pat-1 (Figure 20B). It becomes obvious that the patient domain shows a higher flexibility in most parts if the domain, compared to WT-1 and that the C-terminal region is significantly more dynamic in the patient domain. To analyze how the conformational dynamics change for the V_L domain as part of the full length LC, the same experiment was performed with LC Pat-1 and LC WT-1 (Figure 20C). For this experiment, the LC with a C216S mutation was used to provide only monomeric LCs. The exchange rates of both WT-1 and Pat-1 V_L as part of the LC are lower than the V_Ls alone. Also, the differences in exchange rates of the C-terminal region are not detectable anymore. The loop harboring residue 15 still showed a higher flexibility in LC Pat-1 than in LC WT-1. To visualize the differences in exchange rates between LC WT-1 and LC Pat-1, a full-length LC crystal structure model of LC Pat-1 was generated using the web-based tool Phyre2 (Figure 20D). 215 out of 217 LC residues (99% of the sequence) could be modelled with 100 % confidence. The linker including the FR4 region differed in H/D exchange rate between patient and germline variant like it is the case for the isolated V_L domain. Only a small part at the end of the V_L domain shows slightly enhanced H/DX values. Hence, the C_L domain, that is the same for both variants, compensates the differences between the two V_L domains. When directly comparing the differences in hydrogen to deuterium exchange between the V_L domain alone and the V_L domain as part of the full-length LC, an overall reduction of the exchange can be observed for almost the complete length of the sequence (Figure 20E). Consequently, the C_L domain has a protective effect and the enhanced conformational dynamics is a consequence resulting from the proteolytic cleavage of the LC.

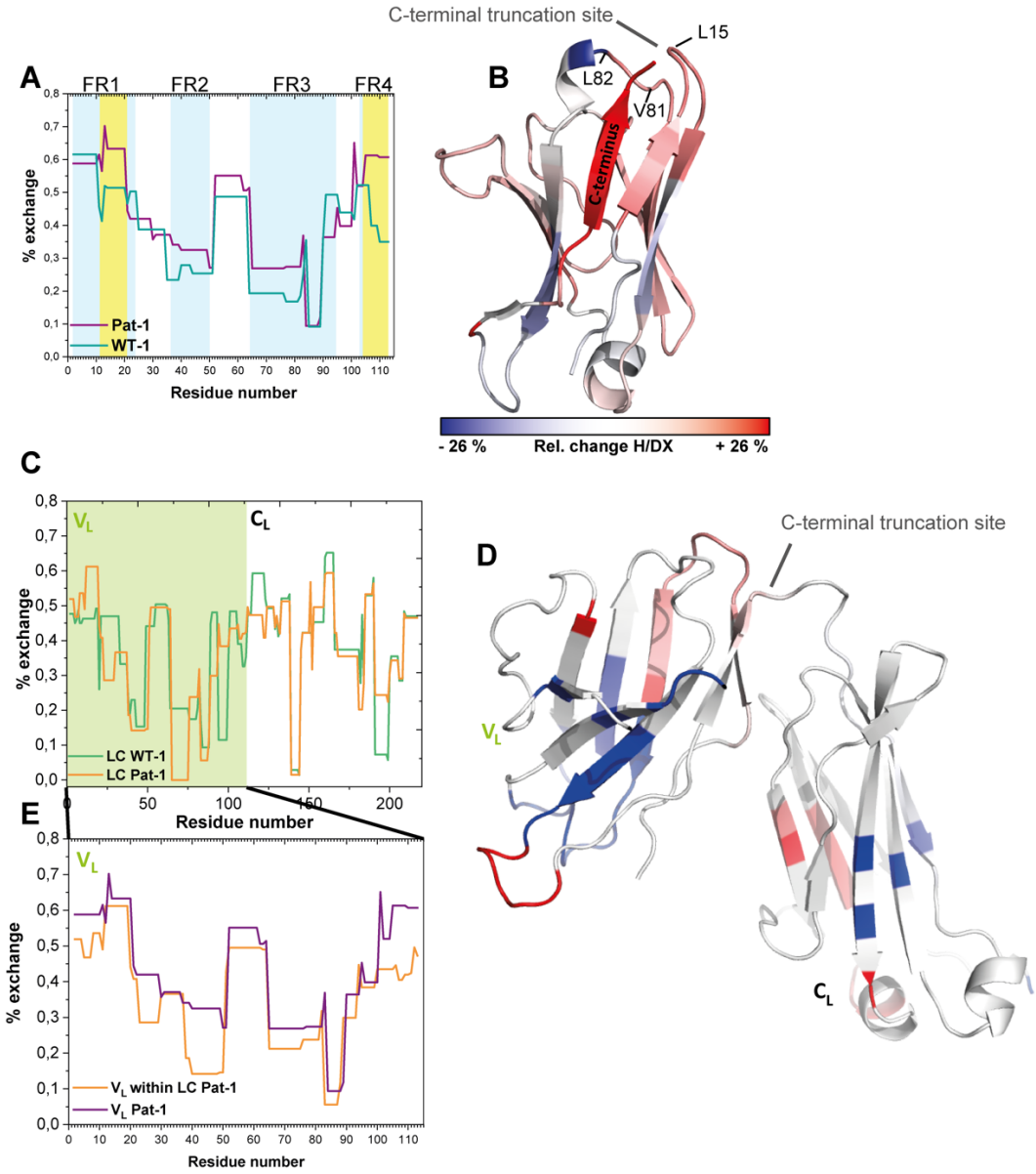

Figure 20. Comparison of HD/X rates of Pat-1 and WT-1 as V_L domains and as part of the full-length LC. A) The % exchange rate for Pat-1 V_L is shown in purple, the one of WT-1 V_L in cyan. Pat-1 shows an overall higher exchange rate. The most affected regions are colored in yellow. The FRs are colored in blue. B) The relative change in fractional uptake between Pat-1 and WT-1 V_L domains is mapped on the Pat-1 crystal structure. Residues with higher or lower exchange in Pat-1 compared to WT-1 are colored from red to blue, respectively. C) The % exchange rates for the full-length LC variants LC Pat-1 (orange) and LC WT-1 (green). The V_L domain is highlighted in green. D) The relative change in fractional uptake between LC Pat-1 and LC WT-1 mapped on a modelled structure of LC Pat-1. The model was generated using the web-based tool Phyre2. E) % exchange rates of the isolated V_L domain of Pat-1 compared to the V_L domain bound to the C_L domain in LC Pat-1.

3.1.7. Altered Hydrophobic Interactions Explain The Differences in Dynamics and Stability

The identified pathogenic residues in the hydrophobic surface area affect domain stability and fibril formation propensity. Enhanced conformational dynamics show a highly flexible C-terminal region where the truncation occurred. To bring these results together and determine the underlying molecular reasons for the differences, the side chain interactions in the crystal structures of both V_L domains were analyzed using the BIOVA Discovery Studio software (Table 4, Figure 21A, B). The results reveal that the mutations of the residues at position 15, 81 and 82 from the ones present in WT-1 to the amino acids of Pat-1 lead to a decrease of the total number of hydrophobic interactions (Figure 21C, D, Table 4). P15 is part of FR1 that shows a high HD/X rate. In WT-1 the proline is not involved in a hydrophobic network. However, L15 in the patient domain interacts with three amino acids of FR3 via hydrophobic interactions. These residues include the two other point mutations of the hydrophobic surface spot. Additionally, the leucine at position 15 interacts with two more residues in the C-terminal region (V111 and L112) through hydrophobic interactions. Consequently, the contact of L15 to the highly dynamic C-terminal segment induces the enhanced conformational dynamics of the respective loop in FR1. The valine residue that is present in Pat-1 forms six hydrophobic interactions with residues in FR2 and FR3, including the residues of the hydrophobic surface area: L15 and L82. With the mutation of residue 82, a hydrophilic amino acid is substituted by a hydrophobic residue. Thus, the hydrophobic patch is decreased in WT-1. L82 forms five hydrophobic interactions with FR2, FR3 and FR4. On the other hand, Q82 forms hydrophilic interactions to four residues, all located in FR3. Thus, the interaction network affecting the C-terminal region of Pat-1 is markedly changed by the mutations at position 15, 81 and 82 which entails a highly dynamic C-terminal segment.

Table 4. Hydrophobic interaction pattern of the three mutated amino acids at positions 15, 81 and 82, located in the altered hydrophobic surface area of the V_L variants Pat-1 and WT-1. Hydrophobic interactions are shown in red, hydrophilic interactions in blue.

Pat-1	FR2		FR3				FR4/C-terminus		
	L15	**I19**	**I78**	**V81**	**L82**	**A83**	**V109**	**V111**	**L112**
L15									
V81									
L82									

WT-1	FR2		FR3				FR4/C-terminus		
	P15	**I19**	**I78**	**L81**	**Q82**	**A83**	**V109**	**V111**	**L112**
P15									
L81									
Q82			R64	E84	D85	E86			

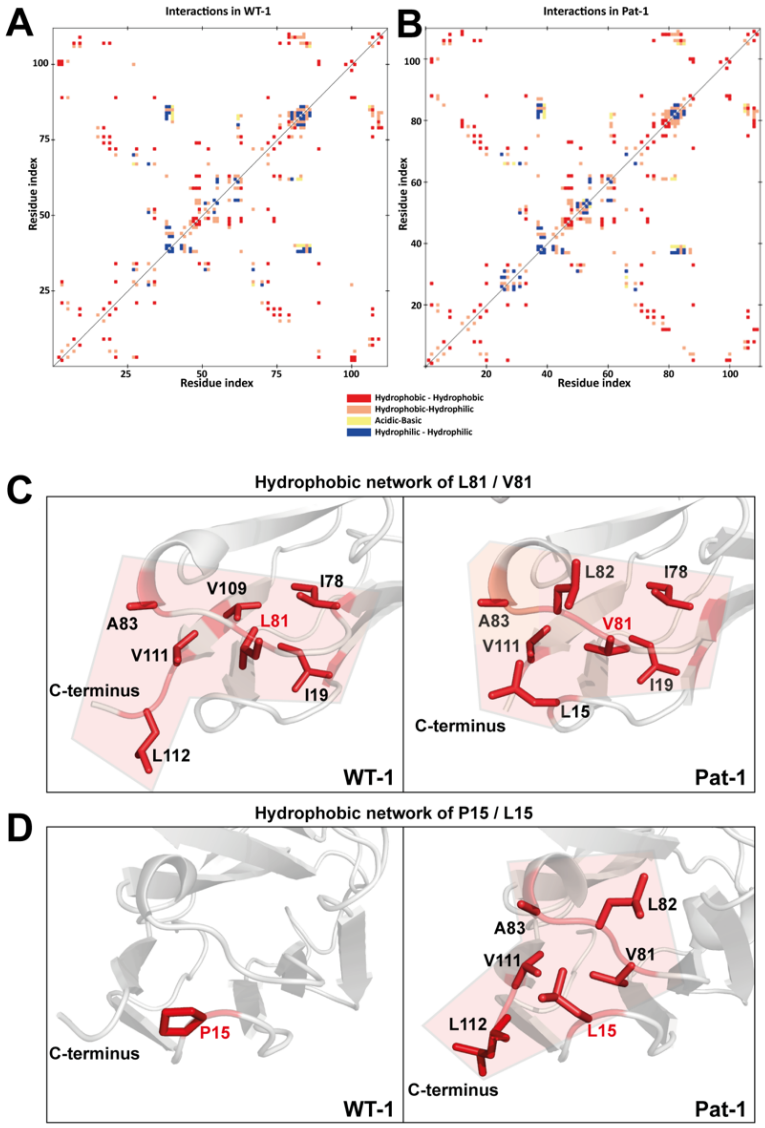

Figure 21. Hydrophobic interactions in WT-1 and Pat-1. Identified interactions in the V_L sequence using the software Discovery Studio of A) WT-1 and B) Pat-1. C) Hydrophobic network of L81 for WT-1 and V81 for Pat-1. D) Hydrophobic network of P15 for WT-1 and L15 for Pat-1. The residues included in the hydrophobic network are shown as red sticks. The network area is highlighted in light red.

3.1.8. Modified Interaction Pattern Favors Dissociation of the C-Terminal Region

To further investigate the protective effect of the V81L back mutation and the contrary effect of the L15P mutation, molecular dynamics (MD) free energy simulations were performed by Prof. Martin Zacharias and Daniela Pulido Cendales. Using Umbrella Sampling (US) simulations, the dissociation of the C-terminal region (residues 102 onwards), was induced for WT-1, Pat-1, Pat-1 V81L and the double mutant Pat-1 P15L V81L and the change in free energy was calculated for each domain. For this, the free energy of dissociating the C-terminal end of the domain from the otherwise folded protein serves as a relative estimate for the

influence of the specific mutation on the stability of the protein fold. The C-terminal dissociation was mapped on the crystal structures of Pat-1 and WT-1 (Figure 22). Calculated free energy profiles of WT-1 and V81L exhibit similar dissociation free energies. Compared to Pat-1, the values were higher by ~1 kcal mol^{-1}. The double back mutation P15L V81L showed even lower values as Pat-1 (Figure 22B). The results indicate an increased protein stability for WT-1 and the V81L point mutant. The effect of the V81L substitution is mainly because of a small cavity that is present for V81. Replacing this residue with a slightly larger one (L81), this cavity is filled. The destabilizing effect of the double back mutation produces a significant reduction of the dissociation free energy (~1 kcal mol^{-1}) relative to the patient mutant Pat-1. This can be explained by a change in the local protein backbone due to the L15P substitution that leads to a change in the local packing geometry and offsets the effect of V81L. RMSD values are shown in Figure 22C.

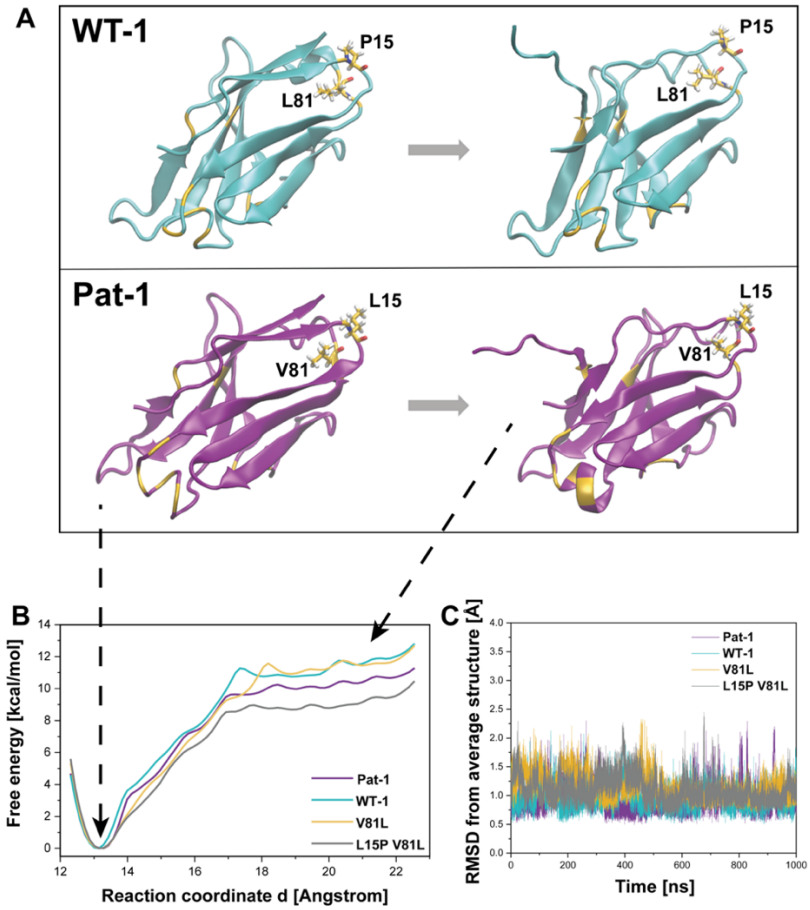

Figure 22. MD simulations of WT-1, Pat-1, V81L and L15P V81L. A) Snapshot of and B) Potential mean force (PMF) for the dissociation of the C-terminal region. The free energy along the reaction coordinate was calculated by means of umbrella sampling simulations. The reaction coordinate corresponds to the distance between the center of mass of the α carbons of the rest of the protein (1-102). C) Root mean square deviation (RMSD) from corresponding time-averaged structures during MD Simulations. The coordinate RMSD was calculated over 1 period of 1 µs of free MD simulations at 300 K. High stability of the structure is reflected by a RMSD <2.5 Å for all conformations.

3.1.9. Full Length LCs Differ in Linker Accessibility and Susceptibility to Proteolytic Cleavage

It became clear that the difference between the patient and germline V_L domains regarding stability and fibril formation propensity is based on changes in hydrophobic interactions. These concern the residue 15, located in a loop region of FR1, and residues 81 and 82, both located in FR4 and the C-terminal region that evolves from proteolytic cleavage of the LCs in the patient. The H/DX data for the LCs were already described in the context of the V_L domains in chapter 3.1.6. A detailed look on the crystal structure models of LC WT-1 and LC Pat-1 reveals that the loop region harboring residue 15 is still significantly more dynamic in LC Pat-1 than in WT-1 even though the high flexibility of the C-terminal segment is reduced (Figure 23). As described before, residue L15 in Pat-1 forms hydrophobic interactions to the C-terminal end of the V_L, which is the linker in the context of the full-length LC. These interactions can possibly explain a higher susceptibility of the linker region due to the flexibility of the loop. The linker between V_L and C_L domain in LC Pat-1 shows a higher H/D exchange rate over time compared to LC WT-1, indicating that the two domains are more prone to move apart from each other.

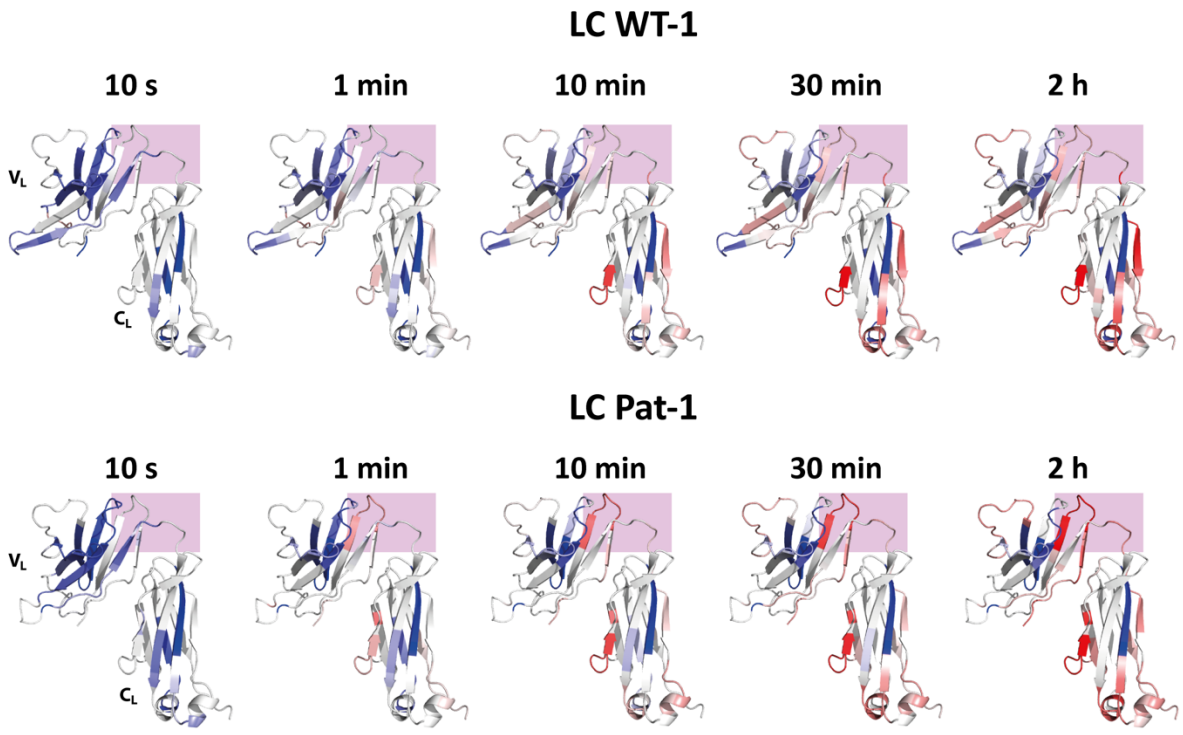

Figure 23. H/DX rates mapped on the crystal structures models of LC WT-1 (top) and LC Pat-1 (bottom). Residues are colored according to their H to D exchange rates from blue for no exchange to red for ~60 % exchange at the specific time point. The linker area and the loop region harboring residue 15 in close proximity to the truncation site are highlighted by a purple square.

To analyze how the H/DX-MS data correlate with actual proteolysis, limited proteolysis experiments using proteinase K were performed with the LC constructs. Proteolysis at a low enzyme to substrate ratio constitutes a highly discriminating tool to compare very flexible and solvent-exposed sites of native globular proteins and thus to monitor their focal stability in the surface topology (Mangione et al., 2014). In the context of LCs, endoproteolysis is described to be an approach to access LC kinetic stability based on the model, that an enzyme can cleave LCs whenever they access an extended unfolded conformation (Morgan and Kelly, 2016b). The juxtaposition of susceptibility to cleavage by proteinase K revealed a clear difference between the digestion kinetic of LC Pat-1 (Figure 24A) and LC WT-1 (Figure 24B). Digestion of LC Pat-1 occurred rapidly with a $t_{1/2}$ of only 0.5 min while LC WT-1 was digested at lower rates, resulting in a $t_{1/2}$ of 6.3 min.

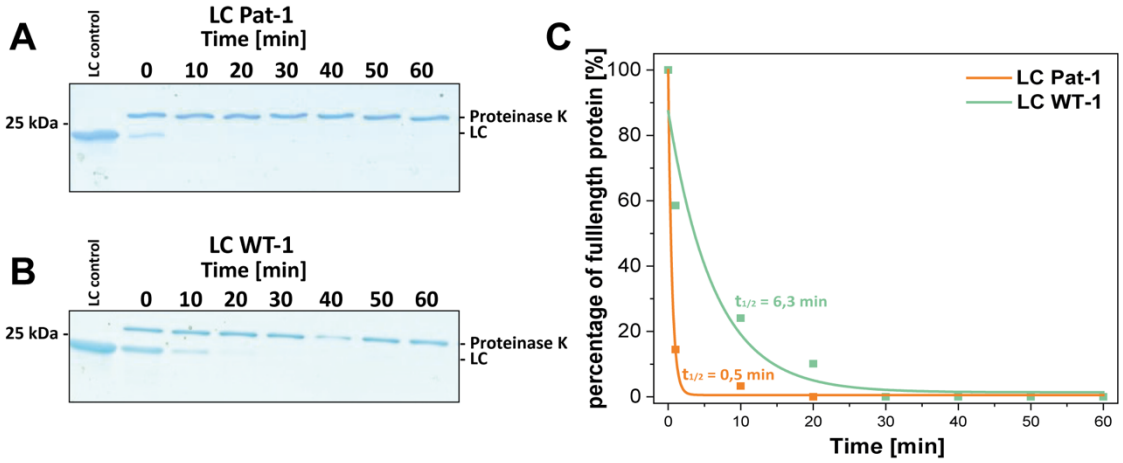

Figure 24. Susceptibility of full-length LCs to proteolysis by proteinase K. A) SDS-PAGE analysis of 10 µM LC Pat-1 and B) LC WT-1 incubated with 100 nM proteinase K over a period of 1 h in PBS at 37 °C. C) Quantitation of SDS-PAGE bands was done by ImageJ. Data were fit to an exponential decay function.

Further experiments over a longer period of time were performed with the proteases trypsin and chymotrypsin. The experiments confirmed the lower resistency and stability of LC Pat-1 (Figure 25A, C) to proteolysis by all enzymes compared to the germline. LC WT-1 was only marginally degraded (Figure 25B, C). Even without any additional protease, LC Pat-1 showed a higher degradation propensity than LC WT-1. After 160 h, only about 40 % of LC Pat-1 was left without protease, whereas 60 % was left of LC WT-1. As the LCs in AL amyloidosis patients are thought to undergo proteolytic cleavage in the blood, experiments in the presence of whole plasma were used to monitor possible proteolysis by plasma factors. LC Pat-1 showed enhanced degradation by plasma components, compared to PBS. This correlation is consistent with the previous results that showed the predominant deposition of truncated Pat-1 LCs in fibrils deriving from abdominal fat tissue of the patient (see chapter 3.1.1).

Interestingly, LC WT-1 seems to be slightly stabilized by the addition of plasma which indicates that the difference in flexibility, stability and linker accessibility represents a significant factor for the LC processing in the patient's blood.

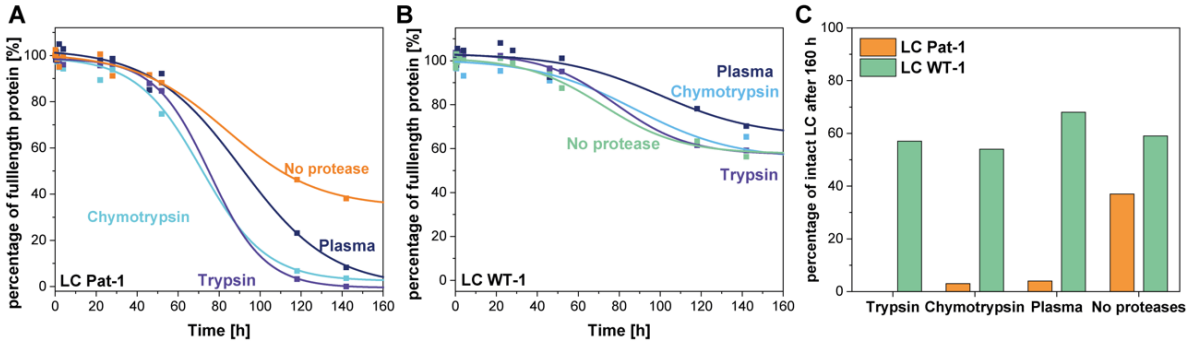

Figure 25. Susceptibility of the LCs to cleavage and degradation. Percentage of remaining full length LC (start concentration: 10 µM) for A) LC Pat-1 and B) LC WT-1 after treatment with 100 nM of the proteases Trypsin, Chymotrypsin, incubation in whole plasma or with no treatment. Bands from SDS-PAGE (4-20 %) were quantified with Image J. Data points were fitted to a Boltzmann function. C) Comparison of remaining LC after 160 h of different treatments.

3.1.10. V81L Protects the LC from Protease Triggered Fibril Formation

Based on the findings of the preceding sections, a specific endoproteolysis event is necessary for Pat-1 to form fibrils. Incubation of the intact LC Pat-1 didn't result in amyloid structure (see chapter 3.1.1). Thus, proteases with different cleavage sites were screened for their ability to trigger amyloid formation of LC Pat-1 (Figure 26A). This experiment was performed to identify truncation sites regardless of the pathophysiological plausibility of the used proteases. While ThT-assays revealed no fibril formation for LC Pat-1 in the presence of proteinase K, chymotrypsin and plasma, the fluorescence intensity increased after ~60 h for the LC incubated with trypsin, indicating the appearance of amyloid structures. To investigate if fibril formation propensity is still specific for the patient mutant, the same experiment was performed with LC WT-1. This variant did not show an increase of ThT fluorescence intensity and thus no amyloid formation (Figure 26B). The back mutation V81L that was shown to protect the Pat-1 patient truncation from depositing as fibrils was tested in respect to a protective effect for the full-length LC against proteolytic cleavage and fibril formation. As expected, also the V81L containing Pat-1 LC did not yield fibrillary structures. This further emphasizes the importance of the stabilizing interactions of this residue to the linker region between V_L and C_L regarding domain flexibilities and protease susceptibility. The absence or presence of fibrils was confirmed by TEM micrographs (Figure 26C). The sequence of LC Pat-1 shows 14 potential cleavage sites for trypsin which cuts after arginine and lysine residues (Figure 26D). Two of the truncation sites lie close to the authentic site between the V_L and C_L domains. A cleavage

at these amino acids would lead to constructs that differ from patient variant only in five or three residues, respectively.

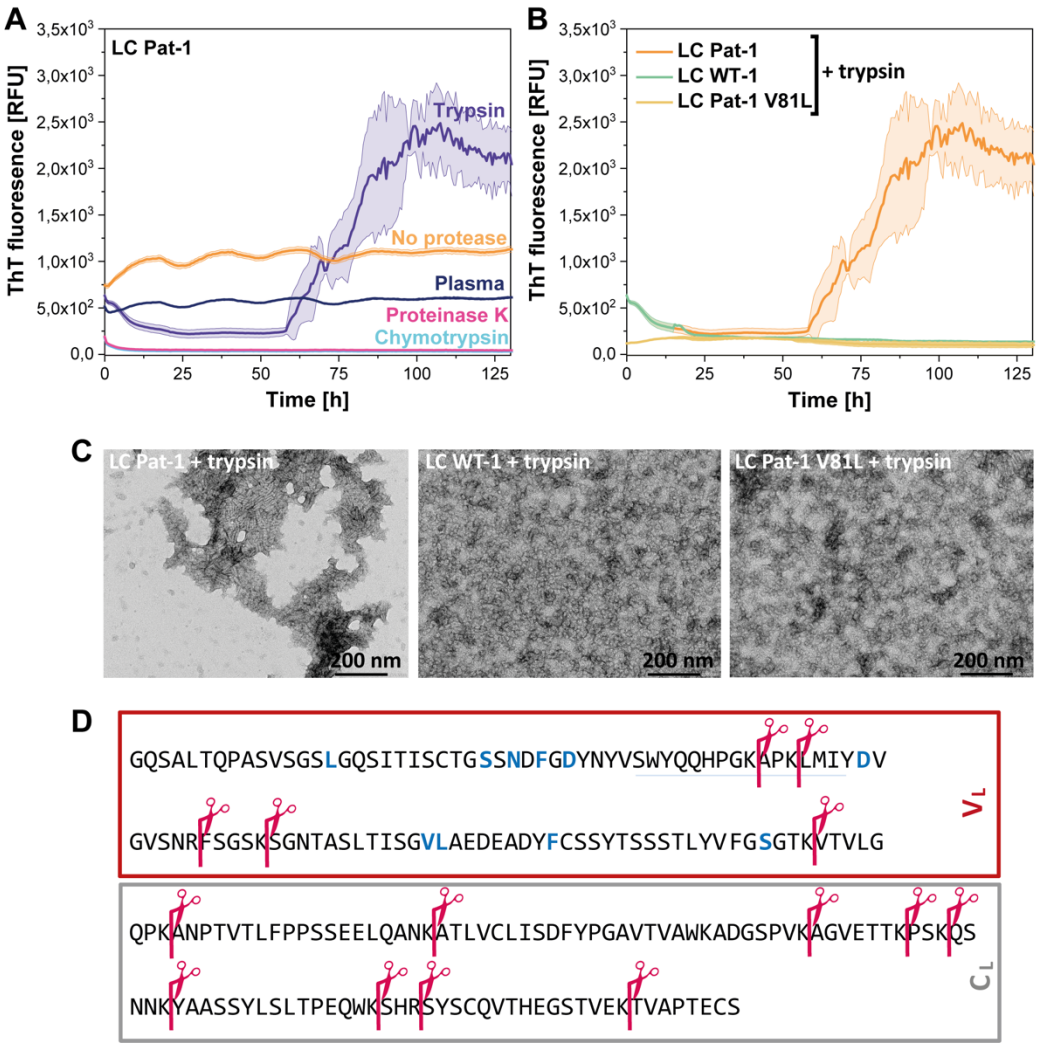

Figure 26. Impact of proteases and plasma on fibril formation. A) Fibril formation of LC Pat-1 in the presence of proteinase K, chymotrypsin, trypsin or plasma followed by ThT fluorescence. B) ThT-assay of LC Pat-1, LC WT-1 and the back-mutation LC Pat-1 V81L. LC to protease ratio was 50:1 (w/w). C) Presence (LC Pat-1) and absence (LC WT-1, LC Pat-1 V81L) of amyloid structures was confirmed with TEM micrographs. D) Trypsin cleavage sites in the sequence of LC Pat-1.

3.2. DISCUSSION

Prior studies reported the predominant deposition of LC truncations comprising mainly the V_L domains and small segments of the C_L domain. Mutations were found to entail thermodynamic destabilization and consequently amyloid formation propensity. As somatic hypermutation affects exclusively the V_L domain, it appears reasonable that the V_L domain is the main component of amyloid deposits. For the patient LC studied in this chapter, amyloid deposits contained mainly the V_L domain and only the V_L domain was able to transform into fibrils. The role of the C_L domain on the pathophysiology of AL amyloidosis is not well understood. Here, it protected the LC from amyloid formation and the proteolytic cleavage in the linker region was shown to be a prerequisite to release the amyloidogenic features. It was previously shown that inter-domain contacts between the C_L and V_L domain are important for structural integrity and a dense but flexible conformation. The linker was found to be a key factor for this (Weber et al., 2018). This fits the present results showing that mutations in the V_L domain of Pat-1 lead to a more dynamic linker region and an overall higher susceptibility of the full length Pat-1 LC to proteolytic cleavage, compared to WT-1. Different truncations of very similar sizes were found in the fat aspirate, suggesting a complex picture concerning the proteases involved in the generation of pathogenic LC truncations. This further leads to the hypothesis, that an exact C-terminal truncation is not crucial. Similar assumptions can be drawn by convening recent cryo-EM structures of AL fibrils that show a diffuse density for the C-terminal residues of the V_L domain indicating a highly flexible orientation (Radamaker et al., 2019; Swuec et al., 2019). Solid state NMR studies of AL fibrils reveal different topologies of V_L domains in amyloid deposits. They either contain well-ordered and rigid C-terminal segments or a highly ordered hydrophobic core domain (Hora et al., 2017; Piehl et al., 2017). Consequently, biopsy analyses of AL amyloidosis patients are indispensable for the disclosure of the deposited LC truncations and a better understanding of the disease and the disease-causing LC species (Annamalai et al., 2016; Ramirez-Alvarado, 2012; Weber et al., 2018).

The mechanism of cellular toxicity is largely unknown and there are different hypotheses on the nature of toxic species in amyloid disease that will be discussed in chapter 5. However, it is obvious that a large amount of insoluble fibril deposits in organs interferes with their function. As their presence can be directly linked to disease, the formation of amyloid structures was considered as evidence for pathogenicity in this chapter.

In vitro fibril formation assays were in line with the predominant deposition of the Pat-1 V_L domain in the patient's abdominal fat tissue: Full length LC Pat-1 was resistant to fibril formation, while Pat-1 V_L readily formed fibrils. Both WT-1 V_L and WT-1 LC didn't result in the formation of amyloid structures. Taken together, the findings suggest a strong effect of the LC context on the Pat-1 V_L domain. The mutations in the V_L of Pat-1 render the LC susceptible to proteolytic cleavage. Once the C_L domain is removed, the point mutations present in the V_L

domain become active, destabilize the domain and lead to amyloid formation. The current view describes an overall thermodynamic destabilization of the V_L domain as a major indicator for fibril formation propensity (Blancas-Mejía et al., 2015; Morgan and Kelly, 2016b; Nokwe et al., 2014; Ramirez-Alvarado, 2012). Even though, this was shown to be not absolutely needed and a global destabilization alone is not always sufficient to induce amyloid formation (Nokwe et al., 2016), the patient truncation Pat-1 fits this general picture. For a mechanistic understanding of AL amyloidosis, the causative sequence differences between patient mutant and corresponding germline have to be identified and characterized. The V_L domains of Pat-1 and WT-1 differ in eleven point mutations. Thus, they comprise ~90 % sequence identity. Serial substitution of every single point mutation in Pat-1 with the respective residue present in WT-1 enabled the identification of the valine to leucine mutation at position 81 as the key modification responsible for enhancing the overall domain stability and reversing the amyloid formation propensity of Pat-1. Thus, the mutation at position 81 confers pathogenicity to Pat-1. Analyzing the amino acid frequencies in antibody sequences indicate a negative effect of a valine residue at this position compared to leucine with 13 % and 77 % occurrence, respectively (Johnson and Wu, 2000b; Wu and Kabat, 1970). Introducing a valine into the germline sequence resulted in amyloid formation of WT-1 V_L and confirmed the importance of this substitution for pathogenicity. The stabilizing and amyloid-preventing effect was very specific to L81. Substitution with the highly similar isoleucine at position 81 did not yield comparable effects. Residue 81 was found to be part of a surface-exposed hydrophobic patch in Pat-1, along with the two other point mutations L15 and L82. Surface hydrophobicity is known to be energetically unfavorable and made these residues conspicuous (Eisenhaber and Argos, 1996; Moelbert and Emberly, 2004; Young et al., 1994). The L82Q substitution was particularly promising since this mutation leads to a change from a hydrophobic to a polar amino acid and thus changes possible interactions. Besides, amino acid frequencies according to the Kabat numbering scheme revealed a much higher probability for a glutamine at position 82 (68 %) than for the leucine (<1 %) in Pat-1, supporting the idea of a severe negative effect on domain architecture (Wu and Kabat, 1970). Against expectation, a L82Q substitution alone did not result in restored stability of Pat-1 or prevention of amyloid formation. However, combining L82Q with V81L further increases the stabilizing and protective effect observed for V81L alone. The double mutant of Pat-1 was able to remain soluble, stressing the important role of the expanded hydrophobic surface area for amyloidogenesis of the patient mutant.

Surprisingly, the L15P back-mutation resulted in a lower thermodynamic stability than Pat-1 itself. Also, in combination with V81L and L82Q, this mutation exhibited negative effects. All P15 containing V_L mutants readily formed fibrils with an even earlier onset than Pat-1. According to the Kabat numbering scheme, leucine at position 15 occurs in 12 % of the cases,

whereas proline is present with a frequency of 61 %. Consequently, this substitution did not comply with the expectations.

Despite the clear evidence for the link between stability changes and fibril formation propensity, the results are not sufficient for mechanistic explanation and the structural consequences of the mutations needs to be considered. In the Pat-1 V_L crystal structure, V81 exhibits six hydrophobic interactions to residues spread over FR2-4. Among others, the interaction partners include the two other residues harbored by the hydrophobic surface area: L15 and L82. Likewise, the residue L81 that is present in WT-1, exhibits six hydrophobic interactions. However, the interactions of L81 reach three hydrophobic residues in the C-terminal segment of the V_L domain (V109, V111 and L112), whereas V81, due to its smaller side chain, only interacts with one C-terminal amino acid (V111). These findings fit the H/DX analysis of Pat-1 and WT-1 V_L that reveal a highly increased flexibility of the C-terminal region in Pat-1 as the underlying reason for destabilization and amyloid formation. Conformational dynamics investigations of the full-length LCs Pat-1 and WT-1 show that this linker stretch only becomes flexible upon removal of the C_L domain, stressing the importance of the proteolytic cleavage event prior to fibril formation. MD simulations demonstrate that a leucine at position 81 leads to a tighter domain packing than a valine residue, which leaves an open, cave-like region. Therefore, neighboring amino acid residues are in closer proximity of L81 and can form more hydrophobic interactions leading to a stabilization of the C-terminal segment of the V_L domain. The altered hydrophobic interactions can also explain the negative effect of P15 compared to L15. A leucine at this position is tightly imbedded into a network of hydrophobic interactions as it facilitates the formation of five hydrophobic contacts to V81, L82 and A83 in FR3 and to two residues in the C-terminal region, V111 and L112. Despite the increase in conformational dynamics of the loop region around residue 15 by the interaction, the contacts to the C-terminal end of the domain positively affect the overall stabilization. A proline residue at this position induces a local change of the protein backbone structure and packing geometry repealing hydrophobic interaction. Thus, the results demonstrate a complex interplay of interactions and dynamics that is responsible for the pathogenicity of the patient-derived LC truncation. Furthermore, the results emphasize that small and seemingly unimportant changes like the V81L mutation can lead to a fatal change of intramolecular interaction that, in case of Pat-1, are of hydrophobic nature and lead to an impaired domain integrity.

It was clearly shown that a proteolysis event is indispensable for disease development of Pat-1. The cleavage between the V_L and C_L domain entails the flexibility of the new C-terminal region at the truncation site. However, the full-length LC of Pat-1 is already deprived by the comprised point mutation that render the LC more susceptible to cleavage by different proteases. The importance of residue 81 was further stressed, as the V81L mutation protects LC truncations from fibril formation. The presence of different LC truncations in fibrillar deposits

in patient tissue hints towards the involvement of different proteases in disease development. So far, the truncation prior to amyloid formation is largely unknown but the cleavage event is of high importance since it can drastically alter the biophysical properties of a polypeptide chain, such as the isoelectric point, solubility, aggregation propensity and conformational stability (Bellotti et al., 2000). Here, different proteases were tested and LC Pat-1 was in all cases more susceptible to proteolytic cleavage. The LC possesses several trypsin cleavage sites, that result in similar but not the same fragments as found in patient deposits. Upon trypsin cleavage, the LC truncations formed fibrils. The involvement of trypsin in disease development is unlikely due to its presence in the digestive system of humans and not in the plasma, indicating the negligible importance of the exact cleavage site (Radamaker et al., 2019; Swuec et al., 2019).

The *in vitro* fibril formation assay is performed under extremely simplified conditions compared to the LC environment in the human body. Many other parameters including more detailed proteolysis events, interactions with plasma factor or shear forces that possibly contribute to fibril formation have to be considered and complicate the full understanding of pathogenicity. Also, it was often shown that amyloid deposits in AL amyloidosis patients and patients with other amyloid diseases consist not only of the disease-causing protein but also contain many other factors like glycosaminoglycans, apolipoprotein E, lipids, plasma factors or other proteins like extracellular chaperones. Many of these factors were already shown to influence fibril formation in the context of amyloid diseases (Gellermann et al., 2005; Wyatt et al., 2012). The mechanistic impact of such factors needs to be determined to generate a detailed molecular understanding of disease progression and offer new perspectives for potential treatment options. Some of these factors will be discussed in the following chapter.

In summary, this part of the study presents detailed analysis and a general strategy how to investigate AL amyloidosis associated LCs. An important starting point is the determination of the LC truncation deposited in the organ or tissue of the affected patient. Identification and classification of the sequential substitutions require a corresponding non-pathogenic germline sequence that comprises high sequence similarity. Biophysical investigations regarding thermodynamic stability and fibril formation propensity enables to distinguish between active and silent mutations. Further combinations of structural and dynamics analyses allow the identification of the underlying molecular mechanism leading to fibril formation.

4. The Effect of Molecular Chaperones and Plasma Factors on Amyloid Formation

Amyloid deposits consist not only of LCs and their truncations but also of i.e. glycosaminoglycans, lipids, proteoglycans, apolipoprotein E, serum amyloid P as well as secreted chaperones. The latter includes ERdj3, the co-chaperone of the ER Hsp70 BiP, that was found to play a role in the UPR (Blancas-Mejía et al., 2015; Gellermann et al., 2005; Genereux et al., 2015). Chaperones selectively bind to non-native regions in proteins to prevent them from aggregation or assist in their folding process. Therefore, it is likely that they play a role in the deposition of insoluble aggregates or fibrils and thus in disease development. Since the amyloid formation pathway is thought to start in the extracellular space, the impact of extracellular or secretion competent chaperones or plasma factors on maintaining extracellular proteostasis is of particular interest. The identification of such factors is essential for the determination of biomarkers and the development of therapies. Therefore, this chapter deals with the influence of different factors with respect to amyloid formation. Since it was found that the V_L domain of Pat-1 is the predominant truncation in fibrils which probably becomes amyloidogenic upon cleavage in the plasma, this truncation variant and the corresponding germline V_L were used for the following experiments. The V_L domains are referred to as Pat-1 and WT-1 unless otherwise stated.

4.1. Results

4.1.1. Inhibition of Fibril Formation By ER Chaperones

The ER chaperone system comprises the Hsp70 family member BiP and the J protein ERdj3. The co-chaperone ERdj3 binds to misfolded proteins, transports them to the ATP-bound BiP and stimulates BiP's ATPase activity via its J domain (Kampinga and Craig, 2010). ERdj3 was already shown to be upregulated upon stress and to influence *in vitro* fibril formation in the case of $A\beta_{40}$ (Genereux et al., 2015). In the absence of stress, mice serum had an ERdj3 concentration of 23 ± 5 nM. Its expression and secretion are up to fourfold upregulated upon activation of the UPR stress sensors ATF6 and XBP1 (Genereux et al., 2015). Consequently, even under stress conditions the chaperones are present in significantly lower concentrations than the LC of the patient (7564 mg/l of Pat-1 FLCs in the serum). Therefore, Pat-1 fibril formation assays were performed in the presence of substochiometric amounts of BiP (100 nM) and ERdj3 (800 nM). ATP (2 mM) was added to the assay buffer to ensure that BiP can fulfill its ATPase activity. The Patient V_L alone shows a conversion into fibrils after ~25 h, while the mixture containing the chaperone system and ATP did not result in an increase of ThT fluorescence intensity indicating no fibril formation during the time of the assay (Figure 27A). As a control reaction, just ATP was added to Pat-1 to confirm that only the chaperones

are responsible for the inhibition of fibril formation. The presence and absence of fibrillar structures was monitored by TEM (Figure 27B).

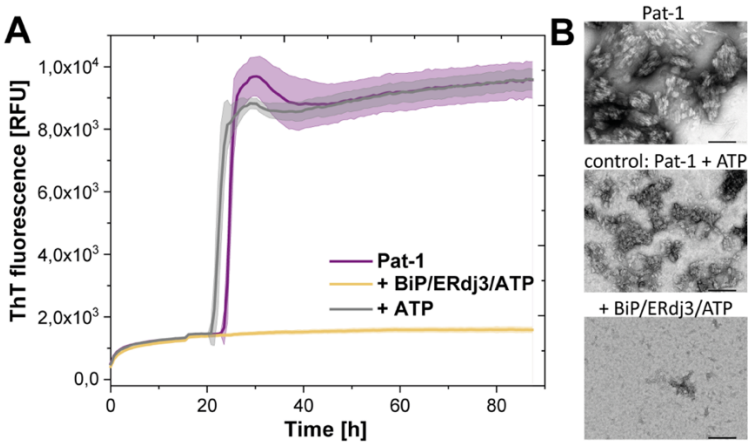

Figure 27. Fibril formation of Pat-1 in the presence of the ER chaperone system consisting of BiP, ERdj3 and ATP. A) Monitoring of the ThT fluorescence intensity increase during incubation of the samples containing 15 µM Pat-1 (purple), Pat-1 and 2 mM ATP (grey) or Pat-1 with 100 nM BiP, 800 nM ERdj3 and 2 mM ATP in HKM buffer containing 0.5 mM SDS. B) The presence (Pat-1, Pat-1+ATP) or absence (Pat-1 + chaperone system) of amyloid structures was analyzed with TEM.

4.1.2. Concentration-Dependent Inhibition of Fibril Formation By BiP

Using the BiP binding site prediction BiPPred (Schneider et al., 2016), several potential binding sites in the Pat-1 sequence could be found indicating that BiP is likely to bind the V_L domain (Figure 28A). The software gives prediction scores for peptide heptamers. Most of the binding hotspots are located in the conserved framework regions of Pat-1 and only barely in the hypervariable CDRs. Mapping the segments with the highest scores on the crystal structure of LC Pat-1 did not provide an obvious correlation with the mutations of with the interaction of V_L and C_L (Figure 28B). However, the BiP binding site with the highest BiPPred scores overlaps with the V_L/V_H interface which could be one reason that the LC does not bind to the corresponding HC. To test if BiP alone is able to inhibit fibril formation, a ThT assay was performed with increasing concentrations of BiP incubated with Pat-1 (Figure 28C). The concentration ratios of Pat-1 to BiP ranged from 1:150 to 1:15. Already concentrations of 100 nM BiP (1:100 ratio) were able to slightly delay fibril formation. This effect was enhanced at higher BiP concentrations. At 200 nM, the lag phase was extended by almost four times. At 400 nM or above, no fluorescence intensity increase, and thus no fibril formation could be observed anymore. This finding suggests that BiP binds to Pat-1 in a concentration-dependent manner and inhibits fibril formation.

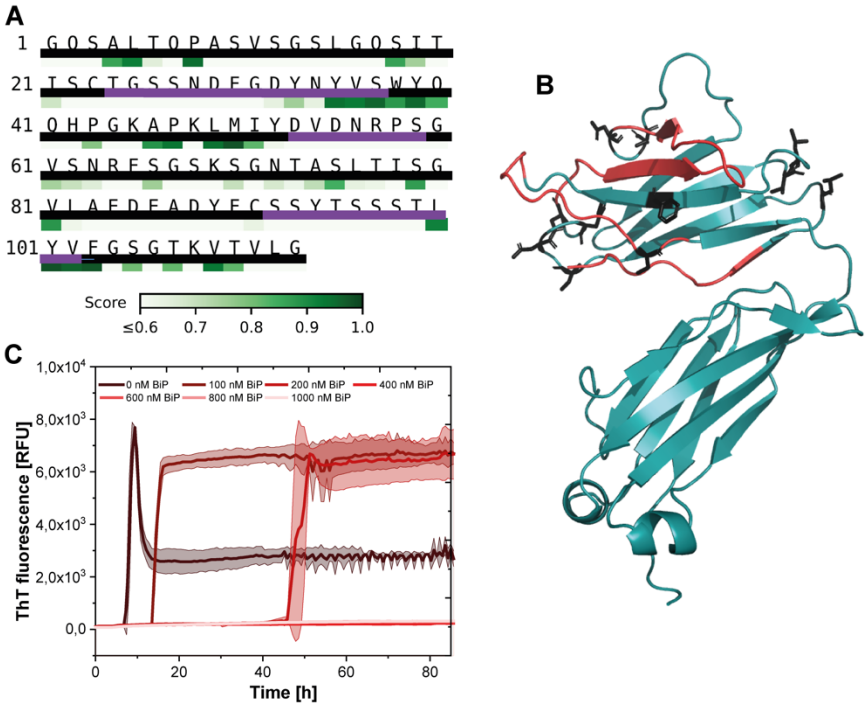

Figure 28. Binding of BiP to Pat-1 and the impact on fibril formation. A) BiPPred prediction scores for all peptide heptamers in Pat-1. Colored boxes under a specific residue implicate binding of BiP to the heptapeptide of three residues left and right from the location of the box. Black underlined sequence streches are framework regions, CDRs are underlined in purple. B) The segments in Pat-1 with the highest scores for BiP binding were mapped on the LC Pat-1 crystal structure model and colored in red. The mutated residues are depicted as black sticks. C) ThT assay of 15 µM Pat-1 with increasing concentrations of BiP. The assay was performed in HKM buffer containing 0.5 mM SDS and 2 mM ATP.

4.1.3. Concentration-Dependent Inhibition of Fibril Formation By ERdj3

Even though BiP showed a strong effect on fibril formation, it is not a promising candidate for inhibiting amyloidogenesis in the patient as its secretion from the ER is unlikely (Jin et al., 2017). Besides, the ATP that is needed as an energy source for the chaperone activity is present in a much lower concentration in the extracellular space compared to the ER (Farias et al., 2005; Wyatt et al., 2012). In contrast, ERdj3 lacks the KDEL ER retention signal, is thus secretion-competent and could assist Pat-1 folding in the extracellular space. Fibril extracts from the patient's abdominal fat tissue and patient serum were analyzed by Western blot for the presence of ERdj3 (Figure 29A). Recombinant ERdj3 served as a positive control. In the lane of the dissolved fibrils derived from fat tissue deposits a faint band positive for the anti-ERdj3 antibody became visible. Thus, very low concentrations of ERdj3 co-deposited with Pat-1 truncations in the fibrils. The patient serum lane did not show an ERdj3 band which is probably due to the high dilution in the patient serum. To test the individual impact of the co-chaperone on fibril formation, different Pat-1 to ERdj3 ratios reaching from 1:300 to 1:18.75 were incubated in a ThT assay (Figure 29B). Without co-chaperone, the sample with only Pat-1 showed an increase of ThT fluorescence after ~25 h. In the presence of only 50 nM ERdj3,

the lag phase was almost doubled (Figure 29C). Upon further increase of concentration, the lag phase was prolonged more but the differences became smaller until at 700 nM Erdj3 and higher no increase of ThT fluorescence could be detected anymore. Thus, the co-chaperone functions highly substochiometrically. Since ERdj3 is not able to fold proteins and has no ATPase activity, the inhibition is not based on the refolding of intermediate Pat-1 species but rather on a holdase activity. As a consequence, it is surprising that these low amounts of co-chaperone are sufficient to inhibit amyloid formation. To test if ERdj3 only comes into play during the events happening in the lag phase or intervenes from the beginning, it was added during the lag phase, one and two hours after the start of incubation (Figure 29D). This experiment showed that complete inhibition of Pat-1 fibrillization could only be obtained with ERdj3 present from the beginning of the reaction. The addition at later timepoints lead to a delay of the growth phase. This indicates that important rearrangement events happen very early during the lag phase and that these rearranged molecules are already part of an off-pathway reaction or that the presence of a high number of intermediates cannot be kept from amyloid formation. The presence and absence of fibrils was confirmed with TEM micrographs (Figure 29E).

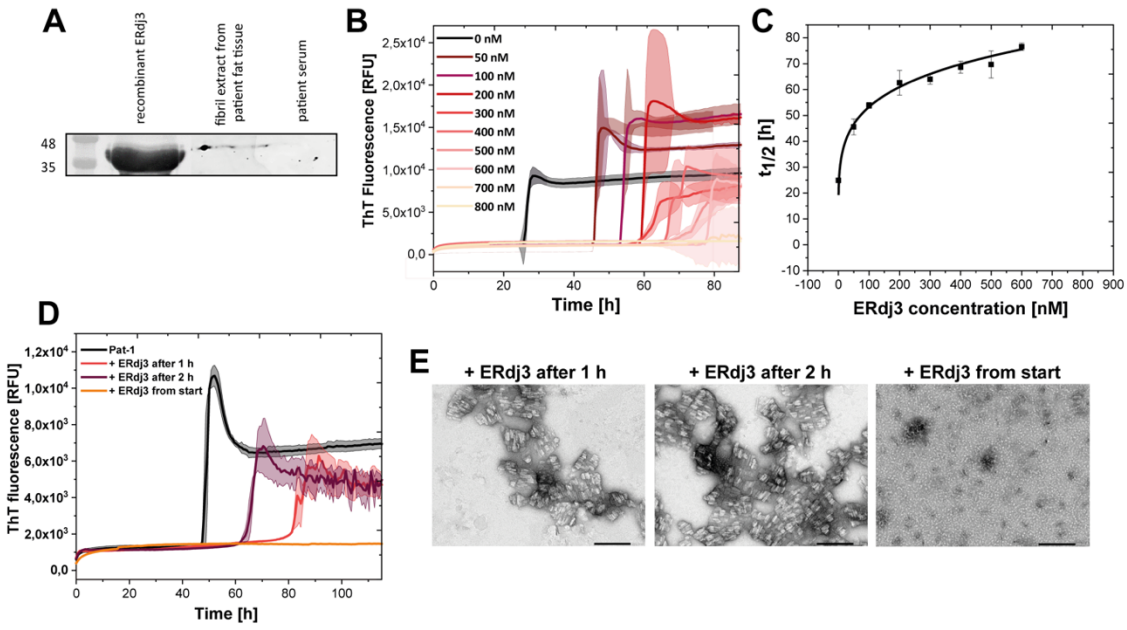

Figure 29. Impact of ERdj3 on fibril formation of Pat-1. A) Western blot analysis of solubilized fibrils from abdominal fat tissue of the patient and serum using an anti-ERdj3 antibody. Recombinant ERdj3 in was used as a positive control. B) Fibril formation assay of Pat-1 followed by ThT fluorescence in the presence of increasing ERdj3 concentrations (50 – 800 nM). The assay was performed in PBS containing 0.5 mM SDS. C) $t_{1/2}$ values of fibril formation in the presence of ERdj3 plotted against ERdj3 concentration. D) ThT assay with addition of 800 nM ERdj3 1 and 2 h after assay start. E) The absence and presence of fibrils was analyzed with TEM.

4.1.4. BINDING OF ERDJ3 TO DESTABILIZED V_L DOMAINS

To determine the binding affinity of ERdj3 to the V_Ls, MicroScale Thermophoresis (MST) measurements were performed. For this experiment, Pat-1 and WT-1 were fluorescently labelled at lysine residues with the Monolith Protein Labeling Kit RED-NHS. The change in fluorescence intensity was monitored for the V_L domains with increasing concentrations of ERdj3 during a temperature gradient over time. For Pat-1 the difference in fluorescence intensity between the lowest and the highest concentration of ERdj3 was higher than for WT-1 (Figure 30A, B). Plotting the normalized fluorescence against the ERdj3 concentration results in a dissociation constant K_d (Figure 30C). K_d and affinity correlate inversely. Thus, the higher the K_d, the lower the affinity. The calculated dissociation constant K_d for WT-1 was more than tenfold higher than the K_d for Pat-1 with 3.7 µM and 0.2 µM, respectively. Consequently, the affinity of ERdj3 to Pat-1 is much higher than to WT-1.

Since chaperones usually bind to hydrophobic regions in a protein, ANS-binding of the domains was measured. The apolar dye ANS specifically recognizes surface-exposed hydrophobicity in proteins. Upon binding, the fluorescence intensity is enhanced and the peak of emission at λ_{max} is blue-shifted. In PBS buffer, Pat-1 and WT-1 did not bind ANS (Figure 30D). However, when using the assay buffer which contains 0.5 mM SDS to induce fibril formation, a clear shit of λ_{max} and an increase of fluorescence intensity becomes visible for both V_L domains (Figure 30E). The magnitude of the effect was bigger for Pat-1 than for WT-1, explaining the higher binding affinity of ERdj3 to Pat-1. Indeed, when analyzing Pat-1 to ERdj3 binding with MST in regular PBS buffer, no significant change in fluorescence in the presence of low and high amounts of ERdj3 as binding partner and thus no interaction could be detected (Figure 30F).

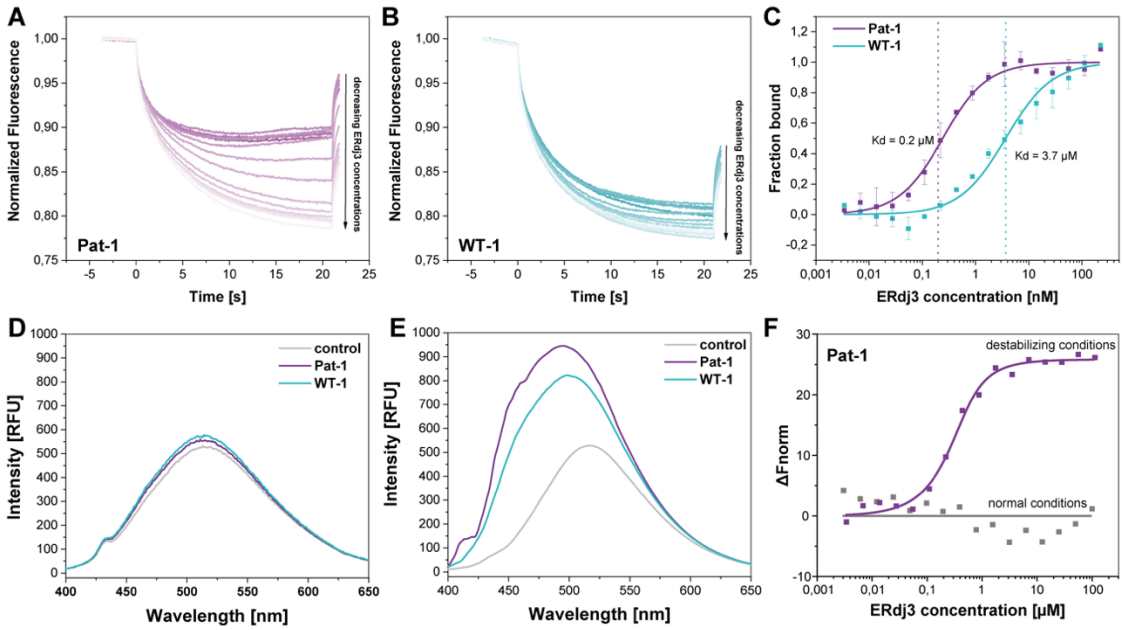

Figure 30. Binding of ERdj3 to Pat-1 and WT-1. MicroScale Thermophoresis was used to measure the change in fluorescence with a range of ERdj3 concentrations for A) Pat-1 and B) WT-1. C) Fitting of the fluorescence data against ERdj3 concentration with the NanoTemper fitting software reveals a more than 10-fold higher K_d for WT-1 compared to Pat-1. D) ANS-fluorescence analysis of Pat-1 and WT-1 in PBS buffer and E) in PBS buffer with 0.5 mM SDS. F) Fitting of the fluorescence data in the absence and presence of SDS against the ERdj3 concentration.

4.1.5. Plasma Factors And Amyloid Formation

Besides stress-related protein secretion, many factors that are regularly found in the bloodstream and thus come into close proximity to the LCs or LC truncations can possibly interfere with their processing. One example is apolipoprotein E (ApoE) which is a major cholesterol carrier protein that regulates lipid homeostasis. It is mainly produced by the liver and macrophages (Mahley and Rall, 2000). The polymorphism of ApoE alleles is causative for some diseases, whereby the presence of the ε4 allele particularly increases the risk for hyperlipidaemia, hypercholesterolemia but also Alzheimer's disease (Huang and Mahley, 2014; Liu CC, Kanekiyo T, Xu H, 2013). ApoE4 was also identified as an abundant component of LC deposits in the context of AL amyloidosis (Nielsen et al., 2014). Thus, the effect of different concentrations of ApoE4 on the fibril formation of Pat-1 and WT-1 was tested. Also for this protein, a concentration-dependent impact of the substochiometrically added protein could be observed (Figure 31A). However, in this case the fibril formation was not delayed or inhibited but the maximal intensity of ThT fluorescence at the final plateau stage of fibril formation changed. At ApoE4 concentrations of 10 nM and lower, Pat-1 showed an increase of maximal intensity compared to Pat-1 alone. Higher concentrations resulted in a stepwise decrease of endpoint fluorescence intensity. No concentration of ApoE4 induced fibril formation of WT-1. Interestingly, the plasma factor also seems to affect the fibril morphology

(Figure 31B). While at high concentrations well defined and long fibrils are visible, length and cluster formation increase at lower ApoE4 concentrations. In the absence of ApoE4 fibrils equal the ones at medium ApoE4 concentrations. Overall, the ThT fluorescence intensity correlates with the amounts of fibrils.

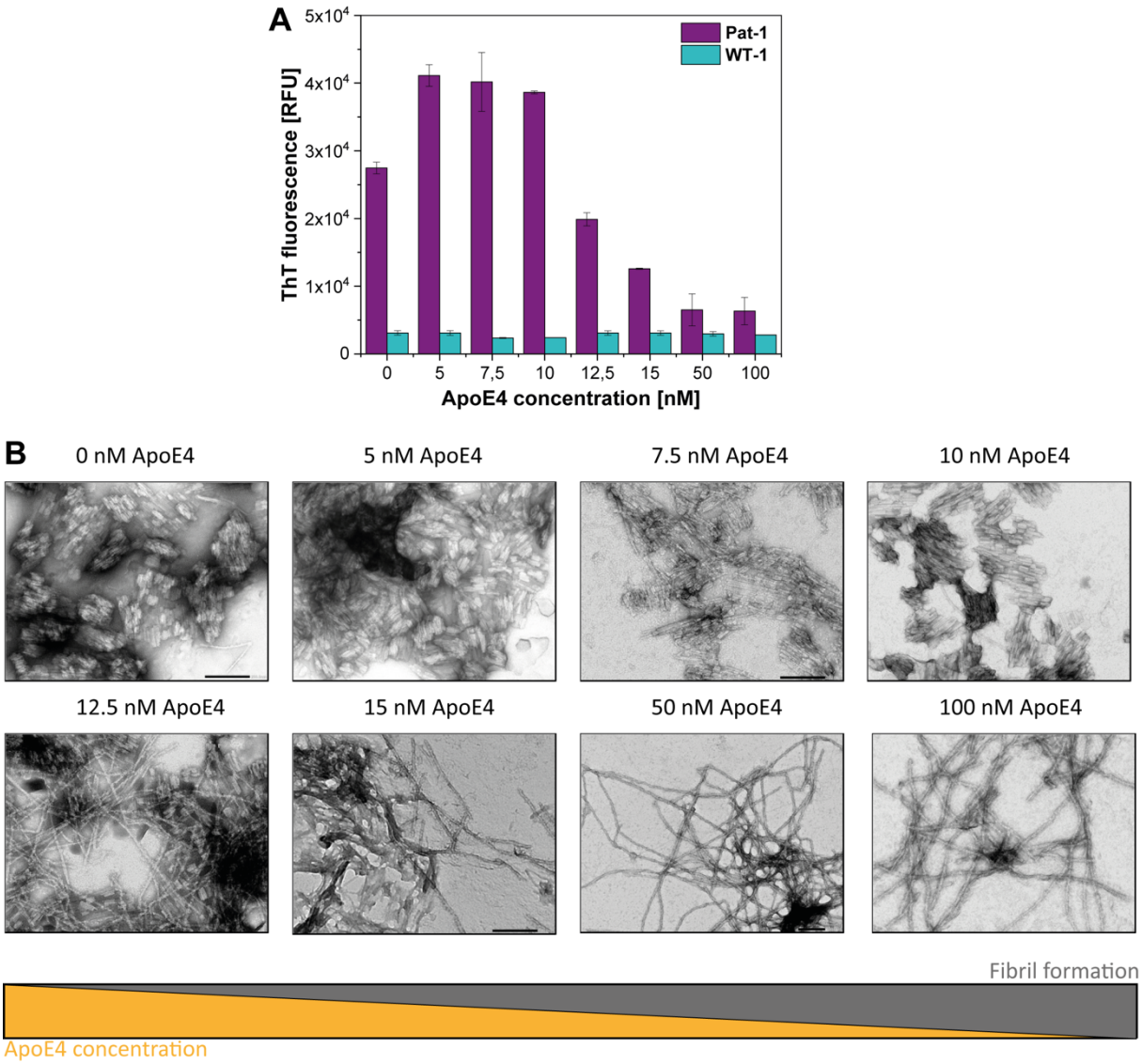

Figure 31. Impact of Apolipoprotein E4 on fibril formation of Pat-1 and WT-1. A) Change of maximal fluorescence intensity at the final plateau phase of fibril formation upon addition of increasing concentrations of ApoE4. The data show a mean of triplicates with SD. B) TEM analysis of Pat-1 fibrils with increasing ApoE4 concentrations.

4.2. DISCUSSION

Molecular chaperones are known to interact with client proteins in order to stabilize or assist in folding and acquire their native conformations. In the ER, the chaperone system comprising the ER Hsp70 BiP, the Hsp40 co-chaperone ERdj3, ATP as an energy source for BiPs ATPase function and many other factors play an important role in antibody folding and quality control (Hartl et al., 2011; Marcinowski et al., 2011; Shen and Hendershot, 2005). A transient interaction of BiP with immunoglobulin LCs shortly after translation and a role in sensing LCs for degradation was already shown in other studies (Knittler and Haas, 1992). BiP binds many substrates with no obvious sequence similarities. Usually the binding sites comprise stretches of 5-7 preferably hydrophobic amino acids (Feige et al., 2009; Flynn et al., 1991; Rüdiger et al., 1997). For Pat-1, multiple potential binding sites have been predicted that spread over the whole sequence and possibly impair the V_L/V_H interaction face. Here, it was shown that BiP binds to Pat-1 V_L domains and that this binding has an effect on its aggregation behavior, as it delays or even inhibits amyloid formation in a concentration dependent manner. In an ATP bound state, BiP's substrate binding domain is open and the monomeric chaperone has a low substrate affinity with high on and off rates, which might be the reason for the delay or inhibition of fibril formation of Pat-1 (Kassenbrock and Kelly, 1989; Pobre et al., 2019). Even though, BiP clearly prevents Pat-1 V_L aggregation *in vitro,* it is not a very likely candidate for influencing pathogenicity in the human body upon LC secretion from the ER and proteolysis. BiP possesses a C-terminal KDEL retrieval motif. Upon secretion or co-secretion of BiP from the ER, KDEL receptors in the post-ER compartments recognize the motif and arrange the return of BiP to the ER via COPI vesicular transport (Jin et al., 2017).

In contrast, ERdj3 lacks the ER retention (KDEL) signal and can be detected in the extracellular space during ER stress. It was already shown to co-secrete with misfolding-prone clients (Genereux et al., 2015). Indeed, traces of ERdj3 could be found in amyloid deposits of fat aspirates of the affected AL amyloidosis patient, stressing the contribution of the co-chaperone in disease development. The effect on *in vitro* fibril formation was, similar to BiP, concentration-dependent and sub-stochiometric. ERdj3 seems to affect early stages of amyloid formation, since the delayed addition of ERdj3 to the fibrillization reaction resulted in retardation of the onset but could not fully inhibit amyloid formation. This indicates either the occurrence of important off-pathway intermediates in the absence of ERdj3 or that the co-chaperone has a stabilizing effect on early folding intermediates. Thus, ERdj3 can only keep the LC from amyloid formation, when it is co-secreted. An interaction between ERdj3 and destabilized Pat-1 V_L was clearly shown and the K_D was to be 10-fold higher than that for the corresponding germline V_L. The destabilization was a necessary requirement for the binding. Small amounts of SDS were used to induce destabilization and increasing surface-exposed hydrophobicity while at the same time maintaining the secondary structure fold. Based on the results, a model

for the fibril formation pathway and the involvement of ERdj3 during ER stress is presented (Figure 32). It describes the fibril formation pathway and possible ER exit strategies of ERdj3 alone or co-secreted bound to an intermediate fold of Pat-1 and the further reaction into amyloid fibrils in the extracellular space.

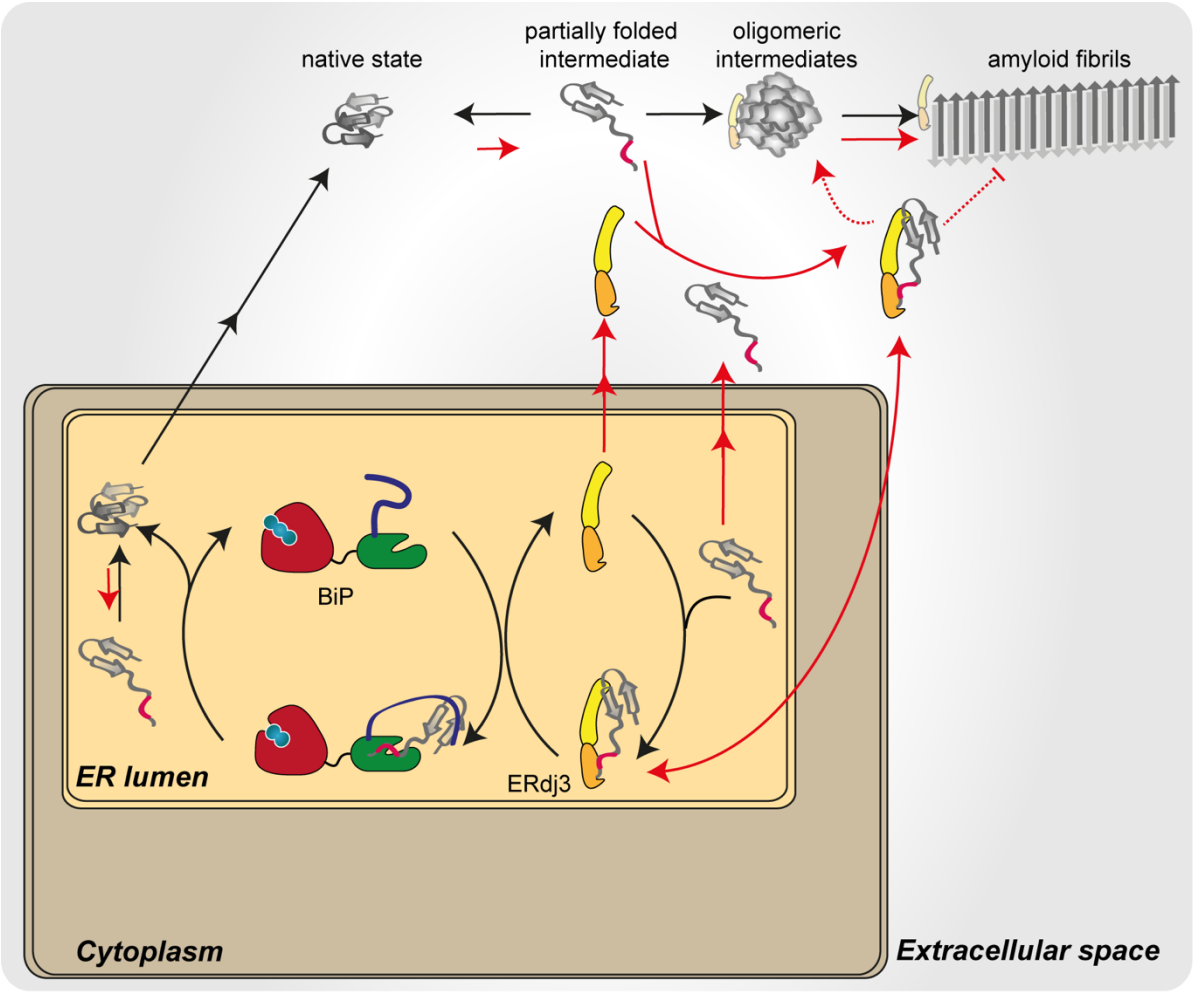

Figure 32. Model of basic LC and ERdj3 pathways during ER stress. ERdj3 can be secreted alone or together with LCs. LC intermediates result in the formation of amyloid fibrils. ERdj3 can inhibit aggregation if present at early stages of the pathway, otherwise it can delay the amyloid formation.

Besides the secretion-competent ERdj3, extracellular chaperones or plasma factors are very likely to play a role in pathogenesis. The chaperone activity and impact on early events during pathogenesis of i.e. clusterin has been studied *in vitro.* Many investigations were performed in the context of Alzheimer's disease (AD) with $A\beta_{40}$ and $A\beta_{42}$ peptides (Wyatt et al., 2009; Yerbury et al., 2009, 2007; Yerbury and Wilson, 2010). Little is known about treatment strategies using extracellular chaperones or plasma factors regarding extracellular proteostasis or their utility as biomarkers (Wyatt et al., 2012). In this study, the effect of the extracellular chaperone ApoE4 on fibril formation of Pat-1 was tested. ApoE, a constituent of

certain plasma lipoprotein fraction which is important for transport of cholesterol and triglycerides, exists in three isoforms. The allele for ApoE4 is a known risk factor for developing AD. The exact mechanism of function is unknown (Hashimoto et al., 2012; Liu et al., 2017). ApoE4 was earlier described as a pathological chaperone that reduces the stability and mediates the formation of β-pleated amyloid formation (Wisniewski and Frangione, 1992). Adding different substochiometric concentrations of ApoE4 to the fibril formation assay of Pat-1 revealed a concentration-dependent impact on the reaction, whereby low concentrations increase and high concentrations reduce the amount of fibrils. These results indicate that the binding of ApoE4 to intermediates prior to fibrils prevent further reaction. Thus, when ApoE4 is present in high enough concentrations, the overall amount of Pat-1 reacting into fibrils is reduced. Low concentrations of ApoE4 support amyloid formation, suggesting an incorporation into insoluble Pat-1 fibrils by stabilizing an otherwise unstable intermediate conformation of Pat-1 that acts like a nucleus for fibril formation. This hypothesis is strengthened by the fact that ApoE4 is found as part of amyloid deposits in tissues of patients with different amyloid related diseases (Furumoto et al., 1998; Navarro et al., 2003; Röcken et al., 1997). Similar results were found by analyzing the effect of clusterin, ApoE and serum amyloid P component (SAP) on different amyloid formatting proteins (Hamazaki, 1995; Hughes et al., 1998; Huynh et al., 2017; Matsubara et al., 1996; Yerbury et al., 2007). Further, the different fibril morphologies support the theory that the fibril formation pathways in the presence of different concentrations of ApoE4 are different. A model is presented to summarize the results (Figure 33).

This chapter demonstrates the involvement of protein factors that come into contact with disease-causing LCs during pathogenesis, starting from folding in the ER. Yet, it remains unclear at which stages during pathogenesis especially the extracellular chaperones play a role and to what extent they could serve as biomarkers or even as potential treatment options. A further characterization of these and other promising plasma factors is indispensable and promising in the future.

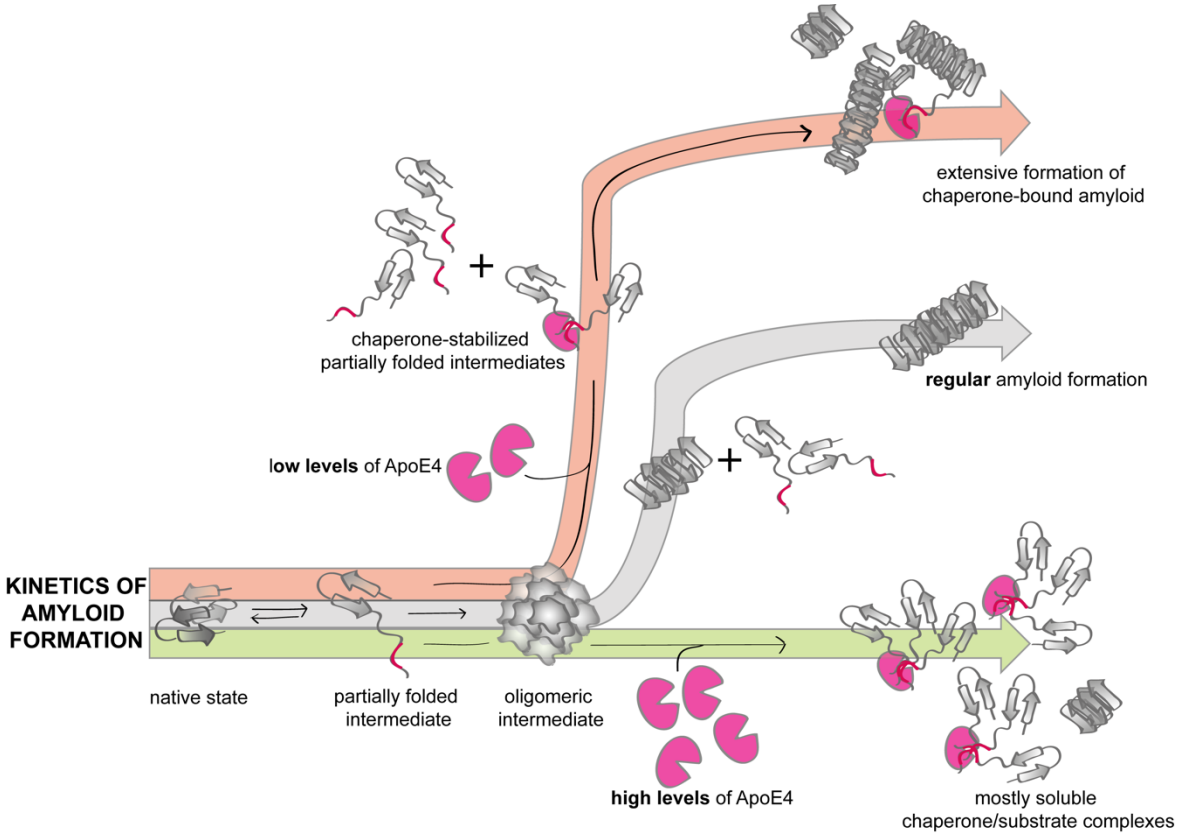

Figure 33. Model of the biphasic interplay between amyloidogenic LCs and the extracellular chaperone ApoE4 (adapted with permission from Wilson et al., 2007). Low concentrations of ApoE4 increase fibril formation by serving as a nucleus for a different fibril morphology. Without chaperone, regular amyloid fibrils are formed. High levels of ApoE4 lead to a decrease of overall fibril amount by keeping large amounts of the LC soluble.

5. Dissection of the Amyloid Formation Pathway in AL Amyloidosis

The previous chapter gave rise to the assumption that important events shifting LCs irreversibly towards amyloid formation occur during the lag phase. So far, little is known on the structural events taking place during this period. As described in chapter 1.7, capturing intermediate states, most likely oligomers, before eventually transforming into amyloid fibrils, is difficult due to their transient appearance. Additionally, the high energy state makes intermediates and oligomers hard to preserve. However, it is of great importance to understand the molecular pathway of amyloid formation to identify opportunities for therapeutic intervention at early stages of disease. The experiments in this chapter aimed at the elucidation of the processes taking place during the amyloid formation pathway of the pathogenic LC truncation Pat-1. Since fibril formation of Pat-1 in the standard ThT-assays takes between 10-25 h, it was necessary to accelerate this process and with thus enable analysis in reasonable time period. Therefore, the assays were performed in 1.5 ml Eppendorf tubes and the shaking rate was increased to 700 rpm. The protein concentration was increased from 10 µM to 15 µM.

5.1. Results

5.1.1. Appearance of Insoluble Fibrils Follows Disappearance of Soluble Pat-1

The benchmarks of the amyloid formation pathway of Pat-1 is the transformation of soluble monomeric protein into insoluble fibril deposits. It is assumed that fibril formation happens in a nucleation reaction (Arosio et al., 2015). Once the nucleus is formed, fibrils evolve very fast. To confirm that Pat-1 exhibits the same behavior and the transition from soluble into insoluble V_L is a sudden event, samples of a fibril formation assay were taken at different timepoints, separated into soluble and insoluble fractions by centrifugation and analyzed by denaturing SDS-PAGE (Figure 34A). Quantification of the bands revealed a simultaneous decrease of soluble Pat-1 and an increase of protein in the insoluble fraction ($t_{1/2}$ of 1.79 h for the decrease and 1.71 h for the increase) and a comparable slope for both fitting curves (0.438 and 0.530 for decrease and increase, respectively) (Figure 34B). The analysis of the increase in ThT shows that fibrils emerge after the removal of soluble Pat-1 from the reaction with a $t_{1/2}$ of 2.57 h.

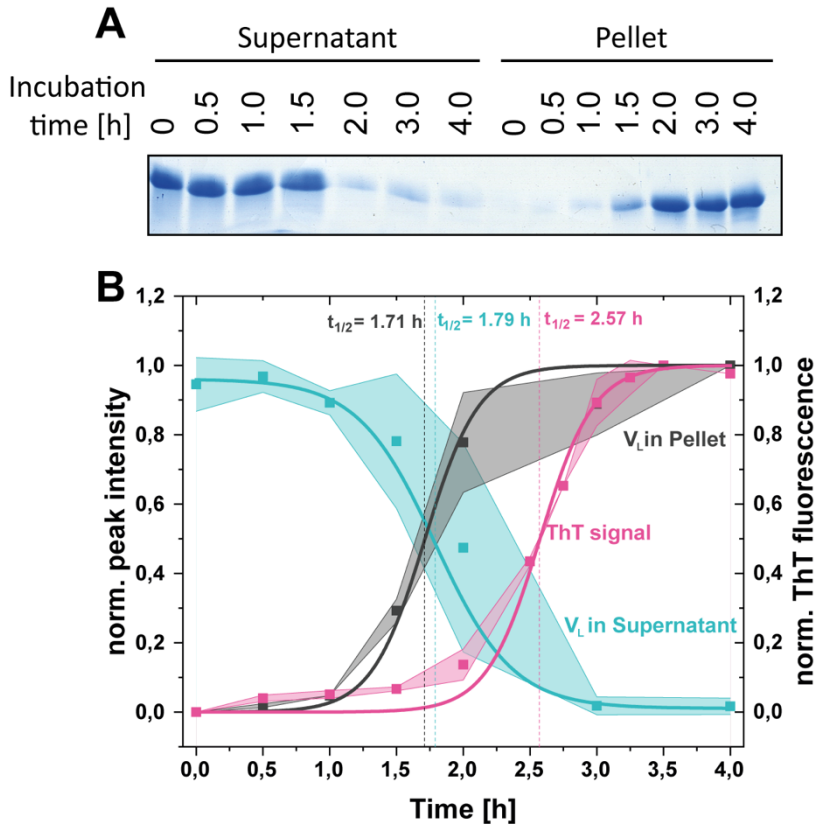

Figure 34. Transition of soluble Pat-1 into insoluble amyloid fibrils. A) Reducing SDS-PAGE (18 %) of soluble and insoluble fraction of Pat-1 over time during fibril formation assay at 37 °C and 700 rpm. B) Normalized quantification of soluble (cyan) and insoluble (black) fraction during the assay and correlation with fibril formation followed by increase of ThT fluorescence (pink). The data show the mean of triplicates with SD (shaded areas). Values were fit to a Boltzmann function to get $t_{1/2}$ values. The slopes of the curves derive from fitting to a linear function.

5.1.2. Different Oligomeric States Form During The Lag Phase of The Amyloid Pathway

The abrupt appearance of fibrils on the one hand and the extremely different structural characteristics of monomeric protein and fibrillary structure on the other hand suggest significant domain rearrangements taking place in the lag phase. To identify the events, the molecular size of sample components at different timepoints during the assay was characterized using analytical ultracentrifugation (AUC). With this method, the sedimentation of molecules is monitored by absorbance optics at 280 nm over time. At the start of the reaction time, most of Pat-1 was present as monomers and small amounts were dimeric (Figure 35A, C). Monomers decreased with a halftime of 1.27 h, while oligomers started to increase (Figure 35B, C). When still more than half of Pat-1 exists as monomers after 45 min, the amounts of oligomers reaches their maximal appearance. After that, monomers and oligomers rapidly decrease and are not detectable anymore after 2 h, when fibrils start to evolve. Four clear

peaks for oligomeric species are visible that remain present until oligomers vanish completely after 2 h. The concentration of oligomers is much smaller than the amounts of monomers at all times, which becomes clear from the peak heights. The low amounts lead to a comparably indistinct resolution of the oligomeric peaks which impedes with the exact elucidation of species present. However, fitting the sedimentation profiles with the SedFit software predicts molecular weights that might correspond to the initial monomers and dimers followed by hexamers and a multiple of four to five hexamers until fibrils occur (Figure 35D). TEM micrographs after 15, 30 and 60 minutes of reaction confirm the clear increase of non-homogeneous oligomers (Figure 35E).

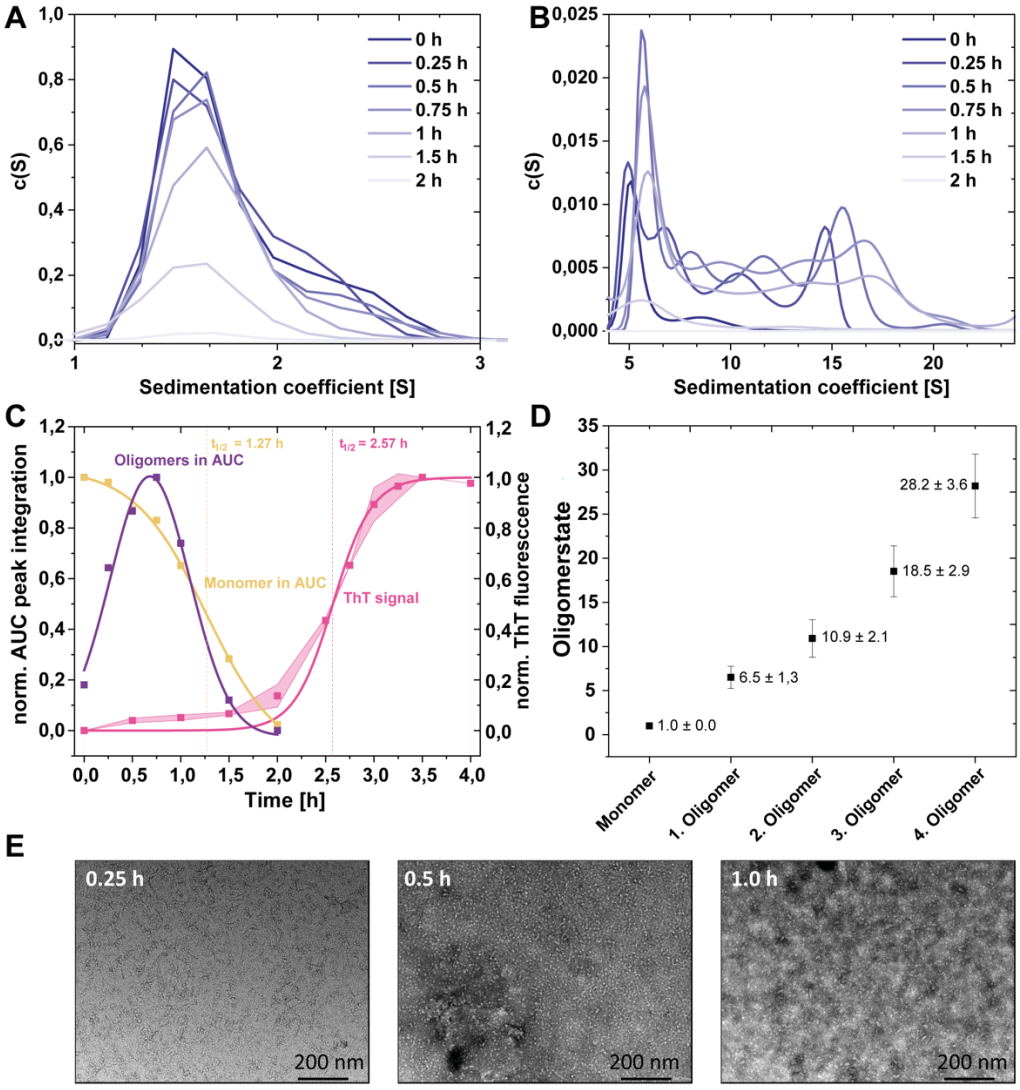

Figure 35. Oligomeric species of Pat-1 during the lag phase of amyloid formation. A) Analytical ultracentrifugation (AUC) data showing the change of monomeric species and B) of oligomeric species over time. C) Normalized integration of monomeric (yellow) and joint oligomeric (purple) AUC peaks. The data of monomeric peaks was fit to a Boltzmann function. Monomers decline with a $t_{1/2}$ of 1.27. Oligomer data were fit to a Gaussian function. D) Mean occuring oligomeric species with SD calculated from the predicted molecular weights of oligomeric AUC peaks by SedFit.

To exclude the possibility that the formed oligomers that occur prior to fibril formation are disulfide linked, SDS-PAGE analysis was performed (Figure 36). Samples at different timepoints during the lag phase of the reaction were taken and treated under reducing and non-reducing conditions, with and without β-Mercaptoethanol, respectively. As expected, no disulfide-links between oligomers were found and Pat-1 was only present as monomer under denaturing, non-reducing conditions.

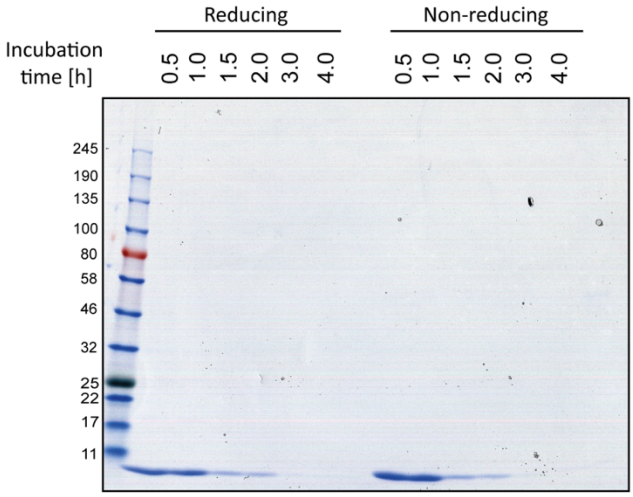

Figure 36. Analysis of disulfide bond formation in oligomers occuring during the fibril formation lag phase. Samples in reducing (left) and non-reducing (right) sample buffer were run on a 4-20 % SDS-PAGE gel. Neither of the samples revealed intermolecular disulfide-bonds.

5.1.3. Structural Changes in Pat-1 During The Lag Phase

In the past, domain swapping was suspected to be causative for the rearrangement of the Ig fold of monomeric LC truncations into the cross-β structure of fibrils, presuming the presence of native like structure in the fibril core (Sonnen et al., 2010). However, more recent studies based on NMR chemical shift analysis revealed that secondary chemical shifts of fibrils show no correlation to the native precursor protein, suggesting that the mechanism of domain swapping is unlikely (Hora et al., 2017). Consequently, considering the presence of anti-parallel β-sheets in the native and parallel β-sheets in fibrils, major secondary structure rearrangements have to take place during the lag phase of amyloid formation (Cordeiro et al., 2006). The secondary structure changes were monitored over time by far UV circular dichroism (CD) spectroscopy. The initial native Pat-1 at 0 h of incubation showed a clear minimum at 218 nm, as expected for an anti-parallel β-sheets rich Ig domain (Figure 37A) (Goto and Hamaguchi, 1979). After 0.5 h incubation, the signal intensity of the minimum at 218 nm increases and the signal increase into the positive towards 197 nm decreases. Considering the spectra of a folded (20 °C) and unfolded (90 °C) V_L domain (Figure 37B), the changes in intensity while the overall shape remains might be indications of an opening or unfolding of

parts of the secondary structure elements. This trend continues in the samples taken during the first 1.5 h of the fibril formation assay. After 1.75 h the signal abruptly changes and the minimum shifts to 220 nm with an increased amplitude. Additionally, the signal rise towards 197 decreases significantly. The shift of minimum and the intersection of the wavelength x-axis at $\theta_{MRW} = 0$ towards higher wavelength was reported for parallel β-sheets. Consequently, this timepoint marks the important rearrangement from anti-parallel to parallel β-sheets. The effect is further enhanced after 1.9 h and a maximum in the lower wavelength region starts to emerge. After 2 h the maximum shows another shift to 224 nm and a defined maximum at 204 nm, representing the characteristic far UV spectrum of supramolecular β-sheet rich structures like amyloid (Sahoo et al., 2019). This correlates well with the increase in ThT fluorescence and thus the appearance of fibrils after 2 h (Figure 37C).

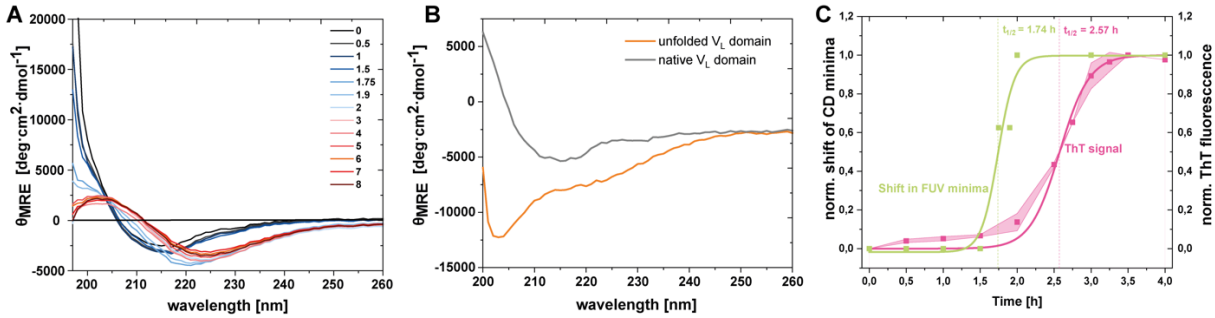

Figure 37. Secondary structure changes of Pat-1 during the lag phase of fibril formation. A) Comparison of the secondary structure followed be far UV CD-spectroscopy. B) far UV CD-spectra of a folded (20 °C) and unfolded (90 °C) V_L domain. CD spectra show a mean of 10 individual measurements. C) Normalized change in CD minima in comparison with the increase of ThT fluorescence over time.

The buried Trp residue was used to probe the domain opening during rearrangement in the lag phase, since the fluorescence emission is increased when the side chain moves away from the quenching disulfide bridge. During oligomer formation a steady increase of fluorescence emission could be observed indicating an opening of the V_L structure (Figure 38A, C). The increase reached its maximum after 2 h, at the same time when fibrils start to evolve. After that, the emission intensity shows a slight decrease, suggesting a tighter packing in the fibrillar structure. Not only the Trp in the hydrophobic core of the domain but also other hydrophobic amino acids are likely to become accessible and solvent-exposed during a domain opening. ANS binding experiments were used to confirm the hypothesis. The fluorescence of ANS increases upon binding to hydrophobic regions in a protein. The results show a fast increase of ANS fluorescence emission in the first hour of the assay, confirming the increased solvent exposure of amino acids from the hydrophobic core of the antibody domain and thus hinting towards a structural opening of the core (Figure 38B, C). After 1.5 h the fluorescence

decreased again, suggesting that the domain rearrangements and/or inter-domain interactions took place resulting in a changed environment of aromatic amino acids. Upon complete fibril formation after 3 h, the ANS fluorescence was drastically decreased and the hydrophobic amino acids seem to be buried in the fibril core.

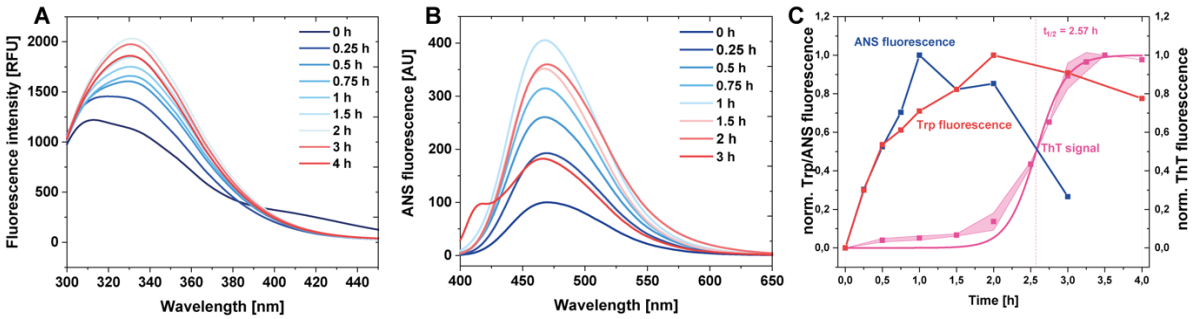

Figure 38. Conformational changes of Pat-1 during the lag phase of fibril formation. A) Change of Trp and B) ANS fluorescence emission over time. The measurements show a mean of three individual measurements. C) Comparison of Trp and ANS fluorescence emission intensities to fibril formation over time.

5.1.4. Changes in Conformational Dynamics During the Lag Phase

H/DX-MS measurements were used to follow the changes in conformational dynamics of samples taken at different timepoints during the fibril formation reaction. Astonishingly, when comparing the control V_L domain in regular PBS buffer to the Pat-1 in the fibril inducing assay buffer, decreased conformational dynamics of the C-terminal segment were found (Figure 39A). Also, the loop region harboring residue 15 was less dynamic during assay conditions. This loop and the C-terminal stretch were earlier found as factors crucial for the stability difference between Pat-1 and WT-1. Despite the less dynamic C-terminal segment compared to the V_L in regular PBS buffer, this stretch still comprised high conformational dynamics in the context of the V_L domain. In contrast to the control V_L, this dynamic C-terminal region was extended under destabilizing conditions. It expanded over FR4 and spanned the full CDR3 loop reaching a few residues of FR3. Also, the CDR2 loop harboring the two point mutations D53 and D55 and a segment in FR3 showed enhanced conformational dynamics under assay conditions. Furthermore, no significant changes in dynamics occured during the first hour of the lag phase (Figure 39A, B). After 1.5 h, the conformational dynamics highly increased over most of the structure, indicating major structural changes. This is in line with the secondary structure analysis by CD-spectroscopy that showed the starting point of major rearrangements at approximately 1.5 h. It has to be noted, that the peptides detected by MS decreased at this timepoint and no complete sequence coverage could be obtained.

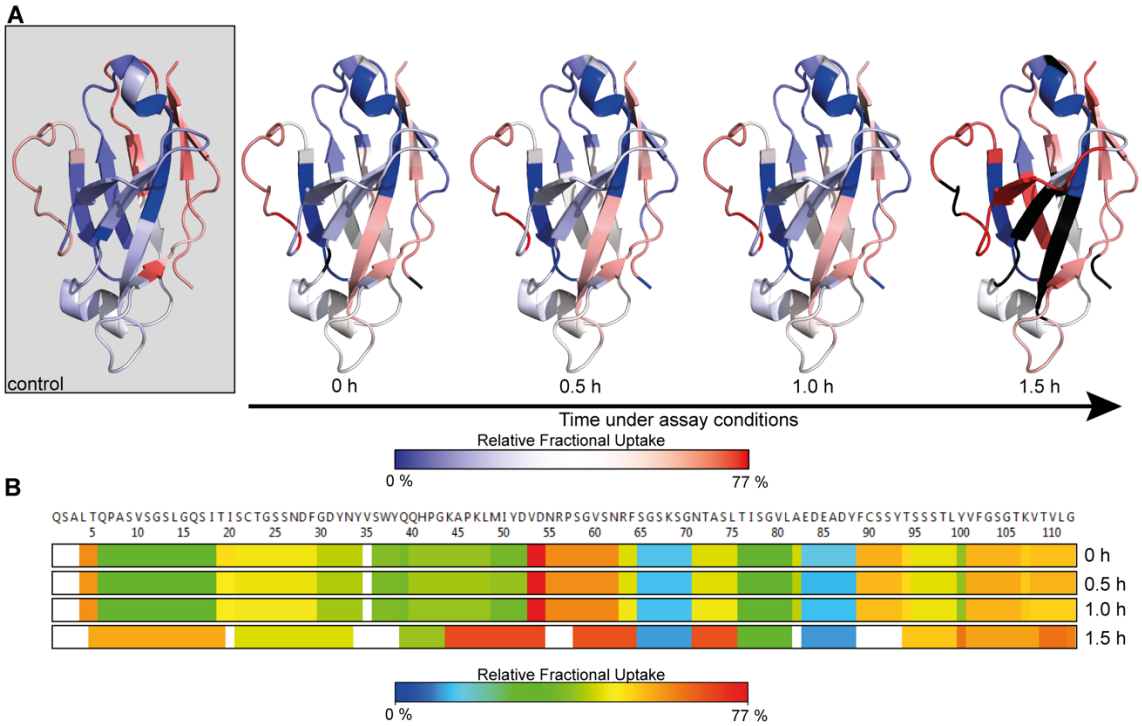

Figure 39. Changes in conformational dynamics at different timepoints during the lag phase of fibril formation followed by H/DX-MS. A) B-values showing the relative fractional uptake of deuterium per residue were visualized on the Pat-1 V_L crystal structure and colored according to the % uptake from blue (no exchange) to red (highest exchange). B) H/D exchange for the single amino acids in the Pat-1 primary sequence colored from blue (no exchange) to red (highest exchange).

5.1.5. ERdj3 Allows the Formation of Stable Oligomers

In chapter 4.1.3 and 4.1.4, the influence of ERdj3 on fibril formation was elucidated. It was shown, that ERdj3 can inhibit fibril formation completely if present in high enough concentrations, but only delays the reaction if the concentrations are lower. To investigate how ERdj3 prevents Pat-1 monomers from entering the amyloid formation pathway, the oligomerization of the patient antibody domain was studied by AUC measurements in the presence of 800 nM ERdj3. The ERdj3 concentration was low enough to not interfere with the absorption during the AUC runs. The sedimentation profiles showed that the monomer peaks do not comprise the same drastic decrease as without the chaperone, indicating a stabilization (Figure 40A, C). Nevertheless, the same oligomer pattern appeared after a short time of incubation already (Figure 40B). However, the level remained similar and did not decrease as it did in the absence of the chaperone (Figure 40C). The findings suggest that ERdj3 does not prevent Pat-1 monomers from entering the off-pathway, but it stabilizes the intermediates and prevents them from further reactions if the ratios are sufficient.

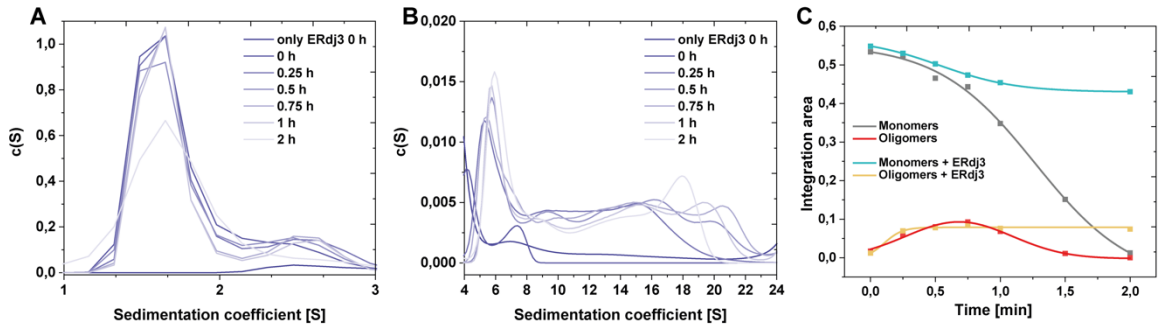

Figure 40. Analysis of oligomeric species formed by Pat-1 in the presence of ERdj3. Sedimentation profiles show the development over time of A) monomer and dimer peaks and B) oligomeric species of Pat-1 appearing over time during incubation. AUC raw data were analyzed with SedFit. C) Comparison of the amounts of monomers and oligomers formed in the absence (grey and red lines, respectively) and in the presence (turquoise and yellow lines) of ERdj3. The data points show the integrated and normalized peak area of the specific monomeric and oligomeric fractions.

Oligomers exhibit high Gibbs free energy and are very transient. Crosslinking with glutaraldehyde was performed as an attempt to stabilize the oligomers, make them durable and determine the oligomeric states over time. The crosslink is formed by an interaction of one glutaraldehyde molecule with two lysine side chains of proteins. However, depending on the location of lysines the crosslinks may vary in different oligomeric states, the crosslinking reaction features a relatively low specificity. Thus, this experiment was not suitable for giving information about the real oligomeric species in the sample. However, it allowed a comparison of the oligomer patterns in the presence and absence of ERdj3 by performing SDS-PAGE analysis. Besides the monomer band, a clear dimer band was visible from the very start of the reaction and this remained present for both the sample preparations (Figure 41). The ERdj3 band at ~35 kDa became smeary in the presence of Pat-1, but did not show a big shift, indicating binding to the Pat-1 monomer (~11 kDa). During the assay a smeer over a range of higher oligomeric sizes appeared after 15 min already. After 1 h of incubation, a clear band at ~60 kDa became visible that could correspond to a hexamer of Pat-1. As expected from the AUC sedimentation profiles, the pattern of oligomers observed by glutaraldehyde crosslinking didn't show a significant difference between absence and presence of ERdj3. While Pat-1 became completely insoluble after 2 h, the oligomeric pattern with the chaperone was still the same, clearly indicating the stabilizing effect of ERdj3 on all forms of Pat-1.

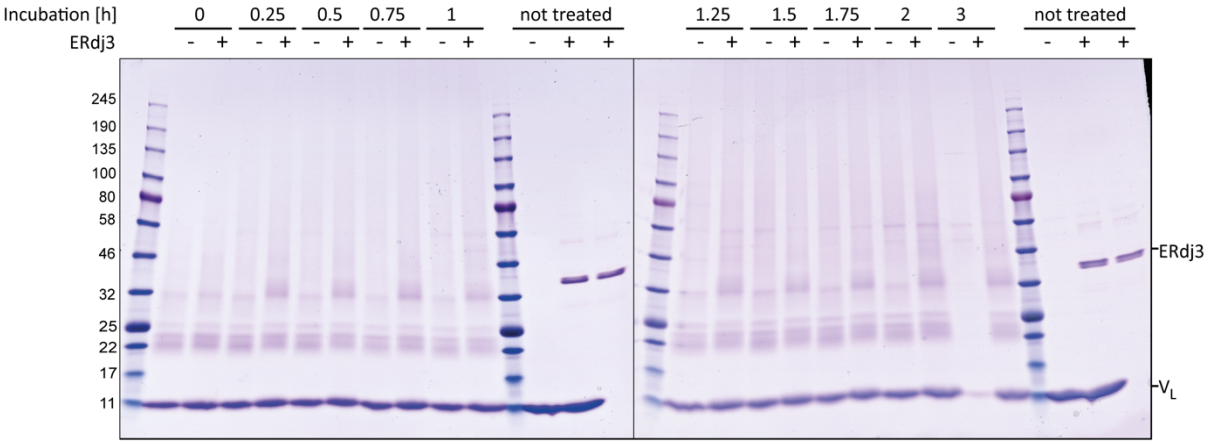

Figure 41. Glutaraldehyde crosslinking of Pat-1 in the presence and absence of ERdj3 at different timepoints during incubation. For crosslinking, samples were incubated with 0.1 % Glutaraldehyde for 3 min at 37 °C. Controls show samples without Glutaraldehyde treatment. A precast gradient gel with 4-20 % acrylamide was used.

5.2. DISCUSSION

Insoluble amyloid fibrils are widely believed to be a pathogenic species during disease development of various amyloid-related diseases like Alzheimer's or Parkinson's disease and different kinds of amyloidoses. It is perspicuous that the deposition of insoluble fibrillar aggregates on organs and in tissues interferes with the biological functions and causes organ impairment (Pepys, 2006). However, the presence of oligomers during fibril formation attracts increasing interest, as many hypotheses allocate the most cytotoxic effects to these intermediate states and point out the importance of a characterization of early events during the amyloid formation pathway (Arosio et al., 2015; Perfetti et al., 2012). This chapter aimed to elucidate the events happening in the lag phase before fibrils occur and which role the secretion-competent ER co-chaperone ERdj3 could play.

The V_L domain of Pat-1 follows the overall known kinetics of fibril formation including a lag phase, where no increase in ThT fluorescence can be observed, a fast growth phase where fibrils elongate as observed by an increase of ThT signal and a final plateau phase, where the monomer concentration is at equilibrium (Arosio et al., 2015). These kinetics are sigmoidal indicating a nucleated polymerization process causing fibril formation (Serrano et al., 2017). The transition phase happens very fast and is accompanied by the disappearance of soluble V_L domain from the reaction and its integration in insoluble fibrils. The reaction is initiated from a solution containing exclusively monomeric Pat-1. The significantly slower lag phase compared to the growth phase hints towards the occurrence of major structural changes including of large energy barriers separating intermediates (Arosio et al., 2015; Serrano et al., 2017). Here, the presence of a specific oligomer pattern in the lag phase prior to fibrillization of the disease-causing LC truncation Pat-1 was discovered. The initial amounts of monomers decrease over time, while the oligomer concentration increases first and then decreases again until complete disappearance of oligomers upon fibril formation. This hints toward the formation of pre-fibrillar oligomeric species that act as nuclei for fibril elongation (Chatani and Yamamoto, 2018; Crespo et al., 2012). In line with energetic expectations, monomers are the predominant soluble species at all timepoints until insoluble fibrils are present. This is in agreement with the notion that oligomers exhibit the highest Gibbs free energy and are thus always lower in concentration than soluble monomers or insoluble fibrils (Arosio et al., 2015; Buell et al., 2012). Considering that antibody domains are folded into a compact two-layer sandwich structure composed of antiparallel β-strands and that amyloid fibrils in AL amyloidosis patients are assembled from a repetitive parallel β-sheet topology, an overall mandatory structural rearrangement has to occur prior to fibril formation (Feige et al., 2010; Guo et al., 2004; Huber et al., 1976; Radamaker et al., 2019; Swuec et al., 2019). FUV spectra clearly show the characteristic spectra of the anti-parallel β-sheet Ig fold for the first species present in the early phase of the lag phase, oligomers assemble from this fold, giving rise for the assumption that

after initial dimer formation from folded monomers, a subsequent addition of further dimers occurs to stabilize part of the V_L domain and prevent the complete unfolding. This fits the H/DX data that show an overall stabilization of the otherwise very dynamic C-terminal region under assay conditions and no change of the overall conformational dynamics during the oligomerization that happens by retaining the Ig fold of Pat-1. Directly before fibrils are formed, a shift of the FUV spectra minima can be observed, which is thought to display the rearrangement of β-sheets, whereupon the typical fold of the cross-β supramolecular structure becomes apparent in the spectra (Sahoo et al., 2019). Since this rearrangement takes place instantaneously before fibril formation, the arising species is thought to display the nucleus for the addition of monomers and consequent fibril elongation.

While the overall secondary structure of the early oligomeric species does not change, ANS binding and Trp fluorescence measurements clearly show partial unfolding and opening of the V_L domain during the lag phase. ANS binding is used as an indicator for surface exposed hydrophobicity that is in general energetically unfavored (Moelbert and Emberly, 2004; Young et al., 1994). Therefore, the binding of ANS and the consequent increase of ANS fluorescence intensity informs about intramolecular structural changes that influence the position of hydrophobic amino acids (Horowitz and Criscimagna, 1985). The increase in surface hydrophobicity and thus the solvent-exposure of hydrophobic residues during the lag phase lead to the conclusion that oligomer formation includes conformational transformation that potentially change the globular protein fold. As a logical energetic consequence of the solvent-exposed hydrophobicity, oligomers assemble to bury these hydrophobic groups during the event of a hydrophobic collapse followed by structural rearrangements (Eisenhaber and Argos, 1996; Moelbert and Emberly, 2004; Young et al., 1994). Intrinsic Trp fluorescence intensity changes over time confirm these findings. The microenvironment of the buried Trp the fluorescence of which is quenched by the close proximity to the intramolecular disulfide bond (Feige et al., 2010), changes over time indicating similar conformational opening events that were suggested by the results of ANS binding experiments.

Putting the results of FUV CD-spectroscopy, ANS binding, intrinsic Trp fluorescence and H/DX-MS measurements together gives rise to the hypothesis that despite the retaining of the overall secondary structure of the Pat-1 monomer during oligomerization, an intermediate state arises in the lag phase of fibril formation that is accompanied by an opening of the tight structural packing of the V_L domain and the solvent-exposure of hydrophobic residues. The naturally highly dynamic C-terminal region and the energetically unfavored surface hydrophobicity is stabilized and covered in the oligomers. The molecular weight prediction for the different oligomeric species hint towards a dimerization that goes along with a structural domain opening, followed by the assembly of dimers to hexamers and the consequent appearance of multiples of the latter.

The ER-resident co-chaperone ERdj3 was identified as a potent inhibitor of fibril formation. The existence of a potential off-pathway that leads to fibril formation was tested by including ERdj3 in the oligomerization assay and analyzing the occuring oligomeric species. The same oligomers that were found in the absence of ERdj3 were also found in the presence of the co-chaperone, indicating that the intermediate forms don't necessarily display off-pathway products, but rather ERdj3 stabilizes the misfolding-prone Pat-1 V_L domain. This however, contradicts with prior descriptions of on- and off-pathways for the Aβ peptide (Bieschke et al., 2012; Chimon et al., 2007; Mastrangelo et al., 2006). The results obtained in the scope of this thesis indicate that ERdj3 has a transient stabilizing effect on the monomeric and oligomeric forms of Pat-1. However, only an initial stabilization of the earliest Pat-1 species results in the inhibition of fibril formation. Since the appearance of oligomers is transient and the further reaction happens very fast, ERdj3 is not able to keep Pat-1 completely soluble. Based on the results, the model of the ERdj3 involvement in fibril formation was expanded (Figure 42).

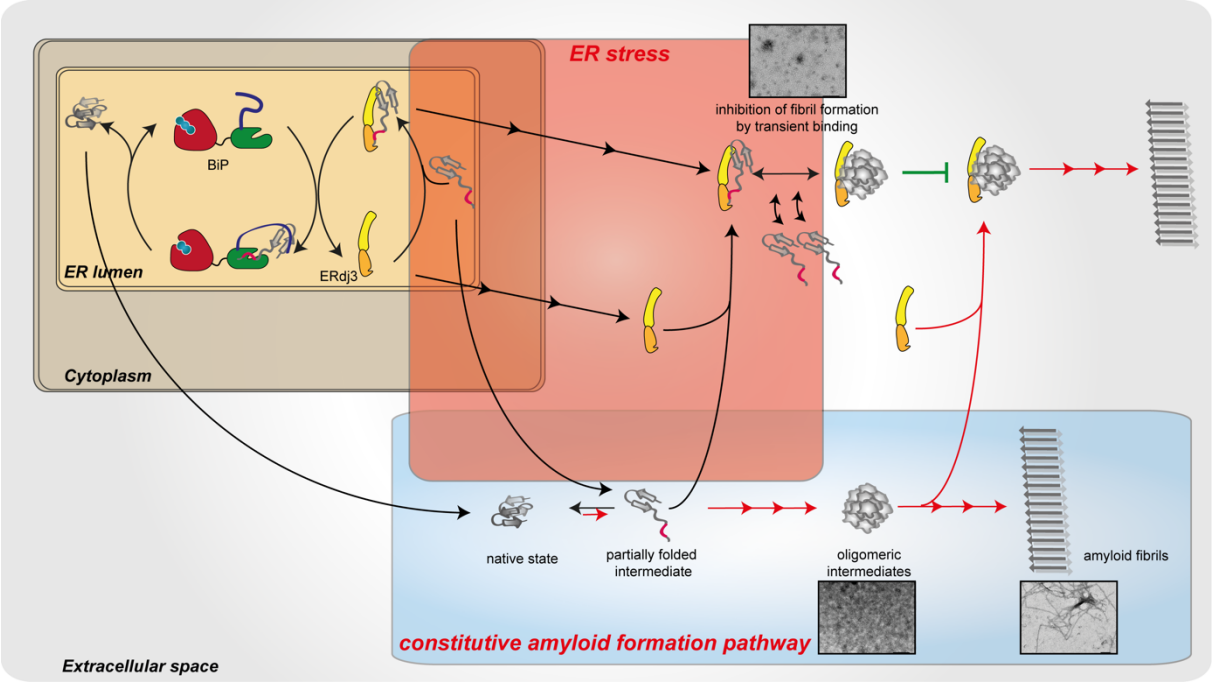

Figure 42. Model of the secretion of ERdj3 and amyloidogenic LCs. ER stress leads to the increased secretion of misfolding-prone LCs and ERdj3 either alone or as a complex. The individually secreted LC can misfold in the extracellular space and react into fibrils. ERdj3 can possibly inhibit the further reaction of the misfolded species. Once to many oligomers are present, ERdj3 can only delay the fibril formation.

6. Antibody Light Chain Integrity in AL Amyloidosis

The preceding chapters mainly described the processing and behavior of LCs upon secretion. However, to obtain a comprehensive image about AL amyloidosis, it is important to also consider the initial events occuring during disease development. ERQC dictates the balance between secretion and degradation of proteins in the ER and depends on ER homeostasis, a network comprising folding, secretion and degradation pathways. The goal is to prevent misfolded and non-functional proteins from secretion into the extracellular space (Wiseman et al., 2007). In AL amyloidosis aggregation-prone LCs are predominantly secreted independently of HCs, either as monomers or as homodimers (Bence-Jones proteins) (Zolle et al., 1970). The subsequent chapter aims at elucidating the behavior of different LCs in living cells regarding expression, folding, secretion and aggregation. The experiments described in this section were performed in the group of Linda Hendershot at St. Jude Children's Research Hospital in Memphis, TN, USA. Most experiments were performed with Pat-1-3 and WT LCs, since these showed the most interesting features that differed between each other. All SDS-PAGE gels used were 13 %.

6.1. Results

6.1.1. Patient Information and Sequences of LCs

The pathogenic LC sequences used for cell culture experiments derived from AL amyloidosis patients (Pat-1 – Pat-6) treated in the Amyloidosis Center in Heidelberg, Germany. Primary structures were deduced from cDNA of the disease-causing plasma cell clone. The corresponding germline sequences (WT-1 – WT-6) were determined using the web-based tools IgBLAST and abYsis. All sequences were of λ-subtype. The patients differed in organ involvement, disease severity, underlying germline V gene, the number of mutations and free LC level in the plasma (Table 4).

Table 4. Patient and LC information. The patient LCs were named Pat-1-6, the corresponding germline sequences WT-1-6. They differ in the number of mutations, the underlying germline V gene, the free LC level at diagnosis (κ and λ). The affected organs and cardiac and renal scores indicating disease severity are listed.

Nomination					Organ involvement				Scores	
Thesis ID	Heidelberg ID	Mutations	Germline V gene	FLC at Diagnosis [mg/l]	Number	Heart	Kidney	Liver	Cardiac Mayo	Renal
Pat-1	p3807a	11	IGLV2	7564	4	yes	yes	no	IV	III
WT-1	wt3807a									
Pat-2	p3706	5	IGLV3	318	1	yes	no	no	IV	I
WT-2	wt3706									
Pat-3	p2597a	10	IGLV1	64	2	yes	yes	no	II	III
WT-3	wt2597a									
Pat-4	p3931b	9	IGLV1	36	4	no	yes	yes	I	II
WT-4	wt3931b									
Pat-5	p3891a	8	IGLV1	114	3	yes	yes	yes	II	III
WT-5	wt3891a									
Pat-6	p3142	10	IGLV1	137	1	yes	no	no	III	I
WT-6	wt3142									

Table 5 shows the sequences of the patient LCs and their germline sequences. The patient LC sequences show no visible pattern of the mutated amino acid characteristics or the affected CDRs or FRs. Overall, the CDRs comprise more mutations than FRs. However, this was expected due to the fact that CDRs are naturally hypervariable. For expression of the LC in living cells, the sequences were cloned into pcDNA 3.1(+) vectors.

Table 5. Sequences of patient LCs (Pat-1-6) and their corresponding germline LCs (WT-1-6). The CDRs of the V_L domains are depicted in black, the FRs in blue. Mutations are highlighted in red. C_L domains are shown in green.

Pat-1	QSALTQPASVSGSLGQSITISCTGSSNDFGDYNYVSWYQQHPGKAPKLMIYDVDNRPSGVSNRFSGSKSGNTASLTISGVLAED
WT-1	QSALTQPASVSGSPGQSITISCTGTSSDVGGYNYVSWYQQHPGKAPKLMIYEVSNRPSGVSNRFSGSKSGNTASLTISGLQAED
Pat-1	EADYFCSSYTSSSTLYVFGSGTKVTVLGQPKANPTVTLFPPSSEELQANKATLVCLISDFYPGAVTVAWKADGSPVKAGVETTKP
WT-1	EADYYCSSYTSSSTLYVFGTGTKVTVLGQPKANPTVTLFPPSSEELQANKATLVCLISDFYPGAVTVAWKADGSPVKAGVETTKP
Pat-1	SKQSNNKYAASSYLSLTPEQWKSHRSYSCQVTHEGSTVEKTVAPTECS
WT-1	SKQSNNKYAASSYLSLTPEQWKSHRSYSCQVTHEGSTVEKTVAPTECS

Pat-2	SSELTQDPAVSVALGQTVRITCQGDSLRSYSASWYQQKPGQAPVLVIFRKSNRPSGIPDRFSGSSSGNTASLTITGAQAED
WT-2	SSELTQDPAVSVALGQTVRITCQGDSLRSYYASWYQQKPGQAPVLVIYGKNNRPSGIPDRFSGSSSGNTASLTITGAQAE
Pat-2	EADYYCNSRDSSANHQVFGGGTKLTVLGQPKAAPSVTLFPPSSEELQANKATLGCLISDFYPGAVTVAWKADSSPVKAGVETTTP
WT-2	EADYYCNSRDSSGNHQVFGGGTKLTVLGQPKAAPSVTLFPPSSEELQANKATLGCLISDFYPGAVTVAWKADSSPVKAGVETTTP
Pat-2	SKQSNNKYAASSYLSLTPEQWKSHRSYSCQVTHEGSTVEKTVAPTECS
WT-2	SKQSNNKYAASSYLSLTPEQWKSHRSYSCQVTHEGSTVEKTVAPTECS

Pat-3	QSVLTQPPSVSGAPGQRVTISCTGSSSNIGAGYVVHWYQQLPGTAPKLLIYGNSNRPSGVPDQFSGSKSGTSASLAITGLQSED
WT-3	QSVLTQPPSVSGAPGQRVTISCTGSSSNIGAGYDVHWYQQLPGTAPKLLIYGNSNRPSGVPDRFSGSKSGTSASLAITGLQAED
Pat-3	EADYYCKAWDNSLNAPWVFGGGTKLTVLGQPKAAPSVTLFPPSSEELQANKATLVCLISDFYPGAVTVAWKADSSPVKAGVETTTP
WT-3	EADYYCQSYDSSLSGYWVFGGGTKLTVLGQPKAAPSVTLFPPSSEELQANKATLVCLISDFYPGAVTVAWKADSSPVKAGVETTTP
Pat-3	SKQSNNKYAASSYLSLTPEQWKSHKSYSCQVTHEGSTVEKTVAPTECS
WT-3	SKQSNNKYAASSYLSLTPEQWKSHKSYSCQVTHEGSTVEKTVAPTECS

Pat-4	QSVLTQPPSASGTPGQRVTISCSGSSSNIGGHPVNWYQQLPGTAPKLLIYSNDERPSGVSDRFSGSKSGTSASLAISGLQSDD
WT-4	QSVLTQPPSASGTPGQRVTISCSGSSSNIGSNTVNWYQQLPGTAPKLLIYSNNQRPSGVPDRFSGSKSGTSASLAISGLQSED
Pat-4	EAYYYCAASDDNLNGPVFGGGTKLTVLGQPKAAPSVTLFPPSSEELQANKATLVCLISDFYPGAVTVAWKADSSPVKVGVETTTP
WT-4	EADYYCAAWDDSLNGPVFGGGTKLTVLGQPKAAPSVTLFPPSSEELQANKATLVCLISDFYPGAVTVAWKADSSPVKVGVETTTP
Pat-4	SKQSNNKYAASSYLSLTPEQWKSHKSYSCQVTHEGSTVEKTVAPTECS
WT-4	SKQSNNKYAASSYLSLTPEQWKSHKSYSCQVTHEGSTVEKTVAPTECS

Pat-5	QSVLTQPPSVSAAPGQKVTISCSGSSSNIGNNYVSWYQQLPGTAPKFLLYDNNQRPSGIPDRFSGSKSGTSATLGITGLQAGD
WT-5	QSVLTQPPSVSAAPGQKVTISCSGSSSNIGNNYVSWYQQLPGTAPKLLIYDNNKRPSGIPDRFSGSKSGTSATLGITGLQTGD
Pat-5	EADYYCGTWDTSLDSWVFGGGTKLTVLSQPKAAPSVTLFPPSSEELQANKATLVCLISDFYPGAVTVAWKADSSPVKAGVETTTP
WT-5	EADYYCGTWDSSLSAWVFGGGTKLTVLGQPKAAPSVTLFPPSSEELQANKATLVCLISDFYPGAVTVAWKADSSPVKAGVETTTP
Pat-5	SKQSNNKYAASSYLSLTPEQWKSHKSYSCQVTHEGSTVEKTVAPTECS
WT-5	SKQSNNKYAASSYLSLTPEQWKSHKSYSCQVTHEGSTVEKTVAPTECS

Pat-6	QSVLTQPPSASGTPGQRVTISCSGRSSNIGRNLVKWYQQFPGTAPKLLIYSNDQRPSGVPDRFSGSKSGTSASLAVSGLQSED
WT-6	QSVLTQPPSASGTPGQRVTISCSGSSSNIGSNTVNWYQQLPGTAPKLLIYSNNQRPSGVPDRFSGSKSGTSASLAISGLQSED
Pat-6	EADYYCAAWDATLNAWVFGGGTKLTVLSQPKAAPSVTLFPPSSEELQANKATLVCLISDFYPGAVTVAWKADSSPVKAGVETTTP
WT-6	EADYYCAAWDDSLNAWVFGGGTKLTVLGQPKAAPSVTLFPPSSEELQANKATLVCLISDFYPGAVTVAWKADSSPVKAGVETTTP
Pat-6	SKQSNNKYAASSYLSLTPEQWKSHRSYSCQVTHEGSTVEKTVAPTECS
WT-6	SKQSNNKYAASSYLSLTPEQWKSHRSYSCQVTHEGSTVEKTVAPTECS

6.1.2. Expression of LCs in HEK 293T And Cos-1 Cells

To decide which cell line to use for the experiments, a transfection and expression test in the human cell line HEK 293T (Figure 43A) and in the monkey cell line Cos-1 (Figure 43B) was performed. For both transfections, the GeneCellin DNA transfection reagent was used. Further, it was tested if the co-expression of BiP influences the expression level of the LCs. For the initial test, Pat-1, Pat-2 and Pat-3 with corresponding WT LCs were used. All LCs were successfully transfected and expressed from both cell lines. 293T cells showed an overall slightly higher expression level and BiP co-transfection did not significantly change the amount of expressed LC. Pat-3 and WT-3 show an unusual difference in gel migration due to unknown reasons that are further described in chapter 6.1.7. Interestingly, the trend of amount of patient LCs produced is in line with the FLC concentrations in the patient: Pat-1 showed the highest and Pat-3 the lowest FLC level in the blood (see Table 4).

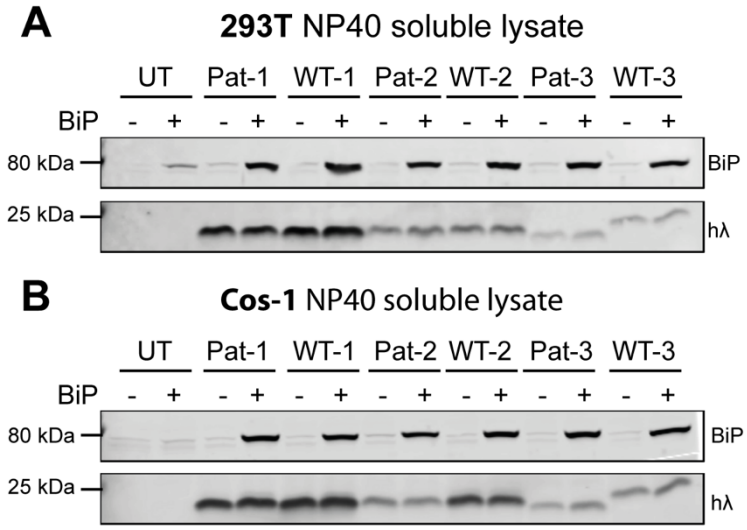

Figure 43. Transfection and expression test of LCs Pat-1-3 and WT-1-3 with and without BiP co-transfection. Transfection and expression in A) 293T and B) Cos-1 cells. Pat-1 and WT-1 expression levels were highest, Pat-3 and WT-3 lowest.

6.1.3. Secretion of LCs

The high serum FLC concentrations (see Table 4) facilitate proteotoxic aggregation in organs and tissue of AL patients and point out the ability of the patient-derived LCs to escape ERQC. To investigate the secretion efficiency of cells transfected with the specific LCs, 293T cells were starved for 30 min and metabolically labelled with ^{35}S as a radioactive marker for 3 h. SDS-PAGE of the NP40-soluble lysate as well as medium after immunoprecipitation with an anti-human λ antibody and consequent visualization using phospho-imaging showed a band for every protein that was pulled down with the LCs (Figure 44A). The pcDNA3.1(+) vectors that were used for protein expression in the cell lines contain a strong promoter for high-level

expression in mammalian cells. This leads to a possible realistic expression level for patient-derived LCs, however, not for the germlines. In this case, germline LCs serve as controls and give information about the influence of the underlying primary sequence differences. As expected, all LCs were expressed and found in the NP40 soluble lysates migrating at ~25 kDa. Interestingly, Pat-3 was not secreted at all while WT-3 is regularly secreted and Pat-2 showed a clearly thinner band for secretion compared to WT-2. Pat-1 and WT-1 obtained the highest visible secretion. Another band at ~80 kDa that was pulled down with Pat-2 was striking that was even more pronounced for Pat-3 but not with their corresponding germline LCs. The migration height of the band could correspond to BiP. For LCs 4-6 no peculiarities were observed. The experiment was performed in doublicates and quantification of the secreted LC bands showed no significant difference in secretion between patient and germline LC with the exception of LC 3 (Figure 44B).

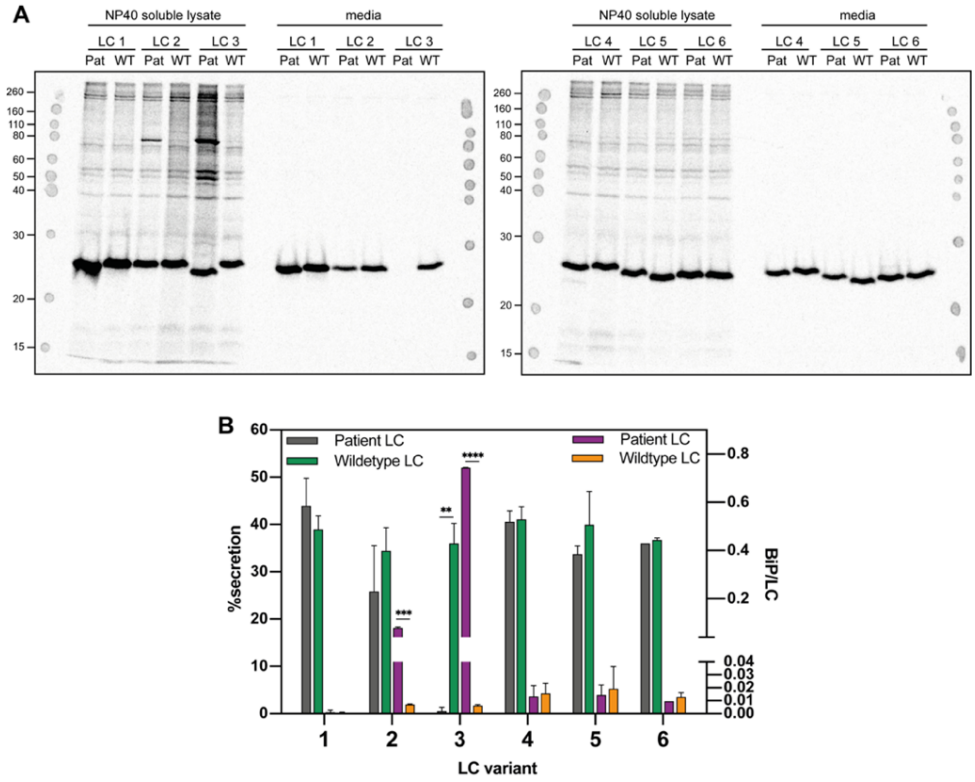

Figure 44. Comparison of LC expression and secretion in HEK 293T cells. A) Phospho-imaging of SDS-PAGE gels showing NP40 soluble lysates and media of cells. After transfection with patient and germline LC constructs, cells were metabolically labeled and the media and cell lysate treated with an anti-human λ antibody for immunoprecipitation. B) Quantification of the intracellular and media LCs for detection of % secretion. Secretion of patient and germline LCs are shown in grey and green, respectively. The BiP/LC ratio was determined by dividing quantified BiP bands by the corresponding LC band. BiP/LC ratios for patient and germline LCs are shown in purple and orange, respectively. Two sets of experiments were used for quantification.

However, a difference between Pat-2 and WT-2 was visible. These two patient LCs are the ones that show the additional presumptive BiP band. Quantification and calculation of the BiP/LC ratio showed a highly significant change in pull-down of BiP for Pat-2 and Pat-3 compared to their corresponding WT LCs. Taking together the impaired secretion and the binding by BiP, could indicate a recognition of the patient LCs by ERQC.

LCs 2 and 3 showed the most striking behavior regarding secretion and BiP pull-down in 293T cells. To confirm that this is not a cell-specific effect, the same experiment was performed in Cos-1 cells for Pat-2, Pat-3 and the WT LCs. As expected, all LCs were expressed and found in the NP40 soluble lysates (Figure 45A). The pull-down of other proteins seemed to be more pronounced in Cos-1 than in 293T cells. However, also the LC bands were stronger. The specific BiP pull-down by the patient LCs could be observed in Cos-1 cells, too. Additionally, the secretion impairment for Pat-2 compared to WT-2 was more distinct. Pat-3 did not show any secretion in Cos-1 cells, as well. Quantification of the LC and presumptive BiP bands resulted in the same trend like in 293T cells, but the difference between secretion of Pat-2 and WT-2 and thus the relation between secretion and BiP binding was clearly observable (Figure 45B).

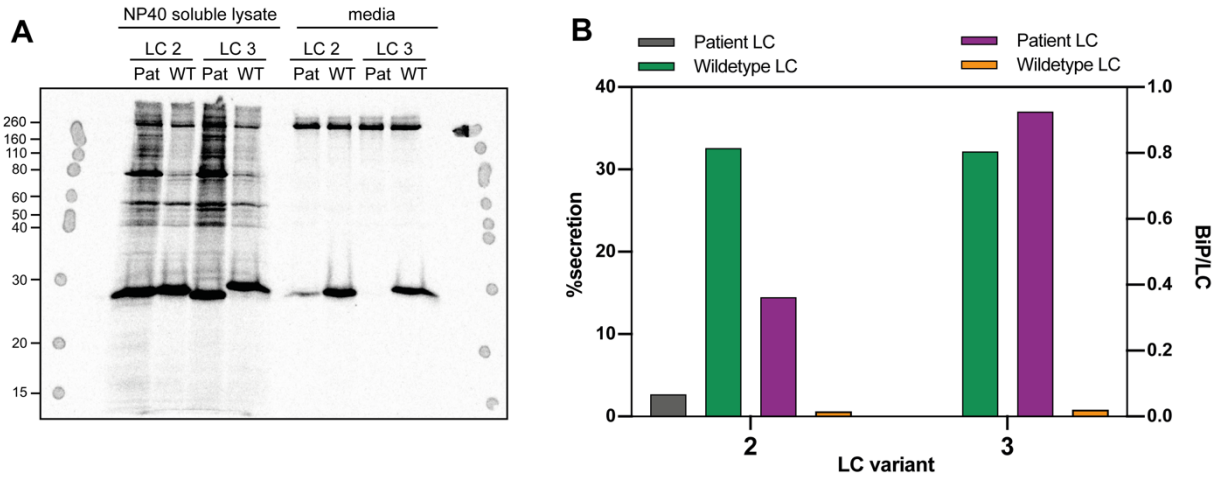

Figure 45. Comparison of LC expression and secretion in Cos-1 cells. A) Phospho-imaging of SDS-PAGE gels showing NP40 soluble lysates and media of cells transfected with LCs 1 and 2. After transfection with patient and germline LC constructs, cells were metabolically labeled and the media and cell lysates treated with an anti-human λ antibody for immunoprecipitation. B) Quantification of the intracellular and media LCs for detection of secretion. Secretion of patient and germline LCs are shown in grey and green, respectively. The BiP/LC ratio was determined by dividing quantified BiP bands by the corresponding LC band. BiP/LC ratios for patient and germline LCs are shown in purple and orange, respectively. Two sets of experiments were used for quantification.

So far, the band at 80 kDa was only presumed to correspond to BiP. To confirm the binding and co-immunoprecipitation of BiP with the LCs Pat-2 and Pat-3, cells were transfected with LCs and BiP. 24 h after transfection, an immunoprecipitation of NP40 soluble lysate with anti-

human λ antibody followed by Western blot analysis with an anti-human λ antibody and anti-BiP antiserum was performed (Figure 46A). While the highly enhanced expression of Pat-1 and WT-1 was observable again, enhanced binding and pull-down of BiP was clearly confirmed for Pat-2 and Pat-3 in 293T cells. Cos-1 cells showed the same trends. However, when co-expressing BiP, all other LCs pulled down small amounts of BiP, too. Quantification showed the increased BiP binding of Pat-2 and Pat-3 compared to their corresponding germline LCs (Figure 46B). The difference between Pat-3 and WT-3 was a multiple of Pat-2 compared to WT-2. Comparing Pat-1 to WT-1 revealed no visible differences in BiP binding, as it did not for secretion levels.

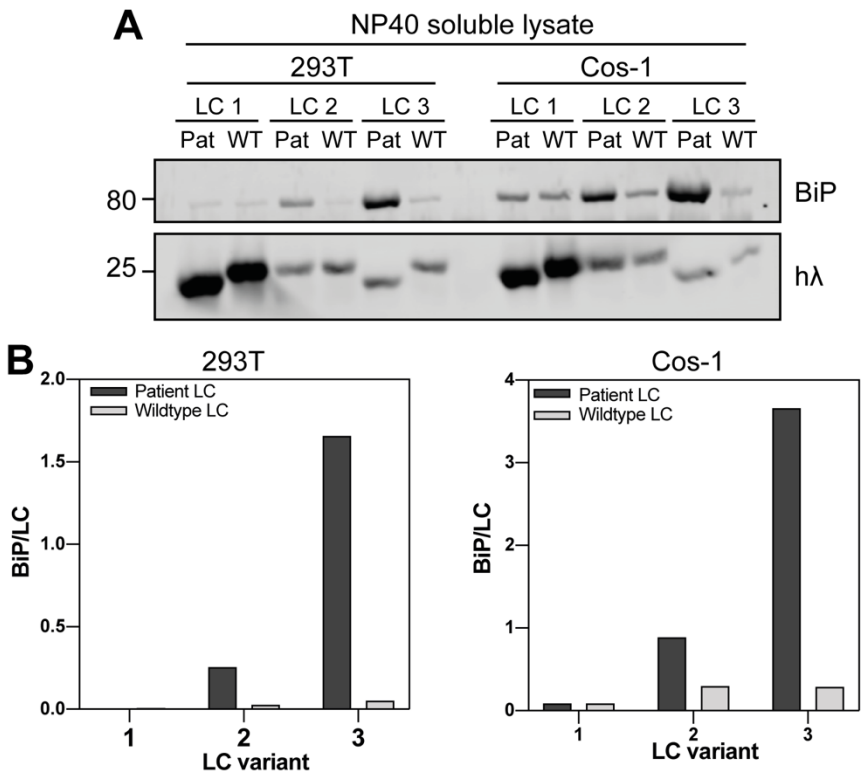

Figure 46. Binding of BiP to LC variants. A) Western blot of 293T and Cos-1 NP40 soluble lysate after immunoprecipitation with anti-human λ antibody. Cells were lysed 24 h after co-transfection of LC variants and BiP. The PVDF membrane was cut, the upper part blotted against BiP and the lower part against human λ. B) BiP/LC ratios were calculated by quantification of BiP and LC bands.

6.1.4. Dimerization of LCs

Since Pat-1-3 showed the most striking differences between each other but also between patient and germline LCs, these three pairs were used for further analysis. The LCs showed similar behavior in Cos-1 and 293T. Due to the easier handling, all further experiments were only performed in Cos-1 cells.

One possible explanation for the BiP binding and the impaired secretion could be the inability of the LCs to form dimers. In their monomeric form, LCs possess a free cysteine residue at the

C-terminal end of the C_L domain. Free cysteines, like exposed hydrophobic surfaces, are features of un- or misfolded proteins and serve as a recognition site for ER chaperones and ER quality control (Araki and Nagata, 2012). To determine the formation of monomers and covalently bound dimers, SDS-PAGE and Western blotting was performed under non-reducing conditions (Figure 47A). Every LC variant except Pat-3 exhibited a dimer band migrating at ~40 kDa. Quantification of monomer and dimer bands from four experiment sets revealed a significant difference of dimers between Pat-2 and WT-2 and between Pat-3 and WT-3, where ~50 % less were formed by the patient LC, respectively. Pat-1 and WT-1 did not feature a significant difference in dimerization. Both LCs were present as dimers to ~50 %. However, comparing the dimer/monomer ratios for each patient and its corresponding germline LC revealed a significant difference for all three pairs, also for Pat-1 and WT-1. In contrast to the other two pairs and against expectations, Pat-1 more preferentially formed dimers than WT-1. Besides the dimerization behavior, the non-reducing gels revealed a migration difference between Pat-1 and WT-1. This will be further analyzed in chapter 6.1.7.

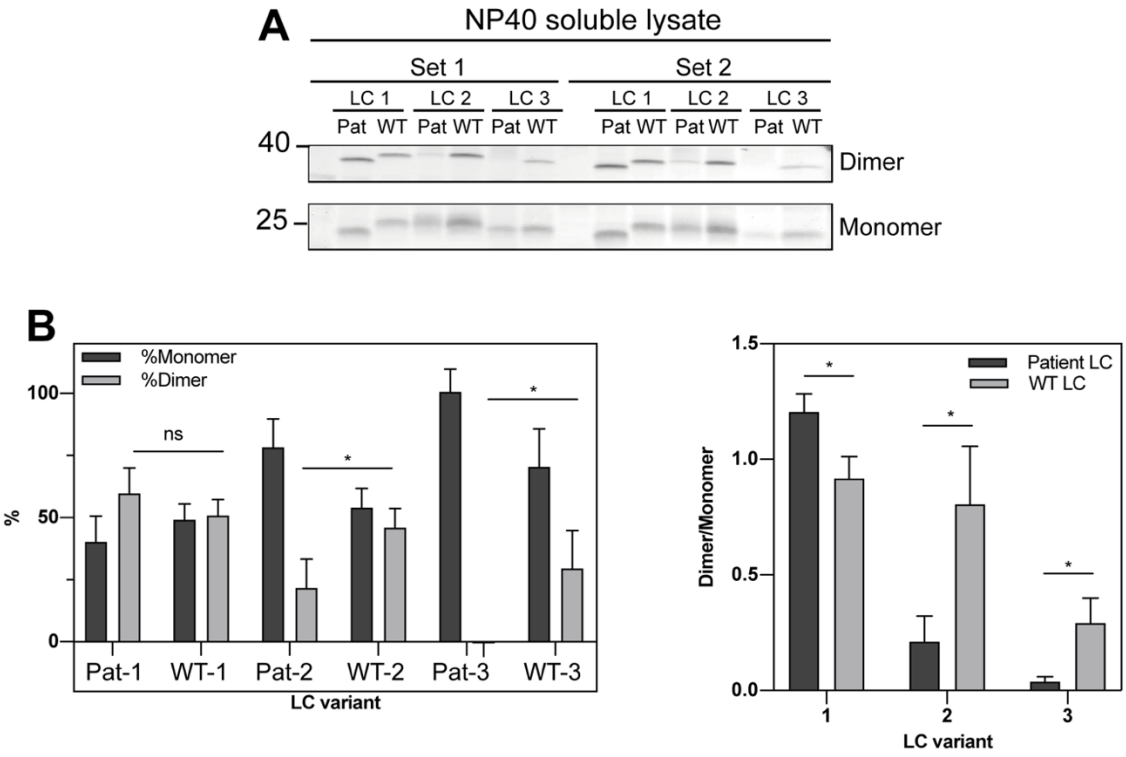

Figure 47. Monomer and dimer formation of LCs in Cos-1 cells. A) Non-reducing SDS-PAGE of NP40 soluble lysate of cells transfected with the specific LCs followed by Western blot against human λ shows LC dimer bands at ~40 kDa and monomer bands at ~25 kDa. B) Band quantification and calculation of the monomer and dimer percentage.

The LC dimerization results in cells fit the secretion impairment, whereby less dimerization entails less secretion and no dimerization leads to no secretion. To investigate this hypothesis, secreted LCs were immunoprecipitated from the media and analyzed under non-reducing conditions. Since BiP binding is thought to cause LC retention in the ER, the experiment was additionally performed with co-transfected BiP. For this reason, the media were immunoprecipitated with anti-human λ antibody and 100 % of the protein was subjected to non-reducing SDS-PAGE with subsequent Western blot with anti-human λ antibody (Figure 48A). The additional band above the respective LC dimer band belongs to the precipitating antibody and was visible for all samples including the control (UT). An additional Western blot was performed under reducing conditions, to confirm that the additional band is the LC of the precipitating antibody. For quantification of the monomer bands, the precipitating antibody band of the untreated sample was subtracted. There was no visible difference between co-transfection of BiP with LCs and only LCs. Against expectations, the percentage of monomer and dimer after secretion did not change significantly compared to the percentage inside the cell, indicating that monomeric LCs can be secreted (Figure 48B). Interestingly, the secreted dimers were visible as a double band that could correspond to different intramolecular disulfide bond formations.

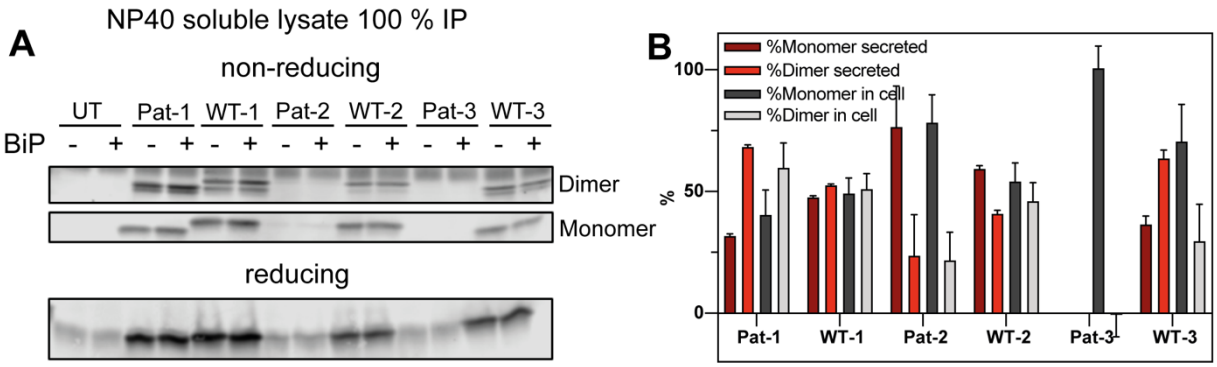

Figure 48. Secretion of monomeric and dimeric LCs from Cos-1 cells. A) Non-reducing SDS-PAGE gel after immunoprecipitation of NP40-soluble lysate of cells transfected with the specific LC alone and co-transfected with BiP. The membrane was blotted against human λ. Reducing conditions served as controls for showing the precipitating antibody. B) Quantification of monomer and dimer bands from the media and comparison with the percentage inside the cells. Dark red and light red bars show secreted monomers and dimers, respectively. Dark grey bars show monomers and light grey bars show dimers formed inside the cell.

6.1.5. AGGREGATION OF LCS IN CELLS

Stability and aggregation are major issues for amyloidogenic LCs and the strong promoter of the pcDNA3.1(+) vector causes high expression and a folding load in the ER for folding. To gain insight in the aggregation behavior of the LCs in cells, NP40 soluble lysate and the insoluble pellet fractions were analyzed and compared by Western blot (Figure 49A). The bands were quantified and the aggregation in the cells was calculated (Figure 49B). Interestingly, the patient LC exhibiting the highest expression level in the cells, Pat-1, showed the lowest aggregation (5 %), indicating that this LC not only escapes ER quality control but is protected against aggregation and thereby degradation before leaving the cell. The aggregation level of Pat-1 was even 2-fold lower than that of its corresponding germline LC WT-1 (10 %). Pat-2 was 3 % and Pat-3 9 % more aggregation prone than their corresponding germline LCs WT-2 and WT-3. With 19 % Pat-2 showed the overall highest aggregation rate but also WT-2 and Pat-3 were aggregating with 16 %. Immunofluorescence (IF) microscopy showed that Pat-1 co-localized homogeneously with the ER marker calnexin throughout the ER network (Figure 49C). Cells transfected with the LCs Pat-2 and WT-2 displayed localized puncta indicating the formation of aggregates inside the ER.

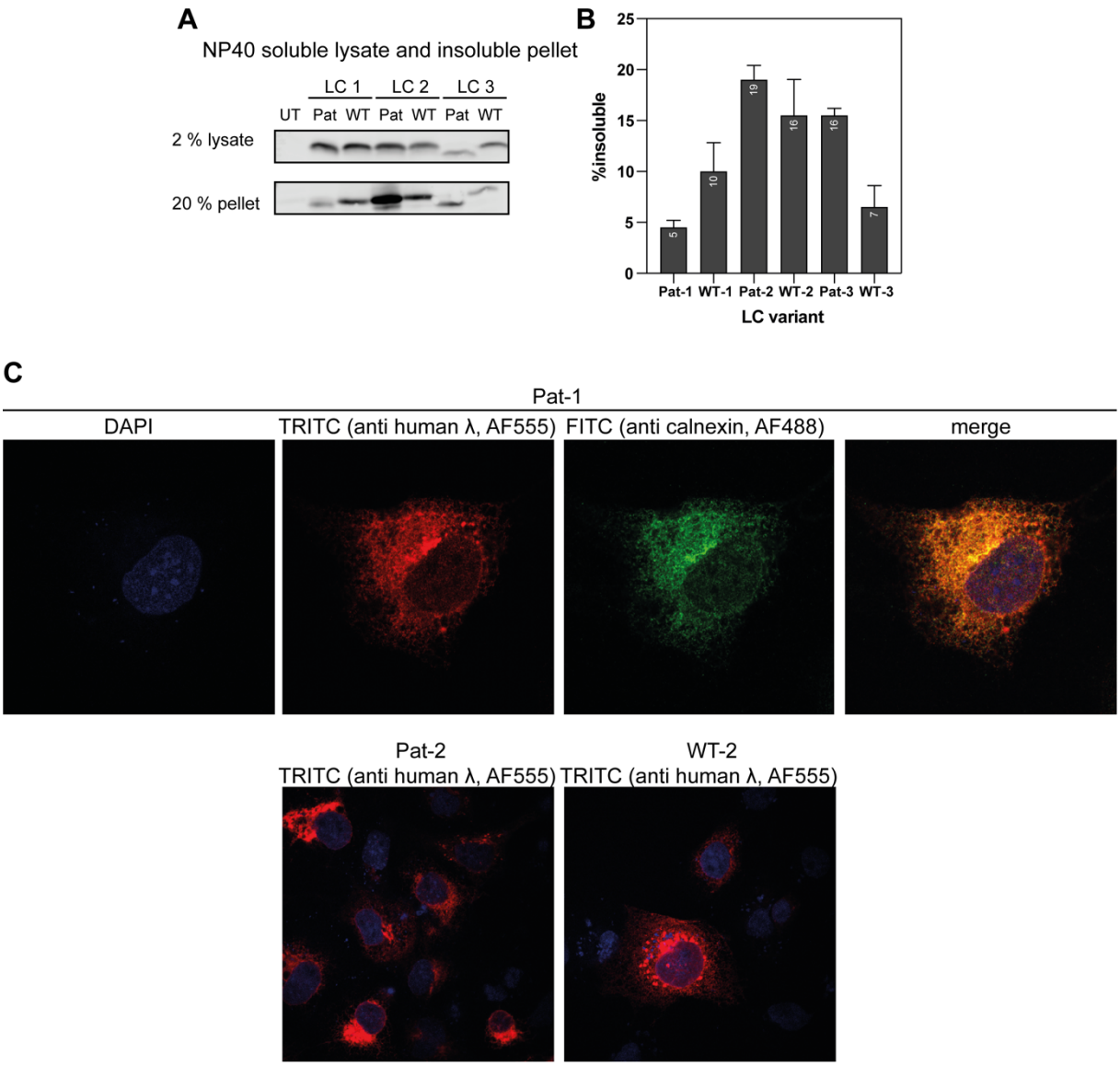

Figure 49. Aggregation of LCs in the cells in Cos-1 cells. A) Western blot of 2 % NP40 soluble lysate and 20 % insoluble pellet with anti-human λ antibodies. B) Quantification of the bands for soluble and insoluble LCs and calculation of the percentage of insoluble LC. The bars represent the mean of two experiments with SD. C) Immunofluorescence microscopy images in Cos-1 cells of Pat-1 on the top with DAPI stain in blue, anti-human λ antibody in red, anti-calnexin antibody in green and the merged picture. In the bottom, microscopy picture show Cos-1 cells with Pat-2 (left) and WT-2 (right) stained with anti-human λ antibody in red.

6.1.6. ERDJ3 KNOCK-OUT STRAIN

In chapter 5.1.5, the ER co-chaperone ERdj3 was identified as a stabilizing factor for Pat-1 during the amyloid formation pathway. Further, it was found to co-deposit with Pat-1 fibrils in abdominal patient tissue and thus potentially plays a role in pathogenicity. To investigate the role of ERdj3 on intracellular LC integrity, Chinese hamster ovary (CHO) and CHO ERdj3 knock-out (CHO j3 KO) cell lines were used to compare LC aggregation in the cell and LC secretion into the media. CHO cell lysates were separated into NP40 soluble lysate and insoluble pellet fractions for LCs 1-3 and analyzed by Western blot against human λ (Figure 50A). As expected from the experiments with Cos-1 cells, most of LCs Pat-1 and WT-1 were found in the soluble fraction. Quantification of the bands and calculation of the percentage of insoluble LCs revealed no difference between CHO WT and CHO j3 KO cells for these two LC variants (Figure 50B). The LCs for Pat-2 and WT-2 both showed strong aggregation bands. While the aggregation did not change between CHO WT and CHO j3 KO cells for WT-2 (~20 % insoluble, both), the percentage of Pat-2 in the insoluble fraction was 5 % higher in CHO WT cells. Besides that, Pat-2 and WT-2 showed similar aggregation behavior. WT-3 remained mostly soluble in both CHO cell lines, while for Pat-3 the same trend as for Pat-2 could be observed: the percentage of insoluble LC was higher in CHO WT cells (~20 %) than in CHO j3 KO cells (~10 %).

For LC secretion analyses, 30 % of the respective media were subjected to immunoprecipitation with anti-human λ antibody and subsequent Western blot with the same antibody (Figure 50C). The secretion bands were quantified to compare differences between CHO WT and CHO j3 KO cells. As seen in prior experiments, Pat-2 showed decreased and Pat-3 no secretion in both, CHO WT and CHO j3 KO cells (Figure 50D). The corresponding WT LCs were secreted by both cell lines. Pat-1 and WT-1 showed the highest secretion levels. For all LC variants, the secretion was slightly lower in CHO j3 KO cells than in CHO WT cells. However, this experiment was only performed once and the significance of this decrease in secretion caused by ERdj3 KO was not confirmed further.

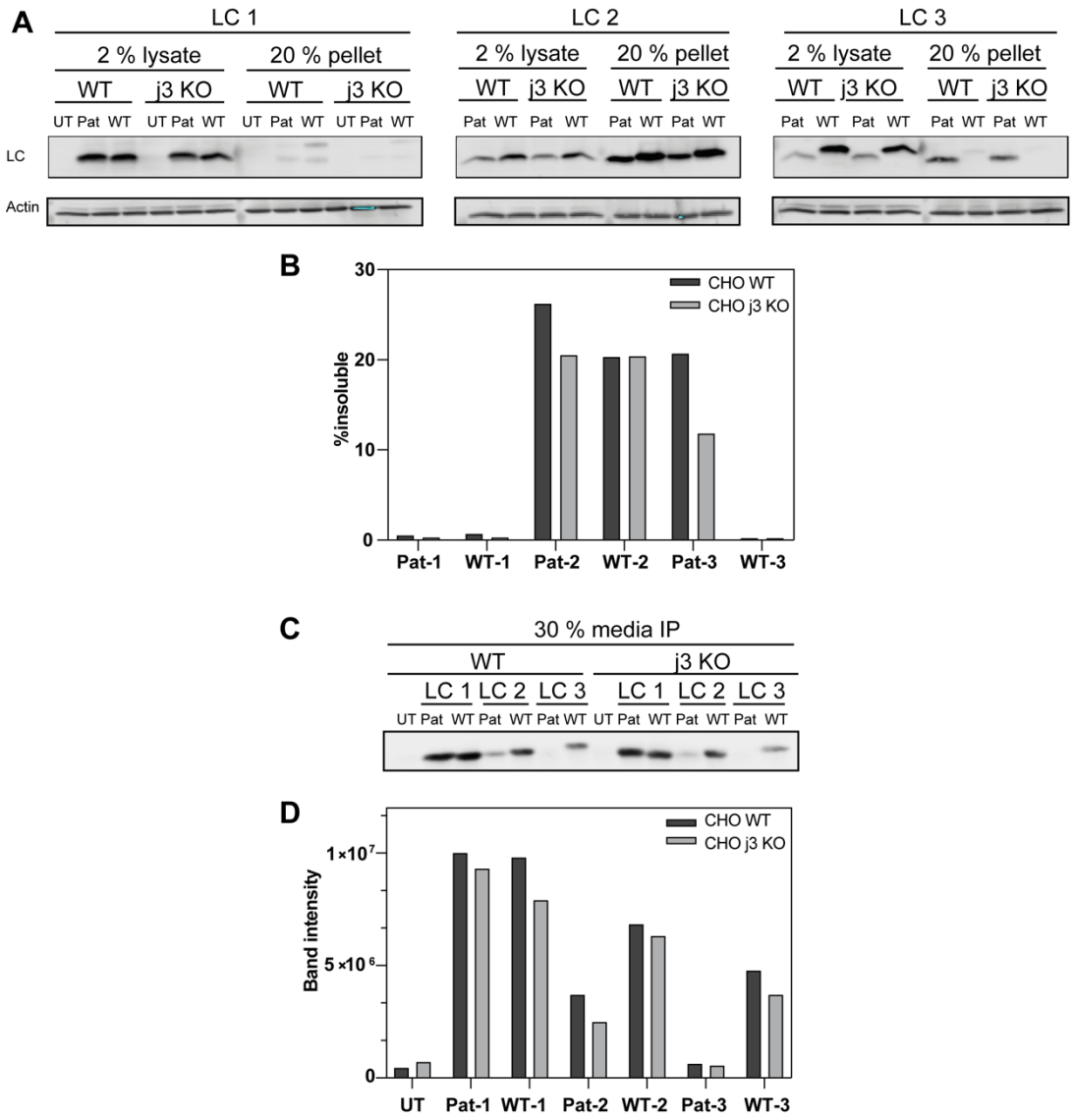

Figure 50. Aggregation and secretion of LCs in CHO WT and CHO j3 KO cells. A) Western blots of NP40 soluble lysates and insoluble pellet fractions of CHO WT and CHO j3 KO cells transfected with the respective LCS. B) Quantification and calculation of the insoluble LC in CHO WT and CHO j3 KO cells. Dark grey bars correspond to insolubility of LCs in CHO WT cells, light grey bars to CHO j3 KO cells. C) Western blot against human λ of the media immunoprecipitation from CHO WT and CHO j3 KO cells. D) Quantification of the secretion bands from the Western blot. Dark grey bars correspond to the band intensity of LCs in CHO WT media, light grey bars to CHO j3 KO media.

6.1.7. LC PAT-3 IS UNABLE TO FORM BOTH INTRAMOLECULAR DISULFIDE-BONDS

Besides the prior analyzed LC behavior regarding aggregation, secretion and dimerization, two conspicuous features concerning the LC migration in SDS-PAGE gels became visible during the experiments. The first is the difference in migration of Pat-1 and WT-1 under non-reducing conditions. Regardless of the monomeric or dimeric state, Pat-1 migrates slightly faster than WT-1. Under reducing conditions, they migrate at the same height (Figure 51A). A step-wise reduction was performed that showed a smeary dissolving of the disulfide bonds for both Pat-1 and WT-1. Pat- 1 possesses 17 negatively and 16 positively charged amino acids and thus a netto charge of -1. WT-1 however has a netto charge of +1 with 15 negatively and 16 positively charged residues. The change of migration could potentially be assigned to the difference slightly more negative charge of Pat-1, that is more representative in a tighter domain packing due to the intact disulfide bond under non-reducing conditions.

The other peculiarity was the difference in migration between Pat-3 and WT-3 under reducing conditions, while migrating on the same height under non-reducing conditions. Performing a step by step reduction of the intramolecular disulfide bonds by progressively reducing the amount of β-Mercaptoethanol in the sample buffer, revealed that Pat-3 lacks one disulfide bond, as the stepwise reduction only showed two bands of Pat-3 (Figure 51C). WT-3 however showed three clear bands indicating the presence of three different states of the LC: two, one and no disulfide bond. These results and the fact that mostly V_L domains are responsible for amyloid deposition, lead to the conclusion that the V_L domain of Pat-3 is unable to form the native disulfide bond. However, this does not explain the difference in migration of the fully reduced Pat-1 and WT-1 samples. For completeness, the stepwise reduction was also performed for Pat-2 and resulted in three resolved bands for the three oxidation states of the LC (Figure 51B).

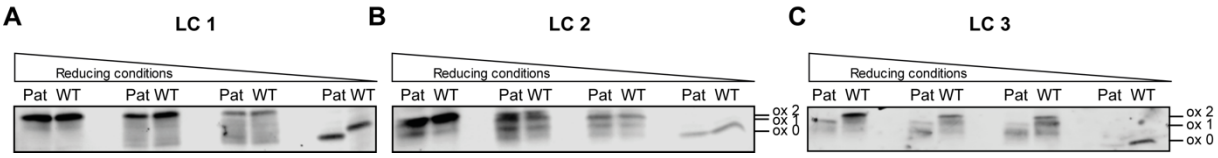

Figure 51. Stepwise reduction of LCs 1-3 dissolves the oxidative states for A) LC 1, B) LC 2 and C) LC 3. For decreasing the reducing conditions, 5x Laemmli buffer containing β-Mercaptoethanol was mixed 1:10 with non-reducing 5x Laemmli buffer and concentrations were continuously reduced 1:1 with non-reducing buffer. The ox2 band corresponds to the LC with two intramolecular disulfide bonds, ox1 state has one disulfide bond and ox0 none.

6.2. DISCUSSION

AL amyloidosis is characterized by a multiorgan deposition of amyloid fibrils that derive from free LCs (FLCs) (Gertz, 2016). Among patients, the levels of circulating FLCs are often increased (Witteles and Liedtke, 2019). Noteworthy, free monoclonal LCs are not only a feature of AL amyloidosis patients but are also common in urine and serum of mostly older humans and don't necessarily result in the formation of fibrils (Blancas-Mejía and Ramirez-Alvarado, 2013). These FLCs are called Bence-Jones proteins and can be found in the urine of patients affected with malignancy of B lymphocytes. They are often secreted either as covalent or non-covalent homodimers that mask the hydrophobic surfaces on each domain (Reddy et al., 1996; Ribatti, 2018). In AL amyloidosis, changes in thermodynamic stability and mutations are the basis for amyloid formation, independent of monomer or dimer formation of FLCs (Ramirez-Alvarado, 2012). Both forms can be found for this disease. However, the ERQC machinery controls the formation of disulfide bonds within the cell and the dimerization prior to secretion might be an exit strategy of FLCs. In the cell culture experiments performed here, the patient-derived LCs showed significantly different dimerization and secretion behavior. In addition to the fact that monomers and dimers were both present (except for Pat-3), both species were also found to be secreted. Interestingly, Pat-1, that showed the highest secretion as well as dimerization propensity, also comprised the highest FLC level in the patient's serum. Pat-3 that had the lowest FLC level in the patient serum, did not dimerize but also did not show any secretion. Pat-2 was a cross between Pat-1 and Pat-3. In comparison with the corresponding germlines, the trend also followed from WT-1 that was secreted and formed dimers comparable to Pat-1, over WT-2 that differed from Pat-2 by dimerizing and secreting more, to WT-3, that behaved completely different from Pat-3 by being secreted and forming dimers. Consequently, the specific formation of dimers or monomers is not a prerequisite for disease development but it probably influences severity, as secretion propensity was in line with dimerization propensity.

Consistent with impaired secretion and decreased dimer formation, the LCs Pat-2 and Pat-3 bound to BiP in the ER. This indicates that ERQC recognizes these two LCs as defective (Araki and Nagata, 2012). Interestingly, Pat-1 that was highly secretion-competent prone did not show BiP binding. This might explain the high secretion level in the experiments, as well as in the patient serum and consequently the disease severity that goes along with the FLC level in patient's serum (Bochtler et al., 2008). It is not clear which feature of Pat-2 and Pat-3 marks the LCs for BiP recognition, since also Pat-1 and the WT LCs partially form monomers and do not result in any long-term BiP binding. For Pat-3, *in vitro* experiments investigating the recombinant V_L domain of Pat-3 revealed the inability of this domain to fold correctly into the Ig fold, which is likely the reason for recognition by ERQC and ER detention (Feige et al., 2010). This LC yielded striking results and the integrity of WT-3 compared to Pat-3 affirms the

importance of few differences in the primary sequence on the structure of LCs, despite the overall high variability. The folding deficiency of Pat-3 was confirmed by performing a step-wise reduction of the disulfide bonds. For Pat-3, the results showed only two oxidized forms: one disulfide bond and no disulfide bond, whereas for all other investigated LCs, three oxidized states could be observed. The migration difference between patient LC 3 and corresponding germline could indicate an early interference of the ERQC.

The ability of Pat-1 to maintain integrity in the presence in high concentrations, could also be shown by the analysis of intracellular LC aggregation. Here, Pat-1 even resulted in less aggregation than all germline LCs. This could be an explanation for the high disease severity in this patient, since this LC shows excellent performance in the ER and Golgi which leads to very high amounts of initially intact LCs that can spread their pathogenic potential upon extracellular cleavage (Kazman et al., 2020; Weber et al., 2018). The successful secretion and ERQC escape of disease-causing proteins that comprise a native-like fold was also observed previously for transthyretin mutants (Sörgjerd et al., 2006).

The involvement of the ER resident co-chaperone ERdj3 was discussed in the previous chapters. The analysis of LCs in respective WT and ERdj3 knock-out cell strains did not reveal any conspicuities for any of the LCs regarding their aggregation propensity. However, these experiments have to be expanded in the future to obtain insights in i.e. a difference of secretion or co-secretion behavior in these cell lines and the influence of other J proteins or other differences upon ERdj3 deletion.

In summary, the three disease-causing LCs investigated, together with their corresponding germline LCs, all showed different behavior in terms of expression, secretion, dimerization and aggregation. However, these LCs also showed different FLC levels in the patient's serum, varying affected organ patterns and disease severities. The cell culture studies described were the first experiments directed towards the start instead of the endpoint of the disease. They display the potential of prospective experiments with a specific choice of LCs. In the future this can lead to the exploration of different patterns of disease initiation and potential early stage contact points for the identification of therapeutic targets.

7. CONCLUSION AND PERSPECTIVES

This thesis provides investigations on molecular determinants and mechanisms of antibody light chains in the context of the disease AL amyloidosis. Disease-causing mutations were discovered and the mechanism effects leading to amyloid fibril deposition in patients were deciphered.

In the first part of the study the amyloid forming LC truncation, Pat-1, was determined and used for investigations towards identification of the primary sequence change leading to pathogenicity. A valine at position 81 was found to be decisive for domain stability. Further, changes in domain stability was found to go along with fibril formation propensity. The V81L back mutation leads to a change of hydrophobic surface area in Pat-1 and an increase of hydrophobic interactions to the C-terminal region. The additional interactions stabilize the C-terminal segment of the LC truncation preventing it from high conformational dynamics and thus from fibril formation. Further, it was found that the pathogenic mutations only become effective upon proteolytic cleavage and removal of the C_L domain. However, the mutations already lead to a more accessible linker region and thus a higher susceptibility for cleavage. Further investigations are needed to determine if this molecular mechanism can be transferred to other patient-derived LC truncations and possibly also to other amyloid forming proteins.

The studied V_L domain of Pat-1 was used for identification of factors influencing fibril formation. The ER chaperone BiP comes into contact with LCs directly upon translation into the ER. It is an important folding factor for antibody domains. The interaction with BiP resulted in a concentration-dependent inhibition of Pat-1 fibril formation. However, BiP is not a likely factor for impacting pathogenicity in the human body, as it is not secretion competent. The co-chaperone ERdj3 however lacks the ER retention motif and was found to be readily secreted upon ER stress. It was found as co-aggregated protein in fibril extracts from patient-derived abdominal fat tissue. Similar to BiP, the ER Hsp40 ERdj3 was found to specifically interact with Pat-1 and inhibit its amyloid formation in a concentration-dependent manner. Further investigations on possible co-secretion of ERdj3 with pathogenic LCs from the ER *in vivo* and the impact of ERdj3 on other LC truncations are needed for more detailed information on the role of the co-chaperone in disease development. Also, immunohistochemical studies on the co-aggregation of ERdj3 are required to identify the scope of involvement.

The plasma factor ApoE4 that is known to act as an extracellular chaperone in other amyloid related diseases like Alzheimer's Disease. In the case of Pat-1, ApoE4 was found to enhance fibril formation if it is added in low concentrations and to decrease fibril formation propensity it if present in high concentrations. The correlation of different alleles of ApoE and AL amyloidosis needs to be investigated to allow the evaluation of ApoE4 as a potential risk factor for the development of amyloid diseases and early diagnosis.

The investigations on the LC truncations of Pat-1 were extended towards the rearrangements taking place in the lag phase preceding fibril formation. Currently, a high cytotoxic effect is attributed to oligomeric intermediates of amyloid-forming proteins and peptides. Thus, the identification and characterization of oligomeric species is important to obtain possibilities for early stage treatments. A specific pattern of oligomers was found for Pat-1, whereby oligomers were always present in lower concentrations than the comparably stable monomers and fibrils. It was found that the assembly to oligomers was a result of destabilization and exposure of hydrophobic residues of Pat-1 monomers. Thus, oligomers served to decrease hydrophobic surfaces and stabilize the highly dynamic C-terminal region of Pat-1. Nevertheless, the high Gibbs free energy of oligomers leads to structural rearrangements affecting secondary structure that leads to Pat-1 stabilization in the form of fibrils. To gain deeper structural insights in the rearrangements and the basics of monomer assembly, further studies with other LCs have to be performed and sophisticated methods like NMR need to be included. The high energy state of oligomers complicates capturing the intermediates at a fixed timepoint due to the short lifetime. Improvements on cross-linking reactions could enable the stabilization of oligomeric species.

The last study in this thesis comprised the investigations of different patient-derived LCs regarding their behavior in living cells. As the ERQC escape is still largely enigmatic and the LCs display sequence variability, the early events differentiating between diseased and healthy LC are important. The analysis of mainly three different pathogenic LCs and their corresponding germlines resulted in three different patterns of LC behavior affecting expression, secretion, dimerization and aggregation. A link to disease severity could be drawn. The analysis of further LCs is necessary to confirm these patterns and allow conclusions based on sequence differences and disease severity or affected organs.

In summary, this work provides new insights into the molecular mechanism of disease development for one LC reaching from the earliest events to the final deposition of amyloid structures. At the same time the studies present a general strategy how to investigate LCs associated with AL amyloidosis. Furthermore, detailed information on potent factors inhibiting or influencing amyloid formation are given. These information can contribute to better and earlier diagnosis and treatment options in the long run.

8. ABBREVIATIONS

AL	antibody light chain
Aβ	Amyloid-beta peptide
ANS	1-anilinonaphtalene-8-sulfonate
APS	Ammonium Persulfate
AUC	Analytical Ultracentrifugation
B-cell	Bone marrow derived lymphocyte
CD	Circular Dichroism
CDR	Complementarity determining region
C_H1	Constant heavy chain domain 1
C_H2	Constant heavy chain domain 2
C_H3	Constant heavy chain domain 3
C_H4	Constant heavy chain domain 4
C_L	Constant light chain
c_M	GdmCl concentration at which 50 % of the protein is unfolded
Cryo-EM	Cryo electron microscopy
DNA	Deoxyribonucleic acid
dNTP	Deoxynucleotide
E. coli	*Escherichia Coli*
EM	Electron microscopy
ER	Endoplasmic reticulum
Fab	Fragment antigen binding
Fc	Fragment crystallizable
FLC	Free light chain
FR	Framework region
FUV	Far ultraviolet
GdmCl	Guanidinium chloride
H/DX	Hydrogen/deuterium exchange
HC	Heavy chain
IB	Inclusion bodies
Ig	Immunoglobulin
IMGT	International ImMunoGeneTics information system
kDa	Kilo dalton
LB_0	Luria-Bertani medium
LC	Light chain

MD	Molecular dynamics
MS	Mass spectrometry
NMR	Nuclear magnetic resonance
OD	Optical density
Pat	Patient-derived LC (truncation)
PBS	Phosphate buffered saline
PCR	Polymerase Chain Reaction
PDB	The Protein Database
RDC	Residual dipolar couplings
RMSD	Root-mean-square deviation
Rpm	Rounds per minute
RT	Room temperature
S	Svedberg
SD	Standard deviation
T_{50}	Timepoint with 50 % maximal ThT signal intensity
TEM	Transmission electron microscopy
ThT	Thioflavin T
T_M	Melting temperature (°C)
US	Umbrella sampling
UV-Vis	Ultraviolet and visible light wavelengths
v/v	Volume per volume
V_H	Variable heavy chain
V_L	Variable light chain
WT	Wild type
w/v	Weight per volume
w/w	Weight per weight

Amino acids, one and three letter codes

Amino acid	Three letter code	One letter code
Alanine	Ala	A
Arginine	Arg	R
Asparagine	Asn	N
Aspartate	Asp	D
Cysteine	Cys	C
Glutamine	Gln	Q
Glutamic acid	Glu	E
Glycine	Gly	G
Histidine	His	H
Isoleucine	Ile	I
Leucine	Leu	L
Lysine	Lys	K
Methionine	Met	M
Phenylalanine	Phe	F
Proline	Pro	P
Serine	Ser	S
Threonine	Thr	T
Tryptophan	Trp	W
Tyrosine	Tyr	Y
Valine	Val	V

9. REFERENCES

Abraham RS, Geyer SM, Price-Troska TL, Allmer C, Kyle RA, Gertz MA, Fonseca R. 2003. Immunoglobulin light chain variable (V) region genes influence clinical presentation and outcome in light chain-associated amyloidosis (AL). *Blood* **101**:3801–3808. doi:10.1182/blood-2002-09-2707

Abraham RS, Geyer SM, Ramírez-Alvarado M, Price-Troska TL, Gertz MA, Fonseca R. 2004. Analysis of somatic hypermutation and antigenic selection in the clonal B cell in immunoglobulin light chain amyloidosis (AL). *J Clin Immunol* **24**:340–353. doi:10.1023/B:JOCI.0000029113.68758.9f

Ajit Tamadaddi C, Sahi C. 2016. J domain independent functions of J proteins. *Cell Stress Chaperones* **21**:563–570. doi:10.1007/s12192-016-0697-1

Anfinsen CB, Haber E, Sela M, White FH. 1961. The kinetics of formation of native ribonuclease during oxidation of the reduced polypeptide chain. *Proc Natl Acad Sci* **47**:1309–1314. doi:10.1073/pnas.47.9.1309

Annamalai K, Gührs K-H, Koehler R, Schmidt M, Michel H, Loos C, Gaffney PM, Sigurdson CJ, Hegenbart U, Schönland S, Fändrich M. 2016. Polymorphism of amyloid fibrils in vivo. *Angew Chem Int Ed Engl* **55**:4822–4825. doi:10.1002/anie. 201511524

Araki K, Nagata K. 2012. Protein folding and quality control in the ER. *Cold Spring Harb Perspect Biol* **4**:1–25. doi:10.1101/cshperspect.a015438

Arosio P, Knowles TPJ, Linse S. 2015. On the lag phase in amyloid fibril formation. *Phys Chem Chem Phys* **17**:7606–7618. doi:10.1039/c4cp05563b

Baden EM, Owen BAL, Peterson FC, Volkman BF, Ramirez-Alvarado M, Thompson JR. 2008a. Altered dimer interface decreases stability in an amyloidogenic protein. *J Biol Chem* **283**:15853–15860. doi:10.1074/jbc.M705347200

Baden EM, Randles EG, Aboagye AK, Thompson JR, Ramirez-Alvarado M. 2008b. Structural insights into the role of mutations in amyloidogenesis. *J Biol Chem* **283**:30950–30956. doi:10.1074/jbc.M804822200

Bail Y, Englander W. 1996. Future directions in Folding: The Multi-State Nature of Protein Structure. *Proteins* **24**:145–151. doi:10.1002/(SICI)1097-0134(199602)24:2

Baldwin AJ, Knowles TPJ, Tartaglia GG, Fitzpatrick AW, Devlin GL, Shammas SL, Waudby CA, Mossuto MF, Meehan S, Gras SL, Christodoulou J, Anthony-Cahill SJ, Barker PD, Vendruscolo M, Dobson CM. 2011. Metastability of native proteins and the phenomenon of amyloid formation. *J Am Chem Soc* **133**:14160–14163. doi:10.1021/ja2017703

Bartlett AI, Radford SE. 2009. An expanding arsenal of experimental methods yields an explosion of insights into protein folding mechanisms. *Nat Struct Mol Biol* **16**:582–588. doi:10.1038/nsmb.1592

Baumal R, Potter M, Scharff MD. 1971. Synthesis, Assembly, and Secretion of Gamma

Globulin By Mouse Myeloma Cells. *J Exp Med* **134**:1316–1334. doi:10.1084/jem.134.5.1316

Bellotti V, Mangione P, Merlini G. 2000. Review: Immunoglobulin light chain amyloidosis - The archetype of structural and pathogenic variability. *J Struct Biol* **130**:280–289. doi:10.1006/jsbi.2000.4248

Bennhold H. 1922. Specific staining of amyloid by Congo red (in German). *Muenchner Medizinische Wochenschrift* **69**:1537–1538.

Berg JM, Tymoczko JL, Stryer L. 2011. Biochemistry: International edition, 7th editio. ed.

Bergman LW, Kuehl WM. 1978. Temporal Relationship of Translation and Glycosylation of Immunoglobulin Heavy and Light Chains. *Biochemistry* **17**:5174–5180. doi:10.1021/bi00617a017

Bernard O, Hozumi N, Tonegawa S. 1978. Sequences of Mouse Immunoglobulin Light Chain Genes before and after Somatic Changes. *Cell* **15**:1133–1144. doi:10.1016/0092-8674(78)90041-7

Bertolotti A, Zhang Y, Hendershot LM, Harding HP, Ron D. 2000. Dynamic interaction of BiP and ER stress transducers in the unfolded-protein response. *Nat Cell Biol* **2**:326–332. doi:10.1038/35014014

Bieschke J, Herbst M, Wiglenda T, Friedrich RP, Boeddrich A, Schiele F, Kleckers D, Lopez Del Amo JM, Grüning BA, Wang Q, Schmidt MR, Lurz R, Anwyl R, Schnoegl S, Fändrich M, Frank RF, Reif B, Günther S, Walsh DM, Wanker EE. 2012. Small-molecule conversion of toxic oligomers to nontoxic β-sheetg-rich amyloid fibrils. *Nat Chem Biol* **8**:93–101. doi:10.1038/nchembio.719

Blancas-Mejía LM, Horn TJ, Marin-Argany M, Auton M, Tischer A, Ramirez-Alvarado M. 2015. Thermodynamic and fibril formation studies of full length immunoglobulin light chain AL-09 and its germline protein using scan rate dependent thermal unfolding. *Biophys Chem* **207**:13–20. doi:doi: 10.1016/j.bpc.2015.07.005

Blancas-Mejía LM, Ramirez-Alvarado M. 2013. Systemic Amyloidoses. *Annu Rev Biochem* **82**:745–774. doi:10.1146/annurev-biochem-072611-130030

Bochtler T, Hegenbart U, Heiss C, Benner A, Cremer F, Volkmann M, Ludwig J, Perz JB, Ho AD, Goldschmidt H, Schönland SO. 2008. Evaluation Of The Serum-Free Light Chain Test In Untreated Patients With AL Amyloidosis. *Haematologica* **93**:459–462. doi:10.3324/haematol.11687

Bork P, Holm L, Sander C. 1994. The Immunoglobulin Fold. *J Mol Biol*. doi:10.1006/jmbi.1994.1582

Braakman I, Hebert DN. 2013. Protein folding in the endoplasmic reticulum. *Cold Spring Harb Perspect Biol* **5**. doi:10.1101/cshperspect.a013201

Brenner DA, Jain M, Pimentel DR, Wang B, Connors LH, Skinner M, Apstein CS, Liao R.

2004. Human Amyloidogenic Light Chains Directly Impair Cardiomyocyte Function Through an Increase in Cellular Oxidant Stress. *Circ Res* **94**:1008–1010. doi:10.1161/01.RES.0000126569.75419.74

Brown PH, Schuck P. 2006. Macromolecular Size-and-Shape Distributions by Sedimentation Velocity Analytical Ultracentrifugation. *Biophys J* **90**:4651–4661. doi:10.1529/biophysj.106.081372

Brumshtein B, Esswein SR, Landau M, Ryan CM, Whitelegge JP, Phillips ML, Cascio D, Sawaya MR, Eisenberg DS. 2014. Formation of amyloid fibers by monomeric light chain variable domains. *J Biol Chem* **289**:27513–27525. doi:10.1074/jbc.M114.585638

Bryngelson JD, Onuchic JN, Socci ND, Wolynes PG. 1995. Funnels, pathways, and the energy landscape of protein folding: A synthesis. *Proteins Struct Funct Bioinforma* **21**:167–195. doi:10.1002/prot.340210302

Buchner J. 1996. Supervising the fold: functional principles of molecular chaperones. *FASEB J* **10**:10–19.

Buck TM, Wright CM, Brodsky JL. 2007. The Activities and Function of Molecular Chaperones in the Endoplasmic Reticulum. *Semin Cell Dev Biol* **18**:751–761. doi:10.1016/j.semcdb.2007.09.001

Buell AK, Dhulesia A, White DA, Knowles TPJ, Dobson CM, Welland ME. 2012. Detailed analysis of the energy barriers for amyloid fibril growth. *Angew Chemie - Int Ed* **51**:5247–5251. doi:10.1002/anie.201108040

Bulleid NJ. 2012. Disulfide bond formation in the mammalian endoplasmic reticulum. *Cold Spring Harb Perspect Biol* **4**. doi:10.1101/cshperspect.a013219

Buxbaum J. 1986. Aberrant Immunoglobulin Synthesis in Light Chain Amyloidosis. *J Clin Investig Inc* **78**:798–806.

Camilloni C, Bonetti D, Morrone A, Giri R, Dobson CM, Brunori M, Gianni S, Vendruscolo M. 2016. Towards a structural biology of the hydrophobic effect in protein folding. *Sci Rep* **6**:1–9. doi:10.1038/srep28285

Chatani E, Yamamoto N. 2018. Recent progress on understanding the mechanisms of amyloid nucleation. *Biophys Rev* **10**:527–534. doi:10.1007/s12551-017-0353-8

Cheetham ME, Caplan AJ. 1998. Structure, function and evolution of DnaJ: Conservation and adaptation of chaperone function. *Cell Stress Chaperones* **3**:28–36. doi:10.1379/1466-1268(1998)003<0028:SFAEOD>2.3.CO;2

Chen K, Qu S, Chowdhury S, Noxon IC, Schonhoft JD, Plate L, Powers ET, Kelly JW, Lander GC, Wiseman RL. 2017. The endoplasmic reticulum HSP 40 co-chaperone ER dj3/ DNAJB 11 assembles and functions as a tetramer . *EMBO J* **36**:2296–2309. doi:10.15252/embj.201695616

Chen VB, Arendall WB, Headd JJ, Keedy DA, Immormino RM, Kapral GJ, Murray LW,

Richardson JS, Richardson DC. 2010. MolProbity: All-atom structure validation for macromolecular crystallography. *Acta Crystallogr Sect D Biol Crystallogr* **66**:12–21. doi:10.1107/S0907444909042073

Chimon S, Shaibat MA, Jones CR, Calero DC, Aizezi B, Ishii Y. 2007. Evidence of fibril-like β-sheet structures in a neurotoxic amyloid intermediate of Alzheimer's β-amyloid. *Nat Struct Mol Biol* **14**:1157–1164. doi:10.1038/nsmb1345

Chiti F, Dobson CM. 2017. Protein Misfolding, Amyloid Formation, and Human Disease: A Summary of Progress Over the Last Decade. *Annu Rev Biochem* **86**:27–68. doi:10.1146/annurev-biochem-061516-045115

Clothia C, Joney EY. 1997. THE MOLECULAR STRUCTURE OF CELL ADHESION MOLECULES. *Annu Rev Biochem* **66**:823–62. doi:10.1146/annurev.biochem.66.1.823

Connors LH, Jiang Y, Budnik M, Théberge R, Prokaeva T, Bodi KL, Seldin DC, Costello CE, Skinner M. 2007. Heterogeneity in Primary Structure, Post-Translational Modifications, and Germline Gene Usage of Nine Full-Length Amyloidogenic κ1 Immunoglobulin Light Chains. *Biochemistry* **46**:14259–14271. doi:10.1021/bi7013773

Cordeiro Y, Kraineva J, Suarez MC, Tempesta AG, Kelly JW, Silva JL, Winter R, Foguel D. 2006. Fourier transform infrared spectroscopy provides a fingerprint for the tetramer and for the aggregates of transthyretin. *Biophys J* **91**:957–967. doi:10.1529/biophysj.106.085928

Cox JS, Shamu CE, Walter P. 1993. Transcriptional induction of genes encoding endoplasmic reticulum resident proteins requires a transmembrane protein kinase. *Cell* **73**:1197–1206. doi:10.1016/0092-8674(93)90648-A

Crespo R, Rocha FA, Damas AM, Martins PM. 2012. A generic crystallization-like model that describes the kinetics of amyloid fibril formation. *J Biol Chem* **287**:30585–30594. doi:10.1074/jbc.M112.375345

D.A. Case, D.S. Cerutti, T.E. Cheatham, III, T.A. Darden, R.E. Duke, T.J. Giese, H. Gohlke, A.W. Goetz, D. Greene, N. Homeyer, S. Izadi, A. Kovalenko, T.S. Lee, S. LeGrand, P. Li, C. Lin, J. Liu, T. Luchko, R. Luo, D. Mermelstein, K.M. Merz, G. Monard, H. G, Monard H, Nguyen I, Omelyan A, Onufriev F, Pan R, Qi DR, Roe A, Roitberg C, Sagui CL, Simmerling WM, Botello-Smith J, Swails RC, Walker J, Wang RM, Wolf X, Wu L, Xiao DM, Kollman Y and PA. 2016. Amber 2016. *Univ California, San Fr*.

Desport E, Bridoux F, Sirac C, Delbes S, Bender S, Fernandez B, Quellard N, Lacombe C, Goujon JM, Lavergne D, Abraham J, Touchard G, Fermand JP, Jaccard A. 2012. AL Amyloidosis. *Orphanet J Rare Dis* **7**:1–13. doi:10.1186/1750-1172-7-54

Dispenzieri A, Gertz MA, Kyle RA, Lacy MQ, Burritt MF, Therneau TM, McConnell JP, Litzow MR, Gastineau DA, Tefferi A, Inwards DJ, Micallef IN, Ansell SM, Porrata LF, Elliott MA, Hogan WJ, Rajkumar SV, Fonseca R, Greipp PR, Witzig TE, Lust JA, Zeldenrust SR,

Snow DS, Hayman SR, McGregor CGA, Jaffe AS. 2004. Prognostication of survival using cardiac troponins and N-terminal pro-brain natriuretic peptide in patients with primary systemic amyloidosis undergoing peripheral blood stem cell transplantation. *Blood* **104**:1881–1887. doi:10.1182/blood-2004-01-0390

Dobson CM. 2003. Protein folding and misfolding. *Nature* **426**:884–890.

Eanes ED, Glenner GG. 1968. X-Ray diffraction studies on amyloid filaments. *J Histochem Cytochem* **16**:673–7. doi:10.1177/16.11.673

Eisenhaber F, Argos P. 1996. Hydrophobic regions on protein surfaces : definition based on hydration shell structure and a quick method for their computation. *Protein Eng* **9**:1121–1133. doi:10.1093/protein/9.12.1121

Ellgaard L, Helenius A. 2003. Quality control in the endoplasmic reticulum. *Nat Rev Mol Cell Biol* **4**:181–191. doi:10.1038/nrm1052

Emsley P, Lohkamp B, Scott WG, Cowtan K. 2010. Features and development of Coot. *Acta Crystallogr Sect D Biol Crystallogr* **66**:486–501.

Fairbanks G, Steck TL, Wallach DFH. 1971. Electrophoretic analysis of the major polypeptides of the human erythrocyte membrane. *Biochemistry* **10**:2606–2617. doi:10.1021/bi00789a030

Fändrich M. 2012. Oligomeric intermediates in amyloid formation: Structure determination and mechanisms of toxicity. *J Mol Biol* **421**:427–440. doi:10.1016/j.jmb.2012.01.006

Fändrich M, Dobson CM. 2002. The behaviour of polyamino acids reveals an inverse side chain effect in amyloid structure formation. *EMBO J* **21**:5682–5690.

Farias M, Gorman MW, Savage M V., Feigl EO. 2005. Plasma ATP during exercise: Possible role in regulation of coronary blood flow. *Am J Physiol - Hear Circ Physiol* **288**:1586–1590. doi:10.1152/ajpheart.00983.2004

Feige MJ, Groscurth S, Marcinowski M, Shimizu Y, Kessler H, Hendershot LM, Buchner J. 2009. An unfolded CH1 domain controls the assembly and secretion of IgG antibodies. *Mol Cell* **34**:569–579. doi:10.1016/j.molcel.2009.04.028

Feige MJ, Hendershot LM, Buchner J. 2010. How antibodies fold. *Trends Biochem Sci* **35**:189–198. doi:10.1016/j.tibs.2009.11.005

Flynn GC, Pohl J, Floccot MT, Rothman JE. 1991. Peptide-binding specificity of the molecular chaperone BiP. *Nature* **353**:726–730. doi:10.1038/353726a0

Furumoto H, Shimizu T, Asagami C, Muto M, Takahashi M, Hoshii Y, Ishihara T, Nakamura K. 1998. Apolipoprotein E is present in primary localized cutaneous amyloidosis. *J Invest Dermatol* **111**:417–421. doi:10.1046/j.1523-1747.1998.00294.x

Gaut JR, Hendershot LM. 1993. Mutations within the nucleotide binding site of immunoglobulin-binding protein inhibit ATPase activity and interfere with release of immunoglobulin heavy chain. *J Biol Chem* **268**:7248–7255.

Geddes AJ, Parker KD, Atkins EDT, Beighton E. 1968. “Cross-β” conformation in proteins. *J Mol Biol* **32**:343–358. doi:10.1016/0022-2836(68)90014-4

Gellermann GP, Appel TR, Tannert A, Radestock A, Hortschansky P, Schroeckh V, Leisner C, Lütkepohl T, Shtrasburg S, Röcken C, Pras M, Linke RP, Diekmann S, Fändrich M. 2005. Raft lipids as common components of human extracellular amyloid fibrils. *Proc Natl Acad Sci U S A* **102**:6297–6302. doi:10.1073/pnas.0407035102

Genereux JC, Qu S, Zhou M, Ryno LM, Wang S, Shoulders MD, Kaufman RJ, Lasmézas CI, Kelly JW, Wiseman RL. 2015. Unfolded protein response-induced ER dj3 secretion links ER stress to extracellular proteostasis . *EMBO J* **34**:4–19. doi:10.15252/embj.201488896

Gertz MA. 2016. Immunoglobulin light chain amyloidosis: 2016 update on diagnosis, prognosis, and treatment. *Am J Hematol* **91**:947–956. doi:10.1002/ajh.24433

Gertz MA, Lacy MQ, Dispenzieri A. 2002. Immunoglobulin light chain amyloidosis and the kidney. *Kidney Int* **61**:1–9. doi:10.1046/j.1523-1755.2002.00085.x

Glenner GG, Harbaugh J, Ohms JI, Harada M, Cuatrecasas P. 1970. An Amyloid Protein: The Amino-Terminal Variable Fragment Of An Immunoglobulin Light Chain. *Biochem Biophys Res Commun* **41**:1287–1289. doi:10.1016/0006-291X(70)90227-5

Goto Y, Hamaguchi K. 1979. Light Role of the Intrachain of the Constant Disulfide Fragment Bond in the Conformation and Stability of the Immunoglobulin by measuring Intact CL was more resistant than reduced CL to guanidine In a previous paper (1) we reported on the refolding of B. *J Biochem* **86**:1433–1441. doi:10.1093/oxfordjournals.jbchem.a132661

Guo JT, Wetzel R, Xu Y. 2004. Molecular modeling of the core of Aβ amyloid fibrils. *Proteins Struct Funct Genet* **57**:357–364. doi:10.1002/prot.20222

Hamazaki H. 1995. Amyloid P Component Promotes Aggregation of Alzheimer's β-Amyloid Peptide. *Biochem Biophys Res Commun*. doi:10.1006/bbrc.1995.1819

Hao G, Wesolowski JS, Jiang X, Lauder S, Sood VD. 2015. Epitope characterization of an anti-PD-L1 antibody using orthogonal approaches. *J Mol Recognit* **28**:269–276.

Harper JD, Lansbury PT. 1997. MODELS OF AMYLOID SEEDING IN ALZHEIMER'S DISEASE AND SCRAPIE:Mechanistic Truths and Physiological Consequences of the Time-Dependent Solubility of Amyloid Proteins. *Annu Rev Biochem* **66**:385–407. doi:10.1146/annurev.biochem.66.1.385

Hartl FU. 2017. Protein misfolding diseases. *Annu Rev Biochem* **86**. doi:10.1146/annurev-biochem- 061516- 044518

Hartl FU, Bracher A, Hayer-Hartl M. 2011. Molecular chaperones in protein folding and proteostasis. *Nature* **475**:324–332. doi:10.1038/nature10317

Hartl FU, Hayer-Hartl M. 2009. Converging concepts of protein folding in vitro and in vivo.

Nat Struct Mol Biol **16**:574–581. doi:10.1038/nsmb.1591

Hashimoto T, Serrano-Pozo A, Hori Y, Adams KW, Takeda S, Banerji AO, Mitani A, Joyner D, Thyssen DH, Bacskai BJ, Frosch MP, Spires-Jones TL, Finn MB, Holtzman DM, Hyman BT. 2012. Apolipoprotein e, especially apolipoprotein E4, increases the oligomerization of amyloid β peptide. *J Neurosci* **32**:15181–15192. doi:10.1523/JNEUROSCI.1542-12.2012

Holden HM, Ito M, Hartshorne DJ, Rayment I. 1992. X-ray structure determination of telokin, the C-terminal domain of myosin light chain kinase, at 2.8 Å resolution. *J Mol Biol* **227**:840–851. doi:10.1016/0022-2836(92)90226-A

Hopkins CW, Le Grand S, Walker RC, Roitberg AE. 2015. Long-Time-Step Molecular Dynamics through Hydrogen Mass Repartitioning. *J Chem Theory Comput* **11**:1864–1874. doi:10.1021/ct5010406

Hora M, Sarkar R, Morris V, Xue K, Prade E, Harding E, Buchner J, Reif B. 2017. MAK33 antibody light chain amyloid fibrils are similar to oligomeric precursors. *PLoS One* **12**:1–14. doi:10.1371/journal.pone.0181799

Horowitz PM, Criscimagna NL. 1985. Differential Binding of the Fluorescent Probe 8-Anilinonaphthalene-2-sulfonic Acid to Rhodanese Catalytic Intermediates. *Biochemistry* **24**:2587–2593. doi:10.1021/bi00332a001

Howie AJ. 2019. Origins of a pervasive, erroneous idea: The “green birefringence” of Congo red-stained amyloid. *Int J Exp Pathol* **100**:208–221. doi:10.1111/iep.12330

Hozumi N, Tonegawa S. 1976. Evidence for somatic rearrangement of immunoglobulin genes coding for variable and constant regions. *Proc Natl Acad Sci USA* **73**:3628–3632. doi:10.1073/pnas.73.10.3628

Huang Y, Mahley RW. 2014. Apolipoprotein E: Structure and Function in Lipid Metabolism, Neurobiology, and Alzheimer’s Diseases. *Neurobiol DIs* **72PA**:3–12. doi:10.1016/j.nbd.2014.08.025

Huber R, Deisenhofer J, Colman PM, Matsushima M, Palm W. 1976. Crystallographic structure studies of an IgG molecule and an Fc fragment. *Nature* **264**:415–420. doi:10.1038/264415a0

Hughes SR, Khorkova O, Goyal S, Knaeblein J, Heroux J, Riedel NG, Sahasrabudhe S. 1998. A2-Macroglobulin Associates With B-Amyloid Peptide and Prevents Fibril Formation. *Proc Natl Acad Sci U S A* **95**:3275–3280. doi:10.1073/pnas.95.6.3275

Hurle MR, Helms LR, Li L, Chan W, Wetzel R. 1994. A role for destabilizing amino acid replacements in light-chain amyloidosis. *Proc Natl Acad Sci* **91**:5446–5450.

Huynh TP V., Davis AA, Ulrich JD, Holtzman DM. 2017. Apolipoprotein E and Alzheimer’s disease: The influence of apolipoprotein E on amyloid-β and other amyloidogenic proteins. *J Lipid Res* **58**:824–836. doi:10.1194/jlr.R075481

Iñaki Guijarro J, Sunde M, Jones JA, Campbelli ID, Dobson CM. 1998. Amyloid fibril formation by an SH3 domain. *Proc Natl Acad Sci U S A* **95**:4224–4228. doi:10.1073/pnas.95.8.4224

Jablonski A. 1933. Efficiency of Anti-Stokes Fluorescence in Dyes. *Nature* **131**:839–840.

Jahn TR, Tennent GA, Radford SE. 2008. A common b-sheet architecture underlies in vitro and in vivo ??2-microglobulin amyloid fibrils. *J Biol Chem* **283**:17279–17286. doi:10.1074/jbc.M710351200

Jerabek-Willemsen M, André T, Wanner R, Roth HM, Duhr S, Baaske P, Breitsprecher D. 2014. MicroScale Thermophoresis: Interaction analysis and beyond. *J Mol Struct* **1077**:101–113. doi:10.1016/j.molstruc.2014.03.009

Jin H, Komita M, Aoe T. 2017. The role of BiP retrieval by the KDEL receptor in the early secretory pathway and its effect on protein quality control and neurodegeneration. *Front Mol Neurosci* **10**:1–8. doi:10.3389/fnmol.2017.00222

Johnson G, Wu TT. 2000a. Kabat Database and its applications: 30 years after the first variability plot. *Nucleic Acids Res* **28**:214–218.

Johnson G, Wu TT. 2000b. Kabat Database and its applications: 30 years after the first variability plot. *Nucleic Acids Res* **28**:214–218. doi:10.1093/nar/28.1.214

Jomaa A, Fu YHH, Boehringer D, Leibundgut M, Shan SO, Ban N. 2017. Structure of the quaternary complex between SRP, SR, and translocon bound to the translating ribosome. *Nat Commun* **8**:1–9. doi:10.1038/ncomms15470

Jorgensen WL, Chandrasekhar J, Madura JD, Impey RW, Klein ML. 1983. Comparison of simple potential functions for simulating liquid water. *J Chem Phys* **79**:926–935. doi:10.1063/1.445869

Jung D, Alt FW. 2004. Unraveling V (D) J Recombination : Insights into Gene Regulation V (D) J recombination assembles antigen receptor **116**:299–311. doi:10.1016/S0092-8674(04)00039-X

Jung S jun, Kim JEH, Reithinger JH, Kim H. 2014. The Sec62-Sec63 translocon facilitates translocation of the C-terminus of membrane proteins. *J Cell Sci* **127**:4270–4278. doi:10.1242/jcs.153650

Kabsch W. 1993. Automatic processing of rotation diffraction data from crystals of initially unknown symmetry and cell constants. *J Appl Crystallogr* **26**:795–800. doi:10.1107/S0021889893005588

Kampinga HH, Craig EA. 2010. The Hsp70 chaperone machinery: J-proteins as drivers of functional specificity. *Nat Rev Mol Cell Biol* **11**:579–592. doi:doi:10.1038/nrm2941

Kassenbrock CK, Kelly RB. 1989. Interaction of heavy chain binding protein (BiP/GRP78) with adenine nucleotides. *EMBO J* **8**:1461–1467. doi:10.1002/j.1460-2075.1989.tb03529.x

Kastritis E, Anagnostopoulos A, Roussou M, Toumanidis S, Pamboukas C, Migkou M, Tassidou A, Xilouri I, Delibasi S, Psimenou E, Mellou S, Terpos E, Nanas J, Dimopoulos MA. 2007. Treatment of light chain (AL) amyloidosis with the combination of bortezomib and dexamethasone. *Haematologica* **92**:1351 LP – 1358. doi:10.3324/haematol.11325

Kazman P, Vielberg M, Cendales P, Hunziger L, Weber B, Hegenbart U, Zacharias M, Groll M, Buchner J, Scho S. 2020. Fatal amyloid formation in a patient ' s antibody light chain is caused by a single point mutation. *Elife* 1–23.

Kelly SM, Jess TJ, Price NC. 2005. How to study proteins by circular dichroism. *Biochim Biophys Acta - Proteins Proteomics* **1751**:119–139. doi:10.1016/j.bbapap.2005.06.005

Kihara M, Chatani E, Sakai M, Hasegawa K, Naiki H, Goto Y. 2005. Seeding-dependent maturation of β2-microglobulin amyloid fibrils at neutral pH. *J Biol Chem* **280**:12012–12018. doi:10.1074/jbc.M411949200

Knittler MR, Haas IG. 1992. Interaction of BiP with newly synthesized immunoglobulin light chain molecules: cycles of sequential binding and release. *EMBO J* **11**:1573–1581. doi:10.1002/j.1460-2075.1992.tb05202.x

Knowles TPJ, Vendruscolo M, Dobson CM. 2014. The amyloid state and its association with protein misfolding diseases. *Nat Rev Mol Cell Biol* **15**:384–396. doi:10.1038/nrm3810

Kopp MC, Larburu N, Durairaj V, Adams CJ, Ali MMU. 2019. UPR proteins IRE1 and PERK switch BiP from chaperone to ER stress sensor. *Nat Struct Mol Biol* **26**:1053–1062. doi:10.1038/s41594-019-0324-9

Kouroku Y, Fujita E, Tanida I, Ueno T, Isoai A, Kumagai H, Ogawa S, Kaufman RJ, Kominami E, Momoi T. 2007. ER stress (PERK/eIF2α phosphorylation) mediates the polyglutamine-induced LC3 conversion, an essential step for autophagy formation. *Cell Death Differ* **14**:230–239. doi:10.1038/sj.cdd.4401984

Kumar S, Dispenzieri A, Lacy MQ, Hayman SR, Buadi FK, Colby C, Laumann K, Zeldenrust SR, Leung N, Dingli D, Greipp PR, Lust JA, Russell SJ, Kyle RA, Rajkumar SV, Gertz MA. 2012. Revised prognostic staging system for light chain amyloidosis incorporating cardiac biomarkers and serum free light chain measurements. *J Clin Oncol* **30**:989–995. doi:10.1200/JCO.2011.38.5724

Kumar S, Rosenberg JM, Bouzida D, Swendsen RH, Kollman PA. 1992. THE weighted histogram analysis method for free-energy calculations on biomolecules. I. The method. *J Comput Chem* **13**:1011–1021. doi:10.1002/jcc.540130812

Kyle RA, Gertz MA, Greipp PR, Witzig TE, Lust JA, Lacy MQ, Therneau TM. 1997. A trial of three regimens for primary amyloidosis: Colchicine alone, melphalan and prednisone, melphalan, prednisone, and colchicine. *N Engl J Med* **336**:1202–1207. doi:10.1056/NEJM199704243361702

Laue TM, Stafford WF. 1999. Modern applications of analytical ultracentrifugation. *Annu Rev*

Biophys Biomol Struct **28**:75–100. doi:10.1146/annurev.biophys.28.1.75

Layne E. 1957. Spectrophotometric and Turbidimetric Methods for Measuring Proteins. *Methods Enzymol* **3**:447–454.

Levinthal C. 1969. How to fold graciously. *Mössbauer Spectrosc Biol Syst Proc* **24**:22–24.

Levy Y, Onuchic JN. 2006. Water Mediation in Protein Folding and Molecular Recognition. *Annu Rev Biophys Biomol Struct* **35**:389–415. doi:10.1146/annurev.biophys.35.040405.102134

Liao R, Jain M, Teller P, Connors LH, Ngoy S, Skinner M, Falk RH, Apstein CS. 2001. Infusion of light chains from patients with cardiac amyloidosis causes diastolic dysfunction in isolated mouse hearts. *Circulation* **104**:1594–1597. doi:10.1161/circ.104.14.1594

Liu C-C, Zhao N, Yuan F, Wang N, Linares C, Tsai C-W, Bu G. 2017. ApoE4 accelerates early seeding of amyloid pathology. *Neuon* **96**:1024–1032. doi:10.1016/j.neuron.2017.11.013

Liu CC, Kanekiyo T, Xu H BG. 2013. Apolipoprotein E and Alzheimer disease: risk, mechanisms, and therapy. *Nat Rev Neurol* **9**:106–118. doi:10.1038/nrneurol.2012.263.Apolipoprotein

Liu CY, Kaufman RJ. 2003. The unfolded protein response. *J Cell Sci* **116**:1861–1862. doi:10.1242/jcs.00408

Mahley RW, Rall SC. 2000. Apolipoprotein E: Far More Than a Lipid Transport Protein. *Annu Rev Genomics Hum Genet* **1**:507–537. doi:10.1146/annurev.genom.1.1.507

Maki R, Traunecker A, Sakano H, Roeder W, Tonegawa S. 1980. Exon shuffling generates an immunoglobulin heavy chain gene. *Proc Natl Acad Sci USA* **77**:2138–2142. doi:10.1073/pnas.77.4.2138

Makin OS, Serpell LC. 2005. Structures for amyloid fibrils. *FEBS J* **272**:5950–5961. doi:10.1111/j.1742-4658.2005.05025.x

Malmos KG, Blancas-mejia LM, Weber B, Ramirez-alvarado M, Naiki H, Otzen D, Gade K, Blancas-mejia LM, Weber B, Ramirez-alvarado M, Naiki H, Otzen D. 2017. ThT 101 : a primer on the use of thioflavin T to investigate amyloid formation. *Amyloid* **24**:1–16. doi:10.1080/13506129.2017.1304905

Mangione PP, Porcari R, Gillmore JD, Pucci P, Monti M, Porcari M, Giorgetti S, Marchese L, Raimondi S, Serpell LC, Chen W, Relini A, Marcoux J, Clatworthy IR, Taylor GW, Tennent GA, Robinson C V., Hawkins PN, Stoppini M, Wood SP, Pepys MB, Bellotti V. 2014. Proteolytic cleavage of Ser52Pro variant transthyretin triggers its amyloid fibrillogenesis. *Proc Natl Acad Sci U S A* **111**:1539–1544. doi:10.1073/pnas.1317488111

Marcinowski M, Höller M, Feige MJ, Baerend D, Lamb DC, Buchner J. 2011. Substrate

discrimination of the chaperone BiP by autonomous and cochaperone-regulated conformational transitions. *Nat Struct Mol Biol* **18**:150–159. doi:10.1038/nsmb.1970

Marcinowski M, Rosam M, Seitz C, Elferich J, Behnke J, Bello C, Feige MJ, Becker CFW, Antes I, Buchner J. 2013. Conformational selection in substrate recognition by Hsp70 chaperones. *J Mol Biol* **425**:466–474. doi:10.1016/j.jmb.2012.11.030

Mărgineanu I, Ghetie V. 1981. A selective model of plasma protein catabolism. *J Theor Biol* **90**:101–110. doi:10.1016/0022-5193(81)90124-7

Marshall KE, Serpell LC. 2009. Insights into the Structure of Amyloid Fibrils. *Open Biol J* **2**:185–192.

Mastrangelo IA, Ahmed M, Sato T, Liu W, Wang C, Hough P, Smith SO. 2006. High-resolution atomic force microscopy of soluble Aβ42 oligomers. *J Mol Biol* **358**:106–119. doi:10.1016/j.jmb.2006.01.042

Matsubara E, Soto C, Governale S, Frangione B, Ghiso J. 1996. Apolipoprotein J and Alzheimer's amyloid β solubility. *Biochem J* **316**:671–679. doi:10.1042/bj3160671

McCoy AJ, Grosse-Kunstleve RW, Adams PD, Winn MD, Storoni LC, Read RJ. 2007. Phaser crystallographic software. *J Appl Crystallogr* **40**:658–674. doi:10.1107/S0021889807021206

Merlini G, Bellotti V. 2003. Molecular Mechanisms of Amyloidosis. *N Engl J Med* **349**:583–596.

Merlini G, Seldin DC, Gertz MA. 2011. Amyloidosis: Pathogenesis and new therapeutic options. *J Clin Oncol* **29**:1924–1933. doi:10.1200/JCO.2010.32.2271

Moelbert S, Emberly E. 2004. Correlation between sequence hydrophobicity and surface-exposure pattern of database proteins. *Protein Sci* **13**:752–762. doi:10.1110/ps.03431704

Molvarec A, Prohászka Z, Nagy B, Szalay J, Füst G, Karádi I, Rigó J. 2006. Association of elevated serum heat-shock protein 70 concentration with transient hypertension of pregnancy, preeclampsia and superimposed preeclampsia: A case-control study. *J Hum Hypertens* **20**:780–786. doi:10.1038/sj.jhh.1002060

Monsellier E, Chiti F. 2007. Prevention of amyloid-like aggregation as a driving force of protein evolution. *EMBO Rep* **8**:737–742. doi:10.1038/sj.embor.7401034

Morgan GJ, Kelly JW. 2016a. The kinetic stability of a full-length antibody light chain dimer determines whether endoproteolysis can release amyloidogenic variable domains. *J Mol Biol* **428**:4280–4297.

Morgan GJ, Kelly JW. 2016b. The kinetic stability of a full-length antibody light chain dimer determines whether endoproteolysis can release amyloidogenic variable domains. *J Mol Biol* **428**:4280–4297. doi:10.1016/j.jmb.2016.08.021

Muta H, Lee YH, Kardos J, Lin Y, Yagi H, Goto Y. 2014. Supersaturation-limited Amyloid

fibrillation of Insulin revealed by ultrasonication. *J Biol Chem* **289**:18228–18238. doi:10.1074/jbc.M114.566950

Nakatsukasa K, Kamamura T, Brodsky JL. 2014. Recent technical developments in the study of ER-associated degradation. *Curr Opin Cell Biol* **0**:82–91. doi:10.1038/jid.2014.371

Navarro A, Del Valle E, Astudillo A, Del Rey CG, Tolivia J. 2003. Immunohistochemical study of distribution of apolipoproteins e and D in human cerebral β amyloid deposits. *Exp Neurol* **184**:697–704. doi:10.1016/S0014-4886(03)00315-7

Neira JL, Fersht AR. 1999. Exploring the folding funnel of a polypeptide chain by biophysical studies on protein fragments. *J Mol Biol* **285**:1309–1333. doi:10.1006/jmbi.1998.2249

Nicchitta C V., Blobel G. 1993. Lumenal proteins of the mammalian endoplasmic reticulum are required to complete protein translocation. *Cell* **73**:989–998. doi:10.1016/0092-8674(93)90276-V

Nielsen NS, Poulsen ET, Klintworth GK, Enghilf JJ. 2014. Insight into the Protein Composition of Immunoglobulin Light Chain Deposits of Eyelid, Orbital and Conjunctival Amyloidosis. *J Proteomics Bioinform* **s8**. doi:doi:10.4172/jpb.S8-002

Nokwe CN, Hora M, Zacharias M, Yagi H, John C, Reif B, Goto Y, Buchner J. 2015. The Antibody Light-Chain Linker Is Important for Domain Stability and Amyloid Formation. *J Mol Biol* **427**:3572–3586. doi:10.1016/j.jmb.2015.09.012

Nokwe CN, Hora M, Zacharias M, Yagi H, Peschek J, Reif B, Goto Y, Buchner J. 2016. A Stable Mutant Predisposes Antibody Domains to Amyloid Formation through Specific Non-Native Interactions. *J Mol Biol* **428**:1315–1332. doi:doi: 10.1016/j.jmb.2016.01.015

Nokwe CN, Zacharias M, Yagi H, Hora M, Reif B, Goto Y, Buchner J. 2014. A residue-specific shift in stability and amyloidogenicity of antibody variable domains. *J Biol Chem* **289**:26829–26846. doi:10.1074/jbc.M114.582247

Nuvolone M, Merlini G. 2016. Systemic amyloidosis: novel therapies and role of biomarkers. *Nephrol Dial Transpl* **0**:1–10. doi:10.1093/ndt/gfw305

Olsen KE, Sletten K, Westermark P. 1998. Fragments of the constant region of immunoglobulin light chains are constituents of AL-amyloid proteins. *Biochem Biophys Res Commun* **251**:642–647. doi:10.1006/bbrc.1998.9508

Onuchic JN, Wolynes PG. 2004. Theory of protein folding. *Curr Opin Struct Biol* **14**:70–75. doi:10.1016/j.sbi.2004.01.009

Orengo CA, Todd AE, Thornton JM. 1999. From protein structure to function. *Curr Opin Struct Biol* **9**:374–382. doi:10.1016/S0959-440X(99)80051-7

Palladini G, Perfetti V, Obici L, Caccialanza R, Semino A, Adami F, Cavallero G, Rustichelli R, Virga G, Merlini G. 2004. Association of melphalan and high-dose dexamethasone is effective and well tolerated in patients with AL (primary) amyloidosis who are ineligible for stem cell transplantation. *Blood* **103**:2936–2938. doi:10.1182/blood-2003-08-2788

Palladini G, Perfetti V, Perlini S, Obici L, Lavatelli F, Caccialanza R, Invernizzi R, Comotti B, Merlini G. 2005. The combination of thalidomide and intermediate-dose dexamethasone is an effective but toxic treatment for patients with primary amyloidosis (AL). *Blood* **105**:2949–2951. doi:10.1182/blood-2004-08-3231

Palladini G, Sachchithanantham S, Milani P, Gillmore J, Foli A, Lachmann H, Basset M, Hawkins P, Merlini G, Wechalekar AD. 2015. A European collaborative study of cyclophosphamide, bortezomib, anddexamethasone in upfront treatment of systemic AL amyloidosis. *Blood* **126**:612–615. doi:10.1182/blood-2015-01-620302.The

Pauling L, Corey RB, Branson HR. 1951. THE STRUCTURE OF PROTEINS: TWO HYDROGEN-BONDED HELICAL CONFIGURATIONS OF THE POLYPEPTIDE CHAIN. *Proc Natl Acad Sci USA* **37**:205–211.

Pepys MB. 2006. Amyloidosis. *Annu Rev Med* 223–41. doi:10.1146/annurev.med.57.121304.131243

Perfetti V, Garini P, Colli Vignarelli M, Marinone MG, Zorzoli I, Merlini G. 1995. Diagnostic approach to and follow-up of difficult cases of AL amyloidosis. *Haematologica* **80**:409–415.

Perfetti V, Palladini G, Casarini S, Navazza V, Rognoni P, Obici L, Invernizzi R, Perlini S, Klersy C, Merlini G. 2012. The repertoire of λ light chains causing predominant amyloid heart involvement and identification of a preferentially involved germline gene, IGLV1-44. *Blood* **119**:144–150. doi:10.1182/blood-2011-05-355784

Perrakis A, Sixma TK, Wilson KS, Lamzin VS. 1997. wARP: improvement and extension of crystallographic phases by weighted averaging of multiple-refined dummy atomic models. *Acta Crystallogr Sect D Biol Crystallogr* **53**:448–455. doi:10.1107/S0907444997005696

Piehl DW, Blancas-Mejía LM, Wall JS, Kennel SJ, Ramirez-Alvarado M, Rienstra CM. 2017. Immunoglobulin Light Chains Form an Extensive and Highly Ordered Fibril Involving the N- and C-Termini. *ACS Omega* **2**:712–720. doi:10.1021/acsomega.6b00494

Pobre KFR, Poet GJ, Hendershot LM. 2019. The endoplasmic reticulum (ER) chaperone BiP is a master regulator of ER functions: Getting by with a little help from ERdj friends. *J Biol Chem* **294**:2098–2108. doi:10.1074/jbc.REV118.002804

Poshusta TL, Sikkink LA, Leung N, Clark RJ, Dispenzieri A, Ramirez-Alvarado M. 2009. Mutations in specific structural regions of immunoglobulin light chains are associated with free light chain levels in patients with AL amyloidosis. *PLoS One* **4**. doi:10.1371/journal.pone.0005169

Privalov PL, Makhatadze GI. 1993. Contribution of Hydration to Protein Folding Thermodynamics II. The Entropy and Gibbs Energy of Hydration. *J Mol Biol* **232**:660–679.

Quock TP, Yan T, Chang E, Guthrie S, Broder MS. 2018. Epidemiology of AL amyloidosis: A real-world study using US claims data. *Blood Adv* **2**:1046–1053. doi:10.1182/bloodadvances.2018016402

Radamaker L, Lin Y, Annamalai K, Huhn S, Hegenbart U, Schönland SO, Fritz G, Schmidt M, Fändrich M. 2019. Cryo-EM structure of a light chain-derived amyloid fibril from a patient with systemic AL amyloidosis. *Nat Commun* **10**:1–8. doi:10.1038/s41467-019-09032-

Radford SE, Dobson CM. 1999. From computer simulations to human disease: Emerging themes in protein folding. *Cell* **97**:291–298. doi:10.1016/S0092-8674(00)80739-4

Ramakrishnan C, Ramachandran GN. 1964. Stereochemical criteria for polypeptide and protein chain conformations. II. Allowed conformations for a pair of peptide units. *Proc Indian Acad Sci - Sect A* **59**:909–933. doi:10.1007/BF03046447

Rambaran RN, Serpell LC. 2008. Amyloid fibrils Abnormal protein assembly. *Prion* **2**:112–117.

Ramirez-Alvarado M. 2012. Amyloid Formation in Light Chain Amyloidosis. *Curr Top Med Chem* **12**:2523–2533. doi:10.2174/1568026611212220007

Rand KD, Zehl M, Jørgensen TJD. 2014. Measuring the Hydrogen / Deuterium Exchange of Proteins at High Spatial Resolution by Mass Spectrometry : Overcoming Gas-Phase Hydrogen / Deuterium Scrambling. *Acc Chem Res* **47**:3018–3027. doi:10.1021/ar500194w

Reddy P, Sparvoli A, Fagioli C, Fassina G, Sitia R. 1996. Formation of reversible disulfide bonds with the protein matrix of the endoplasmic reticulum correlates with the retention of unassembled Ig light chains. *EMBO J* **15**:2077–2085. doi:10.1002/j.1460-2075.1996.tb00561.x

Reece DE, Hegenbart U, Sanchorawala V, Merlini G, Palladini G, Bladé J, Fermand JP, Hassoun H, Heffner L, Vescio RA, Liu K, Enny C, Esseltine DL, Van De Velde H, Cakana A, Comenzo RL. 2011. Efficacy and safety of once-weekly and twice-weekly bortezomib in patients with relapsed systemic AL amyloidosis: Results of a phase 1/2 study. *Blood* **118**:865–873. doi:10.1182/blood-2011-02-334227

Rennella E, Morgan GJ, Kelly JW, Kay LE. 2019. Role of domain interactions in the aggregation of full-length immunoglobulin light chains. *Proc Natl Acad Sci* **116**:854–863. doi:10.1073/pnas.1817538116

Rezeli M, Zetterberg H, Blennow K, Brinkmalm A, Laurell T, Hansson O, Marko-Varga G. 2015. Quantification of total apolipoprotein E and its specific isoforms in cerebrospinal fluid and blood in Alzheimer's disease and other neurodegenerative diseases. *EuPA Open Proteomics* **8**:137–143. doi:10.1016/j.euprot.2015.07.012

Ribatti D. 2018. A historical perspective on milestones in multiple myeloma research. *Eur J*

Haematol **100**:221–228. doi:10.1111/ejh.13003

Richardson JS. 1981. The Anatomy and Taxonomy of Protein Structure, Adv Protein Chem. doi:10.1016/S0022-2836(77)80048-X

Richter K, Haslbeck M, Buchner J. 2010. The Heat Shock Response: Life on the Verge of Death. *Mol Cell* **40**:253–266. doi:10.1016/j.molcel.2010.10.006

Röcken C, Paris D, Steusloff K, Saeger W. 1997. Investigation of the Presence of Apolipoprotein E, Glycosaminoglycans, Basement Membrane Proteins, and Protease Inhibitors in Senile Interstitial Amyloid of the Pituitary. *Endocr Pathol* **8**:205–214. doi:10.1007/BF02738787

Rüdiger S, Buchberger A, Bukau B. 1997. Interaction of Hsp70 chaperones with substrates. *Nat Struct Biol* **4**:342–349. doi:10.1038/nsb0597-342

Ruggiano A, Foresti O, Carvalho P. 2014. ER-associated degradation: Protein quality control and beyond. *J Cell Biol* **204**:869–879. doi:10.1083/jcb.201312042

Sahoo BR, Genjo T, Nakayama TW, Stoddard AK, Ando T, Yasuhara K, Fierke CA, Ramamoorthy A. 2019. A cationic polymethacrylate-copolymer acts as an agonist for β-amyloid and an antagonist for amylin fibrillation. *Chem Sci* **10**:3976–3986. doi:10.1039/c8sc05771k

Sambrook J, Fritsch EF, Maniatis T. 1989. Molecular cloning: A laboratory manual, 2nd ed, Cold Spring Harbor Laboratory Press. New York, Cold Spring Harbor: Cold Spring Harbor Laboratory Press.

Sanchorawala V. 2006. Light-chain (AL) amyloidosis: diagnosis and treatment. *Clin J Am Soc Nephrol* **1**:1331–1341. doi:10.2215/CJN.02740806

Schmidt A, Annamalai K, Schmidt M, Grigorieff N, Fändrich M. 2016. Cryo-EM reveals the steric zipper structure of a light chain-derived amyloid fibril. *Proc Natl Acad Sci U S A* **113**:6200–6205. doi:10.1073/pnas.1522282113

Schneider M, Rosam M, Glaser M, Patronov A, Shah H, Back KC, Daake MA, Buchner J, Antes I. 2016. BiPPred: Combined sequence- and structure-based prediction of peptide binding to the Hsp70 chaperone BiP. *Proteins Struct Funct Bioinforma* **84**:1390–1407. doi:10.1002/prot.25084

Schroeder HWJ, Cavacini L. 2010. Structure and Function of Immunoglobulins. *J Allergy Clin Immunol* **125**:S41–S52. doi:10.1016/j.jaci.2009.09.046.Structure

Schuck P. 2000. Size-Distribution Analysis of Macromolecules by Sedimentation Velocity Ultracentrifugation and Lamm Equation Modeling. *Biophys J* **78**:1606–1619. doi:10.1016/S0006-3495(00)76713-0

Schwarz DS, Blower MD. 2016. The endoplasmic reticulum: Structure, function and response to cellular signaling. *Cell Mol Life Sci* **73**:79–94. doi:10.1007/s00018-015-2052-6

Serrano AL, Lomont JP, Tu L-H, Raleigh DP, Zanni MT. 2017. A Free Energy Barrier Caused by the Refolding of an Oligomeric Intermediate Controls the Lag Time of Amyloid Formation by hIAPP. *J Am Chem Soc* **129**:16748–16759. doi:10.1021/jacs.7b08830

Shamu CE, Walter P. 1996. Oligomerization and phosphorylation of the Ire1p kinase during intracellular signaling from the endoplasmic reticulum to the nucleus. *EMBO J* **15**:3028–3039. doi:10.1002/j.1460-2075.1996.tb00666.x

Shao S, Hegde RS. 2011. Membrane Protein Insertion at the Endoplasmic Reticulum. *Annu Rec Cell Dev Biol* **27**:25–56. doi:10.1146/annurev-cellbio-092910-154125

Shen Y, Hendershot LM. 2005. ERdj3, a Stress-inducible Endoplasmic Reticulum DnaJ Homologue, Serves as a CoFactor for BiP's Interactions with Unfolded Substrates. *Mol Biol Cell* **16**:40–50. doi:10.1091/mbc.e04-05-0434

Shi J, Guan J, Jiang B, Brenner DA, Del Monte F, Ward JE, Connors LH, Sawyer DB, Semigran MJ, Macgillivray TE, Seldin DC, Falk R, Liao R. 2010. Amyloidogenic light chains induce cardiomyocyte contractile dysfunction and apoptosis via a non-canonical p38α MAPK pathway. *Proc Natl Acad Sci U S A* **107**:4188–4193. doi:10.1073/pnas.0912263107

Shoulders MD, Ryno LM, Genereux JC, Moresco JJ, Tu G, Wu C, Iii JRY, Su AI, Kelly JW, Luke R. 2013. Stress-Independent Activation of XBP1s and/or ATF6 Reveals Three Functionally Diverse ER Proteostasis Environments. *Cell Rep* **3**:1279–1292. doi:10.1016/j.celrep.2013.03.024.Stress-Independent

Sidiqi MH, Gertz MA. 2019. Daratumumab for the treatment of AL Amyloidosis. *Leuk Lymphoma* **60**:295–301. doi:10.1080/10428194.2018.1485914

Skubák P, Pannu NS. 2013. Automatic protein structure solution from weak X-ray data. *Nat Commun* **4**:1–6.

Solomon A, Frangione B, Franklin EC. 1982. Bence Jones proteins and light chains of immunoglobulins. Preferential association of the V(λVI) subgroup of human light chains with amyloidosis AL(λ). *J Clin Invest* **70**:453–460. doi:10.1172/JCI110635

Solomon A, Weiss DT. 1995. Structural and functional properties of human λ-light-chain variable-region subgroups. *Clin Diagn Lab Immunol* **2**:387–394. doi:10.1128/cdli.2.4.387-394.1995

Sonnen AF-P, Yu C, Evans EJ, Stuart DI, Davis SJ, Gilbert RJC. 2010. Domain Metastability: A Molecular Basis for Immunoglobulin Deposition? *J Mol Biol* **399**:207–213. doi:10.1016/j.jmb.2010.04.011

Sörgjerd K, Ghafouri B, Jonsson BH, Kelly JW, Blond SY, Hammarström P. 2006. Retention of misfolded mutant transthyretin by the chaperone BiP/GRP78 mitigates amyloidogenesis. *J Mol Biol* **356**:469–482. doi:10.1016/j.jmb.2005.11.051

Stefani M, Dobson CM. 2003. Protein aggregation and aggregate toxicity: New insights into

protein folding, misfolding diseases and biological evolution. *J Mol Med* **81**:678–699. doi:10.1007/s00109-003-0464-5

Stevens FJ. 2000. Four Structural Risk Factors Identify Most Fibril-Forming Kappa Light Chains. *Amyloid* **7**:200–211. doi:10.3109/13506120009146835

Stevens FJ, Argon Y. 1999. Protein folding in the ER. *Semin Cell Dev Biol* **10**:443–454. doi:10.1006/scdb.1999.0315

Stoscheck CM. 1990. Quantitation of protein. *Methods Enzymol* **182**:50–68.

Street AG, Mayo SL. 1999. Intrinsic β-sheet propensities result from van der Waals interactions between side chains and the local backbone. *Proc Natl Acad Sci U S A* **96**:9074–9076. doi:10.1073/pnas.96.16.9074

Stryer L. 1965. The interaction of a naphthalene dye with apomyoglobin and apohemoglobin. A fluorescent probe of non-polar binding sites. *J Mol Biol* **13**:482–95. doi:10.1016/s0022-2836(65)80111-5

Swuec P, Lavatelli F, Tasaki M, Paissoni C, Rognoni P, Maritan M, Brambilla F, Milani P, Mauri P, Camilloni C, Palladini G, Merlini G, Ricagno S, Bolognesi M. 2019. Cryo-EM structure of cardiac amyloid fibrils from an immunoglobulin light chain AL amyloidosis patient. *Nat Commun* **10**:1–9. doi:10.1038/s41467-019-09133-w

Thambisetty M. 2010. Do extracellular chaperone proteins in plasma have potential as Alzheimers disease biomarkers? *Biomark Med* **4**:831–834. doi:10.2217/bmm.10.108

Thies MJW, Pirkl F. 2000. Chromatographic purification of the C H 2 domain of the monoclonal antibody MAK33. *J Chromatogr B* **737**:63–69. doi:10.1016/S0378-4347(99)00377-1

Tonegawa S. 1983. Somatic generation of antibody diversity. *Nature* **302**:575–581. doi:10.1038/302575a0 ID

Trinkaus-Randall V, Walsh MT, Steeves S, Monis G, Connors LH, Skinner M. 2005. Cellular response of cardiac fibroblasts to amyloidogenic light chains. *Am J Pathol* **166**:197–208. doi:10.1016/S0002-9440(10)62244-4

Tsai J, Douglas MG. 1996. A conserved HPD sequence of the J-domain is necessary for YDJ1 stimulation of Hsp70 ATPase activity at a site distinct from substrate binding. *J Biol Chem* **271**:9347–9354. doi:10.1074/jbc.271.16.9347

Uversky VN, Fink AL. 2004. Conformational constraints for amyloid fibrillation: The importance of being unfolded. *Biochim Biophys Acta - Proteins Proteomics* **1698**:131–153. doi:10.1016/j.bbapap.2003.12.008

Vagin AA, Steiner RA, Lebedev AA, Potterton L, McNicholas S, Long F, Mushudov GN. 2004. REFMAC5 dictionary: organization of prior chemical knowledge and guidelines for its use. *Acta Crystallogr Sect D Biol Crystallogr* **60**:2184–2195. doi:10.1107/S0907444904023510

Vassar PS, Culling CF. 1959. Fluorescent Stains, With special reference to Amyloid and Connective Tissue. *Arch Pathol* **68**:487–98.

Wall J, Schell M, Murphy C, Hrncic R, Stevens FJ, Solomon A. 1999. Thermodynamic instability of human λ6 light chains: Correlation with fibrillogenicity. *Biochemistry* **38**:14101–14108. doi:10.1021/bi991131j

Walsh RC, Koukoulas I, Garnham A, Moseley PL, Hargreaves M, Febbraio MA. 2001. Exercise increases serum Hsp72 in humans. *Cell Stress Chaperones* **6**:386–393. doi:10.1379/1466-1268(2001)006<0386:EISHIH>2.0.CO;2

Walter P, Ron D. 2011. The Unfolded Protein Response: From Stress Pathway to Homeostatic Regulation. *Science (80-)* **334**:1081–1086. doi:10.1126/science.1209038

Walter S, Buchner J. 2002. Molecular Chaperones - Cellular Machines for Protein Folding. *Angew Chemie - Int Ed* **41**:1098–1113. doi:10.1002/chin.200229281

Wang Ji, Kang R, Huang H, Xi X, Wang B, Wang Jianwei, Zhao Z. 2014. Hepatitis C virus core protein activates autophagy through EIF2AK3 and ATF6 UPR pathway-mediated MAP1LC3B and ATG12 expression. *Autophagy* **10**:766–784. doi:10.4161/auto.27954

Weber B., Hora M, Kazman P, Göbl C, Camilloni C, Reif B, Buchner J. 2018. The Antibody Light-Chain Linker Regulates Domain Orientation and Amyloidogenicity. *J Mol Biol* **430**:4925–4940. doi:10.1016/j.jmb.2018.10.024

Weber Benedikt, Hora M, Kazman P, Göbl C, Camilloni C, Reif B, Buchner J. 2018. The Antibody Light-Chain Linker Regulates Domain Orientation and Amyloidogenicity. *J Mol Biol* **430**:4925–4940. doi:10.1016/j.jmb.2018.10.024

Wechalekar AD, Goodman HJB, Lachmann HJ, Offer M, Hawkins PN, Gillmore JD. 2007. Safety and efficacy of risk-adapted cyclophosphamide, thalidomide, and dexamethasone in systemic AL amyloidosis. *Blood* **109**:457–464. doi:10.1182/blood-2006-07-035352

Wechalekar AD, Schonland SO, Kastritis E, Gillmore JD, Dimopoulos MA, Lane T, Foli A, Foard D, Milani P, Rannigan L, Hegenbart U, Hawkins PN, Merlini G, Palladini G. 2013. A European collaborative study of treatment outcomes in 346 patients with cardiac stage III AL amyloidosis. *Blood* **121**:3420–3427. doi:10.1182/blood-2012-12-473066

Wilson MR, Yerbury JJ, Poon S. 2007. Potential roles of abundant extracellular chaperones in the control of amyloid formation and toxicity. *Mol Biosyst* **4**:42–52. doi:10.1039/b712728f

Wilson PC, Bouteiller O de, Liu Y-J, Potter K, Banchereau J, Capra JD, Pascual V. 1998. Somatic Hypermutation Introduces Insertions and Deletions into Immunoglobulin V Genes. *J Exp Med* **187**:59–70. doi:10.1084/jem.187.1.59

Winn MD, Ballard CC, Cowtan KD, Dodson EJ, Emsley P, Evans PR, Keegan RM, Krissinel EB, Leslie AGW, McCoy A, McNicholas SJ, Murshudov GN, Pannu NS, Potterton EA,

Powell HR, Read RJ, Vagin A, Wilson KS. 2011. Overview of the CCP4 suite and current developments. *Acta Crystallogr Sect D Biol Crystallogr* **67**:235–242. doi:10.1107/S0907444910045749

Wiseman RL, Powers ET, Buxbaum JN, Kelly JW, Balch WE. 2007. An Adaptable Standard for Protein Export from the Endoplasmic Reticulum. *Cell* **131**:809–821. doi:10.1016/j.cell.2007.10.025

Wisniewski T, Frangione B. 1992. Apolipoprotein E: A pathological chaperone protein in patients with cerebral and systemic amyloid. *Neurosci Lett* **135**:235–238. doi:10.1016/0304-3940(92)90444-C

Witteles RM, Liedtke M. 2019. AL Amyloidosis for the Cardiologist and Oncologist. *JACC CardioOncology* **1**:117–130. doi:10.1016/j.jaccao.2019.08.002

Wu TT, Kabat EA. 1970. An Analysis of the Sequences of the Variable Regions of Bence Jones Proteins and Myeloma Light Chains and Their Implications for Antibody Complementarity. *J Exp Med* **132**:211–250. doi:10.1084/jem.132.2.211

Wu X, Rapoport TA. 2018. Mechanistic insights into ER-associated protein degradation. *Curr Opin Cell Biol* **53**:22–28. doi:10.1016/j.ceb.2018.04.004

Wyatt AR, Yerbury JJ, Dabbs RA, Wilson MR. 2012. Roles of extracellular chaperones in amyloidosis. *J Mol Biol* **421**:499–516. doi:10.1016/j.jmb.2012.01.004

Wyatt AR, Yerbury JJ, Wilson MR. 2009. Structural characterization of clusterin-chaperone client protein complexes. *J Biol Chem* **284**:21920–21927. doi:10.1074/jbc.M109.033688

Yakupova EI, Bobyleva LG, Vikhlyantsev IM, Bobylev AG. 2019. Congo Red and amyloids: History and relationship. *Biosci Rep* **39**. doi:10.1042/BSR20181415

Yamamoto S, Hasegawa K, Yamaguchi I, Tsutsumi S, Kardos J, Goto Y, Gejyo F, Naiki H. 2004. Low concentrations of sodium dodecyl sulfate induce the extension of β2-microglobulin-related amyloid fibrils at a neutral pH. *Biochemistry* **43**:11075–11082. doi:10.1021/bi049262u

Yerbury JJ, Kumita JR, Meehan S, Dobson CM, Wilson MR. 2009. α2-Macroglobulin and haptoglobin suppress amyloid formation by interacting with prefibrillar protein species. *J Biol Chem* **284**:4246–4254. doi:10.1074/jbc.M807242200

Yerbury JJ, Poon S, Meehan S, Thompson B, Kumita JR, Dobson CM, Wilson MR. 2007. The extracellular chaperone clusterin influences amyloid formation and toxicity by interacting with prefibrillar structures. *FASEB J* **21**:2312–2322. doi:10.1096/fj.06-7986com

Yerbury JJ, Wilson MR. 2010. Extracellular chaperones modulate the effects of Alzheimer's patient cerebrospinal fluid on Aβ1-42 toxicity and uptake. *Cell Stress Chaperones* **15**:115–121. doi:10.1007/s12192-009-0122-0

Young JC, Agashe VR, Siegers K, Hartl FU. 2004. Pathways of chaperone-mediated protein

folding in the cytosol. *Nat Rev Mol Cell Biol* **5**:781–791. doi:10.1038/nrm1492

Young L, Jernigan RL, Covell DG. 1994. A role for surface hydrophobicity. *Protein Sci* **3**:717–729.

Zhang A, Hu P, Macgregor P, Xue Y, Fan H, Suchecki P, Olszewski L. 2014. Understanding the Conformational Impact of Chemical Modi fi cations on Monoclonal Antibodies with Diverse Sequence Variation Using Hydrogen/Deuterium Exchange Mass Spectrometry and Structural Modeling. *Anal Chem* **86**:3468–3475. doi:10.1021/ac404130a

Zolle S, Buxbaum J, Franklin EC, Scharff MD. 1970. Synthesis and Assembly of Immunoglobulins by malignant Human Plasmacytes. *J Exp Med* **132**:148–162. doi:10.1084/jem.132.1.148

10. PUBLICATIONS AND PRESENTATIONS

Publications

Kazman, P., Vielberg, M. T., Pulido Cendales, M. D., Hunziger, L., Weber, B., Hegenbart, U., Zacharias, M., Köhler, R., Schönland, S., Groll, M., & Buchner, J. (2020). Fatal amyloid formation in a patient's antibody light chain is caused by a single point mutation. *eLife*, *9*, e52300. https://doi.org/10.7554/eLife.52300

Weber, B., Hora, M., Kazman, P., Göbl, C., Camilloni, C., Reif, B., & Buchner, J. (2018). The Antibody Light Chain Linker Regulates Domain Orientation and Amyloidogenicity. Journal of molecular biology, 430(24), 4925-4940.

Conference attendances with presentation

Talk: Misfolding of antibody light chains, *Kickoff Meeting DFG FOR 2969, Heidelberg, Germany July 19th, 2019*

Talk: On the mechanism of fibril formation of antibody V_L domains, *3rd Sino-German Symposium on Protein Folding, Redox Regulation and Quality Control, Beijing, China, October 18th, 2017*

Poster: Disease-associated mutations in antibody V_L domains, *13th ER & Redox Club Meeting, Homburg, Germany, April, 2017*

Poster: Antibody light chain integrity in AL amyloidosis, *4th Biophysics of Amyloid Formation Meeting, Ulm, Germany, February, 2020*

Poster: A light chain's amyloidogenicity and the effect of chaperones, *3rd Biophysics of Amyloid Formation Meeting, Ulm, Germany, February, 2019*

Poster: Amyloidogenicity of a patient-derived variable light chain and the impact of ER chaperones, *EMBO Workshop, Protein quality control: From mechanism to disease, Costa de la Calma (Mallorca), Spain, April, 2019*

11. ACKNOWLEDGEMENT

An erster Stelle möchte ich meinem Doktorvater Johannes Buchner danken; für die Möglichkeit meine Doktorarbeit in seinem Labor anzufertigen, für die Unterstützung, das stetige Vertrauen und die Freiheit während der gesamten Doktorarbeitszeit.

Mein Dank gilt auch der gesamten Amyloid Forschergruppe und ihren Mitgliedern aus ganz Deutschland. Es ist toll, zu sehen wie so viele verschiedene Fachbereiche gemeinsam an einem Strang ziehen können. Hierbei möchte ich gesondert Ute Hegenbart und Stefan Schönland danken. Ihr habt mir durch euren ärztlichen Blickwinkel und euer Engagement nach jedem Treffen einen ganz besonderen Motivationsschub gegeben. Vielen Dank auch an meine Kooperationspartner von der TUM: Michael Groll, Marie-Theres Vielberg und Astrid König für die Kristallstrukturen; Martin Zacharias und Daniela Pulido Cendales für die MD Simulationen. Danke an Carsten Peters für die Hilfe mit den TEM Messungen. Vielen Dank Gina Feind und Florian Rührnößl für die Durchführung der HDX Messungen.

A very big thank you to Linda Hendershot and her team from St. Jude Children's Research Hospital in Memphis, TN, USA. It was awesome to visit your lab during my PhD and I am beyond thankful for this opportunity. A special thanks goes to Melissa Mann! I hope that many more "Buchners" get the chance to enjoy a stay in Memphis.

Vielen Dank an den gesamten Lehrstuhl für Biotechnologie! Ich habe durch euch sehr viel, fachlich und persönlich, gelernt. Die spaßigen Abende und Tage, die anstrengenden und weniger anstrengenden Zeiten, die interessante Diskussionen und auch die persönlichen Herausforderungen werden definitiv in Erinnerung bleiben! Ganz besonders möchte ich hierbei Benedikt Weber danken, der mir immer und in jeder Lebenslage mit Rat und Tat zur Seite stand. Danke auch an euch, Moritz Mühlhofer, Mareike Riedl, Jannis Lawatscheck und auch Tuan Nguyen, dafür dass ihr mit mir alle Hochs und Tiefs durchgemacht habt. Vielen Dank an „die Ehemaligen" Sandrine Stiegler, Christina Nickels und Franziska Tippel. Ich bin froh euch kennen gelernt zu haben! Auch meinen zahlreichen Praktikanten und Masteranden möchte ich für ihre Mithilfe danken!

Ganz besonders möchte ich meinen Eltern danken. Für ihre bedingungslose Unterstützung von Anfang an und ihr Vertrauen in mich. Ohne euch wäre das alles nicht möglich gewesen. Danke auch an meine Geschwister Nora, Aida, Timon und Fidel, die alle auf ganz unterschiedliche Weise ihren Teil beigetragen haben.

Danke Jakob! Für alles!

12. DECLARATION

I, Pamina Kazman, hereby declare that this thesis was prepared by me independently and using only references and resources stated here. The work has not been submitted to any audit commission. Parts of this work were published in scientific journals.

Hiermit erkläre ich, Pamina Kazman, dass ich die vorliegende Arbeit selbstständig verfasst und keine anderen als die angegebenen Quellen und Hilfsmittel verwendet habe. Die Arbeit wurde noch keiner anderen Prüfungsbehörde vorgelegt. Teile dieser Arbeit wurden in wissenschaftlichen Journalen veröffentlicht.

_____

Pamina Kazman